

EFFECT OF LEADING EDGE TUBERCLES ON AIRFOIL PERFORMANCE

By

Kristy Lee Hansen

A Thesis submitted in fulfilment of the requirements for the
Degree of Doctor of Philosophy

**SCHOOL OF MECHANICAL
ENGINEERING**



THE UNIVERSITY
of **ADELAIDE**

July 2012

© Kristy Lee Hansen

Abstract of thesis

This thesis provides a detailed account of an experimental investigation into the effects of leading edge sinusoidal protrusions (tubercles) on the performance of airfoils. The leading edge geometry was inspired by the morphology of the Humpback whale flipper, which is a highly acrobatic species. The aim of this study is to investigate the potential advantages and disadvantages of incorporating tubercles into the leading edge of an airfoil. Specific parameters have been varied to identify an optimum tubercle configuration in terms of improved lift performance with minimal drag penalties.

The investigation has shown that for all tubercle arrangements investigated, increased lift performance in the post-stall regime comes at the expense of degraded lift performance in the pre-stall regime. However, it has also been noted that through optimizing the amplitude and wavelength of the tubercles, pre-stall lift performance approaches the values attained by the unmodified airfoil and post-stall performance is much improved. In general, the configuration which demonstrates the best performance in terms of maximum lift coefficient, maximum stall angle and minimum drag has the smallest amplitude and wavelength tubercles. A new alternative modification has also been explored, whereby sinusoidal surface waviness is incorporated into the airfoil, giving a spanwise variation in local attack angle. Results indicate that optimisation of this configuration leads to similar performance advantages as the best-performing tubercle configuration. It is believed that the flow mechanism responsible for performance variation is similar to tubercles.

The deterioration in pre-stall performance for airfoils with tubercles in the current study has been explained in terms of Reynolds number effects and also the relatively weak spanwise flow in the boundary layer. In swept and tapered wings such as the Humpback whale flipper, spanwise flow occurs along the entire span, so the effect of tubercles can be expected to be much larger.

Surface pressure measurements have indicated that the region of separation and reattachment for airfoils with tubercles is restricted to the trough between the tubercles rather than extending across the entire span. Hence, leading-edge separation is initiated at the troughs but occurs at a higher angle of attack for other locations, leading to a delayed overall stall for airfoils with tubercles. In addition, integration of the surface pressures

along the airfoil chord has indicated that lift, and hence circulation, varies with spanwise position, providing suitable conditions for the formation of streamwise vorticity. A spanwise variation in circulation is also predicted for the wavy airfoil since the relative angle of attack varies along the span.

Counter-rotating streamwise vortices have been identified in the troughs between tubercles using particle image velocimetry in a series of cross-streamwise, cross-chordwise planes which have not been investigated previously using this technique. The associated peak primary vorticity and circulation have been found to increase with angle of attack for a given measurement plane. This provides an explanation for the effectiveness of tubercles post-stall since an increased primary vortex strength leads to a greater boundary layer momentum exchange. The results show that the magnitude of the circulation generally increases in the streamwise direction, except when there exist secondary vortex structures of opposite sign on the flow side of the primary vortices. A proposed mechanism for this increasing circulation of the primary vortices is the entrainment of secondary vorticity which is generated between the adjacent primary vortex and the airfoil surface. It is postulated that this process of entrainment alternates between the primary vortices in an unsteady fashion.

Leading edge tubercles have also been found to mitigate tonal noise associated with the NACA 0021 and the NACA 65-021 at all angles of attack in a novel investigation. Elimination of the tonal noise occurred for the majority of modified airfoils and in many cases the broadband noise level was also reduced for certain frequency ranges. It is believed that tonal noise elimination is facilitated by the presence of the streamwise vortices and that the spanwise variation in separation location is also an important factor. Both characteristics modify the stability characteristics of the boundary layer, altering the frequency of velocity fluctuations in the shear layer near the trailing edge. This affects the coherence of the vortex generation downstream of the trailing edge, hence leading to a decrease in trailing edge noise generation.

Statement of Originality

I, Kristy Lee Hansen certify that this work contains no material which has been accepted for the award of any other degree or diploma in any university or other tertiary institution and, to the best of my knowledge and belief, contains no material previously published or written by another person, except where due reference has been made in the text.

I give consent to this copy of my thesis, when deposited in the University Library, being made available for loan and photocopying, subject to the provisions of Copyright Act, 1968.

I also give permission for the digital version of my thesis to be made available on the web, via the University's digital research repository, the Library catalogue and also through web search engines, unless permission has been granted by the University to restrict access for a period of time.

Signed: _____

Kristy Lee Hansen

Date: January 2012

Acknowledgements

I would like to thank all who have helped me during my candidature. I am especially grateful to my supervisors Associate Professor Richard Kelso and Associate Professor Bassam Dally for giving me the opportunity to work on this project and for their contribution and advice. I am also sincerely grateful to my father, Professor Colin Hansen, who continually encouraged me and offered valuable technical support. I also appreciate the support of Associate Professor Con Doolan who made valuable contributions to this work.

I would also like to thank the School's workshop staff, in particular Bill Finch for machining my airfoils with such perfection. I am also grateful to Dave Osborne for building by force measurement apparatus. In addition, I will never forget the workshop humour which always seemed to lift my spirits.

Thanks to my colleagues for their help and support both technically and emotionally. I'm especially grateful to those who engaged in complex intellectual discussions with me, which challenged my ideas and perceptions and broadened my understanding of the topic. I also appreciate those who listened to me asking a question, which I subsequently answered myself simply because I was given the opportunity to communicate my misunderstanding. In addition, I am thankful to those who passed on their knowledge of experimental apparatus, helping me to progress more efficiently.

Finally, thanks to my family and friends for being there for me and for believing in me. Especially to those who stopped asking me when I was going to finish and also expressed an interest in my topic. I also appreciate the encouragement of dear Damon Shokri who convinced me to publish despite my claims that my work was not ready for that. From this moment, I realised that the true value of my work could never be realised until I shared it with others.

Nomenclature

a_o	speed of sound = 343m/s
A	tubercle amplitude
b	airfoil span
c	airfoil chord
c	Pitot probe centreline
\bar{c}	mean airfoil chord
c_i	sensitivity coefficient
c_r	convection velocity of boundary layer instabilities
C	cross-sectional area of wind tunnel
C_{Cf}	chordwise component of form drag coefficient
C_D	drag coefficient
C_{Di}	induced drag coefficient
C_{Du}	uncorrected drag coefficient.
C_L	lift coefficient
C_{Lmax}	maximum lift coefficient
C_{Lu}	uncorrected lift coefficient
$\Delta C_{L,sc}$	change in lift coefficient due to streamline curvature
$C_{M_{1/4}}$	pitching moment coefficient at the quarter-chord position
$C_{M_{1/4u}}$	uncorrected pitching moment coefficient
C_N	normal coefficient
C_p	pressure coefficient
d	Pitot tube diameter
d_{diff}	diffraction limited image diameter
d_o	distance between object and image planes
d_p	particle diameter
d^+	non-dimensional Pitot diameter
D	drag
D_a	aperture diameter.
D_i	diagonal of camera sensor frame
D_o	diagonal of object plane

f	frequency
f	camera focal length
f_n	discrete frequency related to primary tonal peak
f_s	peak tonal frequency
$f_{\#}$	f-number
F_C	chordwise force
F_N	normal force
h_{eff}	effective tubercle height
h	height of wind tunnel test section
h_{max}	airfoil camber
H	shape factor
H	height of wind-tunnel jet
l_c	height or width of CCD array
L	lift
L	suitable length scale
L_c	characteristic length
L	length of aeroacoustic feedback loop
$(L/c)_p$	normalised length of separation bubble on pressure surface
$(L/c)_s$	normalised length of separation bubble on suction surface
k	roughness height
k	coverage factor
M	magnification factor
n	total number of measurements
n_v	number of vectors across the diameter of a vortex
N_{IW}	number of interrogation windows across image
p	pressure at airfoil surface
p_{∞}	freestream statics pressure
q	dynamic pressure
s^+	spanwise spacing between riblets in wall units
s	spanwise spacing between riblets
r_i	residual
r_m	median residual
r_o	conversion factor between pixel units at CCD array to mm

r_0^*	normalised residual
R	half-width of wind tunnel.
Re	Reynolds number
Re_x	Reynolds number based on boundary layer development length
Re_{δ^*}	Reynolds number based on boundary layer displacement thickness
Re_{θ}	Reynolds number based on boundary layer momentum thickness
S	planform area
Stk	Stokes number
t	airfoil thickness
ΔT	time delay between laser pulses
Tu	turbulence intensity
u	velocity component in streamwise (x) direction
u_c	combined standard uncertainty
u_k	velocity of flow at top of roughness element
u_{τ}	frictional velocity
U	expanded uncertainty
U_c	characteristic velocity
U_i	uncertainty component
U_{∞}	freestream velocity
$\overline{u'}$	average fluctuating velocity component in streamwise (x) direction
v	velocity component in vertical (y) direction
ν	degrees of freedom
ν_{eff}	effective degrees of freedom
ν_s	particle settling velocity
ν_0'	estimated vector for outlier replacement
$\overline{v'}$	average fluctuating velocity component in vertical (y) direction
$\tilde{\nu}$	“smoothed” vector value determined using an adaptive Gaussian window
V	volts
\vec{V}_m	local median velocity vector
\vec{V}_0	central displacement vector
V_u	uncorrected velocity
ΔV	axial velocity due to doublet

w	downwash velocity component
w	velocity component in spanwise (z) direction
w_{ij}	weighting coefficient
$\overline{w'}$	average fluctuating velocity component in spanwise (z) direction
W	out-of-plane component of velocity
x	streamwise distance
\overline{x}	mean of data set
x_m	single measurement
x/c	non-dimensional chordwise distance
y	vertical distance
y_c	distance from wall to probe centreline
y^+	non-dimensional wall distance
Δy	streamline displacement correction
z	spanwise distance
Δz	light sheet thickness
ΔZ_0	light sheet thickness
α	angle of attack
α	non-dimensional velocity gradient
α_*	true angle of attack
$\Delta\alpha_{sc}$	change in attack angle due to streamline curvature
α'	actual angle of flow for finite-span airfoil
$\Delta\alpha$	angle induced by downwash from tip vortices
κ	Von Karman's constant
δ	boundary layer thickness
δ	buffer to account for laser jitter
δ^*	boundary layer displacement thickness
$\delta_{\Delta D}$	uncertainty in displacement
δ_e	uncertainty in particle image diameter
δ_g	uncertainty due to velocity gradient
δ_m	magnification uncertainty
δ_N	uncertainty due to sub-optimal particle seeding
δ_p	actual position of the particle

δ_p	perspective uncertainty
δ_l	uncertainty due to laser “jitter”
δ_w	wall proximity correction
ε	angular misalignment of load cell axes
ε	compensating factor for normalised median test
$\varepsilon_{\Delta D}$	relative uncertainty in displacement
ε_e	relative uncertainty in particle image diameter
ε_g	relative uncertainty due to velocity gradient
ε_m	relative magnification uncertainty
ε_N	relative uncertainty due to sub-optimal particle seeding
ε_p	relative perspective uncertainty
ε_l	relative uncertainty due to laser “jitter”
ε_u	random velocity error
ε_{sb}	solid blockage of model in wind tunnel
ε_{wb}	wake blockage of model in wind tunnel
$\varepsilon_{\Gamma-random}$	random error in circulation
$\varepsilon_{\Gamma-bias}$	bias error in circulation
$\varepsilon_{\omega-bias}$	bias error in vorticity
$\varepsilon_{\omega-rand}$	random error in vorticity
Γ	circulation
λ	tubercle wavelength
λ	wavelength of illuminating light
λ_2	shape factor
λ_0	noise transmission ratio
μ	dynamic viscosity
ν	kinematic viscosity
θ	relative rotation angle between a trough and peak for wavy airfoil
θ	boundary layer momentum thickness
ρ, ρ_f	fluid density
ρ_p	particle density
σ	standard deviation

σ_s	uncertainty in particle displacement
τ	particle relaxation time
τ_w	wall shear stress
ω	vorticity
ω_t	vorticity threshold or contour
ζ	similarity variable
Δ	horizontal/vertical grid spacing
Δ_{f-q}	flashlamp q-switch delay

Table of Contents

Abstract of thesis.....	i
Statement of Originality.....	iii
Acknowledgements.....	v
Nomenclature.....	vii
Table of Contents.....	xiii
List of figures.....	xvii
List of tables.....	xxv
Chapter 1 Introduction to Flow Control.....	1
1.1 Introduction.....	1
1.2 Background.....	2
1.3 Flow Control.....	3
1.4 History and Development of Flow Control.....	4
1.5 Classifications of Flow Control.....	6
1.6 Passive Techniques.....	7
1.6.1 Lift Enhancement.....	7
1.6.2 Drag Reduction.....	14
1.7 Active Techniques.....	16
1.7.1 Lift Enhancement.....	17
1.7.2 Drag Reduction.....	24
1.7.3 Manipulation of Near Wall Viscosity.....	24
1.8 Summary and Discussion of Passive/Active Techniques.....	25
1.9 Purpose of Tubercles on Humpback Whale Flipper.....	27
1.10 Potential Applications for Engineered Devices.....	29
Chapter 2 Review of Literature and Associated Patents.....	35
2.1 Introduction.....	35
2.2 Research into Tubercles.....	35
2.2.1 Quantification of Performance Enhancement.....	36
2.2.2 Influence of Tubercle Configuration on Airfoil Performance.....	39
2.2.3 Finite Span Compared with Semi-Infinite Span Results.....	39
2.2.4 Reynolds Number Effects.....	40
2.2.5 Flow Patterns.....	41
2.2.6 Mechanism of Flow Control.....	46
2.3 Airfoil Tonal Noise.....	49
2.4 Existing Patents.....	53
2.4.1 Scalloped Wing Leading edge.....	53
2.4.2 Scalloped Leading edge Advancements.....	53
2.4.3 Scalloped Trailing Edge.....	54
2.4.4 Turbine/Compressor Rotor with Leading edge Tubercles.....	55
2.4.5 Spoked Bicycle Wheel.....	56
2.5 Summary and Discussion.....	57
2.6 Aims and objectives of current research.....	59
2.7 Remainder of Thesis.....	62
2.8 New Work in this Thesis.....	63
Chapter 3 Experimental Equipment and Methodology.....	65
3.1 Introduction.....	65
3.2 Airfoil Design.....	65

3.3	Force Measurements	72
3.3.1	Wind Tunnel	72
3.3.2	Boundary Layer Profile.....	73
3.3.3	Turbulence Intensity	79
3.3.4	Experimental Method for Force Measurements	80
3.3.5	Collection and Processing.....	82
3.3.6	Angular Misalignment Correction	83
3.3.7	Conversion of Rig to Test Half-Span Models.....	84
3.3.8	Boundary Layer Trip Design	85
3.3.9	Corrections of Wind Tunnel Effects for a Full-Span Model	86
3.3.10	Corrections of Wind Tunnel Effects for a Finite-Span Model	89
3.3.11	Force Measurement Uncertainty Analysis.....	94
3.4	Surface Pressure Measurements.....	98
3.4.1	Pressure Taps	99
3.4.2	Scanivalve	100
3.4.3	Pressure Tap Locations	101
3.4.4	Determining Lift and Form Drag From Pressure Distributions.....	103
3.4.5	Pressure Tap Uncertainty Analysis.....	104
3.5	Hydrogen Bubble Visualisation	105
3.5.1	Water Channel	105
3.5.2	Hydrogen Bubble Method.....	107
3.6	Particle Image Velocimetry.....	109
3.6.1	Specific Considerations for Airfoils with Tubercles	110
3.6.2	Thebarton Water Channel.....	112
3.6.3	Tracer Particles	114
3.6.4	Particle Image Size	116
3.6.5	Lasers	117
3.6.6	Light Sheet Optics.....	118
3.6.7	Time Delay Calculations.....	119
3.6.8	Timing and Synchronisation	120
3.6.9	Imaging System	121
3.6.10	PIV Image Processing.....	122
3.6.11	Post-Processing Techniques.....	124
3.6.12	Dynamic Velocity Range.....	127
3.6.13	Dynamic Spatial Range.....	128
3.6.14	Vorticity Estimation.....	128
3.6.15	Circulation Estimation	129
3.6.16	PIV Uncertainty Analysis	130
3.6.17	Summary	131
3.7	Acoustic Measurements	132
3.7.1	Anechoic Wind Tunnel Measurements.....	133
3.7.2	Acoustic Measurement Uncertainty Analysis.....	135
3.8	Airfoil Structural Resonance Frequency Measurements.....	136
Chapter 4	Lift and Drag Forces	141
4.1	Introduction	141
4.2	Full-Span Airfoils.....	142
4.2.1	Comparison with Published Data.....	142
4.2.2	Negative Lift Characteristic of the NACA 65-021 Airfoil	143
4.2.3	Comparison of Airfoils and Effects of Tubercles	147
4.2.4	Performance Effects of Variation in Tubercle Amplitude.....	148

4.2.5	Performance Effects of Variation in Tubercle Wavelength.....	149
4.2.6	Wavy Airfoil Comparison.....	151
4.2.7	Amplitude-to-wavelength Ratio (A/λ).....	152
4.2.8	Effective Device Height to Boundary Layer Thickness (h_{eff}/λ) Ratio	153
4.3	Half-Span Airfoils	155
4.3.1	Comparison of Results for Variation in Tubercle Amplitude.....	158
4.3.2	Comparison of Results for Variation in Tubercle Wavelength	161
4.3.3	Finite Effects on Wavy Airfoil Models	162
4.4	Quantification of Three-Dimensional Effects	163
4.5	Analysis of the Uncertainty Associated with Force Measurements.....	165
4.6	Summary	169
Chapter 5	Surface Pressure Characteristics	173
5.1	Introduction	173
5.2	Unmodified NACA 0021 Airfoil	175
5.2.1	Analysis of Pressure Distribution	175
5.2.2	Lift Coefficient Calculated from Pressure Distribution Data	180
5.2.3	Pressure Contours as a Function of Chordwise Position and Angle of Attack 182	
5.3	Unmodified NACA 65-021 Airfoil	183
5.3.1	Analysis of Pressure Distribution	183
5.3.2	Explanation for Negative Lift Phenomenon	188
5.3.3	Lift Coefficient Calculated from Pressure Distribution Data	190
5.3.4	Pressure Contours as a Function of Chordwise Position and Angle of Attack 191	
5.4	NACA 0021 with $A8\lambda30$ Leading Edge Tubercle Configuration	192
5.4.1	Analysis of Pressure Distribution	192
5.4.2	Lift Coefficient Calculated from Pressure Distribution Data	195
5.4.3	Pressure Contours as a Function of Chordwise Position and Angle of Attack 197	
5.5	Analysis of the Uncertainty Associated with Pressure Measurements	198
5.6	Summary	203
Chapter 6	Analysis of Flow Patterns	207
6.1	Introduction	207
6.2	Hydrogen Bubble Visualisation	208
6.3	Airfoil Selection for Particle Image Velocimetry (PIV)	210
6.4	Suitability of Ensemble Averaging	211
6.5	Vorticity	212
6.5.1	Summary of Vorticity Characteristics	218
6.6	Circulation	219
6.7	Discussion of Circulation	223
6.8	PIV Uncertainty Analysis.....	225
6.8.1	Estimation of Systematic Uncertainty in Particle Displacement	225
6.8.2	Estimation of Random Uncertainty in Particle Displacement	226
6.8.3	Uncertainties in Vorticity Estimation	229
6.8.4	Uncertainties in circulation estimation	230
6.9	Summary	231
Chapter 7	Acoustic Measurements	233
7.1	Introduction	233
7.2	Calibration.....	233
7.3	Acoustic Measurements in Hard-Walled Wind Tunnel	234

7.3.1	Noise Levels Associated with NACA 0021 Airfoil.....	235
7.3.2	Noise Levels Associated with NACA 65-021 Airfoil	239
7.4	Acoustic Measurements in Anechoic Wind Tunnel.....	241
7.4.1	Verification of the choice of frequency range	242
7.4.2	Noise Measurements for NACA 0021 Airfoil.....	242
7.4.3	Noise Measurements for NACA 65-021 Airfoil.....	245
7.4.4	Aeroacoustic Feedback Loop.....	246
7.5	Summary	248
Chapter 8	Conclusions.....	253
Chapter 9	Recommendations for Future Work.....	263
References	267
Appendix A	– Verification of force transducer calibration	285
Appendix B	– Efficiency Plots for Force Measurements	287
Appendix C	– Surface pressure measurement feasibility study.....	289
C1	Expected pressure forces	289
C2	Complexity	290
C3	Difficulty in interpreting images	291
Appendix D	– Airfoil structural resonance frequency measurements	293
Appendix E	– Proposed Flow Topology for a Tubercle.....	297

List of figures

Figure 1.1 - Humpback whale calf with tubercles visible on flipper leading edge (http://www.oceanwideimages.com).	2
Figure 1.2 – (a) Co-rotating vortex generator configuration, (b) counter-rotating vortex generator configuration (Adapted from Godard & Stanislas, 2006).	9
Figure 1.3 – Leading edge serrations (Soderman, 1972).	10
Figure 1.4 – Dye flow visualisation showing leading edge extensions and associated flow pattern (Adapted from Thompson, 1997).	10
Figure 1.5 – (a) Conventional trip strip turbulator, (b) Zig-zag trip strip turbulator.	11
Figure 1.6 – Oil flow visualisation showing the flow pattern and associated interpretation for a wavy wing at $\alpha = 0^\circ$ (Adapted from Zverkov & Zanin, 2009). The waviness is created by extending the grooves and humps of tubercles along the entire chord length.	12
Figure 1.7 – Schematic of movable flaps showing (a) attached flow at a low angle of attack and (b) separated flow at a high angle of attack (Meyer & Bechert, 1999).	13
Figure 1.8 – Various models and aircraft with wing fences used in the experiments by Williams (2009).	14
Figure 1.9 – Experimental investigation by Gaster to determine the response of compliant coatings to the Tollmien-Schlichting waves generated by a disturbance input (Gaster, 1987).	14
Figure 1.10 – Schematic showing scalloped groove riblets with associated velocity profiles (Bechert <i>et al.</i> , 2000).	15
Figure 1.11 – Sketch of airfoil-shaped large-eddy breakup devices in tandem in a turbulent boundary layer (Gad-el-Hak, 1990).	16
Figure 1.12 - The position of the leading edge flaps and slats on an airliner (Airbus A-300). In this picture, both devices are extended (Wikipedia, 2010).	17
Figure 1.13 - Krueger flap, an example of leading edge flap device (Swatton, 2011).	18
Figure 1.14 – Instantaneous image of Gurney flap showing vortex formation as well as upwards deflection of the flow (Carpenter & Houghton, 2003).	19
Figure 1.15 - Schematic of zero net mass flux jet with acoustic actuator (adapted from Gillaranz <i>et al.</i> , 2002).	20
Figure 1.16 - Flow visualisation of the uncontrolled (left) and controlled (right) NACA 0015 airfoil at $\alpha = 18^\circ$ (Tuck and Soria, 2004).	21
Figure 1.17 – Leading edge slots (Dingle & Tooley, 2005).	21
Figure 1.18 – Schematic of vortex generator jet actuator showing pitch angle of 30° and a rotatable plug to vary the skew angle (Khan & Johnson, 2000).	22
Figure 1.19 – Flow visualisation for NACA 0015 airfoil at $\alpha = 12^\circ$ showing separation in the absence of flow control (left) and flow reattachment with plasma (right) (Roth, 2003).	24
Figure 1.20 – Typical Reynolds number range for various applications (Adapted from Lissaman, 1983).	29
Figure 1.21- Surfboard fin with leading edge tubercles (Stafford, 2010)	32
Figure 1.22 - Altra-Air Fan 2.4m with leading edge tubercles (Fanmaster, 2011).	33
Figure 2.1 – (a) Experimental models, (b) Lift Coefficient vs. angle of attack and (c) Lift/drag ratio. Solid lines: unmodified airfoil, triangles: modified airfoil (Miklosovic <i>et al.</i> , 2004).	37
Figure 2.2 – (a) Model whale flippers, sweep angles of 15° & 30° , (b) Lift plots, sweep angle = 15° (Murray <i>et al.</i> , 2005).	37
Figure 2.3 - Panel method simulation of flow over a finite span wing at $\alpha = 10^\circ$ with straight leading edge (<i>left</i>) and leading edge tubercles (<i>right</i>). Colours represent the pressure differences on the wing. (Watts & Fish, 2001).	42
Figure 2.4 - Streamlines at the edge of the boundary layer (Watts & Fish, 2001).	42
Figure 2.5 – Pressure contours and streamlines for NACA 63-021 with and without tubercles (Fish and Lauder, 2006).	43
Figure 2.6 – Dye flow visualisation showing formation of streamwise vortices at $\alpha = 24^\circ$ after stall. (a) Unmodified airfoil and (b) Airfoil with tubercles, $\lambda = 0.05 c$ and $A = 0.12 c$ (right). (Custodio, 2008).	44
Figure 2.7 – (a) Instantaneous vorticity magnitude slices in span-wise direction for $\alpha = 15^\circ$ and (b) Averaged shear-stress lines for $\alpha = 15^\circ$, $Re = 500,000$ (Pedro & Kobayashi, 2008).	45
Figure 2.8 – (a) Leading edge sheet cavitation and tip vortex cavitation on the smooth rudder, $\alpha =$ 17.0° and (b) Cloud cavitation in troughs between tubercles and tip vortex cavitation on	

modified rudder, $\alpha = 15.8^\circ$. $Re = 786,000$ (Weber <i>et al.</i> , 2010). Cavitation is highlighted by black arrows.....	46
Figure 2.9 – Schematic showing movement of vortices towards troughs as predicted using the method of images (Custodio, 2008). Image vortices shown in red are adapted.....	48
Figure 2.10 - Schematic of tonal noise generating mechanism as portrayed by Desquenes (2007).....	52
Figure 2.11 – Cross-sectional view taken from the leading edge of a tubercle to the trailing edge (Watts & Fish, 2006).	54
Figure 2.12 – An illustrative perspective view portraying the invention (Presz Jr. <i>et al.</i> , 1989).....	55
Figure 2.13 – (a) Yacht with invention incorporated on the sail, keel and rudder (b) Gas turbine with external casings taking the form of the invention (c) Stator vane with the invention included on the trailing edge (Presz Jr. <i>et al.</i> , 1989).	55
Figure 2.14 –Bicycle wheel with tubercles on leading edge of spokes (Zibkoff, 2009).....	56
Figure 3.1 – Process used to construct model airfoils with tubercles.	66
Figure 3.2 – Associated whale flipper (Fish & Battle, 1995).	68
Figure 3.3 - Section view of airfoil with tubercles (a) 3D view, (b) Plan view with characteristic dimensions.	70
Figure 3.4 – Set of NACA 0021 and NACA 65-021 airfoils with tubercles (left and right respectively).	70
Figure 3.5 - Process used to model wavy airfoils.....	71
Figure 3.6 – Sections of wavy models with labels, (a) $\theta 4\lambda 15$, (b) $\theta 4\lambda 30$ and (c) $\theta 2\lambda 30$	71
Figure 3.7 – Schematic of the wind tunnel used for force and pressure tapping measurements.....	73
Figure 3.8 – Velocity profile at wind-tunnel contraction exit normalised with respect to mean velocity.	73
Figure 3.9 – Plot of boundary layer profile, $Re = 120,000$	75
Figure 3.10 – Schematic of displacement correction.	76
Figure 3.11 – Schematic of wall proximity correction.	76
Figure 3.12 – Velocity distribution for a turbulent boundary layer.....	78
Figure 3.13 - Plot of output voltage against freestream velocity for hot-wire calibration.....	80
Figure 3.14 – Load cell arrangement	81
Figure 3.15 – Experimental set-up	81
Figure 3.16 - Lift and Drag Forces.....	83
Figure 3.17 – Schematic of airfoil showing relative force transducer axes, F_x and F_y and misalignment, ε	84
Figure 3.18 – Modified mount for analysis of three-dimensional effects, (a) original frame (b) modified lowered frame, (c) structure used to gain height and block hole in test section.	85
Figure 3.19 – Schematic showing method of images used to simulate three-dimensional model.	90
Figure 3.20 – Relative contribution of various sources of drag (Barlow <i>et al.</i> , 1999).	91
Figure 3.21 – Image system for a three-dimensional model in a closed rectangular test section (Barlow <i>et al.</i> , 1999). Note that the model in the current study is mounted vertically.....	92
Figure 3.22 – Image vortex locations for a closed round jet (Barlow <i>et al.</i> , 1999).	93
Figure 3.23 - Block diagram of Scanivalve pressure multiplexer and associated hardware, (a) data logger, (b) Scanivalve controller, (c) Scanivalve and (d) Baratron pressure transducer	101
Figure 3.24 – Timing diagram in reference frame of controller.....	101
Figure 3.25 – Pressure tap locations for unmodified airfoils.	102
Figure 3.26 – Modified airfoil showing three rows of pressure taps.	102
Figure 3.27 – Coordinate system and stress definitions.	104
Figure 3.28 – Water tunnel facility used for hydrogen bubble visualisation.	106
Figure 3.29 – Independent dye visualisation and particle image velocimetry (PIV) for water tunnel calibration (ER Hassan 2011, personal communication).....	107
Figure 3.30 – Mount used in water tunnel for hydrogen bubble visualisation experiments.	108
Figure 3.31 – Examples of generic hydrogen bubble wire designs, (a) horizontal wire probe, (b) vertical wire probe (Smits & Lim, 2000).	109
Figure 3.32 – Section of airfoil at $\alpha = 5^\circ$ with tubercles showing particle image velocimetry measurement planes from a perspective viewpoint.....	111
Figure 3.33 – Typical field of view for PIV experiments.	112
Figure 3.34 – Thebarton water tunnel used for PIV experiments.	113
Figure 3.35 – Particle image velocimetry calibration for Thebarton water tunnel.....	114
Figure 3.36 – Histogram of PIV data showing the “peak-locking” effect (Raffel <i>et al.</i> , 1998).	116
Figure 3.37 – Energy output from laser cavity as a function of Flash lamp – Q switch delay.	118
Figure 3.38 – Optics set-up for particle image velocimetry experiments (not to scale).	119

Figure 3.39 – Timing diagram for laser/camera synchronisation.	121
Figure 3.40 – Schematic of perspective error (not to scale).	131
Figure 3.41 – Schematic of microphone positions.	133
Figure 3.42 – Anechoic wind tunnel facility.	134
Figure 3.43 - Mount for anechoic wind tunnel.	134
Figure 3.44 – Schematic showing accelerometer positions for vertical mount (left) and horizontal mount (right).	138
Figure 3.45 – Structural resonance frequency measurements for unmodified NACA 0021 airfoil. (a) Vertical mount (b) horizontal mount.	140
Figure 3.46 - Structural resonance frequency measurements for NACA 0021 airfoil with $A2\lambda7.5$ tubercle configuration. (a) Vertical mount (b) horizontal mount.	140
Figure 4.1 - Lift coefficient vs. angle of attack for NACA 0021 compared with experimental data for NACA 0020 (Miklosovic, 2007).	142
Figure 4.2 - Drag coefficient vs. angle of attack for NACA 0021 compared with experimental data for NACA 0020 (Miklosovic, 2007).	142
Figure 4.3 - Repeatability and influence of gap on lift coefficient for NACA 0021,	143
Figure 4.4 - Repeatability and influence of gap on drag coefficient for NACA 0021,	143
Figure 4.5 - Lift coefficient plotted against angle of attack for NACA 65-021,	144
Figure 4.6 – Drag coefficient plotted against angle of attack for NACA 65-021,	144
Figure 4.7 – Effect of trip height on lift coefficient for NACA 65-021 ($d = 5\text{mm}$),	145
Figure 4.8 – Effect of trip height on drag coefficient for NACA 65-021 ($d = 5\text{mm}$), $Re = 120,000$	145
Figure 4.9 – Effect of trip position on lift coefficient for NACA 65-021 ($k = 0.4\text{mm}$),	146
Figure 4.10 – Effect of trip position on drag coefficient for NACA 65-021 ($k = 0.4\text{mm}$),	146
Figure 4.11 - <u>Tripped</u> lift coefficient plotted against angle of attack for NACA 65-021,	146
Figure 4.12 - <u>Tripped</u> drag coefficient plotted against angle of attack for NACA 65-021,	146
Figure 4.13 - Tubercle amplitude variation and the effect on lift coefficient for NACA 0021, $Re = 120,000$	147
Figure 4.14 - Tubercle amplitude variation and the effect on drag coefficient for NACA 0021, $Re = 120,000$	147
Figure 4.15 - Further amplitude reduction and the effect on lift coefficient for NACA 0021, $Re = 120,000$	149
Figure 4.16 - Further amplitude reduction and the effect on drag coefficient for NACA 0021, $Re = 120,000$	149
Figure 4.17 - Tubercle wavelength variation and the effect on lift coefficient for	150
Figure 4.18 - Tubercle wavelength variation and the effect on drag coefficient for NACA 0021, $Re = 120,000$	150
Figure 4.19 - Lift coefficient plot for various wavy airfoil configurations and comparison with the most successful tubercle configuration, $Re = 120,000$	151
Figure 4.20 - Drag coefficient plot for various wavy airfoil configurations and comparison with the most successful tubercle configuration, $Re = 120,000$	151
Figure 4.21 - Tubercle A/λ ratio and the effect on lift coefficient for NACA 0021,	152
Figure 4.22 - Tubercle A/λ ratio and the effect on drag coefficient for NACA 0021,	152
Figure 4.23 - The effect of amplitude-to-wavelength ratio on maximum lift coefficient, $Re = 120,000$	153
Figure 4.24 - The effect of amplitude-to-wavelength ratio on stall angle,	153
Figure 4.25 - The effect of amplitude-to-wavelength ratio on maximum lift to drag ratio, $Re = 120,000$	153
Figure 4.26 - Maximum lift coefficient and associated normalised effective tubercle height, $Re = 120,000$	154
Figure 4.27 - Stall angle and associated normalised effective tubercle height,	154
Figure 4.28 – Maximum lift-to-drag ratio and associated normalised effective tubercle height,	155
Figure 4.29 – Comparison of lift coefficient for full-span and half-span NACA 0021 airfoils, $Re = 120,000$	156
Figure 4.30 – Comparison of drag coefficient for full-span and half-span NACA 0021 airfoils, $Re = 120,000$	156
Figure 4.31 - Comparison of lift coefficient for full-span and half-span NACA 65-021 airfoils, $Re = 120,000$	158
Figure 4.32 - Comparison of drag coefficient for full-span and half-span NACA 65-021 airfoils, $Re = 120,000$	158

Figure 4.33 - Tubercle amplitude variation and lift performance for full-span and half-span NACA 0021 models, $Re = 120,000$	159
Figure 4.34 - Tubercle amplitude variation and drag performance for full-span and half-span NACA 0021 models, $Re = 120,000$	159
Figure 4.35 - Tubercle amplitude variation and lift performance for full-span and half-span NACA 65-021 models, $Re = 120,000$	160
Figure 4.36 - Tubercle amplitude variation and drag performance for full-span and half-span NACA 65-021 models, $Re = 120,000$	160
Figure 4.37 – Further reduction in tubercle amplitude and the effects on lift coefficient for NACA 0021 models, $Re = 120,000$	160
Figure 4.38 – Further reduction in tubercle amplitude and the effects on drag coefficient for NACA 0021 models, $Re = 120,000$	160
Figure 4.39 – Tubercle wavelength variation and lift performance for full-span and half-span NACA 0021 models, $Re = 120,000$	161
Figure 4.40 – Tubercle wavelength variation and drag performance for full-span and half-span NACA 0021 models, $Re = 120,000$	161
Figure 4.41 – Wavy airfoils and lift performance for full-span and half-span models, $Re = 120,000$	162
Figure 4.42 - Wavy airfoils and drag performance for full-span and half-span models, $Re = 120,000$	162
Figure 4.43 - Influence of wall proximity on three-dimensional effects affecting the lift force for unmodified NACA 0021 airfoil,.....	163
Figure 4.44 - Influence of wall proximity on three-dimensional effects affecting the drag force for unmodified NACA 0021 airfoil,.....	163
Figure 4.45 - Influence of wall proximity on three-dimensional effects affecting the lift force for A2 λ 7.5 tubercle configuration, $Re = 120,000$	164
Figure 4.46 - Influence of wall proximity on three-dimensional effects affecting the drag force for A2 λ 7.5 tubercle configuration,.....	164
Figure 4.47 - Influence of wall proximity on three-dimensional effects affecting the lift force for θ 4 λ 15 wavy configuration,.....	164
Figure 4.48 - Influence of wall proximity on three-dimensional effects affecting the drag force for θ 4 λ 15 wavy configuration,.....	164
Figure 4.49 – Lift coefficient uncertainty analysis for NACA 0021 full-span models, $Re = 120,000$	165
Figure 4.50 – Drag coefficient uncertainty analysis for NACA 0021 full-span models, $Re = 120,000$	165
Figure 4.51 – Relative pre-stall contribution of uncertainties in lift coefficient for NACA 0021 airfoils, $Re = 120,000$	167
Figure 4.52 – Relative post-stall contribution of uncertainties in lift coefficient for NACA 0021 airfoils, $Re = 120,000$	167
Figure 4.53 – Relative pre-stall contribution of uncertainties in drag coefficient for NACA 0021 airfoils, $Re = 120,000$	167
Figure 4.54 – Relative post-stall contribution of uncertainties in drag coefficient for NACA 0021 airfoils, $Re = 120,000$	167
Figure 4.55 - Relative pre-stall contribution of uncertainties in lift coefficient for NACA 65-021 airfoils, $Re = 120,000$	168
Figure 4.56 - Relative pre-stall contribution of uncertainties in drag coefficient for NACA 65-021 airfoils, $Re = 120,000$	168
Figure 4.57 - Relative pre-stall contribution of uncertainties in lift coefficient for NACA 65-021 airfoils, $Re = 120,000$	169
Figure 4.58 - Relative pre-stall contribution of uncertainties in lift coefficient for NACA 65-021 airfoils, $Re = 120,000$	169
Figure 5.1 – Sketch of laminar separation bubble (Horton, 1968).	174
Figure 5.2 – Normalised pressure distribution plots for NACA 0021 unmodified airfoil, where “top” refers to suction surface and “bottom” refers to pressure surface, $Re = 120,000$. Separation bubble locations found from XFOIL skin friction data are indicated.....	176
Figure 5.3 – Friction coefficient against chordwise position for NACA 0021 at low angles of attack (suction surface),	177
Figure 5.4 - Friction coefficient against chordwise position for NACA 0021 at high angles of attack (suction surface),	177
Figure 5.5 – Explanation for increase in lift curve slope beyond theoretical maximum.	179
Figure 5.6 – Comparison between trapezoidal integration method and XFOIL for lift calculation, $Re = 120,000$	181

Figure 5.7 - Trapezoidal integration method for lift calculation using pressure distribution data, $Re = 120,000$.	181
Figure 5.8 – Normalised pressure contours for suction surface of NACA 0021,	183
Figure 5.9 – Normalised pressure contours for pressure surface of NACA 0021,	183
Figure 5.10 – Normalised pressure distribution plots for NACA 65-021 unmodified airfoil where “top” refers to suction surface and “bottom” refers to pressure surface, $Re = 120,000$. Separation bubble locations found from XFOIL skin friction data are indicated.	185
Figure 5.11 – Friction coefficient against chordwise position for NACA 65-021 at low angles of attack (suction surface),	186
Figure 5.12 - Friction coefficient against chordwise position for NACA 65-021 at high angles of attack (suction surface),	186
Figure 5.13 – Friction coefficient against chordwise position for NACA 65-021 at low angles of attack (pressure surface),	186
Figure 5.14 - Friction coefficient against chordwise position for NACA 65-021 at high angles of attack (pressure surface),	186
Figure 5.15 – Pressure distribution and boundary layer characteristics for NACA 65-021 airfoil at $\alpha = 2^\circ$ (dashed lines indicate the inviscid solution), $Re = 120,000$.	189
Figure 5.16 - Pressure distribution and boundary layer characteristics for NACA 0021 airfoil at $\alpha = 2^\circ$ (dashed lines indicate the inviscid solution), $Re = 120,000$.	189
Figure 5.17 –Lift coefficient against angle of attack for different measurement methods (NACA 65-021), $Re = 120,000$.	191
Figure 5.18 – Normalised pressure contours for suction surface of NACA 65-021,	191
Figure 5.19 – Normalised pressure contours for pressure surface of NACA 65-021,	191
Figure 5.20 – Normalised pressure distribution plots for airfoil with $A8\lambda30$ tubercle configuration, where symbols are chosen as follows: “●” pressure surface “○” suction surface,	194
Figure 5.21 – Lift coefficient for $A8\lambda30$ evaluated from pressure distribution at “peak”, “mid” and “trough” tubercle positions compared to force results, $Re = 120,000$.	196
Figure 5.22 - Normalised pressure contours for suction surface of airfoil with $A8\lambda30$ tubercle configuration, $Re = 120,000$.	197
Figure 5.23 - Normalised pressure contours for pressure surface of airfoil with $A8\lambda30$ tubercle configuration, $Re = 120,000$.	197
Figure 5.24 – Pressure coefficient uncertainty analysis for NACA 0021 at $\alpha = 6^\circ$,	199
Figure 5.25 - Pressure coefficient uncertainty analysis for NACA 0021 at $\alpha = 20^\circ$,	199
Figure 5.26 – Relative uncertainties pre-stall for pressure tappings located on airfoil suction surface (NACA 0021), $\alpha = 6^\circ$, $Re = 120,000$.	200
Figure 5.27 - Relative uncertainties post-stall for pressure tappings located on airfoil suction surface (NACA 0021), $\alpha = 20^\circ$,	200
Figure 5.28 – Pressure coefficient uncertainty analysis for NACA 65-021 at $\alpha = 8^\circ$,	201
Figure 5.29 – Pressure coefficient uncertainty analysis for NACA 65-021 at $\alpha = 20^\circ$,	201
Figure 5.30 – Relative uncertainties pre-stall for pressure tappings located on suction surface of airfoil (NACA 65-021),	201
Figure 5.31 – Relative uncertainties post-stall for pressure tappings located on suction surface of airfoil (NACA 65-021),	201
Figure 5.32 – Pressure coefficient uncertainty analysis for $A8\lambda30$ tubercle configuration at $\alpha = 5^\circ$,	202
Figure 5.33 – Pressure coefficient uncertainty analysis for $A8\lambda30$ tubercle configuration at $\alpha = 20^\circ$,	202
Figure 5.34 – Relative uncertainties pre-stall for tapping located at $x/c = 0.1$ on suction surface of airfoil, $\alpha = 5^\circ$, $Re = 120,000$.	203
Figure 5.35 – Relative uncertainties pre-stall for tapping located at $x/c = 0.1$ on suction surface of airfoil, $\alpha = 20^\circ$, $Re = 120,000$.	203
Figure 6.1 - Hydrogen bubble visualisation at $Re = 4370$, $\alpha = 10^\circ$, $A8\lambda30$ configuration (a) angled top view showing stream-wise vortices, (b) side view in plane of trough (c) side view in plane of peak and (d) top view depicting regions of acceleration. Dashed lines show the outline of the leading edge, flow is from left to right.	209
Figure 6.2 - Hydrogen bubble visualization of the NACA 0021, angled top view: (a) unmodified airfoil, (b) $A4\lambda15$ (c) $A4\lambda30$ (d) $A4\lambda60$ and (e) $A8\lambda30$ ($Re = 5250$, $\alpha = 10^\circ$), flow is from left to right.	210
Figure 6.3 – An example of instantaneous vorticity contours for the $0.4c$ plane at $\alpha = 5^\circ$, where time spacing between images is $0.1s$, $Re = 2230$.	211

Figure 6.4 – Average velocity contours compared with velocity fluctuation contours, $0.4c$ plane at.	212
Figure 6.5 - Comparison between (a) velocity vector field and (b) vorticity contour plot at $\alpha = 15^\circ$, $x/c = 0.4$, $Re = 2230$.	213
Figure 6.6 - Vorticity contours (1/s) for sequential chordwise planes at $\alpha = 5^\circ$, $x/c = 0.4$.	214
Figure 6.7 - Vorticity contours for $x/c = 0.2$ at $\alpha = 10^\circ$.	216
Figure 6.8 - Vorticity contours for sequential chordwise planes at $\alpha = 10^\circ$, (a) $x/c = 0.4$, (b) $x/c = 0.6$, (c) $x/c = 0.8$, (d) $x/c = 1$, $Re = 2230$. Asterisks mark secondary vortex structures. Note that a different vorticity scale is shown for the $x/c = 1$ plane.	216
Figure 6.9 - Vorticity contours for sequential chordwise planes at $\alpha = 15^\circ$, (a) $x/c = 0.4$, (b) $x/c = 0.6$, (c) $x/c = 0.8$, $Re = 2230$.	217
Figure 6.10 - Path of integration and enclosed region for $\alpha = 5^\circ$, where: (a) $x/c = 0.4$, (b) $x/c = 0.6$, (c) $x/c = 0.8$, (d) $x/c = 1$, $Re = 2230$. Red - positive vortex core, blue - negative vortex core.	219
Figure 6.11 - Path of integration and enclosed region for $\alpha = 10^\circ$, $x/c = 0.2$ plane. Red - positive vortex core, blue - negative vortex core.	220
Figure 6.12 - Path of integration and enclosed region for $\alpha = 10^\circ$, where: (a) $x/c = 0.4$, (b) $x/c = 0.6$, (c) $x/c = 0.8$, (d) $x/c = 1$, $Re = 2230$. Red - positive vortex core, blue - negative vortex core. The yellow arrow indicates a possible pathway of vorticity entrainment.	221
Figure 6.13 - Path of integration and enclosed region for $\alpha = 10^\circ$, where: (a) $x/c = 0.4$, (b) $x/c = 0.6$, (c) $x/c = 0.8$, (d) $x/c = 1$, $Re = 2230$. Red - positive vortex core, blue - negative vortex core. Yellow arrows indicate possible pathways of vorticity entrainment.	222
Figure 6.14 – Circulation variation with angle of attack and chordwise position.	223
Figure 6.15 – Schematic showing wall vorticity close to the surface being entrained by the primary vortices at adjacent locations. Dashed arrows indicate transport of vorticity to adjacent troughs between tubercles	224
Figure 6.16 – Vector plot of velocity vectors for $0.4\bar{c}$, $\alpha = 5^\circ$ case, where the dashed red lines cross at the point of maximum positive vorticity, $Re = 2230$.	228
Figure 6.17 – Particle displacement in z with respect to y location, where dashed red line shows the associated maximum gradient, $Re = 2230$.	228
Figure 6.18 – Particle displacement in y with respect to z location, where dashed red line shows the associated maximum gradient, $Re = 2230$.	228
Figure 7.1 – Measured signal after calibration using 94dB calibrator.	234
Figure 7.2 – Measured signal after calibration using 114dB calibrator.	234
Figure 7.3 – Sound pressure level (SPL) against frequency, f , for NACA 0021 at angle of attack, $\alpha = 1-8^\circ$ (microphone at window), $Re = 120,000$.	236
Figure 7.4 - Sound pressure level (SPL) against frequency, f , for NACA 0021 at angle of attack, $\alpha = 1-8^\circ$ (microphone at exit), $Re = 120,000$.	236
Figure 7.5 - SPL against frequency for unmodified NACA 0021 at $\alpha = 5^\circ$ for three separate runs (microphone at window), $Re = 120,000$.	237
Figure 7.6 - SPL against frequency for variation tubercle of amplitude (small A) for	237
Figure 7.7 - SPL against frequency for variation of tubercle amplitude (large A) for NACA 0021 at $\alpha = 5^\circ$ (microphone at window), $Re = 120,000$.	237
Figure 7.8 - SPL against frequency for variation of tubercle wavelength (small λ) for NACA 0021 at $\alpha = 5^\circ$ (microphone at window), $Re = 120,000$.	237
Figure 7.9 - SPL against frequency for wavy NACA 0021 variations at $\alpha = 5^\circ$ (microphone at window), $Re = 120,000$.	237
Figure 7.10 - Strouhal no. against angle of attack for NACA 0021 tubercle configurations with tonal noise	239
Figure 7.11 - Strouhal no. against angle of attack for NACA 0021 tubercle configurations with tonal noise	239
Figure 7.12 - SPL against angle of attack for tubercle configurations with tonal noise (microphone at window), $Re = 120,000$.	239
Figure 7.13 - SPL against angle of attack for tubercle configurations with tonal noise (microphone at exit), $Re = 120,000$.	239
Figure 7.14 - SPL against frequency for NACA 65-021 at angle of attack, $\alpha = 7-10^\circ$ (microphone at window), $Re = 120,000$.	240
Figure 7.15 - SPL against frequency for NACA 65-021 at angle of attack, $\alpha = 7-10^\circ$ (microphone at exit), $Re = 120,000$.	240
Figure 7.16 - SPL against frequency for NACA 65-021 at $\alpha = 8^\circ$ for variation tubercle amplitude (microphone at window), $Re = 120,000$.	240

Figure 7.17 - SPL against frequency for NACA 65-021 at $\alpha = 9^\circ$ for variation tubercle amplitude (microphone at window), $Re = 120,000$.	240
Figure 7.18 - Strouhal no. against angle of attack for NACA 65-021 unmodified airfoil with tonal noise, $Re = 120,000$.	241
Figure 7.19 - SPL against angle of attack for unmodified NACA 65-021 with tonal noise, $Re = 120,000$.	241
Figure 7.20 - SPL for NACA 0021 unmodified airfoil with larger frequency range, $50 \leq f \leq 10,000\text{Hz}$ in AWT, $Re = 120,000$.	242
Figure 7.21 - SPL for $A4\lambda 7.5$ tubercle configuration with larger frequency range, $50 \leq f \leq 10,000\text{Hz}$, in AWT $Re = 120,000$.	242
Figure 7.22 - SPL against frequency measured in anechoic wind tunnel (AWT) for a) unmodified 0021 b) $A2\lambda 7.5$ c) $A4\lambda 7.5$ d) $A4\lambda 15$ e) $A4\lambda 30$ f) $A4\lambda 60$ g) $A8\lambda 30$ h) $\theta 2\lambda 30$ i) $\theta 4\lambda 30$ j) $\theta 4\lambda 15$, $Re = 120,000$.	243
Figure 7.23 - Effect of amplitude-to-wavelength ratio on SPL of tonal noise.	244
Figure 7.24 - Strouhal no. against angle of attack for NACA 0021 airfoils with tonal noise in AWT, $Re = 120,000$.	Error! Bookmark not defined.
Figure 7.25 - SPL against angle of attack for NACA 0021 airfoils with tonal noise in AWT, $Re = 120,000$.	Error! Bookmark not defined.
Figure 7.26 - SPL against frequency measured in AWT for a) unmodified 65-021 b) $A4\lambda 30$ c) $A8\lambda 30$, $Re = 120,000$.	245
Figure 7.27 - Schematic of feedback loop (Arbey & Bataille, 1983).	246

List of tables

Table 1.1 - Flow control devices and their corresponding effects and benefits.....	26
Table 2.1 – Summary of variations in performance for finite span models.	40
Table 3.1 – Considerations affecting chord length selection.....	67
Table 3.2 - Relative wavelength determined from Fish and Battle (1995).....	68
Table 3.3 - Tubercle configurations and adopted terminology.....	69
Table 3.4 – Wavy airfoil configurations and adopted terminology.....	71
Table 3.5 – Determining degrees of freedom for a given uncertainty approximation.....	97
Table 3.6 – Values of relevant parameters for measurement uncertainty analysis	98
Table 3.7 – Pressure tap positions for unmodified airfoil.....	102
Table 3.8 – Pressure tap positions for modified airfoil.....	103
Table 3.9 - Values of relevant parameters for uncertainty analysis.....	105
Table 3.10 – Time delay used for particle image velocimetry measurements of freestream velocity. 113	
Table 3.11 – Summary of measurement planes and associated time delay, ΔT	120
Table 3.12 – Summary of PIV recording parameters.	132
Table 3.13 – Measurement parameters for resonance frequency testing (transfer function).....	137
Table 3.14 – Summary of position combinations for accelerometer and impact hammer.....	138
Table 3.15 - Measurement parameters for resonance frequency testing (auto power spectrum).	139
Table 3.16 - Hard-walled wind tunnel (vertical airfoil mount).....	139
Table 4.1 – Nomenclature used in figures showing uncertainty in force measurements.....	166
Table 5.1 – Chordwise extent of laminar separation bubble determined from the friction coefficient for the suction surface (NACA 0021), $Re = 120,000$	177
Table 5.2 - Chordwise extent of laminar separation bubble and final separation location determined from friction coefficient for the suction surface (NACA 65-021), $Re = 120,000$	187
Table 5.3 – Chordwise extent of laminar separation bubble determined from the friction coefficient for the pressure surface (NACA 65-021), $Re = 120,000$	188
Table 5.4 – Location of separation bubbles for NACA 0021 airfoil with A8 λ 30 tubercles at trough cross-section on suction surface.	195
Table 5.5 - Nomenclature used in figures showing uncertainties in force measurements.....	199
Table 5.6 – Summary of separation characteristics.....	205
Table 6.1 – Positive and negative peak vorticity for chordwise measurements planes ($\alpha = 5^\circ$).....	215
Table 6.2 - Positive and negative peak vorticity for chordwise measurements planes ($\alpha = 10^\circ$).	217
Table 6.3 - Positive and negative peak vorticity for chordwise measurements planes ($\alpha = 15^\circ$).	218
Table 6.4 - Circulation for chordwise measurements planes ($\alpha = 5^\circ$).....	220
Table 6.5 - Circulation for chordwise measurements planes ($\alpha = 10^\circ$).....	221
Table 6.6 - Circulation for chordwise measurements planes ($\alpha = 15^\circ$). Circulation values calculated without erroneous region are shown in brackets.	223
Table 7.1 – Summary of tonal noise characteristics at $\alpha = 5^\circ$ for the NACA 65-021 airfoil	246
Table 7.2 – Separation characteristics calculated using XFOIL at $\alpha = 5^\circ$	248

Chapter 1

Introduction to Flow Control



1.1 Introduction

In this chapter, the feeding behaviour of Humpback whales is explored, which reveals plausible reasons as to why tubercles have evolved as a morphological feature on the leading edges of their flippers. Subsequently a comprehensive discussion of various engineered methods of flow control provides a context for tubercles as a flow control device. Further analysis of the mechanisms behind the various methods of flow control enables identification of specific flow manipulation techniques. Subsequently, parallels are drawn with regards to the way in which tubercles function and their effect on the flow can be categorised. Thereafter, the potential for tubercles as method of flow control for engineering devices is investigated and several possible applications are proposed.

The aim of this project is to investigate the performance enhancement potential of tubercles at low Reynolds numbers. Improved performance is defined in terms of increased lift, reduced drag and lower noise generation. Various tubercle arrangements are considered and the influence of surface roughness and three-dimensional effects is also explored. In addition, alternative geometric modifications similar to tubercles are investigated and their performance characteristics are compared to those of tubercles. A further aim is to identify the mechanism by which tubercles enhance performance and to determine whether more conventional flow control devices affect the flow in a similar way.

1.2 Background

Tubercles are rounded, leading edge protuberances that alter the flow field around an airfoil. It has been suggested that tubercles on the Humpback whale (*Megaptera novaeangliae*) flipper shown in Figure 1.1 function as lift enhancement devices. More specifically, flow attachment is maintained for a larger range of attack angles, thus delaying stall (Fish and Battle, 1995) and increasing the maximum lift coefficient, C_{Lmax} , with minimal drag penalties (Miklosovic, Murray, Howle & Fish, 2004). This is considered an important characteristic for Humpback whale swimming, which involves tight turning manoeuvres to capture prey (Edel & Winn, 1978; Jurasz & Jurasz, 1979; Hain, Carter, Kraus, Mayo & Winn, 1982). The turning radius of these manoeuvres is inversely proportional to the amount of lift generated (Weihs, 1981); therefore any potential increase in maximum lift coefficient would be desirable. Hence a morphological adaptation for delaying stall would be highly beneficial for the Humpback whale as it would increase the maximum attainable lift coefficient, enabling a smaller turning radius. Another advantage of delayed stall is that an equivalent lift coefficient could be achieved at a lower flow velocity for an airfoil with tubercles compared to an unmodified airfoil. There would be a lower associated drag and hence improved efficiency.

NOTE:
This figure/table/image has been removed
to comply with copyright regulations.
It is included in the print copy of the thesis
held by the University of Adelaide Library.

**Figure 1.1 - Humpback whale calf with tubercles visible on flipper leading edge
(<http://www.oceanwideimages.com>).**

It has been reported that the mechanism responsible for the improvement in performance is the generation of streamwise vortices, which enhance momentum exchange within the boundary layer (Fish and Battle, 1995; Miklosovic *et al.*, 2004). Thus, there may be a strong similarity between tubercles and other vortex generating devices currently in use such as strakes and small delta wings (Fish, Howle & Murray, 2008). Other mechanisms

have also been suggested, such as the elimination of spanwise stall progression through flow compartmentalization (Miklosovic & Murray, 2007).

Due to the potential benefits of increased lift with negligible drag penalties provided by tubercles, it is anticipated that they will be broadly adopted for man-made systems in the near future. Several devices with tubercles are already commercially available which include surfboard fins and ceiling fans. Incorporating tubercles into the leading edge could be achieved by either retrofitting the devices on existing wings, fabricating a solid composite structure with tubercles or milling the sinusoidal protuberances into the leading edge depending on the circumstances. These processes increase the complexity of the manufacturing processes but it is anticipated that the additional effort would be justified by notable improvements in performance.

Since tubercles are a method of flow control, it will be instructive to discuss them in the context of flow control methods in general. The following sections provide a description of the concept of flow control, which is followed by a brief history of flow control, outlining its evolution since the first powered flight took place. Subsequently, some well-known flow control devices will be discussed in more detail.

1.3 Flow Control

The idea of manipulating a flow field in order to achieve a particular design objective is the underlying principle of flow control. There are numerous situations where flow control can be applied, however the focus of the following sections will be on manipulation of the external wall-bounded flow developing on the surface of an airfoil. The chosen method of flow control should be optimised to satisfy the requirements of a given performance-enhancement objective. In parallel with consideration of the flow physics, there are other important parameters such as: cost effectiveness, robustness, simplicity of design and minimal maintenance, which need to be taken into account.

The Reynolds number associated with a given airfoil in a flow is also an important factor to consider in the context of flow control. This non-dimensional parameter defines whether the boundary layer is laminar, transitional or turbulent. For a laminar or transitional boundary layer, it is desirable to delay the location of separation in order to increase lift. Transition delay is also employed to reduce skin friction drag. A turbulent boundary layer may also be prone to separation and therefore it is favourable to delay

separation in this case as well. There is also a high skin friction component associated with a turbulent boundary layer and thus it is advantageous to reduce its magnitude.

1.4 History and Development of Flow Control

The first powered flight is generally accepted to have taken place in December 1903 by the Wright brothers, just prior to Prandtl's development of boundary layer theory (Joslin & Miller, 2009). It has also been reported that Richard Pearse achieved powered flight prior to this in March, 1903 (Ogilvie, 2010). Many practical developments followed these achievements including the use of ailerons for turning, which were developed in 1908 (Anderson, 1997). Subsequently in 1914, it was discovered that increased lift could be achieved when both ailerons were deflected downwards and this led to the invention of flaps (Anderson, 1997). In the early 1920s, research was focussed on the use of air jets created by slotted flaps on the wing leading edge as a method of lift enhancement (Anderson, 1997). In the late 1920s, experiments using suction control on airfoils were carried out and it was established that the boundary layer could be made to reattach during flight conditions (Joslin & Miller, 2009). Natural laminar flow using body shape control was established in the 1930s as a means of delaying transition and hence increasing the extent of the favourable pressure gradient (Gad-el-Hak, 1996).

The outbreak of World War II stimulated research into the development of fast, highly manoeuvrable, efficient aircraft, missiles, ships and torpedoes, leading to airfoils with higher wing loading, thinner profiles and smaller planform areas. The use of thin airfoil profiles was accompanied by the undesirable occurrence of leading edge separation (Gault, 1949) and thus distributed suction was used to ameliorate this problem by encouraging the flow to reattach. Additionally, these aircraft required higher landing speeds to avoid stall, which prompted research on methods of separation delay, which would ultimately lead to reduced stall speed as well as reduced take-off distance.

Thus, in the late 1950s, the internally-blown flap was developed, where air is bled from the jet engine compressor and blown over the rear surfaces of the wing to maintain flow attachment. Due to maintenance issues, the use of internally driven boundary layer control became less popular by the late 1960s (Greenblatt & Wyganski, 2000). Instead, externally-blown flaps were implemented where the engine exhaust is blown over the airfoil surface to provide extra lift for take-off and landing. Other notable achievements in

this era (1940-1970) include: suppression of instability modes by suction and heating/cooling; polymer drag-reduction (Gad-el-Hak, 1996); vortex generators (McFadden, 1955); acoustic excitation (Chang, 1961); helical strakes (Scruton & Walsh, 1963) and bluff-body splitter plates (Roshko, 1954).

During the period of 1970-1990, the energy crisis prompted by the 1973 Arab oil embargo, industrialised countries embarked on a search for methods of energy conservation (Gad-el-Hak, 1996). At this time, research effort was directed towards drag reduction for commercial airliners, land vehicles, pipelines and other industrial devices. The accessibility of computers allowed the simulation of complex flow patterns, which had not been attempted analytically. Transition-delaying compliant coatings could be optimised using computers at this stage (Gad-el-Hak, 1996). Other methods of skin friction reduction in turbulent boundary layers such as riblets and large-eddy break-up devices (LEBUs) were also developed.

By the mid 1980s, flow control strategies shifted from controlling the time-averaged state to controlling flow instabilities (Joslin & Miller, 2009). Various active control methods were developed and employed in both open-loop and closed-loop configurations. In general, researchers investigated the optimum forcing frequency and minimal forcing amplitude to affect a desired cancellation or suppression of the predicted or detected disturbances. While the linear stability theory introduced by Tollmein (1929) allows the prediction of the most unstable frequencies and initial growth rates, it is still not possible to predict the final saturated state (Joslin & Miller, 2009).

More recently, there has been a strong focus on the development of more sophisticated actuators capable of controlling the flow at the timescale of the instability. Several different types of actuator are currently available and can be divided into four main categories (Cattafesta III & Sheplak, 2010): fluidic (i.e. zero net mass flux (ZNMF) jets), moving object/surface (i.e. oscillating wire, morphing surface), plasma and other (including electromagnetic, magnetohydrodynamic). However, actuator bandwidth limitations still pose a significant problem for active flow control (Joslin & Miller, 2009; Cattafesta III & Sheplak, 2010). In addition, application to full-scale prototypes of experimentally verified techniques tailored to target flow instabilities is still highly complex, due to scaling issues (Joslin & Miller, 2009; Cattafesta III & Sheplak, 2010).

1.5 Classifications of Flow Control

An important classification to consider for the purposes of this thesis is based on the energy expenditure of the device. If the device requires no additional power input, then it is classified as passive. Conversely, if the device requires supplementary energy to function then it is classified as active. Passive flow control involves either changing the geometry of the airfoil or adding non-moving elements to the airfoil surface; whereas active control encompasses the use of additional energy to operate devices such as actuators.

Active flow control techniques offer various performance advantages over passive flow control methods including: ability to be switched on and off; greater adaptability to changing flight conditions; capacity to target specific instabilities and lower associated drag. However, the implementation of active control is often more complicated and less cost effective than passive control. This is generally due to issues of manufacturing complexity and maintenance. Moreover, there are few examples where active flow control techniques have been successfully transferred from a laboratory model to a full-scale application (Cattafesta, 2010). Hence, investigation into the viability of passive flow control devices is still relevant for modern design as they are generally more reliable and more economically viable to implement.

Another useful classification describes whether the flow control device is designed for “lift enhancement” or “drag reduction” and where possible the focus will be on applications for airfoils. In order to increase the lift generated by an airfoil, the shape can be altered, its orientation relative to the flow can be changed, tip stall can be minimised or the degree of flow attachment and circulation can be enhanced. Hence, lift can be augmented by increasing: wing area; angle of attack; camber; augmentation of circulation and momentum exchange in the boundary layer. In addition, lift can be enhanced by minimising or avoiding tip stall as well as prolonging attachment of flow to the suction surface. In a horizontal wing configuration, the “suction” surface refers to the upper surface and the lower surface referred to as the “pressure” surface.

Flow control methods for drag reduction are focussed on reducing the most significant component of drag. For subsonic flows, the main drag components are form drag, skin

friction drag and induced drag. Some methods of drag reduction for subsonic flows include: avoiding/delaying flow separation (form drag); reducing spanwise flow (induced drag); avoiding/delaying transition to turbulence (skin friction drag); reducing coherence of turbulent structures (skin friction drag) and causing favourable interaction with turbulent fluctuations (skin friction drag).

1.6 Passive Techniques

The methods of passive flow control described in the following paragraphs have been grouped according to their predominant mechanism. Optimisation of the airfoil profile shape involves flow control without spanwise variations of the airfoil geometry, which precludes performance enhancing attachments. Circulation augmentation encompasses flow control methods which enhance the movement of flow around the airfoil. Increased momentum exchange in the boundary layer delays flow separation, allowing a higher angle of attack and hence maximum lift coefficient, to be achieved before stall. This mechanism is responsible for the performance enhancements observed for airfoils with tubercles. Alternative methods can also be implemented to achieve separation delay, which include variation of the surface pressure gradients or alternatively, provision of a barrier which restricts movement of the separation line towards the leading edge. Restriction of spanwise flow is an important objective where there exists a risk of tip stall. Transition delay aims to maintain a laminar boundary layer state for as long as possible to reduce skin friction drag. Where a turbulent boundary layer exists, methods of drag reduction involve reduction of the turbulent fluctuations.

1.6.1 Lift Enhancement

1.6.1.1 Optimisation of Airfoil Profile Shape

The traditional method of performance optimisation involves modifying the design shape of the airfoil. Generally, for a given angle of attack and span, a wing will generate more lift if it has a greater camber and chord length. In addition, it is sometimes beneficial to increase the extent of the laminar boundary layer in order to reduce skin friction drag and in such cases an approach to delay transition is required. This can be achieved by designing the airfoil with maximum thickness location as far aft as possible (Cebeci & Cousteix, 2005). Additionally, the contouring of the airfoil should be carefully designed near the minimum pressure point to ensure transition occurs, rather than separation (Gadel-Hak, 1990). Limitations exist for large sweep angles and high Reynolds numbers due

to the associated instabilities which induce early onset of transition (Cebeci & Cousteix, 2005). In general, the advantages of modifying the design airfoil shape should be weighed against the disadvantage of off-design performance degradation.

1.6.1.2 Circulation Augmentation

Directing the airflow from the engine of an aircraft over the wing can be used as an alternative to flaps or to enhance their effectiveness. This mechanism is called blown flaps and is based on the Coandă effect, which is the term used to describe the attraction of a fluid jet to a nearby surface (Tritton, 1977). Through careful positioning of the flap surface relative to both the blown jet and the main wing, attachment of the flow can be maintained up to flap deflection angles of 60 degrees (Houghton & Carpenter, 2003). If the amount of air blown over the flap exceeds that required to prevent boundary layer separation, then an increase of circulation occurs over the wing surface which leads to lift generation in excess of predictions based on potential flow (McCormick, 1999).

1.6.1.3 Momentum Exchange/Separation Delay

Vortex generators, as shown in Figure 1.2, are small rectangular or delta-shaped winglets, which are used to delay separation and stall. These devices extend in the chordwise direction and conventionally have a height which corresponds to the thickness of the boundary layer (Lin, 2002). More recently, it has been shown that devices with height around 10% of the boundary layer thickness are still fairly effective and have relatively low drag (Lin, 2002; Godard & Stanislas, 2006). Vortex generators protrude into the boundary layer and have discontinuities that create either co-rotating or counter-rotating streamwise vortices, depending on device orientation. The generated vortices improve momentum exchange in the boundary layer, giving an effective mixing region of over three times the height of the device (Lin, Selby & Howard, 1991).

It has also been reported that vortex generators reduce the intensity of acoustic disturbances in the wake region through suppression of the Kármán vortex street formation (Kuethé, 1972). The advantages of vortex generators are that they are simple, robust and inexpensive. However, they add parasitic drag in flow situations in which stall suppression is not required, such as cruise. Most aircraft are fitted with vortex generators at the time of manufacture, but it is also possible to retrofit these generators to existing designs.

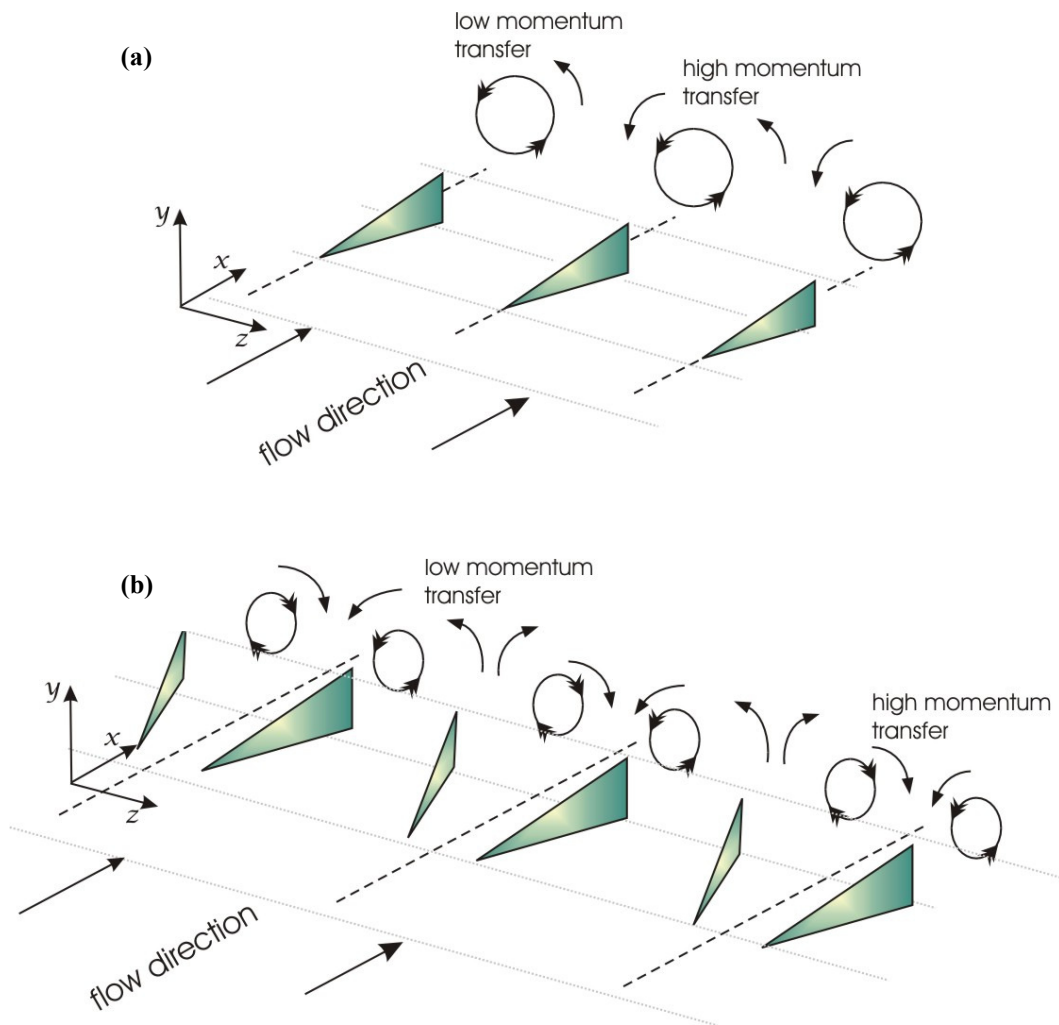


Figure 1.2 – (a) Co-rotating vortex generator configuration, (b) counter-rotating vortex generator configuration (Adapted from Godard & Stanislas, 2006).

Another method of generating counter-rotating streamwise vortices on the suction surface of an airfoil is through placement of small serrations on the pressure surface slightly in front of the stagnation point (Soderman, 1972), as depicted in Figure 1.3. While the serrations are placed on the pressure surface of the airfoil they actually affect the flow over the suction surface since the stagnation point is known to move to the pressure surface with increasing angle of attack. Associated performance improvements included increased maximum lift coefficient with negligible drag effects at low angles of attack and reduced drag at high angles of attack (Soderman, 1972). It was also found that the smallest serrations placed as close as possible in front of the stagnation point gave the largest performance improvements. Additionally, it was noted that size, position and spacing are important parameters.

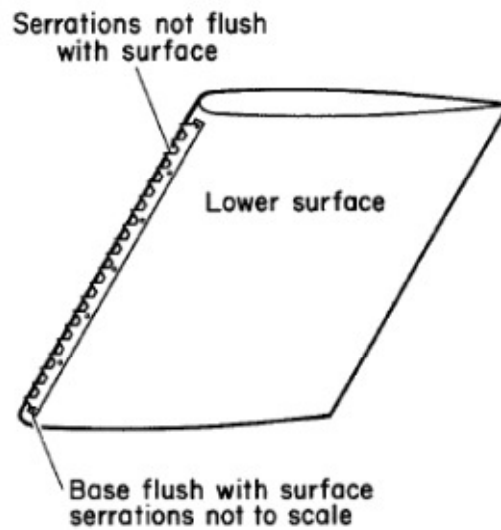


Figure 1.3 – Leading edge serrations (Soderman, 1972).

Leading edge extensions or strakes have little effect on the performance of the aircraft at cruising conditions, however, at moderate to high angles of attack each leading edge extension begins to generate a high-swirl vortex which can be seen in Figure 1.4. This vortex assists in maintaining flow attachment to the top surface of the wing (Thompson, 1997), allowing the wing to produce lift past the expected stall angle. The penalty associated with leading edge extensions is that the process of vortex bursting can occur, which can lead to structural damage of the aircraft tail section (Lee, Brown, Zgela & Poirel, 1990) and wing rock due to the high degree of flow unsteadiness.

NOTE:

This figure/table/image has been removed to comply with copyright regulations. It is included in the print copy of the thesis held by the University of Adelaide Library.

Figure 1.4 – Dye flow visualisation showing leading edge extensions and associated flow pattern (Adapted from Thompson, 1997).

An alternative method for enhancing momentum exchange is through tripping a laminar boundary layer to turbulence (Simons, 1999). This can be achieved by using a turbulator, which often takes the form of a thin raised strip, depicted in Figure 1.5. Turbulators may also be created using distributed roughness elements (Braslow, Hicks & Harris Jr., 1966; Gad-el-Hak, 1990). For a turbulent boundary layer, there is greater momentum exchange with the freestream flow and therefore less likelihood of separation when the boundary layer meets an adverse pressure gradient (Simons, 1999). Turbulators increase the drag at cruise due to the drag of the turbulator itself (minimal if done well) plus the increased skin friction drag of the turbulent boundary layer, as compared with the laminar boundary layer. Hence, the height and position of turbulators are important parameters to optimise in order to ensure their success.

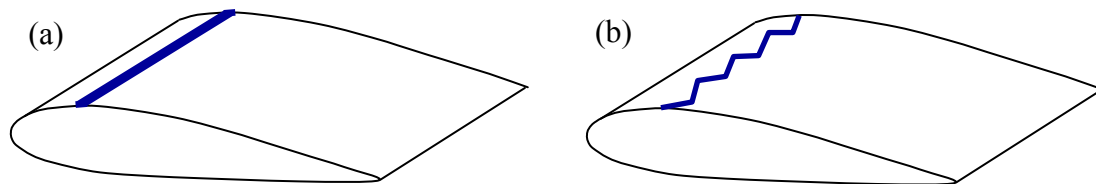


Figure 1.5 – (a) Conventional trip strip turbulator, (b) Zig-zag trip strip turbulator.

Separation delay can also be realised when the pressure gradients at the surface of an airfoil are altered. This occurs when a rippled trailing edge is incorporated into the airfoil. In this case, the undulations are perpendicular to both the free-stream flow and the airfoil chord. The airfoil waviness is believed to cause small but significant lateral pressure gradients which direct the low momentum boundary layer fluid on the suction surface towards a bifurcation line somewhere between the peak and trough (Werle, Paterson & Presz, 1987). More details are provided in Section 2.4.3 in a patent describing this trailing edge modification. Experiments revealed that the maximum lift coefficient and stall angle can be increased with minimal drag penalty (Werle *et al.*, 1987). Zverkov & Zanin (2009) found significant variations in boundary layer structure on a wavy wing compared to a conventional wing at zero angle of attack as shown in Figure 1.6.

NOTE:
This figure/table/image has been removed
to comply with copyright regulations.
It is included in the print copy of the thesis
held by the University of Adelaide Library.

Figure 1.6 – Oil flow visualisation showing the flow pattern and associated interpretation for a wavy wing at $\alpha = 0^\circ$ (Adapted from Zverkov & Zanin, 2009). The waviness is created by extending the grooves and humps of tubercles along the entire chord length.

Laminar-to-turbulent transition for a peak occurred 30% further downstream than that for a trough. In addition, the flow over humps did not separate and thus there was no associated separation bubble at these locations – the separation bubble was confined to the troughs, as indicated in Figure 1.6. It was postulated that such a boundary layer could support a greater adverse pressure gradient than that of an unmodified wing and therefore improved performance (Zverkov & Zanin, 2009).

Another method of separation delay was inspired by the observation that when birds land the covering feathers on the suction surface of their wings rise up. A simplified design was tested in experiments where movable plastic and metal flaps were attached to the suction surface of an airfoil and could pivot to a limited angle (Meyer & Bechert, 1999). The flaps were located close to the trailing edge of the airfoil to avoid the increased drag associated with premature boundary layer transition (Bechert, Bruse, Hage & Meyer, 2000). It was observed that when flow separation begins, the devices lift in response to the local reversed flow as shown in Figure 1.7b. This creates a physical barrier to further flow movement towards the leading edge (Meyer & Bechert, 1999). Problems with premature rising of the flaps were overcome by making the devices porous with a jagged trailing edge, which enables equalisation of the static pressure either side of the flap.

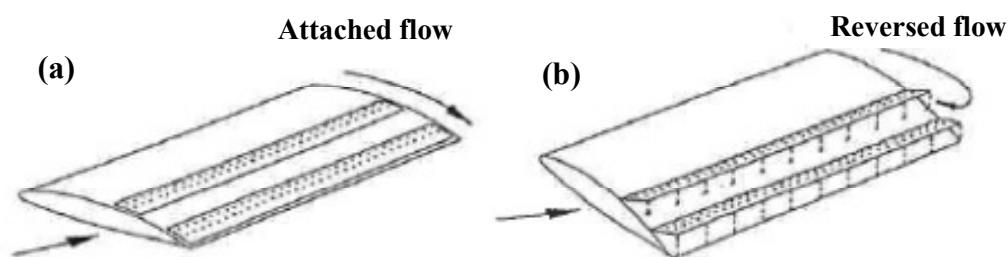


Figure 1.7 – Schematic of movable flaps showing (a) attached flow at a low angle of attack and (b) separated flow at a high angle of attack (Meyer & Bechert, 1999).

A further method of separation delay observed in nature is associated with the comblike fixtures found on the leading edge of owl wings. Flow visualisation experiments conducted by Anderson (1973) revealed that at high angles of attack, the comb creates a spanwise vortex at the wing leading edge, which appears to delay flow separation on the outer half of the wing. It was postulated that this vortex creates a region of low pressure on the wing surface, achieving vortex lift as observed on delta wings. The amount of vortex lift increases with angle of attack until vortex breakdown occurs (Anderson, 1973). Delay in flow separation is expected to be associated with higher values of maximum lift.

1.6.1.4 Restriction of Spanwise Flow

Wing fences, as depicted in Figure 1.8 from Williams (2009), are flat plates fixed perpendicular to the suction surfaces of the airfoil and parallel to the airflow which provide an obstruction to the spanwise flow along the wing. For swept wings, spanwise flow contributes to a higher loading at the tip region compared to the inner portions of the wing, which generally causes stall to initiate at the wing tip (Reithmaier, 1995). This is undesirable because a stalled wing tip leads to reduced effectiveness of the ailerons, especially at slow speeds and high angles of attack (Reithmaier, 1995). Tip stall of a swept wing also causes the centre of pressure to move forward, which produces a nose-up pitching moment that becomes more significant as stall progress further inboard (Bristow, 2002). Eventually this may lead to the highly undesirable deep-stall condition which occurs when excessive downwash over the tail section reduces the effectiveness of the elevator (Swatton, 2011). Other methods of spanwise flow control are the sawtooth leading edge, the notched leading edge and vortex generators. Rather than providing a physical barrier to the spanwise flow, these devices generate streamwise vortices which achieve the same effect (Swatton, 2011).

NOTE:
 This figure/table/image has been removed
 to comply with copyright regulations.
 It is included in the print copy of the thesis
 held by the University of Adelaide Library.

Figure 1.8 – Various models and aircraft with wing fences used in the experiments by Williams (2009).

1.6.2 Drag Reduction

1.6.2.1 Transition Delay

Passive compliant coatings can be used to delay laminar-to-turbulent boundary layer transition through interaction with instability modes such as Tollmien-Schlichting instabilities, travelling-wave flutter and static divergence (Carpenter & Garrad, 1986). A configuration of a passive compliant coating used in an experimental investigation by Gaster (1987) is shown in Figure 1.9.

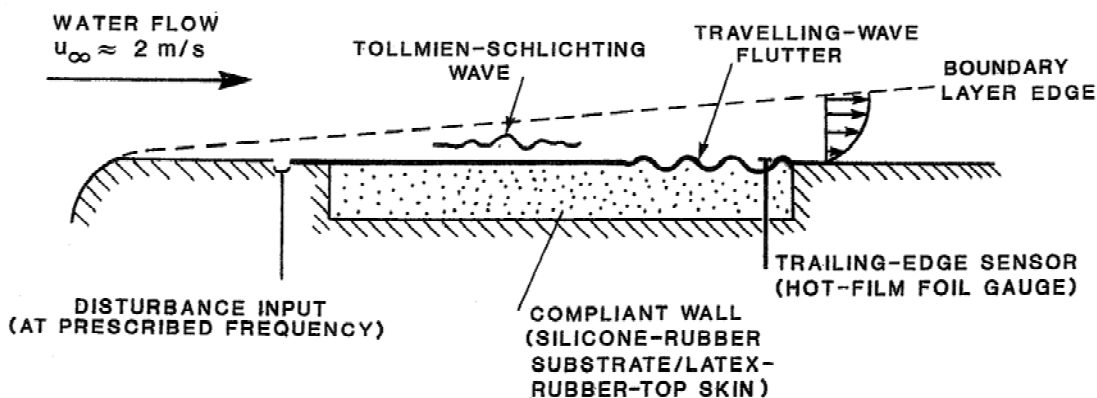


Figure 1.9 – Experimental investigation by Gaster to determine the response of compliant coatings to the Tollmien-Schlichting waves generated by a disturbance input (Gaster, 1987).

Suppression of a given instability mode can lead to transition delay and hence skin friction reduction, provided other modes do not grow in response to the fluid-structure interaction (Gad-el-Hak, 2000). Recent studies have proposed a multi-panel design with each compliant panel tuned to suit the local flow environment (Carpenter, Davies & Lucey, 2000). It has been proposed that transition can be suppressed to indefinitely high

Reynolds numbers with this design (Carpenter et al., 2000). Compliant coatings offer a simple and cost-effective method of flow control, although optimisation of their design can be complex.

1.6.2.2 Reduction of Turbulent Fluctuations

Riblets are minute streamwise ridges and valleys depicted in Figure 1.10 that obstruct the fluctuating turbulent crossflow close to the wall (Bechert, Bruse, Hage & Meyer, 1997). This leads to a reduction in momentum exchange and hence lower skin friction (Bechert *et al.*, 1997). The optimal spanwise spacing between riblets has been established in wall units:

$$s^+ = s\sqrt{\tau_w/\nu} = 10 \text{ to } 20 \quad (1.1)$$

where,

s = spanwise spacing

τ_w = wall shear stress

ν = kinematic viscosity

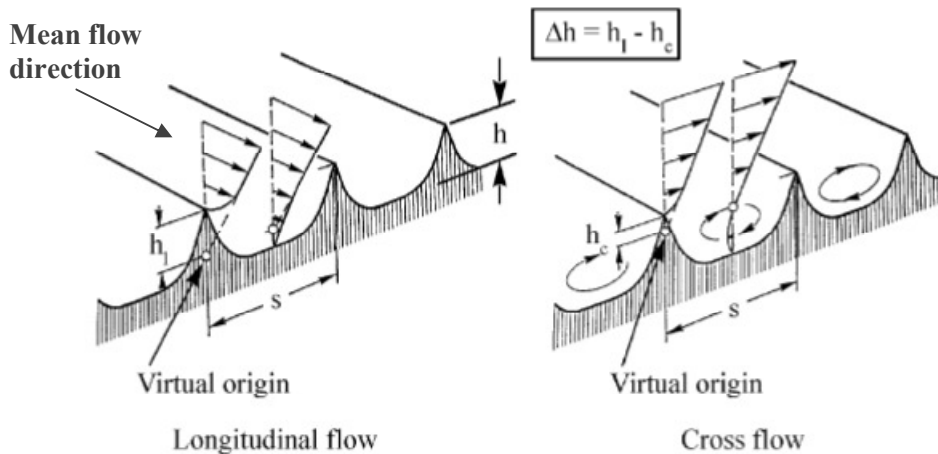


Figure 1.10 – Schematic showing scalloped groove riblets with associated velocity profiles (Bechert *et al.*, 2000).

The corresponding spacing for flight conditions is 25-75 μm (Houghton & Carpenter, 2003). Polymeric riblet film is currently used on commercial flights of the airbus A340-300 aircraft and has also been used for Olympic-class rowing shells and on the hulls of yachts (Houghton & Carpenter, 2003). Similar structures have also been observed on shark skin with a non-dimensional riblet spacing range very similar to the values found to be optimal (Houghton & Carpenter, 2003). However, it is stressed by Bechert *et al.* (2000) that riblets are only applicable for situations where the turbulent wall friction

makes a significant contribution to the overall drag. For separated flows, such as those associated with automobile aerodynamics, where form drag is the dominant component, riblets are considered to be ineffective (Bechert *et al.*, 2000).

Large-eddy break-up devices as shown in Figure 1.11 are short thin plates that are placed in the turbulent boundary layer and can reduce the near-wall velocity fluctuations considerably (Dowling, 1985). This is achieved when the trailing edge vorticity shed by the plates cancels the effects of incident vortices. Hence, these devices reduce the amount of drag/unit area on the wall (Dowling, 1985). The thickness of the plate is an important parameter to consider as it is desirable that a laminar boundary layer is maintained to avoid significant device drag, however, the structural rigidity also needs to be adequate, especially for high speed flows (Walsh & Anders, 1989). Alternatively, large-eddy break-up devices can take the shape of airfoils, giving them greater rigidity (Gad-el-Hak, 1990). A typical arrangement of large-eddy break-up devices consists of one or more placed in tandem as shown in Figure 1.11.

NOTE:
This figure/table/image has been removed
to comply with copyright regulations.
It is included in the print copy of the thesis
held by the University of Adelaide Library.

Figure 1.11 – Sketch of airfoil-shaped large-eddy breakup devices in tandem in a turbulent boundary layer (Gad-el-Hak, 1990).

1.7 Active Techniques

Several active techniques are described in the following section and are grouped with respect to the prevalent mechanism by which they alter the flow. One such method of flow control is to increase the camber of an airfoil, which results in greater flow asymmetry and hence higher lift generation. Another method of lift enhancement is to increase the planform area since it is directly proportional to the lift force when other variables are kept constant. Circulation augmentation is a technique which promotes

greater movement of flow around an airfoil, which also leads to increased lift. Application of suction alters the stability characteristics of the boundary layer as well as restricting its growth. Enhancing momentum exchange prolongs flow attachment and correspondingly there is an increase in the stall angle and maximum lift coefficient. Periodic forcing of the velocity field promotes mixing and entrainment, which leads to boundary layer reattachment (Bar-Sever, 1989). Generation of a body force in air can facilitate separation control and reattachment. Introduction of a vorticity source into a boundary layer can reduce wall shear stress in both laminar and turbulent boundary layers. Altering the near-wall viscosity affects the location at which the boundary layer transitions from laminar to turbulent. Depending on the application, it may be desirable to delay transition or to hasten its onset.

1.7.1 Lift Enhancement

1.7.1.1 Increased Camber/Wing Area

Leading edge slats and trailing edge flaps, as shown in Figure 1.12, both provide a means by which the camber and wing area can be increased simultaneously. These devices can be angled down to generate the necessary lift during low speed take off and landing procedures.

NOTE:
This figure/table/image has been removed
to comply with copyright regulations.
It is included in the print copy of the thesis
held by the University of Adelaide Library.

Figure 1.12 - The position of the leading edge flaps and slats on an airliner (Airbus A-300). In this picture, both devices are extended (Wikipedia, 2010).

Deployment of slats also creates a gap called a slot which further enhances performance. This is discussed in more detail in Section 1.7.1.4. Large modern airliners utilise a triple-slotted flap that produces substantially more lift during take off, which is required for

their greater weight (Khurana, 2009). For cruise conditions, both slats and flaps are retracted into the wing to reduce drag. However, it is not possible to completely eliminate the drag associated with these devices and the actuation mechanism also adds further weight to the aircraft.

An alternative device to a slat is a leading edge flap as shown in Figure 1.13, which also increases the effective camber of a wing. These devices are hinged at the leading edge of the wing and do not have an associated slot, which leads to inferior performance when compared with slats (Swatton, 2011). On the other hand, they are mechanically simpler and are particularly suited to thin wing sections (Torenbeek, 1982). They are often used on the inboard section of the wing in combination with outboard slats to improve longitudinal stability (Torenbeek, 1982).



Figure 1.13 - Krueger flap, an example of leading edge flap device (Swatton, 2011).

1.7.1.2 Circulation Augmentation

A Gurney flap is a flat plate located at the trailing edge of an airfoil perpendicular to the pressure side, as shown in Figure 1.14. Its length is approximately 1% of the airfoil chord and this configuration gives both increased lift and reduced drag (Liebeck, 1978). The device was first used to improve the performance of the spoiler on race cars but has also been shown to be useful for conventional airfoils, particularly those with thick cross-sections (Liebeck, 1978). Experiments have shown that the vortex shedding process associated with the presence of the Gurney flap increases the trailing edge suction (Jeffrey, Zhang & Hurst, 2000). The device also causes a deceleration of the flow at the trailing edge on the pressure side of the airfoil (Jeffrey *et al.*, 2000). These two effects combine to increase the overall circulation associated with a given airfoil (Jeffrey *et al.*, 2000).

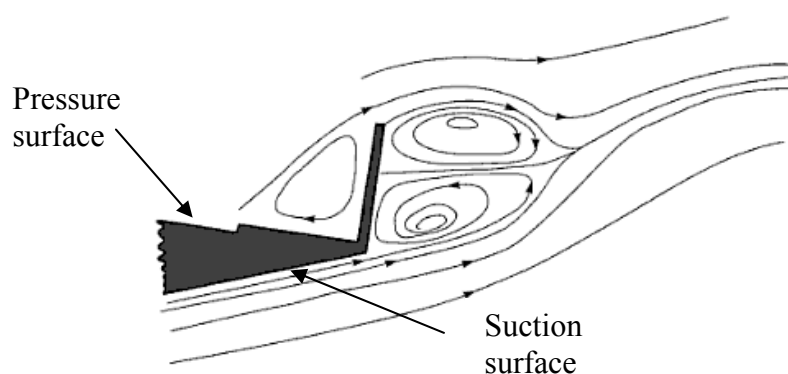


Figure 1.14 – Instantaneous image of Gurney flap showing vortex formation as well as upwards deflection of the flow (Carpenter & Houghton, 2003).

Microtabs are lift-enhancement devices similar to Gurney flaps, except that they are located slightly forward of the trailing edge on the airfoil pressure surface. The presence of a microtab creates a pressure-side vortex which entrains flow from the suction side, ultimately shifting the separation point from to trailing edge to the end of the tab and hence changing the Kutta condition, leading to an effective increase in camber (Johnson, van Dam, & Berg, 2008). The optimum device has a height of 1% chord and is located at the 95% chord position on the pressure surface (Yen, van Dam, Bräuchle, Smith & Collins, 2000).

1.7.1.3 Suction

Suction can be used to stabilise a laminar boundary layer, delaying transition and thereby reducing skin friction drag, or to delay laminar boundary layer separation (McCormick, 1999). This method involves removing a small amount of the boundary layer fluid through a porous surface or a series of spanwise slots. The fluid is removed using a vacuum and directed rearwards using ducts or channels (Swatton, 2011). Applying suction to the entire airfoil would be beneficial, however the amount of power required would not justify its implementation (Swatton, 2011). Therefore suction is generally employed at select locations and used in conjunction with airfoil shape modification (Joslin, 1998). This technique is called hybrid laminar flow control and can be beneficial for take off, landing and cruise conditions. However, application to commercial airliners raises some concerns such as the need for additional systems, uncertainty in maintenance requirements, and the effect on long-term structural integrity (Joslin, 1998).

1.7.1.4 Momentum Exchange/Separation Delay

Zero net mass flux jets or synthetic jets are a more cost-effective alternative of separation control than the preceding methods of steady blowing and steady suction (Koumoutsakos & Mezić, 2006). They usually consist of a sinusoidally oscillating membrane embedded beneath a spanwise slot or row of holes. In each sinusoidal cycle, there is zero net flux of fluid into or out of the actuator, however, the fluid which is drawn in from the boundary layer is forced back out into the flow at a higher trajectory as shown in Figure 1.15 (Gillaranz, Traub, & Rediniotis, 2002).

Zero net mass flux jets promote increased mixing and give rise to a higher entrainment rate in the boundary layer (Tuck & Soria, 2004). In addition, streamlines are deflected from the surface which reduces the local upstream pressure gradient, thus lowering forces which lead to boundary layer separation (Tuck & Soria, 2004). These characteristics substantially delay the stall, enabling the airfoil to generate a larger amount of lift with reduced pressure drag (Tuck & Soria, 2004). Studies have shown that positioning the control actuators closest to the separation point gives the best results (Tuck & Soria, 2004). It is believed that the mechanism of control involves altering the dynamics of the separated shear layer since lift enhancement is not achieved for angles of attack below stall (Tuck & Soria, 2004).

NOTE:
This figure/table/image has been removed
to comply with copyright regulations.
It is included in the print copy of the thesis
held by the University of Adelaide Library.

Figure 1.15 - Schematic of zero net mass flux jet with acoustic actuator (adapted from Gillaranz *et al.*, 2002).

Figure 1.16 illustrates the greater degree of attachment, which can be achieved through the use of synthetic jets. A possible problem with ZNMF jets is that there is a risk of the holes becoming blocked by polish, dirt and moisture.

NOTE:
This figure/table/image has been removed
to comply with copyright regulations.
It is included in the print copy of the thesis
held by the University of Adelaide Library.

Figure 1.16 - Flow visualisation of the uncontrolled (left) and controlled (right) NACA 0015 airfoil at $\alpha = 18^\circ$ (Tuck and Soria, 2004).

Slots allow flow to be guided from the pressure side of the airfoil to the suction side, thereby increasing momentum exchange on the suction surface. As depicted in Figure 1.17 from Dingle and Tooley (2005), slots are suitably shaped apertures which can be incorporated into the wing during manufacture. They are also intentionally created when slats are deployed, in the form of a small gap between the slat and wing leading edge. During cruising conditions, slots remain closed but at high angles of attack, they are opened to enable higher lift generation (Swatton, 2011). Similar flow control mechanisms have been observed in nature in the thumb pinion of the pheasant, split tail of the falcon and the layered feathers of certain birds (Gad-el-Hak, 1990).

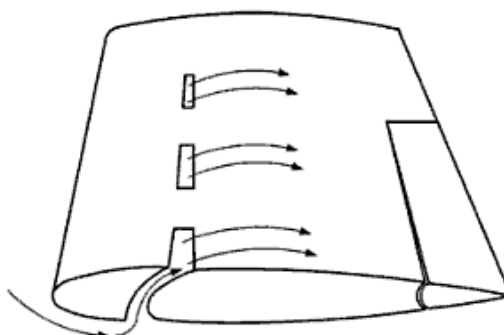


Figure 1.17 – Leading edge slots (Dingle & Tooley, 2005).

Vortex generator jets enhance momentum exchange in a similar manner to traditional vortex generators, however they are more controllable and less intrusive (Johnson *et al.*, 2008). They are orientated at a certain pitch and yaw angle and positioned near the separation point on the suction surface of an airfoil. Figure 1.18 from Khan and Johnson (2000) shows a typical configuration of a vortex generator jet. Optimum configurations of these parameters leads to delayed separation and hence increased maximum lift and stall angle as well as reduced form drag. Streamwise vortices produced by the jets appeared to resemble a weak vortex generated by a solid vortex generator but not a stronger vortex

produced by a solid vortex generator (Compton & Johnston, 1992). It was found that operating vortex jets in pulsed mode could reduce the power requirements for a given lift gain by as much as an order of magnitude (Seifert, Bachar, Koss, Shepshelovich & Wyganski, 1993).

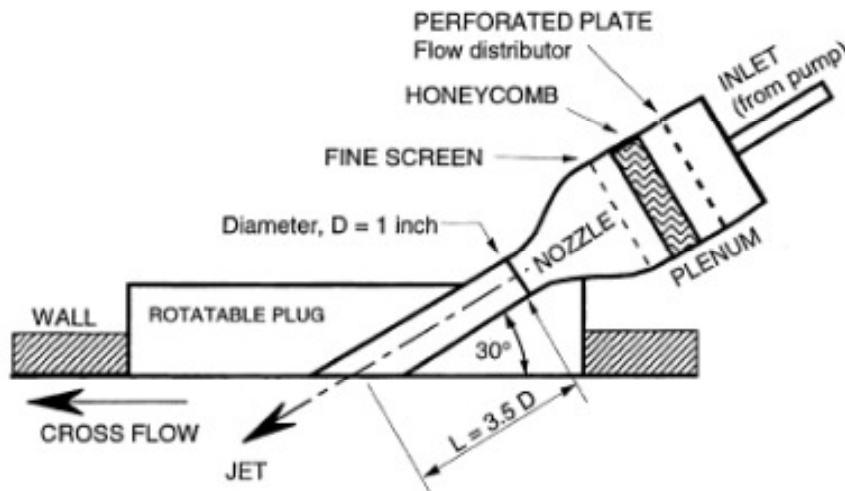


Figure 1.18 – Schematic of vortex generator jet actuator showing pitch angle of 30° and a rotatable plug to vary the skew angle (Khan & Johnson, 2000).

Internal acoustic excitation involves injection of sound from one or more narrow gaps or slots near the leading edge, which reduces the extent of the separated region, hence increasing the lift and decreasing the drag (Huang, Maestrello & Bryant, 1987; Hsiao, Liu, & Shyu, 1990). The mechanism responsible for flow control has been described as an increase in momentum exchange leading to a suction peak at the suction surface of the airfoil (Hsiao *et al.*, 1990). It was also mentioned that there is an increase in entrainment in the early part of the separated shear layer, which narrows the region of separation (Huang *et al.*, 1987). Results for internal acoustic excitation indicate that the sound pressure level required for effective control is much lower than that for external excitation (Hsiao *et al.*, 1990), reducing the energy requirements. It was found that separation control is most effective when the sound amplitude is highest near the region of initial separation (Ahuja & Burrin, 1984; Huang *et al.*, 1987; Hsiao *et al.*, 1990).

1.7.1.5 Periodic Forcing of the Velocity Field

External acoustic excitation can be achieved by using an acoustic driver located below a small hole in the base of the test section (Zaman, Bar-sever & Mangalam, 1987). Application of this technique to an airfoil resulted in a narrowing of the wake and removal of large-scale vortical structures from the wake (Zaman *et al.*, 1987), which

promoted separation delay for a turbulent boundary layer. An appropriate choice of frequency and amplitude of the sound led to an increase in the maximum lift coefficient and stall angle (Ahuja & Burrin, 1984). It was also found that the acoustic standing waves in a wind tunnel induced large transverse velocity fluctuations at the airfoil surface which were the most effective method of separation control (Zaman *et al.*, 1987). This implies that imparting a sound wave may not be the best method of separation control in free flight and thus applications involving enclosures, such as turbines, would be more suitable (Zaman *et al.*, 1987).

Bar-Sever (1989) investigated the effect of introducing transverse velocity fluctuations using an oscillating wire placed slightly upstream of an airfoil's leading edge. The current and tension of the wire were selected to give natural resonance conditions which ensured that the amplitude of oscillation was sufficient. It was shown that the oscillating wire technique gives rise to increased spreading of the velocity profile as well as increased turbulence activity which leads to a substantial delay of separation (Bar-Sever, 1989). Hence, a corresponding increase in the stall angle and maximum lift coefficient as well as reduction of drag were observed.

1.7.1.6 Application of Body Force to Air

Plasma actuators are used for a wide variety of both internal and external flow control applications including airfoil lift augmentation (Corke, Jumper, Post, Orlov, McLaughlin, 2002; Goeksel, Rechenberg, Greenblatt & Paschereit, 2006), airfoil leading edge separation control (Post & Corke, 2004) and turbulent boundary layer control (Wilkinson, 2003). The most commonly used plasma actuator is based on a single dielectric-barrier discharge mechanism and consists of two electrodes that are separated by dielectric material (Corke, Enloe & Wilkinson, 2010). Applying a high AC voltage between the electrodes causes the air to ionise, resulting in a body force on the ambient air (Enloe, McLaughlin, VanDyken, Kachner & Jumper, 2004). The body force can be tailored to specific requirements through optimising the configuration of the electrodes (Corke *et al.*, 2002). It is believed that heating of the air due to plasma generation is negligible (Corke & Post, 2005). Important parameters for plasma actuator optimisation include: AC waveform, electrode geometry, dielectric thickness and AC frequency (Corke, *et al.*, 2010). Plasma has been used successfully for separation control on an unmanned aerial vehicle equipped with a high voltage generator and plasma actuators (Grundmann, Frey

& Tropea, 2009). Flow reattachment for a NACA 0015 airfoil with plasma actuators was highlighted using flow visualisation by Roth (2003) and the results are shown in Figure 1.19. One of the disadvantages of plasma actuators is the need to generate a high voltage which is accompanied by associated energy losses and increased weight (Seifert, 2007).

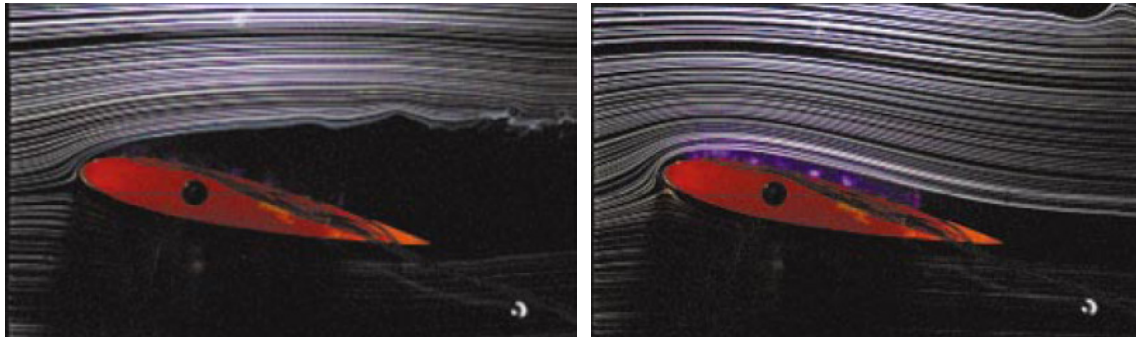


Figure 1.19 – Flow visualisation for NACA 0015 airfoil at $\alpha = 12^\circ$ showing separation in the absence of flow control (left) and flow reattachment with plasma (right) (Roth, 2003).

1.7.2 Drag Reduction

1.7.2.1 Vorticity Source in a Boundary Layer

Magnetohydrodynamic flow control can be used to influence the flow of electrically conducting fluids such as seawater. Arrays of flush-mounted electrodes and sub-surface magnets are used to induce a current-density field and magnetic field in the region of a wall. The resultant three-dimensional Lorentz body force is a source of vorticity which can be controlled both temporally and spatially to influence the boundary layer vorticity field. Wall shear stress reductions were measured by Nosenchuck, Brown, Culver, Eng and Huang (1995) for both laminar and turbulent boundary layers. It was proposed that the mechanism of drag reduction for laminar boundary layers is the restructuring of the vorticity field and for turbulent boundary layers, the interference with coherent motions responsible for turbulence production (Nosenchuck *et al.*, 1995).

1.7.3 Manipulation of Near Wall Viscosity

An effective method of boundary layer control involves changing the near-wall viscosity through wall heating/cooling and injection of fluid having a different viscosity. Reducing the local fluid viscosity has the effect of creating a fuller velocity profile which is more stable. Hence, cooling in air and heating in water or injection of lower viscosity fluids can achieve substantial transition delay (Gad-el-Hak, 1990; Gad-el-Hak, 2000). However, in other cases it is more desirable to reduce the fullness of the velocity profile to decrease

laminar shear stress and hence skin friction drag and thus an increased viscosity may be desired (Gad-el-Hak, 2000).

Surface heating at the leading edge of a body immersed in air can be used to delay laminar-to-turbulent boundary layer transition through attenuation of the Tollmien-Schlichting waves (Filippov, 2002). On the other hand, heating in regions of adverse pressure gradient has been found to speed up transition (Schmidt & Selberg, 1993), which may be desirable if a boundary layer trip is required. The feasibility of wall heating or cooling as a flow control method is limited to applications where a sizeable heat source or sink is available (Gad-el-Hak, 2000). Cryo-fuel such as liquid hydrogen or liquid methane is an example of a realistic heat sink for such applications (Gad-el-Hak, 2000).

1.8 Summary and Discussion of Passive/Active Techniques

This brief introduction to flow control provides a general overview which is mainly focussed on the more common devices available. The overall objective was to establish a relevant context for tubercles, whereby it was highlighted that they are a passive flow control device and increase boundary layer momentum exchange. Other devices were identified as belonging to this category such as vortex generators, leading edge serrations and synthetic jets. Section 2.2.6 provides further detail concerning alternative mechanisms which have been proposed as contributing to performance enhancement for airfoils with tubercles.

Comparison of the performance characteristics and flow patterns of flow control devices was expected to enhance understanding regarding tubercles. In addition, development of a knowledge base of flow control methods allows consideration of the associated advantages and disadvantages of the various devices. It is also possible to identify applications for specific devices and hence establish a suitable niche for leading edge tubercles. Table 1.1 provides a condensed summary of the various flow control devices, how they affect the flow and the associated benefits.

Table 1.1 - Flow control devices and their corresponding effects and benefits.

Device(s)	Effect on flow	Benefits
Tubercles, vortex generators, leading edge serrations, rippled trailing edge, moveable flaps, slots, suction, vortex generator jets, internal/external acoustic excitation, oscillating wire, plasma	Delayed separation	Increased lift/stall angle, possible drag reduction
Flaps, slats, leading edge flaps	Increased velocity on suction surface	Increased lift/stall angle
Blown flaps, Gurney flap	Circulation augmentation	Increased lift/stall angle
Strakes, owl comb	Vortex lift generation	Increased lift/stall angle
Tubercles, wing fences, sawtooth leading edge, notched leading edge, vortex generators	Restricted spanwise flow	Minimisation/avoidance of tip stall
Turbulator, manipulation of near-wall viscosity	Accelerated transition	Avoidance of stall
Shape optimisation, compliant coatings, suction, manipulation of near-wall viscosity	Delayed transition	Reduced skin friction drag
Riblets, large-eddy break up devices	Reduced momentum exchange	Reduced skin friction drag
Magnetohydrodynamic flow control	Restructuring of boundary layer vorticity field	Reduced skin friction drag

Several techniques were not discussed in the previous sections and certain details have been omitted. Thus, the interested reader is referred to more comprehensive publications on the topic (Gad-el-Hak, 2000; Johnson *et al.*, 2008; Joslin & Miller, 2009). Furthermore, several devices which were originally passive have now been tackled in active form such as: compliant coatings (Johnson *et al.*, 2008); vortex generators (Johnson *et al.*, 2008); microtabs/microflaps (passive - Gurney flaps) (Johnson *et al.*, 2008); tubercles (Dewar, Watts & Fish, 2006) and adaptive wings (passive - airfoil shape modification) (Stanewsky, 2001).

Some of the devices discussed in Sections 1.6 and 1.7 were originally motivated by biological observations, indicating that despite the differences between vehicle and animal propulsion there are various adaptations that are mutually beneficial. Some of the adaptations inspired by nature are: riblets (shark skin); trailing edge flaps (bird feathers); compliant coatings (dolphin skin) and slots (pheasant, split tail of the falcon, layered feathers of certain birds). It is instructive to return to analysis of the Humpback whale to develop a brief understanding of its behavioural characteristics. Subsequently, an explanation can be formed concerning the reason that tubercles evolved over time and became an integral part of the flipper leading edge.

1.9 Purpose of Tubercles on Humpback Whale Flipper

The Humpback whale has been named as the most “acrobatic” of baleen whales (Leatherwood, Reeves, Perrin & Evans, 1988) and can even perform underwater somersaults (Jurasz & Jurasz, 1979). The high manoeuvrability of this species can be linked directly with its feeding ecology. These whales consume large quantities of plankton, herring and capelin (Jurasz & Jurasz, 1979; Dolphin, 1988) and in order to capture this prey, there are several techniques that require strong turning, surfacing and diving abilities.

One such method is called, “Lunge Feeding” and involves swimming at approximately 2.6 m/s toward their prey from below at an angle of 30 to 90 degrees (Jurasz & Jurasz, 1979). The flipper Reynolds number can be estimated as $Re \sim 1,100,000$ where the mean chord length, $\bar{c} = 0.51\text{m}$ (as given in Fish & Battle, 1995), $v = 1.17 \times 10^{-6} \text{m}^2/\text{s}$ (for sea water at 16°C, Munson *et al.*, 1990). This indicates that the boundary layer is in the

transitional range during these manoeuvres since this range extends from $Re = 200,000$ to $Re = 3,000,000$ (Munson, Young & Okiishi, 1990).

Another feeding technique is called “Inside Loop” and in this case, the whale swims away from its prey with the flippers abducted and protracted (Edel & Winn, 1978) then rolls 180 degrees, making a sharp U-turn and lunging toward the prey (Hain *et al.*, 1982). Approximately 1.5 – 2 body lengths are required for this manoeuvre, which indicates the compact nature of the turn.

Another feeding method is known as “bubbling,” where a column of bubbles is produced as the Humpback exhales air from its blowhole whilst swimming upwards (Fish and Battle, 1995). The resulting “bubble-net” encircles the prey and concentrates it so that the whale can consume a large quantity as it swims upwards through the centre of the net (Hain *et al.*, 1982). A smaller turning radius implies that the prey would be more densely concentrated in the “bubble-net,” which could potentially increase the effectiveness of the feeding method. The turning radius that can be achieved is found by equating the inertial force acting on the whale to the lifting force generated by the flippers (Howland, 1974; Weihs, 1981). This radius can be represented by Equation (2.1) from Weihs (1981):

$$R = \frac{m_v}{(0.5\rho AC_L \sin \phi)} \quad (2.1)$$

where,

ρ = density of fluid

m_v = whale’s virtual mass

A = total planar area of flippers

C_L = maximum lift coefficient

ϕ = bank angle.

This equation indicates that a tighter turn can be realised with a greater coefficient of lift and/or larger bank angle. Thus it can be deduced that to satisfy the feeding requirements of this animal, it is necessary for the flippers to generate a large amount of lift. It is inferred that tubercles are present to augment the amount of lift that can be achieved.

1.10 Potential Applications for Engineered Devices

Much of the body of the Humpback whale is inflexible, which is an inherent characteristic of manmade vehicles produced with current technology. Thus, through understanding the mechanism behind its turning manoeuvres we can apply this knowledge to the design of turning surfaces, such as hydrofoils and wings, to increase the manoeuvrability of vehicles such as submarines and aircraft. Humpback whales perform turning manoeuvres in the transitional regime as shown in Section 0, which provides an estimate of a suitable Reynolds number range.

As discussed at the beginning of this chapter, the presence of tubercles on the leading edge of an airfoil increases the momentum exchange in the boundary layer, which leads to separation delay (Fish and Battle, 1995; Miklosovic *et al.*, 2004). In addition, the associated streamwise vortices are believed to reduce the extent of spanwise flow (Miklosovic & Murray, 2007). It has also been found that tubercles promote softer stall characteristics (Johari, Henoeh, Custodio & Levshin, 2007). Furthermore, it has been suggested that incorporating tubercles could lead to reduced noise (Dewar *et al*, 2006). Therefore potential applications include lifting surfaces which experience high adverse pressure gradients, have high lift requirements, experience tip stall, operate near the stall angle and generate tonal noise. Some suitable applications can be identified for the Reynolds number range of interest in Figure 1.20, adapted from Lissaman (1983).

NOTE:
This figure/table/image has been removed
to comply with copyright regulations.
It is included in the print copy of the thesis
held by the University of Adelaide Library.

**Figure 1.20 – Typical Reynolds number range for various applications
(Adapted from Lissaman, 1983).**

The most relevant potential application for tubercles is probably for UAVs (Unmanned Air Vehicles). These are tiny aircraft, which typically have wings with a small chord-length and fly at low velocities giving chord Reynolds numbers in the range of $Re \sim 15,000-500,000$ (Mueller & DeLaurier, 2003). As such, their wings operate in the laminar and transitional regimes and therefore the boundary layer tends to separate at a small angle of attack, leading to deterioration in performance (Mueller & DeLaurier, 2003). This problem is most important at take-off and landing when slow flight speeds, hence high angle of attack, are required. The issue would usually be solved by slats or flaps, but the aircraft are too small to incorporate such devices since the excessive weight associated with the actuators would outweigh the potential benefits (Jacob, 1998). Therefore, tubercles offer the possibility of reducing the minimum stall speed without adding significantly to the drag or weight of the vehicle.

Wind turbines often operate in light wind conditions and therefore a method for generating increased lift before stall would enable more power to be generated in such situations (Johnson *et al.*, 2008). Additionally, for variable winds, the operational envelope of the airfoil could be extended due to the increased stall angle associated with tubercles, reducing the likelihood of stall. Measurements have already been taken on wind turbines with tubercles and have indicated that there is a potential for a substantial increase in electrical power output, leading to greater annual energy production (Howle, 2009). In addition, undesirable tonal noise could be reduced or eliminated, which would be beneficial for the community. Moreover, the reduction or elimination of dynamic stall would reduce the rate of fatigue of the turbine blades, reducing maintenance costs. Despite the fact that large megawatt-size wind turbine blades operate at chord Reynolds numbers at least as large as $Re = 6 \times 10^6$ (Somers & Tangler, 2000), research is still focussed on potential flow control devices for transitional Reynolds numbers (Johnson *et al.*, 2008). This indicates that tubercles would have potential application for small wind turbines.

Short-take-off-and-landing aircraft are used when there is a requirement to take off or land in a very short distance. Since runway length is a function of the square of the minimum stall speed, a considerable amount of design effort is spent in reducing this parameter (Khurana, 2009). Thus, if tubercles enabled a larger angle of attack to be achieved before stall, the minimum stall speed would be reduced and an aircraft could

take off or land in a shorter distance. The “softer” stall characteristics of the tubercle-enhanced airfoil would also improve the safety margin.

Helicopter rotors operate at high angles of attack when a large load and high forward speed are required (Tang & Dowell, 1991). However, if the blade angle exceeds the stall angle for a given flow velocity, dynamic stall occurs. Usually this takes place on the retreating blade (Tang & Dowell, 1991) since the velocity of the flow relative to the blade is lowest. Stall results in undesirable vibrations, blade torsion and control system loads (Peters & Chouchane, 1986). Therefore increasing the stall angle and reducing the severity of stall would be useful advantages which could be achieved with tubercles. Such improvements would lead to improved safety, reduced fatigue and increased service life.

An application having a strong analogy with Humpback whale flippers is hydroplanes which are the turning surfaces employed by underwater vehicles (Edel & Winn, 1978). In addition to improving the manoeuvrability of these vehicles through delayed stall and higher maximum lift coefficient, there could also be advantages in terms of stealth. Streamwise vortices generated by the leading edge waviness would reduce the coherence of vortex shedding or eliminate it altogether (Bearman & Owen, 1998), suppressing tonal noise. Tubercles could also be used on the leading edge of propeller blades for the same purpose. Characteristic tones are known to be produced by both hydrofoils and propellers (McAlpine, Nash & Lawson, 1999) and can be identified by enemy hydrophones, so their absence is strongly desirable.

The manoeuvring performance of rudders could be improved by leading edge tubercles since a higher maximum lift coefficient would enable a greater force to be developed on the rudder (Molland & Turnock, 2007). In addition, the less severe stall characteristics associated with tubercles would reduce hysteresis effects. These effects would become apparent if the stall angle of the rudder was exceeded and then reduced since a rudder with tubercles would not experience such a sudden drop in lift at stall and would therefore recover more rapidly. Another advantage of tubercles would be that the minimum stalling speed would be reduced which would enable the rudder to achieve tighter turns at slower speeds (Marchaj, 1979).

Other hydrofoils such as keels and centreboards could also benefit from leading edge tubercles. These hydrofoils provide the balancing force on a yacht, which counteracts the side component of the lift force (Anderson, 2008). Therefore, an increase in maximum lift coefficient would allow a greater lift force to be exerted on the sail, allowing the yacht to sail closer into the wind and/or faster. Additionally, a smaller keel or centreboard could be used to achieve the same result as the unmodified hydrofoil. Furthermore, incorporating tubercles into the leading edge of the sail of a yacht could also provide performance benefits, especially since it requires a relatively large angle of attack ($\alpha \sim 15 - 25^\circ$) (Hoffman & Johnson, 2009). This is because the sail needs sufficient force to overcome the drag created by the keel, hull and the sail itself (Hoffman & Johnson, 2009). Thus improving the efficiency of the sail at high angles of attack and reducing the probability of stall would be highly beneficial and could possibly be achieved through the use of tubercles. Tubercles also improve the performance of surfboard fins, allowing greater lift and control at lower speeds compared to conventional fins. Surfboard fins with tubercles are commercially available from Tim Stafford Surfboards (2010) and are pictured in Figure 1.21.

NOTE:
This figure/table/image has been removed
to comply with copyright regulations.
It is included in the print copy of the thesis
held by the University of Adelaide Library.

Figure 1.21- Surfboard fin with leading edge tubercles (Stafford, 2010).

There are also applications for tubercles on aerodynamic devices such as inverted wings on the rear-deck of race cars, used to generate downforce. An increase in stall angle would allow the spoiler to generate a greater down force, which would add traction to the rear tyres (Katz, 2006). This improves the acceleration characteristics of an automobile as well as enhancing the handling performance (Alexander, 2001). A stalled spoiler is generally undesirable since the drag force increases and the down force is reduced (Alexander, 2001).

In addition, applications have been recognised in the design of blades for fluid-handling devices such as compressors and fans. The highest performance of a compressor is typically reached close to the stall condition since a greater amount of work can be achieved for each compressor stage (Lord, MacMartin & Tillman, 2000). However an adequate stall margin must always be maintained, to avoid premature blade failure (Lord *et al.*, 2000). Tubercles could increase the operational envelope of a compressor due to increased maximum lift and since they also reduce the severity of stall, the stall margin would not be so critical. With regards to fans, increased efficiency associated with leading edge tubercles can provide a significant reduction in energy costs for dairy fans (Ontario Power Authority, 2010). Fans with tubercles have been found to circulate a greater amount of air with increased efficiency and half the number of blades. Flow noise has also been reduced through incorporation of tubercles and there is a lower associated vibration (Ontario Power Authority, 2010). This provides additional benefits such as reduced fatigue and hence increased life-span of the fan. Moreover, the existence of tubercles could suppress tonal noise, which has been identified as a potential problem for fans (Kingan & Pearse, 2009; McAlpine *et al.*, 1999). Fans with tubercles are commercially available from Fanmaster (2011) and a typical model is pictured in Figure 1.22. Tubercles also have the potential to be used on computer fans (Chapdelaine, 2011).

NOTE:
This figure/table/image has been removed
to comply with copyright regulations.
It is included in the print copy of the thesis
held by the University of Adelaide Library.

Figure 1.22 - Altra-Air Fan 2.4m with leading edge tubercles (Fanmaster, 2011).

In summary, leading edge tubercles allow the flow to remain attached on the suction surface of an airfoil up to higher angles of attack. This leads to an increase in stall angle and hence, higher maximum lift coefficient. In addition, complete stall occurs much more

gradually with tubercles since different spanwise sections stall at different angles of attack. There is minimal effect on drag with the presence of leading edge tubercles at low angles of attack. At higher angles of attack, however, a larger lift coefficient could be achieved at a lower velocity with the presence of tubercles and thus there would be a corresponding reduction in drag.

Chapter 2

Review of Literature and Associated Patents



2.1 Introduction

This chapter is focussed on previous studies of the performance enhancement associated with leading edge tubercles. In addition to comparing the performance of models with and without tubercles, the effect of varying the tubercle amplitude and wavelength is also discussed. Moreover, the potential benefits of tubercles are considered in relation to wing tip effects as well as the Reynolds number. The flow patterns related to the existence of tubercles are shown using a range of numerically and experimentally generated images of the flow in the vicinity of the tubercles. Subsequently, the present conception of the mechanism through which tubercles alter the flow characteristics is outlined with reference to previous studies. Additionally, the current understanding of airfoil tonal noise is discussed in order to confirm the viability of tubercles as a device for reducing this tonal noise. Existing patents are outlined briefly to highlight practical applications of tubercles which have already been considered. The chapter concludes with a detailed discussion of the aims and objectives of the current study.

2.2 Research into Tubercles

Several researchers have demonstrated that performance enhancements can be achieved through the incorporation of leading edge tubercles (Watts & Fish, 2001; Miklosovic *et al.*, 2004; Pedro & Kobayashi, 2008). Results show that separation is delayed, increasing the maximum lift attainable and maximum stall angle (Miklosovic *et al.*, 2004). However, some researchers have observed that in certain circumstances tubercles actually cause

deterioration in performance at angles of attack before stall (Stein & Murray, 2005; Johari *et al.*, 2007). Despite this fact, these cases showed that there were still advantages from incorporating tubercles such as softer stall characteristics and higher post-stall lift (Johari *et al.*, 2007).

2.2.1 Quantification of Performance Enhancement

An inviscid numerical model of a NACA 63-021 airfoil reported by Watts and Fish (2001) showed that incorporation of tubercles into the leading edge gave rise to a 4.8% increase in maximum lift, 10.9% reduction in induced drag, and 17.6% increase in lift-to-drag ratio (L/D) at an angle of attack of $\alpha = 10^\circ$. Viscous calculations indicated that tubercles have a negligible effect on drag at zero angle of attack but an 11% increase in form drag was calculated for an angle of attack of $\alpha = 10^\circ$ (Watts & Fish, 2001). A finite-span (aspect ratio = 2.04) with sinusoidally-shaped tubercles was chosen for this analysis (Watts & Fish, 2001).

An experimental study undertaken by Miklosovic *et al.* (2004) revealed that a model Humpback whale flipper with tubercles attained a 40% increase in the stall angle, 6% increase in maximum lift coefficient and a decrease in total drag in the post-stall regime compared to an unmodified equivalent. In addition, the lift-to-drag ratio was shown to be larger for the airfoil with tubercles at all angles except $10^\circ \leq \alpha \leq 12^\circ$. Results were obtained experimentally using idealized scale models (NACA 0020) of the Humpback whale flipper with and without tubercles at $Re = 505,000 - 520,000$. Images of the models and results for lift coefficient, C_L , and lift to drag ratio, L/D , are shown in Figure 2.1.

Variation of the sweep angle for the models shown in Figure 2.1 (a) indicated that performance enhancement could be achieved with tubercles for all sweep angles under investigation (Murray, Miklosovic, Fish, & Howle, 2005). The sweep angle was implemented through addition of material at the airfoil root as shown in Figure 2.2 (a). Performance enhancement followed a similar trend as the unswept case where the maximum lift coefficient and stall angle for a Reynolds number of $Re = 550,000$ were higher for foils with tubercles as shown in Figure 2.2 (b).

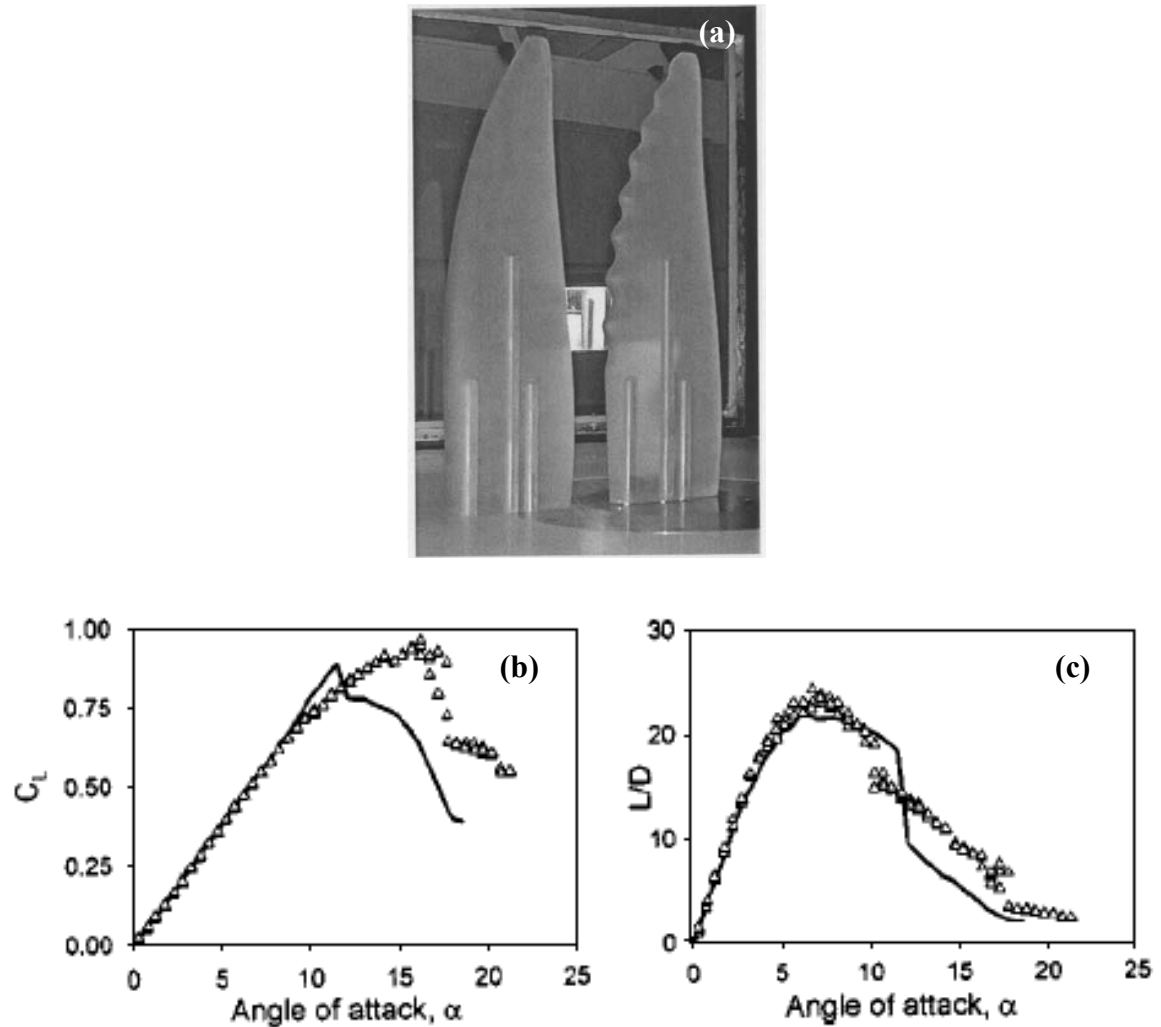


Figure 2.1 – (a) Experimental models, (b) Lift Coefficient vs. angle of attack and (c) Lift/drag ratio.
Solid lines: unmodified airfoil, triangles: modified airfoil (Miklosovic *et al.*, 2004).

NOTE:
This figure/table/image has been removed
to comply with copyright regulations.
It is included in the print copy of the thesis
held by the University of Adelaide Library.

Figure 2.2 – (a) Model whale flippers, sweep angles of 15° & 30°, (b) Lift plots, sweep angle = 15°
(Murray *et al.*, 2005).

On the other hand, Stein and Murray (2005) demonstrated that an airfoil with tubercles experienced reduced lift and increased drag compared with the unmodified airfoil.

Experiments were carried out for $0^\circ \leq \alpha \leq 12^\circ$ at $Re = 250,000$, using a nominally two-dimensional airfoil with sinusoidal tubercles having amplitude and spacing equal to the average values for the Humpback whale. In order to test the hypothesis that tubercles function in a similar way to conventional vortex generators, Stein and Murray, (2005) made a comparison between these two flow control devices. It was found that conventional vortex generators give a slight improvement in lift performance with negligible drag increase for the same flow conditions. Thus it was concluded that in this study, tubercles did not affect the flow in the same way as vortex generators.

Experimental results obtained by Johari *et al.* (2007) at $Re = 183,000$ also demonstrated disadvantages for NACA 63-021 airfoils with tubercles pre-stall. It was found that the stall angle and maximum lift coefficient were reduced and that there was a corresponding drag increase with respect to an unmodified airfoil. However, improvements were noted in the post-stall regime in which airfoils with tubercles achieved lift coefficients as much as 50% greater than the unmodified airfoil (Johari *et al.*, 2007). Based on these results, it was suggested that tubercles could be used as an active control mechanism whereby they would only be deployed in stalled conditions (Johari *et al.*, 2007). This concept was first mentioned in a patent by Watts and Fish (2006) which is discussed in Section 2.4.2.

A further experimental study revealed that the lift and drag performance for rudders with tubercles was similar to the unmodified airfoil in the pre-stall regime, however stall occurred at a lower angle of attack (Weber, Howle & Murray, 2010). This reduced the maximum lift coefficient that could be obtained for rudders with tubercles and caused an associated increase in drag at these angles of attack. This deterioration in performance was explained to be a response to the accelerated onset of cavitation caused by the presence of tubercles (Weber *et al.*, 2010). On the other hand, as noted by Johari *et al.* (2007), stall was more gradual with tubercles and a greater amount of lift was generated post-stall (Weber *et al.*, 2010). However, as the angle of attack was increased further, differences in post-stall performance diminished. The experimental investigation was carried out in water at $Re = 200,000 - 880,000$. Based on the results of this investigation, it was proposed that for a given tubercle geometry there exists a critical Reynolds number beyond which the peak lift-drag ratio decreases. For this study, the critical Reynolds

number was 710,000, below which the maximum lift-drag ratio for the hydrofoils with tubercles was improved relative to the hydrofoil with the smooth leading edge.

2.2.2 Influence of Tubercle Configuration on Airfoil Performance

Johari *et al.* (2007) varied the amplitude and spacing of sinusoidal tubercles and found that airfoils with smaller amplitude tubercles performed best in terms of stall angle and maximum lift coefficient. On the other hand, larger amplitude tubercles promoted softer stall characteristics. Although, the authors commented that the effects of wavelength variation were minor, inspection of the figures presented in their paper reveals that the tubercle configurations with smaller wavelength achieved higher maximum lift coefficient and stall angle with reduced drag. In contrast, Weber *et al.* (2010) observed that reducing the wavelength of tubercles on a rudder could influence the performance characteristics detrimentally. At higher Reynolds numbers, rudders with a larger number of tubercles, hence smaller wavelength, experienced deterioration in performance which was attributed to cavitation effects (Weber *et al.*, 2010).

2.2.3 Finite Span Compared with Semi-Infinite Span Results

Several studies focussed on performance differences between finite-span model Humpback whale flippers with and without tubercles (Miklosovic *et al.*, 2004; Murray *et al.*, 2005; Miklosovic *et al.*, 2007; Pedro & Kobayashi, 2008; Stanway, 2008; van Nierop, E, Alben, S & Brenner, 2008). In general, it was reported that airfoils with tubercles showed improved lift performance and that there was a negligible effect on drag (Miklosovic *et al.*, 2004; Murray *et al.*, 2005; Miklosovic *et al.*, 2007; Pedro & Kobayashi, 2008). The numerical model undertaken by Watts and Fish (2001) of a finite-span, rectangular planform airfoil also demonstrated improved lift for the model with tubercles. This model also showed that induced drag was reduced by the presence of tubercles. On the other hand, Stanway (2008) found that the maximum lift coefficient was lower for the majority of cases under investigation. Weber *et al.* (2010) found inferior performance characteristics for swept rudders with tubercles. In addition, van Nierop *et al.*, (2008) determined theoretically that the lift performance of model whale flippers was inferior to smooth leading edge models. However, these researchers (van Nierop *et al.*, 2008) acknowledged the limitations of their model, highlighting that errors were introduced near the wing tip. Table 2.1 summarises the performance advantages and disadvantages for the finite airfoils with tubercles discussed above.

For full-span airfoil models with and without tubercles, results indicated that performance enhancements could not be achieved with tubercles (Stein & Murray, 2005; Johari *et al.*, 2007; Miklosovic *et al.* 2007). However, it was observed that models with tubercles stalled more gradually and maintained a larger amount of lift post-stall. These studies were all experimental and involved rectangular planform airfoils with cross-sections similar to the Humpback whale flipper.

Table 2.1 – Summary of variations in performance for finite span models.

Researchers	Model	Advantages	Disadvantages
Miklosovic <i>et al.</i> (2004); Murray <i>et al.</i> (2005); Miklosovic <i>et al.</i> (2007); Pedro & Kobayashi (2008)	Experimental/Numerical (Humpback whale flipper model)	Increased lift, negligible effect on drag	-
Stanway (2008)	Experimental (Humpback whale flipper model)	-	Decreased lift for majority of cases
van Nierop <i>et al.</i> (2008)	Theoretical (Humpback whale flipper model)	-	Decreased lift
Weber <i>et al.</i> (2010)	Experimental (Swept rudder)	-	Decreased lift
Watts and Fish (2001)	Numerical/Theoretical (Rectangular planform model)	Increased lift, reduced induced drag	-

2.2.4 Reynolds Number Effects

It is important to acknowledge the Reynolds number when considering the apparent significance of three-dimensional effects. Hence, it can be established that lift enhancement was only achieved for those studies where the Reynolds number was in the range $500,000 \leq Re \leq 631,000$ (Miklosovic *et al.*, 2004; Murray *et al.*, 2005; Miklosovic *et al.*, 2007; Pedro & Kobayashi, 2008). The aforementioned studies were all carried out

with model Humpback whale flippers, which implies that tubercles are only successful when applied to this geometry. Weber *et al.* (2010) found that when tubercles were applied to the leading edge of rudders, the performance worsened for $Re = 200,000 - 880,000$. This was the only study carried out in water at such high Reynolds numbers therefore increased cavitation caused by relatively lower pressure in the troughs may also have been responsible for the deterioration in performance (Weber *et al.*, 2010). Additionally, results were obtained by Stanway (2008) in the low Reynolds numbers range of $44,000 \leq Re \leq 120,000$. It was observed that the maximum lift coefficient was reduced for all tests except $Re = 120,000$. The fact that these results are the only case that a model Humpback whale flipper model has demonstrated inferior performance with tubercles suggests that Reynolds number effects are quite significant.

Miklosovic *et al.* (2007) found that incorporating tubercles into a model whale flipper led to performance enhancement whereas the presence of tubercles on a full-span rectangular planform caused deterioration in performance. It was concluded that tubercles provided a three-dimensional benefit which could not be exploited by full-span models. However, the Reynolds number for the model whale flipper case was $Re = 534,000 - 631,000$, while for the full-span case it was almost half of that with $Re = 274,000 - 277,000$. This Reynolds number difference could account for the inferior performance characteristics of the full-span model before stall, although this was not stated in the article.

2.2.5 Flow Patterns

Pressure distributions and streamlines plotted for the numerical results obtained by Watts & Fish (2001) are shown in Figure 2.3 and Figure 2.4. From the images it can be seen that the pressure behind the troughs is lower than that behind the peaks. In addition, the streamlines are closer in the trough region, indicating that the flow velocity is higher, which is consistent with predictions made by Fish and Battle (1995). The limitation of this study was that the numerical simulation neglected the effects of viscosity and therefore boundary layer development and streamwise vorticity were not modeled (Watts & Fish, 2001).

NOTE:
This figure/table/image has been removed
to comply with copyright regulations.
It is included in the print copy of the thesis
held by the University of Adelaide Library.

Figure 2.3 - Panel method simulation of flow over a finite span wing at $\alpha=10^\circ$ with straight leading edge (*left*) and leading edge tubercles (*right*). Colours represent the pressure differences on the wing. (Watts & Fish, 2001).

NOTE:
This figure/table/image has been removed
to comply with copyright regulations.
It is included in the print copy of the thesis
held by the University of Adelaide Library.

Figure 2.4 - Streamlines at the edge of the boundary layer (Watts & Fish, 2001).

Viscous effects were, however, accounted for in a numerical study which modeled the same airfoil and angle of attack as Watts and Fish (2001) but used an unsteady Reynolds-averaged Navier-Stokes formulation (Fish & Lauder, 2006). It was observed that for regions downstream of the tubercle peaks, separation was delayed almost to the trailing edge as depicted in Figure 2.5. Streamline images indicate the formation of large streamwise vortices in the regions posterior to the troughs between tubercles as predicted by Fish and Battle (1995).

NOTE:
This figure/table/image has been removed
to comply with copyright regulations.
It is included in the print copy of the thesis
held by the University of Adelaide Library.

Figure 2.5 – Pressure contours and streamlines for NACA 63-021 with and without tubercles (Fish and Lauder, 2006).

It can be seen from Figure 2.5 that vortices are formed when the flow curves away from the area behind the tubercles, towards the valleys between. One inconsistency with previous results (Fish and Battle, 1995; Watts and Fish, 2001) is the fact that flow is accelerated behind the tubercles rather than behind the troughs (Fish & Lauder, 2006). The Reynolds number was not reported for this simulation.

Tuft experiments by Johari *et al.* (2007) showed that separation originates in the troughs between the tubercles and that the flow remains attached behind the tubercle peaks. This characteristic is also implied by the results from Fish and Lauder (2006) shown in Figure 2.5 by observing the position at which streamlines begin to deviate from the streamwise direction. Johari *et al.* (2007) noted that separation initiated at lower angles of attack for airfoils with tubercles, however at post-stall angles, the flow over the tubercle peaks was still attached when the flow over the unmodified airfoil had completely separated.

Dye visualization experiments shown in Figure 2.6 (Custodio, 2008), using the same airfoils as Johari *et al.* (2007), indicate that pairs of counter-rotating streamwise vortices were generated in the troughs between tubercles at $Re \sim 1,500$. The images also show that flow remained attached behind tubercle peaks post-stall, despite the fact that it was separated behind the troughs.

NOTE:
This figure/table/image has been removed
to comply with copyright regulations.
It is included in the print copy of the thesis
held by the University of Adelaide Library.

Figure 2.6 – Dye flow visualisation showing formation of streamwise vortices at $\alpha = 24^\circ$ after stall. (a) Unmodified airfoil and (b) Airfoil with tubercles, $\lambda = 0.05 c$ and $A = 0.12 c$ (right). (Custodio, 2008).

These results are consistent with both Fish and Lauder (2006) and Johari *et al.* (2007). Another observation was an apparent bi-periodic nature of the flow pattern, where every second tubercle/trough shows similar characteristics (Custodio, 2008), which is clearly visible in Figure 2.6. On the other hand, CFD simulation results (Watts & Fish, 2001 and Fish & Lauder, 2006) do not show this bi-periodic pattern. It was mentioned that the bi-periodic pattern was due to the fluctuating flow field at the airfoil trailing edge. Another plausible explanation which was not discussed in this article is that end effects may have influenced the results since the models had a relatively short span. The entire span of the airfoil models is depicted in Figure 2.6. It is unlikely that the dye is affecting these results since Johari *et al.* (2007) depicted the phenomenon in their tuft visualization figures.

The existence of streamwise vortices was supported by a computational study published by Pedro & Kobayashi (2008) at $Re = 500,000$. This study found that tubercles altered the vorticity distribution along the span of an idealized Humpback whale flipper model at $\alpha = 15^\circ$ and the results are shown in Figure 2.7 (a). In comparison with an identical model with a smooth leading edge, the model with tubercles experienced increased vorticity downstream of the tubercles and a reduction in tip vortex strength at this same angle of attack. It was also observed that the spanwise extent of leading edge separation in the tip region was reduced and there was a much more uneven trailing-edge separation line on

the central third of the span in the area behind the tubercles as shown in Figure 2.7 (b). In some regions, separation was delayed by the presence of tubercles, which was consistent with the observations of previous researchers (Fish & Lauder, 2006; Johari *et al.*, 2007; Custodio, 2008).

NOTE:
This figure/table/image has been removed
to comply with copyright regulations.
It is included in the print copy of the thesis
held by the University of Adelaide Library.

Figure 2.7 – (a) Instantaneous vorticity magnitude slices in span-wise direction for $\alpha = 15^\circ$ and (b) Averaged shear-stress lines for $\alpha = 15^\circ$, $Re = 500,000$ (Pedro & Kobayashi, 2008)

Recent observations of ceiling fans suggest that compartmentalization of the flow and reduced tip vortex strength are highly beneficial (Ontario Power Authority, 2010). Sweep and centrifugal forces both produce spanwise flow and in both cases, tubercles increase lift with minimal drag penalties.

Stanway (2008) determined the surface normal vorticity using particle image velocimetry to find the components of velocity at a plane parallel with the suction surface of the airfoil. Pairs of vortical structures with opposite sign were identified downstream from each tubercle and these vortices increased in strength with angle of attack in the range $10 \leq \alpha \leq 18^\circ$. A condition for measuring surface normal vorticity would be that separation had taken place such that a component of the streamwise vortices would be in the direction perpendicular to the measurement plane. Hence, increase in vorticity in these experiments could also be caused by increased separation. Nevertheless, the experiments imply the existence of streamwise vorticity.

Weber *et al.* (2010) found that leading edge tubercles accelerated the onset of cavitation and modified the location of where it first occurred, which can be seen in Figure 2.8. In

addition, cavitation was localised to the troughs between tubercles for the modified rudders as opposed to being spread along the entire leading edge as for the unmodified rudder.

NOTE:
This figure/table/image has been removed
to comply with copyright regulations.
It is included in the print copy of the thesis
held by the University of Adelaide Library.

Figure 2.8 – (a) Leading edge sheet cavitation and tip vortex cavitation on the smooth rudder, $\alpha = 17.0^\circ$ and (b) Cloud cavitation in troughs between tubercles and tip vortex cavitation on modified rudder, $\alpha = 15.8^\circ$. $Re = 786,000$ (Weber *et al.*, 2010). Cavitation is highlighted by black arrows.

This discovery is consistent with observations by previous researchers that the local pressure in the troughs is reduced with respect to other spanwise locations (Watts & Fish, 2001; Fish and Lauder, 2006). It can also be seen that the tip vortex is smaller for the rudder with tubercles, suggesting a reduced induced drag component.

2.2.6 Mechanism of Flow Control

There are various explanations for the performance enhancements observed for airfoils with leading edge tubercles. These include: increased boundary layer momentum exchange (Fish & Battle, 1995; Miklosovic *et al.*, 2004; Johari *et al.*, 2007; Custodio, 2008; Pedro & Kobayashi 2008); compartmentalisation of the flow and subsequent minimisation of tip stall (Fish & Battle, 1995; Stein & Murray, 2005; Miklosovic *et al.*, 2007; Pedro & Kobayashi 2008); non-uniform separation characteristics (Fish & Lauder, 2006; Johari *et al.*, 2007; van Nierop, Alben & Brenner, 2008; Pedro & Kobayashi 2008); alteration of the pressure distribution over the airfoil surface (van Nierop *et al.*, 2008) and vortex lift (Miklosovic *et al.*, 2007; Custodio, 2008). In general, these explanations are mutually inclusive and indicate that several benefits can occur simultaneously. On the

other hand, there is limited explanation concerning the failure of tubercles to provide performance enhancement in certain situations.

It was suggested by Custodio (2008) that the formation of streamwise vortices is a result of the spanwise flow associated with the variation in leading edge sweep angle characteristic of tubercles. The existence of these vortices is believed to lead to additional momentum exchange in the boundary layer, which prolongs flow attachment, increasing the maximum attainable lift (Fish & Battle, 1995; Miklosovic *et al.* 2004). An analogy was suggested between conventional tab-like vortex generators and tubercles with regards to the generation of streamwise vortices and the associated increase in momentum exchange (Miklosovic *et al.* 2004). This was first mentioned by Fish and Battle (1995).

However the similarity between conventional vortex generators and tubercles was contested by Stein and Murray (2005) based on their experimental results, mentioned in Section 2.2.1. It was suggested that a more analogous device to tubercles is a wing fence which is known to prevent spanwise stall progression (Stein and Murray, 2005). According to Miklosovic *et al.* (2007), the prevention of spanwise stall progression for a semi-span wing would overcompensate for the disadvantage of premature flow separation at the troughs between tubercles. Pedro and Kobayashi (2008) explained that the streamwise vortices generated by tubercles created a physical barrier to the flow, hence restricting separation to the tip region. Watts & Fish (2001) proposed that flow compartmentalisation also decreased the amount of induced drag associated with a semi-span wing through reduction in the strength of wing tip vortices. Hence, the discrepancy between improved performance for swept wings with tubercles and inferior performance for rectangular wings with tubercles was thought to be directly related to three-dimensional effects (Stein and Murray, 2005; Miklosovic *et al.*, 2007). On the other hand, all experiments with full-span models were undertaken at low Reynolds numbers. Therefore, due to the presence of Reynolds number effects, it is difficult to determine whether the dominant flow control mechanism is increased boundary layer momentum exchange or prevention of spanwise stall progression.

In agreement with Stein and Murray (2005), van Nierop *et al.* (2008) also claimed that it is not possible for tubercles to act as vortex generators since the wavelength and amplitude are much larger than the boundary layer thickness. Instead, it was proposed that since tubercle peaks and troughs have different chord lengths but similar thicknesses,

the pressure gradient must be higher for a trough, which causes separation to initiate in this region. This theory is supported by experimental and numerical observations of delayed separation behind tubercle peaks (Fish & Lauder, 2006; Johari *et al.*, 2007; Custodio, 2008). It was also postulated that the separation behind tubercle peaks is further delayed by a non-uniform downwash component, which leads to a reduced effective angle of attack (van Nierop *et al.*, 2008). Furthermore, the gradual onset of global stall was explained in relation to the variation of local stall angles with respect to span-wise location (van Nierop *et al.*, 2008). Hence, it was suggested that the stall angle could be identified as the point at which the amount of lift generated begins to decrease with angle of attack rather than when the airfoil experiences a sudden loss of lift (Johari *et al.*, 2007). In reality, the airfoils with tubercles would be only partially stalled at this angle of attack since the flow would still be attached at spanwise locations corresponding to the tubercle peaks.

Another explanation for lift enhancement was provided by Custodio (2008). It was suggested that the counter-rotating streamwise vortices migrate towards the troughs between tubercles according to the method of images (Custodio, 2008). This phenomenon is shown in Figure 2.9 and the arrows represent the direction of the velocity induced by the image vortex.

NOTE:
This figure/table/image has been removed to comply with
copyright regulations. It is included in the print copy of the
thesis held by the University of Adelaide Library.

Figure 2.9 – Schematic showing movement of vortices towards troughs as predicted using the method of images (Custodio, 2008). Image vortices shown in red are adapted.

The subsequent “coalescence” of the vortices was thought to be responsible for the low pressure regions observed behind the troughs on the suction surface (Custodio, 2008). An associated vortex lift was believed to be generated which could be considered analogous to that observed on a delta wing (Custodio, 2008). It was proposed that in the pre-stall regime, the amount of vortex lift generated was not enough to counteract the reduction in suction lift caused by the earlier onset of separation at the troughs (Custodio, 2008). After stall, however, it was suggested that the increased angle of attack would lead to generation of stronger vortices, hence explaining the lift enhancement achieved by tubercles post-stall. Since the amplitude of the tubercles is directly related to the tubercle

sweep angle, an increase in amplitude was proposed to increase the vortex strength. Therefore, the higher post-stall lift observed for larger amplitude tubercles was believed to be the result of increased vortex strength. The vortex-dominated nature of the post-stall flow was also reflected by a fivefold increase in the standard deviation for a given data set in experiments undertaken by Miklosovic *et al.* (2007).

2.3 Airfoil Tonal Noise

There are various flow effects promoted by the presence of tubercles which suggest that these leading edge modifications could successfully reduce or eliminate tonal noise. For example, the generation of streamwise vortices reduces the coherence of the wake (Bearman & Owen, 1998) and several researchers have shown evidence of this streamwise vortex formation (Fish & Lauder, 2006; Pedro & Kobayashi, 2008; Custodio, 2008). Furthermore, it has been observed that due to varying locations of separation along the span-wise direction, the separation line becomes somewhat interrupted (Pedro & Kobayashi, 2008). This would also lessen the coherence of vortex shedding in the wake. According to Nash, Lowson and McAlpine (1999), airfoil tonal noise is associated with the vortex shedding process and the von Kármán vortex street is shed with the same frequency as the acoustic tone. Suppression of the von Kármán vortex street formation and associated reduction of acoustic disturbance intensity was discussed by Kuethe (1972) in relation to vortex generators which generate a similar disturbance to the flow as tubercles.

Despite the fact that noise reduction has been identified as a potential benefit associated with tubercles (Watts & Fish, 2006; Dewar *et al.*, 2006), there have been no previous studies of the effect of tubercles on airfoil self-noise. This is important, because if aspects of tubercles were to be incorporated into new hydrofoil, airfoil and rotor designs, then it is important to firstly understand how noise is modified, and secondly, to exploit any noise-reduction capability that they may have.

Airfoil tonal noise is a high-pitched whistling sound that has been identified as a potential problem for wind turbines, gliders, small aircraft, rotors and fans (McAlpine *et al.*, 1999; Kingan & Pearse, 2009). According to McAlpine *et al.* (1999), tonal noise also occurs in underwater applications such as hydrofoils and propellers and is quite common on fast

yachts and dinghys. The phenomenon has been investigated by numerous researchers and was first discussed in detail by Paterson, Vogt, Fink and Munch (1973).

Paterson *et al.* (1973) proposed that the frequency of the tonal noise was related to the periodic vortex shedding experienced by an airfoil in a flow. The associated Strouhal number was based on twice the thickness of the boundary layer (99% velocity thickness) at the trailing edge for a thin flat plate. The researchers also mentioned that the tonal noise only occurred when the boundary layer on at least the pressure surface of the airfoil was laminar. In addition, it was shown that multiple tones could be generated simultaneously for a given flow condition.

Tam (1974) presented a comprehensive argument in opposition to the Strouhal number dependency discussed above. It was highlighted that the vortices initiated by wake instabilities would be formed at a considerable distance from the trailing edge, making it difficult to associate them with the noise source, which is known to be close to the trailing edge. Additionally it was pointed out that a solid streamlined body is not known to generate two vortex systems at different frequencies coexisting with one other. Tam (1974) put forward an alternative theory involving the existence of a self-excited acoustic feedback loop. The proposed feedback loop is initiated by instabilities in a laminar boundary layer on the pressure surface of an airfoil, which become amplified as they move downstream. When these instabilities reach large enough amplitude, they cause a lateral oscillation of the wake, which induces acoustic wave emission in all directions. Increased boundary layer oscillation is instigated by the waves reaching the pressure surface of the airfoil near the trailing edge. For reinforcement to occur, the phase change around the loop should be an integral multiple of 2π . Tam (1974) highlighted that the frequency of the unstable disturbances is bounded by a neutral stability curve. The simultaneous existence of multiple tones was attributed to the existence of more than one feedback loop for these cases (Tam, 1974).

An experimental and theoretical investigation by Arbey and Bataille (1983) found that the noise spectrum associated with an airfoil in a laminar flow consists of a broadband contribution with a peak frequency at f_s and a set of equally spaced, discrete frequencies, f_n . The broadband contribution was attributed to diffraction of Tollmien-Schlichting (T-S) waves at the trailing edge, which was initially proposed as a noise radiation mechanism

by Fink (1978). The discrete frequencies, f_n , were believed to be the result of an aeroacoustic feedback loop between the maximum velocity point on the airfoil and the trailing edge (Arbey and Bataille, 1983).

A detailed study by McAlpine *et al.* (1999) found that tonal noise is closely related to a region of separated flow near the airfoil trailing edge and suggested that it is dependent on the existence of a separation bubble. It was proposed that tonal noise would be undetectable when transition to turbulence occurred sufficiently far upstream of the trailing edge of the airfoil. This was alluded to earlier by Tam (1974) who stated that the “no tone regime corresponds to a turbulent regime.” This idea is supported by the fact that tonal noise only occurs at low angles of attack. The authors used a linear stability model to predict the radiated tone frequency and found excellent agreement with their experimental results. The feedback model proposed by these researchers (McAlpine *et al.*, 1999) was similar to Tam (1974) except that it was specified as forced boundary layer receptivity (wavelengths of boundary layer and disturbance are comparable) in the region containing the separation bubble. Additionally, the “critical point” of coupling between the sound waves travelling upstream and the T-S waves travelling downstream in the boundary layer was suggested to be near the point of separation rather than where the flow initially became unstable.

It was emphasized in the experimental study by Nash *et al.* (1999) that the maximum amplification of T-S instabilities occurred in regions of the flow with inflectional velocity profiles caused by an adverse pressure gradient. For tonal noise generation, this region of inflected or separated flow should exist close to the trailing edge of the structure if it is to remain periodic. Also, the adverse pressure gradient should not be too severe, as this would initiate random turbulence having low coherence. In their theoretical analysis, the frequencies with maximum growth rates near the trailing edge corresponded closely with the observed acoustic tone. These researchers also carried out flow visualization with a strobed laser sheet, which showed a highly coherent wake structure at the frequency of the tone.

In the numerical study by Desquesnes, Terracol and Saguat (2007) the mechanism of tonal noise generation detailed in Nash *et al.* (1999) was verified. In addition, an explanation for the secondary discrete vortices, f_n , identified by Arbey and Bataille (1983)

was provided. The researchers proposed that these discrete frequencies were the consequence of a periodic modulation of the amplitude of the main tonal frequency, f_s . The observed secondary frequency spacing was identified to correspond to the period of this modulation. The role of the suction surface in the noise spectra was discussed for the first time since Arbey and Bataille (1983) and it was noted that the suction side boundary layer is highly receptive to the tone frequency. Visualization of flow at the trailing edge revealed that the phase difference between the instabilities on the pressure and suction sides has a large impact on the acoustic waves generated. A phase difference of 180 degrees resulted in radiation of a higher amplitude acoustic wave in contrast to phase locking which led to a weak acoustic wave radiation. Figure 2.10 depicts the mechanism of tonal noise generation where the “main feedback loop” is associated with the primary tone and the “secondary feedback loop” is related to the modulation of the primary tone.

NOTE:
This figure/table/image has been removed
to comply with copyright regulations.
It is included in the print copy of the thesis
held by the University of Adelaide Library.

Figure 2.10 - Schematic of tonal noise generating mechanism as portrayed by Desquenses (2007).

Kingan & Pearse (2009) developed a theoretical model based on the Orr-Sommerfield equation and compared it with existing empirical models (McAlpine *et al.*, 1999; Paterson, 1973; Arbey and Bataille, 1983; Brooks, Pope & Marcolini, 1989) in regards to predicting tonal noise frequencies for four different sets of experimental results. It was shown that the theoretical model could be used to predict the boundary layer instability noise for arbitrary airfoil shapes with reasonable accuracy. By contrast, the empirical results gave varied predictions since they had been derived for a specific airfoil shape. They argued that this made the theoretical model much more widely applicable (Kingan & Pearse, 2009).

There are still some aspects of tonal airfoil noise generation that remain to be explained or experimentally confirmed. Furthermore, there has been no study of the effect of leading edge modifications on tonal noise. A relationship between the coherence of the wake and tonal noise generation has been observed (Nash *et al.*, 1999). Also, the significance of the suction surface in tonal noise generation has been highlighted (Arbey and Bataille, 1983; Desquesnes *et al.* 2007). Moreover, it is believed that the phase difference between instabilities reaching the trailing edge has a significant impact on tonal noise amplitude (Desquesnes *et al.* 2007). Therefore, since tubercles generate streamwise vortices which affect the coherence of the wake and most likely change the stability characteristics of the boundary layer on the suction surface, there is a strong probability that they would interfere with the tonal noise generation mechanism.

2.4 Existing Patents

2.4.1 Scalloped Wing Leading edge

A patent was taken out by Watts and Fish (2002), which describes modifications to the leading edge of a wing in the form of smoothly varying forward-and-aft swept protrusions (tubercles). The aim of the invention is to maximise the lift for a given airfoil, whilst minimising the drag. Various specifications concerning the placement, amplitude, wavelength, chordwise extension, and fore-and-aft protrusion slope are described. It is stated that the devices will be preferably separable from the wing, allowing them to be manufactured separately and possibly added to existing wings at a later date. In such cases, they could be attached to the wing leading edge via rivets. In other situations, it is suggested that the best option may be to design a single wing section consisting of a solid, composite structure. Placement on slats or wing extensions is considered as a possibility. Overall, tubercles are portrayed as lightweight, inexpensive and non-complex.

2.4.2 Scalloped Leading edge Advancements

Some new specifications have been made to this initial patent (Watts & Fish, 2006) by the same researchers. These include: the use of tubercles for housing instruments; making the tubercles deployable, retractable or both and implementing tubercles for noise reduction purposes. Figure 2.11 shows a schematic diagram which illustrates the potential layout of the actuator and equipment.

NOTE:
This figure/table/image has been removed
to comply with copyright regulations.
It is included in the print copy of the thesis
held by the University of Adelaide Library.

**Figure 2.11 – Cross-sectional view taken from the leading edge of a tubercle to the trailing edge
(Watts & Fish, 2006).**

Several types of instruments that could be mounted in the tubercles are suggested and include sensors, emitters, transmitters and transceivers. The advantages of mounting the instruments in this way are outlined as: improved viewing position, ease of removability and negligible performance deterioration.

Some examples of deployable and retractable scallop mechanisms are also outlined. The idea of a flexible leading edge is introduced which expands in response to mechanical actuation, electrical stimulation or thermal stimulation. Other associated benefits are described such as removal of ice build-up, instrument timing control and instrument protection upon retraction.

Noise reduction is required in circumstances when stealth needs to be optimised, such as on the fins and propeller of a submarine that needs to pass undetected. The absence of noise could also provide an improved operating environment for the instruments located within.

2.4.3 Scalloped Trailing Edge

This invention describes an airfoil with a relatively thin trailing edge incorporating a series of troughs and ridges as shown in Figure 2.12, that are designed to delay or prevent two-dimensional separation without creating additional drag penalties (Presz Jr, Paterson, & Werle, 1989). The concept was investigated by Werle *et al.* (1987) as a method of increasing the maximum lift coefficient of an airfoil. Other objectives of the invention highlighted in this patent are to reduce the sensitivity to stall onset under various operating conditions and to reduce the drag at high loading. The reason for inclusion of this patent is that the concept bears strong similarity to tubercles. Specifications are

outlined which relate to the dimensions, upstream extension, rate of convergence of the trough passages and edge curvature of both troughs and ridges.

NOTE:
This figure/table/image has been removed
to comply with copyright regulations.
It is included in the print copy of the thesis
held by the University of Adelaide Library.

Figure 2.12 – An illustrative perspective view portraying the invention (Presz Jr. *et al.*, 1989)

Various applications for the above invention were also suggested. These are illustrated in Figure 2.13 and include: sails (i.e. for yachts), keels, rudders, gas turbine engines, compressors, stator vanes and rotor blades.

NOTE:
This figure/table/image has been removed
to comply with copyright regulations.
It is included in the print copy of the thesis
held by the University of Adelaide Library.

Figure 2.13 – (a) Yacht with invention incorporated on the sail, keel and rudder (b) Gas turbine with external casings taking the form of the invention (c) Stator vane with the invention included on the trailing edge (Presz Jr. *et al.*, 1989).

2.4.4 Turbine/Compressor Rotor with Leading edge Tubercles

This patent describes the incorporation of tubercles into the leading edge of a turbine/compressor rotor blade (Dewar *et al.*, 2006). The main focus of the invention is on applications involving the use of wind and other moving fluids (i.e. water and steam) for power generation. The aim of the invention is to enhance lift, improve resistance to stall, reduce drag and lower noise in order to improve the performance of a turbine/compressor

(Dewar *et al.*, 2006). More specifically, enhanced lift performance enables more power to be captured from available fluid flows, which translates to increased efficiency. Increasing the stall angle widens the operating envelope of a turbine/compressor, allowing it to function over a greater range of fluid flow rates. A reduction in drag for a given wind speed allows for a reduction in the structural strength of supporting structures. Lowering the noise produced by turbines/compressors is important to ensure minimal disturbance to the surrounding community and environment.

In order to accommodate changes in fluid flow rates, the shape or spacing of the tubercles can be altered using a control system and a separate control system can change the rotor blade pitch (Dewar *et al.*, 2006). The outer material for an active tubercle control mechanism is described as a flexible material which is stretched over a supporting substrate. Actuators can be used to change the blade shape and hence vary the tubercle configuration (Dewar *et al.*, 2006).

A retro-fit option for implementing the tubercle design on existing blades is also outlined and it is specified that the device should preferably be implemented on rotor blades with pitch-based power control (Dewar *et al.*, 2006).

2.4.5 Spoked Bicycle Wheel

This invention encompasses the application of sinusoidal protrusions to the leading edges of airfoil-shaped spokes on the wheel of a bicycle as shown in Figure 2.14 (Zibkoff, 2009). Various details of the protrusion arrangement are disclosed in the patent including: placement, number of peaks/valleys and amplitude (Zibkoff, 2009).

NOTE:
This figure/table/image has been removed
to comply with copyright regulations.
It is included in the print copy of the thesis
held by the University of Adelaide Library.

Figure 2.14 –Bicycle wheel with tubercles on leading edge of spokes (Zibkoff, 2009).

Additionally, it was suggested that the protrusions could also be placed on the trailing edge. The aim of the protrusions is to reduce the drag and noise associated with the spokes. A reduction in drag leads to improved efficiency of a bicycle which correlates with lower energy expenditure of the cyclist to maintain a given speed (Zibkoff, 2009).

2.5 Summary and Discussion

Previous research focussed on comparing the performance of airfoils with tubercles having different combinations of amplitude and wavelength (Johari *et al.*, 2007). However, only a limited number of tubercle configurations were investigated and the experiments were carried out on airfoils with the same profile shape. Therefore, it was observed that there was still an opportunity to carry out a more comprehensive investigation into the effects of changing the amplitude and wavelength parameters of tubercles. In addition, a comparison between two airfoil profile shapes with and without tubercles had not been made before the current study. Generally, previous studies used models with profile shapes closely matched to that of the Humpback whale flipper (Watts & Fish, 2001; Miklosovic *et al.*, 2004; Murray *et al.*, 2005; Stein & Murray, 2005; Johari *et al.*, 2007; Miklosovic *et al.*, 2007; van Nierop *et al.*, 2008; Pedro & Kobayashi, 2008; Stanway, 2008). Therefore there was an opportunity to investigate an alternative profile shape which bore no resemblance to the Humpback whale flipper.

Results indicate that whale flipper models demonstrate superior performance in comparison to full-span rectangular planforms. However, the benefits of tubercles have only been realised at $Re > 500,000$ in previous studies (Miklosovic *et al.*, 2004; Murray *et al.*, 2005; Pedro & Kobayashi, 2008). Hence, the fact that all full-span rectangular planform models were tested at $Re < 300,000$ (Stein & Murray, 2005; Johari *et al.*, 2007; Miklosovic *et al.*, 2007) indicates that more data are required before a comprehensive conclusion can be drawn about three-dimensional and Reynolds number effects.

In the literature, there is limited discussion on the effect of the boundary layer state on performance for airfoils with tubercles. Additionally, the pressure distribution for airfoils with tubercles had not been measured experimentally and had only been discussed briefly in the numerical study by Watts and Fish (2001) prior to this work. Locating points of separation and reattachment and determining the pressure distribution were considered valuable tasks which could ultimately assist in the interpretation of results. Moreover, this

information could also lead to an explanation for the lack of success of tubercles at low Reynolds numbers.

A detailed experimental investigation into the characteristics and strength of the streamwise vorticity generated by the presence of the tubercles has not been undertaken previously. Streamline images from a numerical simulation indicated the formation of large streamwise vortices in the regions posterior to the troughs between tubercles (Fish and Lauder, 2006), however their strength was not quantified. In addition, several important details were not included in the discussion of this study, including the chosen numerical solver and the value of the Reynolds number. Pedro and Kobayashi (2008) revealed the existence of streamwise vorticity and plotted vorticity contours for a numerical model of a Humpback whale flipper. However, the magnitude of the streamwise vorticity was not discussed. Stanway (2008) conducted particle image velocimetry in the plane parallel to both the flow and the airfoil chord. However, streamwise vorticity was parallel to the measurement plane until separation occurred. Thus, it was a requirement that the flow needed to have separated in order for vorticity to be present. In this case, the measured vorticity would only be a component of the actual streamwise vorticity. In addition, the method used for estimating vorticity from discrete data was not discussed and hence the viability of the results was questionable. Therefore there exists an opportunity to do a more thorough and comprehensive study using particle image velocimetry to investigate the cross-streamwise, cross-chordwise plane. The streamwise vorticity and subsequently circulation could be calculated through knowledge of the velocity components in this plane.

Finally, a major opening exists in the aeroacoustics realm, whereby no published data exists on the noise reduction capabilities of leading edge tubercles. This was despite the fact that researchers have alluded to the potential benefits attainable (Dewar *et al.*, 2006).

Hence, it has been discovered that the current understanding of tubercles and their effect on the flow is still incomplete. A critical analysis of the existing body of knowledge has enabled current gaps to be identified, which could be addressed in this study to contribute to the present understanding of tubercles and their function. Previous studies have established an excellent basis to build upon and have provided unanswered questions which have motivated the pathways of analysis pursued during this study.

2.6 Aims and objectives of current research

The overall objective of this investigation is to develop a comprehensive understanding of the way in which tubercles influence the flow over airfoils at low Reynolds numbers. In addition, it is considered important to carry out a more comprehensive investigation into the effects of changing the amplitude and wavelength parameters of tubercles than has been attempted previously. From the tubercle configurations tested, the objective is to identify the optimal combination of amplitude and wavelength for a sinusoidal tubercle arrangement. It is also considered desirable to compare the performance of tubercles for different airfoil profiles. This will reveal the effect of boundary layer characteristics on tubercle performance as well as determining the applicability of tubercles to other airfoil profile shapes distinct from that of the Humpback whale flipper.

The Reynolds number is a relevant parameter in this investigation since it defines the boundary layer state as well as the location of transition from a laminar to a turbulent boundary layer. In the laminar regime, where the Reynolds number $Re_c < 5 \times 10^5$, the boundary layer separates at relatively low angles of attack, typically in the range $8 - 12^\circ$. At higher Reynolds numbers, typically $5 \times 10^5 < Re_c < 5 \times 10^6$ (NACA Tech. Mem., 1949), the boundary layer undergoes transition from a laminar to a turbulent state, with the transition point moving upstream as the Reynolds number is increased. For higher Reynolds numbers again, typically $Re_c > 5 \times 10^6$, the boundary layer becomes turbulent, leading to a decreased tendency to separate. In the turbulent regime, the stall angle increases typically to 18° or more, depending on the airfoil profile. These changes cause the lift and drag characteristics to be strongly dependent on the Reynolds number.

Other phenomena add to the complexity of the flow, such as the tendency for laminar boundary layers to separate and reattach on some airfoil profiles. An understanding of the effects of tubercles across the full laminar-to-turbulent Reynolds number range is required to enable the benefits of tubercles to be exploited. However, due to the small-scale, low-speed facilities available for this study, the flow is restricted to the laminar regime. Nevertheless, this enables direct comparison with other investigations, the majority of which are also in the laminar regime (e.g. Stein & Murray, 2005; Johari, 2007).

In addition to exploring the effects of a sinusoidal variation on the leading edge of the airfoils, a modification in the form of sinusoidal surface waviness is considered. The objective of this aspect of the study is to elucidate whether or not similar performance effects can be observed. This indicates the viability of surface waviness as an alternative to leading edge tubercles.

A further intention of the investigation is to analyse quantitative results for models with and without tubercles having different span lengths. This enables a comparison to be made of full-span and semi-span results for the same experimental set-up, which highlights the importance of three-dimensional effects on tubercle performance for non-swept wings. Since these particular results are collected under the same experimental conditions with equivalent Reynolds number, the three-dimensional effects can be analysed in isolation.

Due to the complex nature of the flow at low Reynolds numbers, an understanding of the surface pressure characteristics is deemed necessary. This facilitates the detection of separation bubbles, which are known to have a significant effect on the performance characteristics of airfoils. Investigation into the airfoil performance with boundary layer trips is also carried out to quantify the effects of separation bubbles on performance and to determine whether tubercles remain effective when the boundary layer is turbulent.

Another objective is to determine the differences in surface pressures at various chordwise cross-sections for airfoils with tubercles. This enables development of a greater insight into the flow behaviour associated with the presence of tubercles and also provides data for determination of the effective lift at a given spanwise location. Comparison of the relative lift at a trough, peak and midway between can reveal differences in circulation, hence providing a reason for streamwise vortex generation.

A more complete understanding of the flow patterns associated with the presence of tubercles is desired so methods of visualising specific features of the flow are required. Qualitative measurements are considered sufficient to emphasise the general flow behaviour. However, it is also considered necessary to undertake quantitative measurements of the streamwise vorticity and circulation generated by the tubercles. A more detailed understanding of the nature of the streamwise vortices is desired in addition to information pertaining to their evolution as a function of chordwise position. It is also

considered necessary to investigate variations in streamwise vorticity and circulation with angle of attack.

An additional objective is to make a quantitative comparison between the tonal noise level with and without tubercles. This enables conclusions to be drawn as to whether the presence of tubercles can perceptively alter the noise emission in a beneficial manner.

The aims are summarised as follows:

- To understand the effect of the boundary layer state and tubercle geometry on tubercle performance.
- To determine whether there are differences in tubercle performance for semi-infinite-span and finite-span airfoils.
- To determine whether other geometric modifications similar to tubercles can provide tubercle-like effects.
- To determine the mechanism by which tubercles enhance airfoil performance.
- To understand the mechanism, if any, by which tubercles alter the acoustic emission from airfoils.

The objectives can be summarised as follows:

- Measure lift and drag performance for a set of NACA 0021 and NACA 65-021 airfoils having different tubercle configurations.
- Optimise amplitude and wavelength parameters of tubercles based on lift and drag performance.
- Investigate an alternative modification in the form of angular waviness and compare with the leading-edge tubercle results.
- Determine whether there are any additional performance advantages of tubercles for semi-span airfoils in comparison with full-span airfoils.
- Identify locations of separation and reattachment and compare pressure distributions at a tubercle peak, trough and midway between.
- Investigate the influence of boundary layer trips on tubercle performance.
- Establish flow patterns associated with tubercles both qualitatively and quantitatively.

- Determine the variation in vorticity and circulation of the tubercle-induced streamwise vortices at various angles of attack.
- Measure noise emission for airfoils with and without tubercles.

2.7 Remainder of Thesis

Experimental methods are discussed in Chapter 3 and details of the experimental set-up are also provided. The chosen methods are justified on the basis of the objectives discussed in Section 2.6. An uncertainty range is provided for the experimental analyses where possible to give an estimation of the accuracy of the results. The non-standard equipment and apparatus used in the experiments are discussed in detail in Chapter 3. Specifications and performance measures are included as well as schematic diagrams to give a visual representation of the equipment and apparatus.

Results from the experimental investigations are presented and discussed in Chapters 4-7. Wherever possible, figures and diagrams are incorporated to illustrate the concepts under discussion. Similarities and differences with the existing body of literature are identified and considered. An attempt is made to generate a cohesive interpretation of the results by recognising areas in which the results from various experimental investigations overlap. The results are examined critically to arrive at an explanation for the way in which tubercles affect the flow and reasons behind this behaviour. A detailed uncertainty analysis is included where applicable to verify the integrity of the data presented and to highlight the primary sources of error. The key findings are summarised at the end of each chapter to emphasise the main points of the discussion and to provide a brief overview of the material covered.

The conclusions of this study are given in Chapter 8 and include a refined description of the mechanism by which tubercles alter the flow past an airfoil. In addition, the extent to which the aims and objectives stated in Section 2.6 are met is addressed. Suggestions for future work are given in Chapter 9 and are based on gaps which were identified during the course of the research.

2.8 New Work in this Thesis

This is the first study to investigate such a large range of tubercle amplitude and wavelength configurations. This has enabled a more accurate interpretation to be formed on the influence of these parameters on performance. The key geometric variables defining tubercle performance have also been identified for the first time in this study and include: the amplitude-to-wavelength (A/λ) ratio, the effective tubercle height to boundary layer thickness (h_{eff}/δ) ratio and the Reynolds number. Investigation into their relevance with regards to performance enhancement has also been undertaken. Additionally, the analysis of semi-span and full-span airfoils has not previously been undertaken at the same Reynolds number and this has allowed a more exact comparison to be made, shedding more light on three-dimensional effects.

Incorporating a roughened strip to trip the boundary layer to turbulence at low Reynolds numbers on an airfoil with tubercles has not previously been attempted. In addition, the performance of two dimensional airfoils at high Reynolds numbers has not been investigated. Hence, this study provides the first analysis of the effects of tubercles for a fully turbulent boundary layer.

Surface pressure measurements on an airfoil with tubercles have been undertaken for the first time, revealing spanwise pressure variations and locations of separation bubbles and separation without reattachment. The associated results facilitate predictions of flow movement along the airfoil, assisting in the interpretation of flow visualisation images. In addition, integration of the pressure distribution has enabled calculation of the effective lift at various chordwise positions providing a unique representation of the spanwise lift distribution.

Particle image velocimetry (PIV) experiments reveal the development of the streamwise vortices through analysis of the velocity fields for several cross-sectional planes perpendicular to both the airfoil and the flow at three angles of attack. This is the first time that Particle Image Velocimetry (PIV) has been used to observe the vorticity field in this particular plane, allowing a novel examination of the vorticity and circulation of the streamwise vortices.

Noise measurements were made on airfoils with tubercles for the first time despite the fact that potential noise benefits had already been alluded to. These measurements have explored a unique advantage of tubercles which has received minimal attention in the past and has never been investigated formally.

Chapter 3

Experimental Equipment and Methodology



3.1 Introduction

This chapter provides a description of the facilities used for the experiments as well as information concerning specific custom-built apparatus for this study. Details pertaining to standard equipment used in the analysis are omitted. The applied experimental techniques are introduced and more detailed information is provided where methodology is specific to the current investigation. Where necessary, justification of the chosen method of investigation is included. Post-processing procedures are also discussed where relevant. This chapter begins with a description of the airfoil models, which is followed by relevant specifications of the wind and water tunnel facilities. Force, acoustic and flow measurement systems are also discussed, along with their associated errors.

3.2 Airfoil Design

Tubercle configurations were modelled for two different airfoils: NACA 0021 and NACA 65-021. These airfoils have different chord-wise positions of maximum thickness and are designed for different flow regimes. Thus, it was envisaged that incorporation of tubercles into these profiles would provide two different insights into the effects of tubercles on aerodynamic performance due to the variation in boundary layer and separation characteristics. The NACA 0021 airfoil was selected as it closely

matches the cross-sectional profile of the Humpback whale flipper (Miklosovic, 2004). The maximum thickness of this profile is located at 30% of the chord. For comparison, the NACA 65-021 airfoil was utilised as it has a maximum thickness position further aft at 50% of the chord. The results for the NACA 0021 airfoil could be compared with those published in previous work on tubercles, which used similar airfoils. Thick airfoil sections are also used for wind turbine blades due to their “softer” stall characteristic (Hansen, 2000) and thus the chosen airfoil profiles have suitable application.

Airfoils were modelled using the computer aided drawing package “Solid Edge.” Models with tubercles consist of a series of two-dimensional profiles with varying chord lengths (Figure 3.1). These profile sections are combined into a swept protrusion which follows the path of a sinusoid at the leading edge. The trailing edge of all profiles lies at the same streamwise location. A programmable NC milling machine was used for fabrication of the models.

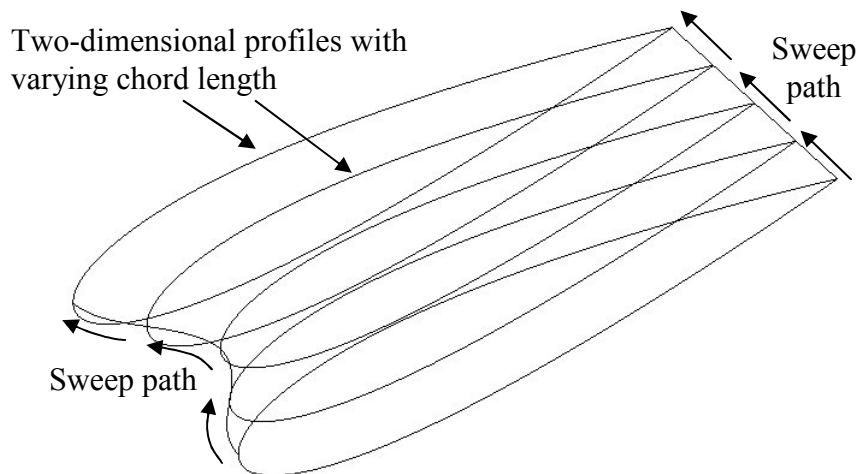


Figure 3.1 – Process used to construct model airfoils with tubercles.

The airfoils were machined from aluminium and anodized in matte black to ensure good visual contrast for visualization of hydrogen bubbles and to reduce laser reflections while taking the particle image velocimetry measurements. An aspect ratio of 7 was chosen because it delivered a compromise between the aspect ratio and the Reynolds number. The maximum attainable span length is governed by the test section dimensions (500mm x 500mm), thus chord length was selected based on the following considerations:

Table 3.1 – Considerations affecting chord length selection

Increasing chord length	Reynolds number increases	desirable
	Blockage increases	<i>undesirable</i>
	Aspect ratio decreases	<i>undesirable</i>

A large Reynolds number was desirable to give a flow in the high laminar range as required. Minimal blockage was necessary to improve accuracy of the results. The aspect ratio was preferably large to ensure that the airfoil models could be considered two-dimensional, reducing the influence of the wind tunnel walls on the measurements. In addition, the aspect ratios, AR , that were used by previous groups in this area of research were considered. For example, Miklosovic *et al.* (2004) used $AR = 4.3$ in their wind tunnel experiments and Watts & Fish (2001) used $AR = 2.04$. In their morphological analysis of the Humpback whale flipper, Fish and Battle (1995) found that the flipper had $AR = 6.1$. Finally, it was also necessary to ensure that the stiffness of the model was adequate to minimise velocity-induced vibration. Additionally, the wing area needed to be sufficient to give accurate readings using the available instrumentation. Lower forces would be measured less accurately as they would be close to the noise floor of the load cell. Therefore, the full-span airfoil models have a mean chord of $c = 70\text{mm}$ and span of $s = 495\text{mm}$, giving a planform area of $S = 0.035\text{m}^2$.

The average amplitude and wavelength of the tubercles on the Humpback whale flipper was determined using an average taken from the results of Fish and Battle (1995). In the analysis of their results, it was difficult to ascertain the exact position of the tubercles since it was not stated in distinct terms. There was, however, a graph showing the relative wavelength of the tubercles as a percentage of the chord and using this data it was possible to approximate the average wavelength as shown in Table 3.2. The corresponding intervals of measurement are given in Figure 3.2, which shows a planform view of the Humpback whale flipper. At regularly spaced locations, the flipper profile is shown to illustrate its variation with spanwise position.

Table 3.2 - Relative wavelength determined from Fish and Battle (1995)

Interval	Spacing (%)	Spacing (m)
1	12.3	0.31
2	8.5	0.21
3	8.62	0.22
4	7.46	0.19
5	7.25	0.18
6	6.8	0.17
7	6.55	0.16
8	4.6	0.12
9	3.16	0.08
10	1.69	0.04
average wavelength		0.17
mean chord		0.41
average wavelength 70mm chord		0.0286

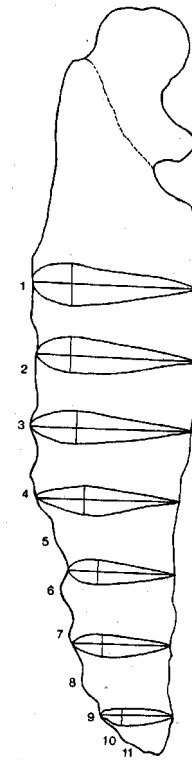


Figure 3.2 – Associated whale flipper (Fish & Battle, 1995).

This involved calculating the average chord, \bar{c} , based on an aspect ratio (AR) of 6.1 and a span (b) of 2.5m. The planform area was approximated as a rectangle for this calculation, thus allowing use Equation (3.1):

$$AR = \frac{b}{\bar{c}} \quad (3.1)$$



This gave a result of $\bar{c} = 0.41\text{m}$, which was used to normalise the calculated wavelength for the case of the whale flipper and then multiply by 70mm, giving the new average wavelength of 28.6mm.

Fish and Battle (1995) also provided a plot showing the variation of chord length according to segment number. In this study, the distal and medial flipper sections were dissected into 71 cross-sections of 2.5cm width. The program “Digitize it” was used to determine the amplitude of each tubercle and the corresponding chord length. All tubercle amplitudes were then normalised and summed together to determine the average normalised tubercle amplitude which is $A/\bar{c} = 0.05$. For a chord length of

70mm, the corresponding amplitude is $A \sim 3.5\text{mm}$. Figure 3.2 shows an illustration of the whale flipper that was used in the analysis.

Thus, it was decided that a wavelength of 30mm and amplitude of 4mm would be chosen as a reference configuration. The tubercle shape was selected to be sinusoidal as this most closely matches the morphology of the tubercles on the Humpback whale flipper (Miklosovic, 2004). Subsequently, models with various combinations of tubercle amplitude and wavelength in this range were designed to illustrate the effect of changing a single parameter on the lift and drag performance. Tubercle configurations are illustrated in Figure 3.3 and the corresponding dimensions are summarised in Table 3.3. The key dimensionless parameters were identified as the amplitude-to-wavelength (A/λ) ratio, the effective tubercle height to boundary layer thickness (h_{eff}/λ) ratio and the Reynolds number.

Table 3.3 - Tubercle configurations and adopted terminology.

0021 airfoils 			65-021 airfoils 		
Configuration	Label	A/λ Ratio	Configuration	Label	A/λ Ratio
0021 unmodified	0021 unmod	-	65-021 unmodified	65021 unmod	-
$A = 2\text{mm}$ (0.03c) $\lambda = 7.5\text{mm}$ (0.11c)	$A2\lambda 7.5$	0.27	-	-	-
$A = 4\text{mm}$ (0.06c) $\lambda = 7.5\text{mm}$ (0.11c)	$A4\lambda 7.5$	0.53	-	-	-
$A = 4\text{mm}$ (0.06c) $\lambda = 15\text{mm}$ (0.21c)	$A4\lambda 15$	0.27	-	-	-
$A = 4\text{mm}$ (0.06c) $\lambda = 30\text{mm}$ (0.43c)	$A4\lambda 30$	0.13	$A = 4\text{mm}$ (0.06c) $\lambda = 30\text{mm}$ (0.43c)	6 $A4\lambda 30$	0.13
$A = 4\text{mm}$ (0.06c) $\lambda = 60\text{mm}$ (0.86c)	$A4\lambda 60$	0.07	-	-	-
$A = 8\text{mm}$ (0.11c) $\lambda = 30\text{mm}$ (0.43c)	$A8\lambda 30$	0.27	$A = 8\text{mm}$ (0.11c) $\lambda = 30\text{mm}$ (0.43c)	6 $A8\lambda 30$	0.27

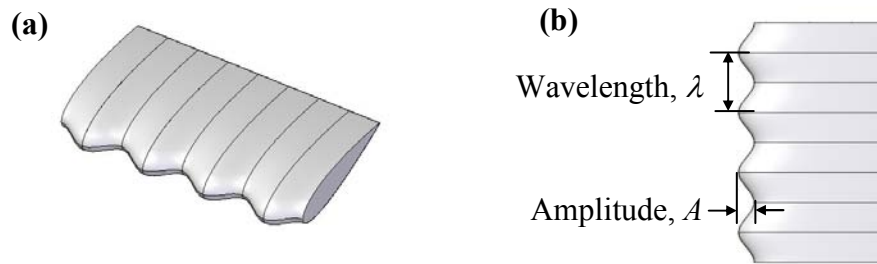


Figure 3.3 - Section view of airfoil with tubercles (a) 3D view, (b) Plan view with characteristic dimensions.

Pictures of the entire set of airfoil models with various tubercle configurations are shown in Figure 3.4.



Figure 3.4 – Set of NACA 0021 and NACA 65-021 airfoils with tubercles (left and right respectively).

A further set of three “wavy” airfoils were manufactured to investigate the effect of sinusoidally undulating the airfoil in the cross-streamwise direction (i.e. producing a sinusoidal variation in the local angle of attack). The motivation behind this study was to observe whether the airfoil performance of these models was similar to that observed for airfoils with tubercles. The airfoils were created from a series of airfoil cross-sections which were rotated with respect to one another about the trailing edge. The relative rotation angle between a trough and a peak, θ , is specified in Table 3.4. The wavelength, or distance between successive peaks and troughs is also displayed in Table 3.4. The amplitude-to-wavelength ratio, A/λ , is determined by considering the peak-to-peak distance divided by the wavelength.

Table 3.4 – Wavy airfoil configurations and adopted terminology.


0021 wavy airfoils		
Configuration	Label	A/λ Ratio
$\theta = 2^\circ$ $\lambda = 30\text{mm}$ (0.11c)	$\theta 2\lambda 30$	0.08
$\theta = 4^\circ$ $\lambda = 15\text{mm}$ (0.11c)	$\theta 4\lambda 15$	0.33
$\theta = 4^\circ$ $\lambda = 30\text{mm}$ (0.21c)	$\theta 4\lambda 30$	0.16

Figure 3.5 shows the construction method used to create the wavy airfoils using the Solid Edge drawing package. Figure 3.6 depicts the final models.

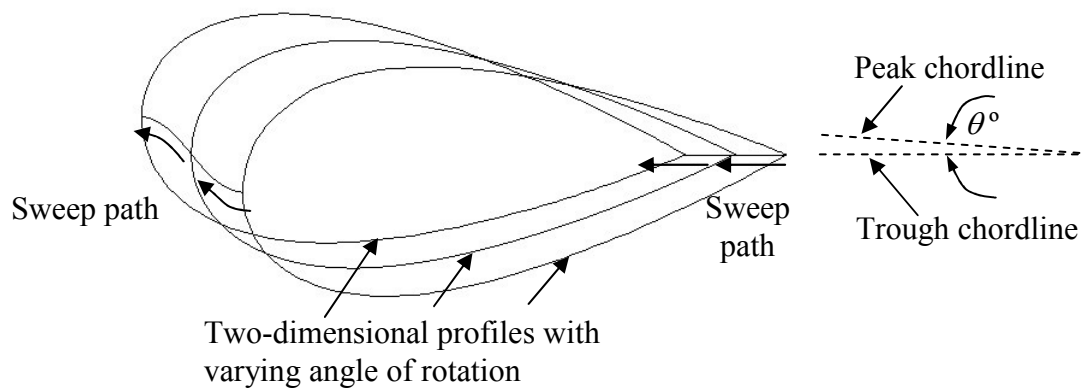
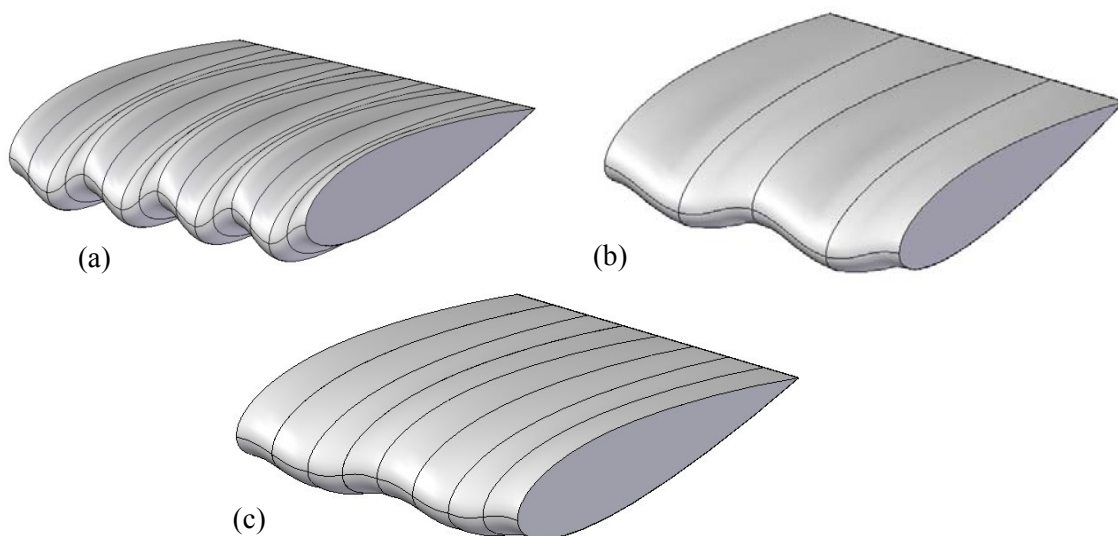


Figure 3.5 - Process used to model wavy airfoils.

Figure 3.6 – Sections of wavy models with labels, (a) $\theta 4\lambda 15$, (b) $\theta 4\lambda 30$ and (c) $\theta 2\lambda 30$.

3.3 Force Measurements

The most frequently used method for obtaining force measurements on a model is to use a balance system (Barlow *et al.*, 1999). Since strain gauges have been used with a satisfactory level of success and are relatively simple to set up and calibrate, this was the chosen method for lift, drag and pitching moment measurement. To ensure that a high degree of accuracy was maintained, a commercially-available device containing strain gauges in a Wheatstone bridge configuration was utilised. This load cell was purchased from JR3, has model number 45E15A-163 and is capable of measuring three components of force and three components of moment. External digital electronics were purchased with the device for signal conditioning and analogue-to-digital conversion. The system was calibrated by the manufacturer and prior to measurement, it was simply necessary to zero the device and then appropriate offsets were determined automatically.. However, the calibration was verified using a pulley system and a set of weights as discussed in Appendix A. The procedure used to determine the uncertainty associated with the force measurements is discussed later in this section.

3.3.1 Wind Tunnel

Force measurements were undertaken in the closed section of the 0.5m x 0.5m wind tunnel at the University of Adelaide, which is an open-jet facility. This flow facility has a maximum velocity of approximately 30m/s and turbulence intensity, $Tu \sim 0.6 - 0.8\%$ (the effect of the freestream turbulence level on transition location for an object placed in the flow is discussed in Section 3.3.3). The air flow is driven by a fan and passes through a series of bends equipped with turning vanes which increase flow uniformity and reduce eddy formation. The air then enters the settling chamber and passes through a set of 3 brass and stainless steel mesh screens with 58% open area which reduce turbulence intensity. The flow proceeds to the 6:1 area ratio contraction where it accelerates and the turbulence intensity is further reduced. A schematic diagram of the wind tunnel apparatus is shown in Figure 3.7. Note that the coordinate system shown is used throughout this thesis.

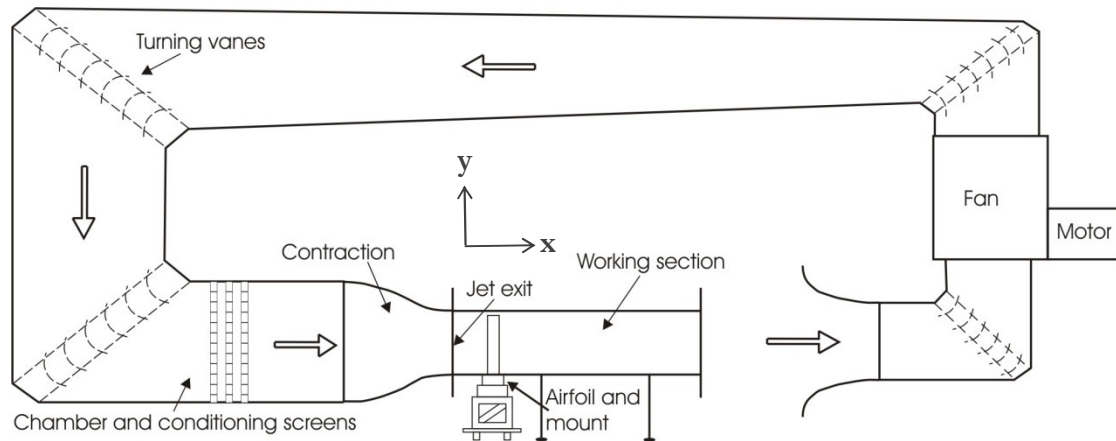


Figure 3.7 – Schematic of the wind tunnel used for force and pressure tapping measurements.

The velocity profile associated with the contraction exit was measured using a Dick Smith electronic wind speed meter. Freestream velocity data were collected at the wind tunnel contraction exit at 50mm intervals in the plane perpendicular to the flow. It can be seen in Figure 3.8 that the flow is reasonably uniform at the contraction exit.

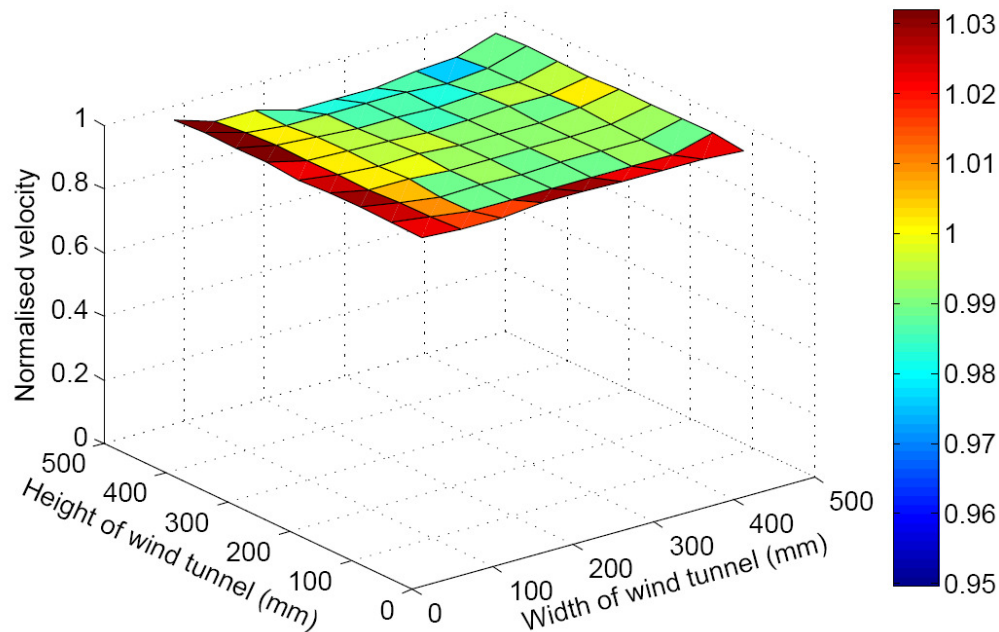


Figure 3.8 – Velocity profile at wind-tunnel contraction exit normalised with respect to mean velocity.

3.3.2 Boundary Layer Profile

It was necessary to establish that the thickness of the boundary layer was greater than the 3mm air gap between the airfoil and test section ceiling. This was to ensure that the wing tip vortices would be practically eliminated, hence creating two-dimensional flow and trading secondary flow losses for viscous losses at the wing tip. Therefore,

boundary layer measurements were carried out in the wind tunnel at a location corresponding to the streamwise position of the airfoil leading edge, which was 400mm from the wind tunnel outlet. Additional information pertaining to the nature of the boundary layer at this location could also be obtained from the measurements.

3.3.2.1 Pitot Tube Measurements

A miniature Pitot tube with 1.5mm internal diameter was used to measure the local velocity profile at the position of the airfoil leading edge with the airfoil removed. The Pitot tube was lowered in 1mm spatial increments starting from the test section ceiling. The traverse used for boundary layer measurements was manually controlled and had a resolution of 0.01mm. Each step was sampled at 1kHz for 60 seconds. The boundary layer thickness was calculated from linear interpolation of the velocity profile to determine the point at which the local velocity, u , was 0.99 of the mean freestream velocity, U_∞ . At this streamwise location, the boundary layer thickness, δ , was found to be $\delta \sim 9.4$ mm. The corresponding displacement thickness, δ^* , and momentum thickness, θ , are defined as follows:

$$\delta^* = \int_0^\delta \left(1 - \frac{u}{U_\infty}\right) dy \quad (3.2)$$

$$\theta = \int_0^\delta \frac{u}{U_\infty} \left(1 - \frac{u}{U_\infty}\right) dy \quad (3.3)$$

These equations were solved through numerical integration using the trapezoidal rule. The analytical solution was also found for verification and involved fitting a 4th order polynomial curve to the data and integrating the resulting polynomial. The values obtained using the numerical and analytical methods are within 2% for δ^* and 1% for θ . The average values calculated from the two integration methods are: $\delta^* = 1.09$ mm and $\theta = 0.86$ mm. The corresponding Reynolds numbers are $Re_{\delta^*} = 1850$ and $Re_\theta = 1460$.

Figure 3.9 shows the boundary layer profiles \bar{u}/U_∞ plotted against the similarity variable, ζ :

$$\zeta = \frac{y}{2x} \sqrt{Re_x} \quad (3.4)$$

where,

y = vertical distance of probe from wall

x = boundary layer development length

Re_x = Reynolds number based on boundary layer development length.

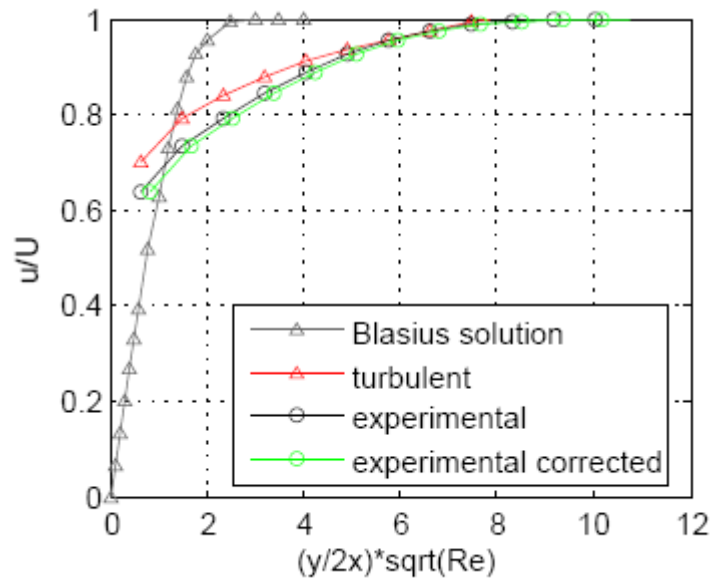


Figure 3.9 – Plot of boundary layer profile, $Re = 120,000$.

Other plots are included on the same set of axes for comparison to determine the nature of the boundary layer at this streamwise location. These include the Blasius solution for a laminar boundary layer on a flat plate (Young, 1970) as well as an empirical plot for a turbulent boundary layer based on experimentally observed turbulent profiles for a flat plate using a power law profile with $n \sim 7$ (Munson *et al.*, 1998). It can be seen that the data match closely with the turbulent boundary layer profile, which indicates that the boundary layer is turbulent. Further understanding with regards to the nature of the boundary layer can be established by determining the shape factor ($H = \delta^*/\theta$). From the values of displacement thickness and momentum thickness calculated earlier, the shape factor is found to be $H = 1.27$ which also indicates that the boundary layer is turbulent. The development length Reynolds number, Re_x , is arbitrarily based on half of the contraction length added to the distance from the wind tunnel exit to the airfoil model. This allows for boundary layer thinning associated with flow acceleration through the contraction as well as growth of the boundary layer along the wall. The calculated value of Re_x is of the order of 10^6 which also suggests that transition to turbulence has taken place.

3.3.2.2 Boundary Layer Corrections

The measurement of pressure using a Pitot tube is an invasive technique and thus appropriate corrections need to be applied to the data. The procedure for applying these corrections was obtained from McKeon, Jiang, Morrison and Smits (2003). According to these researchers, the most significant errors are due to streamline displacement and wall proximity effects. The effects of turbulence are implicitly accounted for in the McKeon *et al.* method and therefore a specific turbulence correction is not required. The effects of viscosity are ignored since the Reynolds number based on the probe diameter is greater than 1000.

The streamline displacement correction, Δy , accounts for the deviation of streamlines in a shear flow due to the presence of the probe as shown in Figure 3.10. This phenomenon causes the Pitot probe to register a velocity which is higher than the actual velocity at the height of the geometric centre of the probe. The wall proximity correction, δ_w , as shown in Figure 3.11 takes into account the additional streamline displacement away from the wall considering that the probe resembles a forward-facing step. The recommended procedure for both effects involves correcting the probe position rather than the velocity (McKeon *et al.*, 2003).

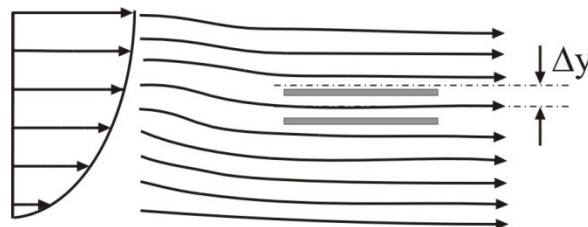


Figure 3.10 – Schematic of displacement correction.

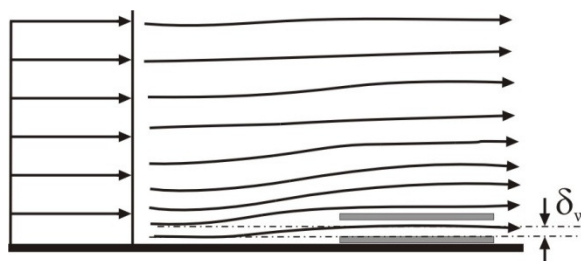


Figure 3.11 – Schematic of wall proximity correction.

The displacement correction, Δy , is given by the following equation:

$$\frac{\Delta y}{d} = 0.15 \tanh(4\sqrt{\alpha}) \quad (3.5)$$

where,

d = Pitot tube diameter

$$\alpha = \text{non-dimensional velocity gradient, } \alpha = \frac{d}{2u \times y_c} \left. \frac{du}{dy} \right|_c \quad (3.6)$$

c = probe centreline

u = true local mean velocity

y_c = distance from wall to probe centreline.

The wall correction, δ_w , is given by the following relationship:

$$\frac{\delta_w}{d} \begin{cases} 0.15 & \text{for } d^+ < 8 \\ 0.125 & \text{for } 8 < d^+ < 110 \\ 0.085 & \text{for } 110 < d^+ < 1600 \end{cases} \quad (3.7)$$

where,

$$d^+ = \text{non-dimensional Pitot diameter, } d^+ = \frac{du_\tau}{\nu} \quad (3.8)$$

$$u_\tau = \text{frictional velocity, } u_\tau = \sqrt{\frac{\tau_w}{\rho}} \quad (3.9)$$

$$\tau_w = \text{wall shear stress, } \tau_w = \mu \left(\frac{du}{dy} \right)_{y=0} \quad (3.10)$$

The nature of the Pitot tube measurement technique does not allow an accurate estimate of the wall shear stress since it is not possible to measure the velocity close enough to the wall to correctly determine du/dy . Hence, the Clauser chart method (Clauser, 1953) can be used instead to find u_τ . According to this method, turbulent boundary layers are of similar shape when plotted on a set of universal coordinates. Through simultaneous optimisation of a series of parameters, collected data can be matched to a standard curve. The method was adapted by Coles (1968) to find optimal values for his boundary layer wake function and it was found that this adaptation gave

a better curve fit to the measured data in the current study. The equation given by Coles (1968) is as follows:

$$\frac{u}{u_\tau} = \frac{1}{\kappa} \ln\left(\frac{yu_\tau}{\nu}\right) + C + \frac{2\Pi}{\kappa} \sin^2\left(\frac{\pi y}{2\delta_\pi}\right) \quad (3.11)$$

Von Kármán's constant is assumed to have the value $\kappa = 0.41$. The values of the remaining parameters, u_τ , Π , δ_π , C are optimised by minimising the mean square difference between the experimental mean velocity data and the theoretical model. The friction velocity is determined from the logarithmic portion of the mean velocity distribution and thus the optimisation is carried out for data in the y^+ range of $30 < y^+ < 500$. It is desirable to match experimental data as closely as possible to the theoretical curve in this range as shown in Figure 3.12. The value of the friction velocity which gives the best curve-fit is: $u_\tau = 1.13$. The overall error of the curve fitting process is $0.14u_\tau$, which is 0.63% of the freestream velocity.

Hence the final corrections can be determined, where the wall proximity correction, δ_w , is applied for increasing y^+ until $y/d < 2$, after which point the displacement correction, Δy , is applied instead (McKeon *et al.*, 2003). The calculated values of the corrections are $\delta_w = 0.13\text{mm}$ and $\Delta y_{\max} = 0.225\text{mm}$ and the corrected data are shown in Figure 3.9.

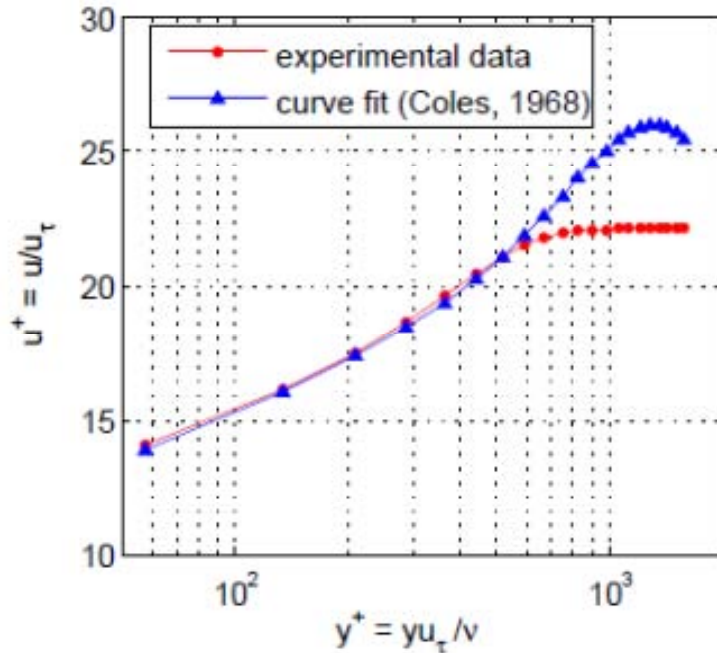


Figure 3.12 – Velocity distribution for a turbulent boundary layer.

3.3.3 Turbulence Intensity

Turbulence intensity, Tu , is defined as (Schlichting & Gersten, 2000):

$$Tu = \sqrt{\frac{1}{3}(\overline{u'^2} + \overline{v'^2} + \overline{w'^2})} / U_{\infty} \quad (3.12)$$

where,

$\overline{u'}$ = average fluctuating velocity component in streamwise (x) direction

$\overline{v'}$ = average fluctuating velocity component in vertical (y) direction

$\overline{w'}$ = average fluctuating velocity component in spanwise (z) direction

U_{∞} = free-stream velocity.

It is important that turbulent fluctuation levels in a testing facility are as low as possible to ensure accurate measurements can be obtained. The degree of turbulence in the freestream affects the boundary layer characteristics of an object placed in the flow. A tunnel with high turbulence would cause the transition point to move forwards, giving a corresponding change in force and moment coefficients, most notably increasing the drag coefficient for streamlined bodies (Pankhurst & Holder, 1968). Acceptable values of turbulence levels for developmental testing are around 0.5% in the streamwise direction however there is no general agreement on a precise value (Barlow *et al.*, 1999).

3.3.3.1 Hot-Wire Measurements

A single hot-wire probe was used to determine the velocity fluctuations in the streamwise direction for the velocity at which the force and pressure measurements were carried out (25m/s). It was necessary to calibrate the hot-wire since the relationship between velocity and voltage is non-linear and thus applying standard deviation and mean calculations to the raw data is inaccurate.

Calibration involved measuring the voltage output from the hot-wire and determining the corresponding mean freestream velocity using a Baratron pressure transducer. A Baratron pressure transducer provides good accuracy for determining the mean flow velocity but its poor frequency response precludes its use for measurement of the velocity fluctuations. Data were collected for a series of 18 wind tunnel freestream

velocities spanning 0.2m/s - 29.3m/s. A sample rate of 1kHz was employed and a total of 60,000 samples for each flow velocity were collected. A polynomial curve fit was applied to the data and it was found that the best fit could be achieved using a 4th order polynomial. The calibration was performed 3 times and averaged to improve accuracy of the results as shown in Figure 3.13.

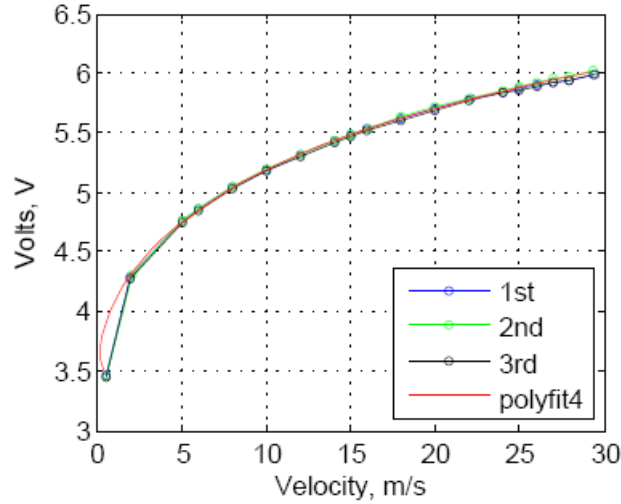


Figure 3.13 - Plot of output voltage against freestream velocity for hot-wire calibration.

Once the calibration had been established, a custom-written Matlab code was used to convert each voltage in the data set of interest to a velocity using the coefficients determined from the 4th order polynomial. The turbulence intensity, Tu , was calculated assuming isotropic turbulence, which is an acceptable assumption “at some distance behind the wind tunnel mesh screen” (Schlichting & Gersten, 2000). Also, it was assumed that a wire normal to the mean flow is sensitive only to the u' component as derived by Perry (1982). Therefore, the simplified equation below could be utilised:

$$Tu = \sqrt{u'^2} / U_{\infty} \quad (3.13)$$

The turbulence intensity for a freestream velocity of 25m/s was established for each test run and the final calculated value of $Tu = 0.66\%$ is an average of these results.

3.3.4 Experimental Method for Force Measurements

Force measurements were undertaken in the closed working section of the wind tunnel at the University of Adelaide described in Section 3.3.1. The free-stream velocity was measured using a Pitot-static tube located at the centre of the wind tunnel, which was removed for airfoil force measurements. The Pitot-static tube was

connected to a 10 Torr MKS Baratron pressure transducer with Signal Conditioner. The data were averaged over one minute and transferred to a computer using a National Instruments USB 6009 data acquisition system. The Reynolds number was $Re = 120,000$, based on the freestream velocity of $U_\infty = 25\text{m/s}$ and chord length of the airfoil. The free-stream velocity was set manually for each test set which included the range of airfoil attack angles under investigation. Fine adjustments were made to ensure that the flow velocity between test runs was as consistent as possible.

Lift, drag and moment measurements were obtained using the 6-component load cell discussed in the introduction to this section. This was fixed to a rotary table and rotated together with the airfoil. Care was taken to ensure the airfoil was mounted as accurately as possible with regard to the free-stream flow. The top of the mount was aligned with the floor of the test section and occupied a circular hole which was cut specifically for this application. A clearance of 1 - 2mm was maintained between the sides of the mount and the test section as a compromise between avoiding erroneous force readings due to surface contact and minimising flow losses. The base of the load cell, as shown in Figure 3.14, consisted of a heavy steel base plate to inhibit the effects of floor vibration and a stiff frame to minimize vibrational disturbances generated by the airflow. These vibrations could potentially cause inaccuracies in the measurements. The angle of attack of the airfoil was set using a Vertex brand 200mm diameter rotary table.

The working section which has cross-sectional dimensions of 500mm by 500mm and a length of 2400mm is shown in Figure 3.15 and was inserted into the wind tunnel. The attached flange was bolted to the face of the contraction exit with a foam sealing strip located at the interface.

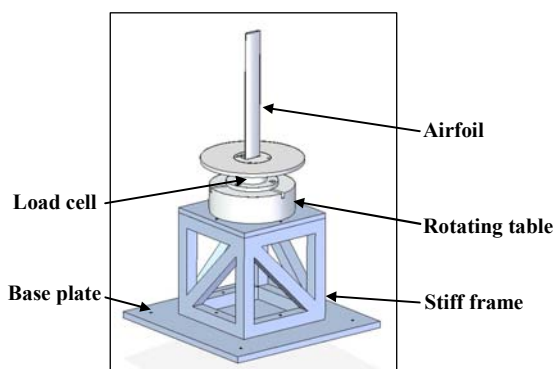


Figure 3.14 – Load cell arrangement

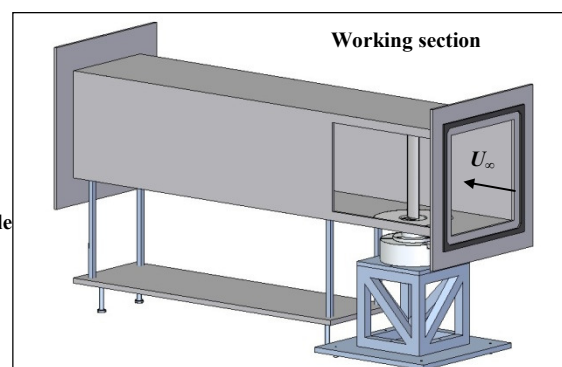


Figure 3.15 – Experimental set-up

Due to slight tolerance errors associated with fabrication of the test section, the actual height at the position of the airfoil was 498mm instead of 500mm. Thus, the resulting gap between the top of the airfoil and the test section ceiling was 3mm. This gap size was chosen to minimize three-dimensional effects whilst simultaneously allowing the airfoil to be conveniently mounted and rotated. The value is within the range of the suggested maximum gap of $0.005 \times \text{span}$ (Barlow *et al.*, 1999) required to avoid the effects of flow leakage around the tip. End-plates were considered unfeasible since they produce a pair of shed vortices unless they are attached to the wall. This effect destroys the concept of a two-dimensional wing (Barlow *et al.*, 1999).

3.3.5 Collection and Processing

The sampling period of the analogue-to-digital converter connected to the force transducer was 16ms and it was ensured that at least 1000 samples were collected for each angle of attack. Due to the unsteady nature of the flow at post-stall angles, the number of collected samples was increased to 3000 for these cases.

Three sets of measurements were taken for each airfoil for the range of angles $-4^\circ \leq \alpha \leq 25^\circ$. The average results for the lift and drag coefficients for the tested airfoils were then plotted and compared. The NACA 0021 and NACA 65-021 airfoils were plotted on separate axes due to their different characteristics but the relative influence of tubercles for the two airfoils was compared. The maximum solid blockage calculated as a ratio of the projected airfoil frontal area divided by the test section area was approximately 6% at $\alpha = 25^\circ$.

The chordwise force, F_C , and normal force, F_N , as shown in Figure 3.16, were converted into lift, L , and drag, D , forces for a given angle of attack, α , using equations (3.14) and (3.15):

$$L = F_N \cos\alpha - F_C \sin\alpha \quad (3.14)$$

$$D = F_N \sin\alpha + F_C \cos\alpha \quad (3.15)$$

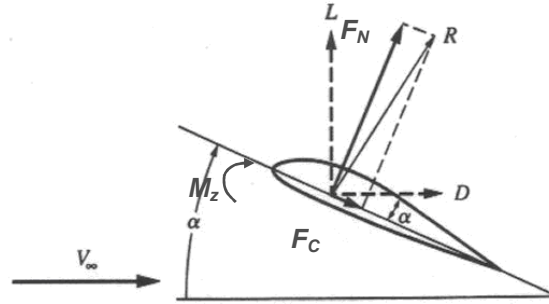


Figure 3.16 - Lift and Drag Forces.

Subsequently, the lift and drag forces were converted into dimensionless lift and drag coefficients, C_L and C_D respectively, using the following equations:

$$C_L = \frac{L}{1/2\rho U_\infty^2 S} \quad (3.16)$$

$$C_D = \frac{D}{1/2\rho U_\infty^2 S} \quad (3.17)$$

where,

ρ = density of air

U_∞ = freestream velocity

b = airfoil span

c = airfoil chord length

S = planform area, $b \times c$.

3.3.6 Angular Misalignment Correction

There is a small angular misalignment, ε between the axes of the load cell and the airfoil axes as shown in Figure 3.17. This is caused by accumulated inaccuracies associated with tolerance limitations. The actual magnitude of the error, ε can be determined by adjusting the value in a rotational transform matrix given by Equation (3.18). This is continued until the plot of drag coefficient against angle of attack is symmetrical about the y-axis (i.e. the drag coefficient for $\alpha = 5^\circ$ is the same as that for $\alpha = -5^\circ$), giving $\varepsilon = 1^\circ$. The lift coefficient is insensitive to the angular misalignment due to the fact that it is an order of magnitude larger than the drag coefficient. The transformation matrix used is as follows:

$$\begin{bmatrix} L \\ D \end{bmatrix} = \begin{bmatrix} \cos(\alpha + \varepsilon) & -\sin(\alpha + \varepsilon) \\ \sin(\alpha + \varepsilon) & \cos(\alpha + \varepsilon) \end{bmatrix} \begin{bmatrix} F_N \\ F_C \end{bmatrix} \quad (3.18)$$

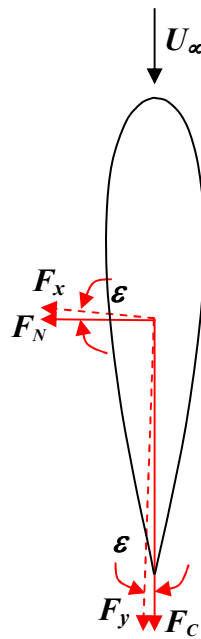


Figure 3.17 – Schematic of airfoil showing relative force transducer axes, F_x and F_y and misalignment, ϵ .

3.3.7 Conversion of Rig to Test Half-Span Models

Since a large number of airfoils had been manufactured for analysis in the two-dimensional case, it was neither cost effective nor efficient to machine equivalent half-span models. Additionally, it was undesirable to cut the airfoils at the mid-span location because they still needed to be used for other experiments. Hence, the only feasible option was to adjust the force transducer mount so that the airfoil was lowered by the necessary amount. This involved manufacturing a new force transducer support frame having a reduced height as shown in Figure 3.18 (b).

Another requirement was to create a plate with the airfoil profile shape cut out, which was positioned level with the floor of the test section. This ensured that the hole in the test section previously occupied by the mount was blocked. A clearance of 1-2 mm was allowed about the periphery of the plate as discussed in Section 3.3.4. The plate was screwed to steel rods which compensated for the height lost in lowering the mount. These rods were then connected securely to the load cell mount as shown in Figure 3.18 (c).

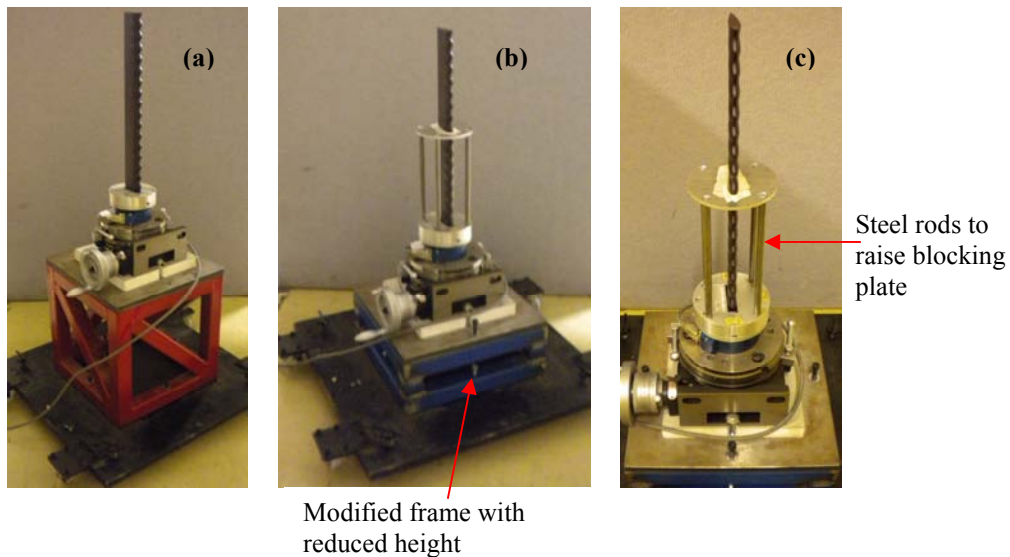


Figure 3.18 – Modified mount for analysis of three-dimensional effects, (a) original frame (b) modified lowered frame, (c) structure used to gain height and block hole in test section.

3.3.8 Boundary Layer Trip Design

In some experiments reported in this thesis boundary layer trips were added to the suction and pressure surfaces of each airfoil to promote transition to a turbulent boundary layer. The height and position of the airfoil boundary layer trips was optimized to give the lowest possible drag and maximum lift, while maintaining a linear relationship between C_L and α in the pre-stall regime. The roughness height, k , was estimated according to the guidelines proposed by Braslow, Hicks and Harris (1966). Here, the Reynolds number is defined based on the roughness height and has a value of $Re_k = 600$.

$$Re_k = \frac{u_k k}{\nu_k} \quad (3.19)$$

where,

u_k = velocity of flow at top of roughness element

k = roughness height

ν_k = kinematic viscosity of air.

Initial experiments found that the optimum trip position for a given roughness height was at 7% chord from the leading edge. It was assumed that the boundary layer up to this point was laminar, allowing estimation of the boundary layer height, δ , through the Blasius equation:

$$\delta = 5 \sqrt{\frac{\nu_x x}{U_\infty}} \quad (3.20)$$

where,

ν_x = kinematic viscosity of air

x = boundary layer development length = 5mm

U_∞ = freestream velocity = 25m/s.

The boundary layer thickness was hence determined as $\delta \sim 2.7 \times 10^{-4}$ m. Assuming that the profile is approximately linear, the following equation can be applied:

$$\frac{k}{\delta} = \frac{u_k}{U_\infty} \quad (3.21)$$

Combining equations (3.19) and (3.21) gives an equation which can be used to calculate the roughness height, k .

$$k = \sqrt{\frac{\delta \nu_k \text{Re}_k}{U_\infty}} \quad (3.22)$$

A roughness height of $k = 0.3$ mm was calculated and subsequently refined through trial and error. The empirical prediction proved to be an excellent first order estimate since the most successful roughness height was $k = 0.4$ mm.

3.3.9 Corrections of Wind Tunnel Effects for a Full-Span Model

Flow in a wind tunnel differs from that in an unbounded domain and hence it is necessary to apply corrections to the measured data. The necessary corrections were estimated using the guidelines proposed by Barlow, Rae and Pope (1999). Other guidelines are available from Pankhurst & Holder (1968) and from data sheets provided by the Engineering Sciences Data Unit (2011), which are available online. However, it was believed to be more consistent to select one set of guidelines only and those provided by Barlow *et al.* (1999) were deemed to be reliable since they are based on a significant number of research studies on the topic and are frequently referenced.

For the two-dimensional case, the relevant corrections included consideration of solid blockage, wake blockage and streamline curvature. A buoyancy correction was deemed unnecessary since it is considered to be insignificant in most cases for wings (Barlow *et al.*, 1999). A downwash correction was also unwarranted since the wing tip vortices from the small 3mm gap would escape into the test section boundary layer and hence would be weak enough to ignore (Barlow *et al.*, 1999).

3.3.9.1 Tunnel Solid Blockage

A model in a wind tunnel provides an obstruction to the flow, reducing the effective cross-sectional area through which flow can travel. As a result, the wind tunnel velocity increases according to the law of continuity and this must be taken into account. The solid blockage for a two-dimensional body can be found from a doublet summation and the associated velocity increment is defined by Glauert (1933) as:

$$\varepsilon_{sb} = \left(\frac{\Delta V}{V_u} \right)_{total} = \frac{\pi^2}{3} \frac{\lambda_2}{4} \frac{t^2}{h^2} = 0.822 \lambda_2 \frac{t^2}{h^2} \quad (3.23)$$

where,

ΔV = axial velocity due to doublet

V_u = uncorrected velocity

λ_2 = shape factor = 1.5 (found from Figure 9.16 in Barlow *et al.*, 1999)

t = airfoil thickness

h = height of wind tunnel test section.

3.3.9.2 Wake Blockage

At the rear of a body placed in a flow, a wake forms which has a lower mean pressure and velocity than the freestream. To preserve continuity, the flow speed outside of the wake in a closed wind tunnel must be higher than the freestream. According to Bernoulli's principle, this is accompanied by a lowered pressure which becomes more significant as the boundary layer on the body thickens and eventually becomes the wake. This pressure gradient effect results in an increased velocity at the surface of the test object. To determine the required correction, a mathematical model can be constructed where the wake is represented as a line source at the wing trailing edge. To preserve continuity, a sink of equal strength must be placed far downstream. With the wind tunnel ceiling and floor characterised as a pair of streamlines, the image-system (method of images) concept requires that there exists an infinite vertical row of source-sink pairs. A horizontal velocity is induced at the model exclusively by the image sinks. Following this mathematical analysis, Maskell (1965) proposed that the velocity correction for a two-dimensional model should be:

$$\varepsilon_{wb} = \frac{\Delta V}{V_u} = \frac{c/h}{2} C_{Du} \quad (3.24)$$

where,

ΔV = induced horizontal velocity at the model

V_u = uncorrected velocity

c = airfoil chord

h = height of wind tunnel test section

C_{Du} = uncorrected drag coefficient.

3.3.9.3 Streamline Curvature

The curvature of the streamlines around a lifting body is affected by the presence of the wind tunnel side walls for a vertically-mounted airfoil. This results in an apparent increase in camber of the model. Therefore, an airfoil in a closed wind tunnel will experience a higher amount of lift and pitching moment than it would in free air. This effect is predicted through approximating the airfoil as a single vortex at its quarter-chord location. Once again, the image-system concept is employed and the vortices of alternating signs extend to infinity above and below the airfoil. The horizontal components of the image pairs cancel, however, the vertical components augment. Hence, there is a degree of boundary-induced upwash and this can be taken into account as an angle-of-attack correction. Using the theoretical relationship between lift and angle of attack, $C_L = 2\pi\alpha$, the additive lift and moment corrections respectively are given by:

$$\Delta C_{L,sc} = \sigma C_L \quad (3.25)$$

where,

$$\sigma = \frac{\pi^2}{48} \left(\frac{c}{h} \right)^2 \quad (3.26)$$

and c and h are as defined above.

A more complex analysis was carried out by Allen and Vincenti (1944), where vorticity was distributed along the airfoil chord rather than being concentrated at the quarter-chord location. According to Barlow *et al.* (1999), equation (3.25) is still valid but the angle of attack correction is slightly different. This correction was used in the current study and is given by the following equation:

$$\Delta\alpha_{sc} = \frac{57.3\sigma}{2\pi} (C_{Lu} + 4C_{M_{1/4u}}) \quad (3.27)$$

where,

C_{Lu} = uncorrected lift coefficient

$C_{M_{1/4u}}$ = uncorrected pitching moment coefficient.

Since the airfoil chord in the current study is less than 0.7 tunnel height, wall effects on the distribution of lift are deemed to be negligible (Barlow *et al.*, 1999).

3.3.9.4 Summary

A summary of the necessary corrections is provided below. The subscript “u” refers to the uncorrected parameters.

The corrected velocity is given by:

$$V = V_u(1 + \varepsilon) \quad (3.28)$$

where,

$$\varepsilon = \varepsilon_{sb} + \varepsilon_{wb} \quad (3.29)$$

Corrected terms for α , C_L and C_D are:

$$\alpha = \alpha_u + \frac{57.3\sigma}{2\pi} (C_{Lu} + 4C_{M_{1/4}u}) \quad (3.30)$$

$$C_L = C_{Lu}(1 - \sigma - 2\varepsilon) \quad (3.31)$$

$$C_D = C_{Du}(1 - 3\varepsilon_{sb} - 2\varepsilon_{wb}) \quad (3.32)$$

where,

α = angle of attack

C_L = lift coefficient

C_D = drag coefficient

$C_{M_{1/4}}$ = pitching moment coefficient at the quarter-chord position.

For the unmodified full-span NACA 0021 airfoil at the highest angle of attack in the pre-stall regime ($\alpha = 12^\circ$), the corrections yield an overall increase in α of 0.4%, a decrease in C_L of 1.6% and a decrease in C_D of 1.3%.

3.3.10 Corrections of Wind Tunnel Effects for a Finite-Span Model

The basic principles behind corrections of wind tunnel effects of three-dimensional flows are the same as for two-dimensional flows. However, analysis in three dimensions is far more complicated and requires consideration of additional factors that will be discussed

in the following sub-sections. In addition, an extra correction which accounts for the effects of downwash must be included for the three-dimensional case.

The airfoil considered in the three-dimensional analysis consisted of one free end and one fixed end, where the model spans half of the test section. Hence, in order to ensure that the procedure outlined in Barlow *et al.* (1999) was valid, the method of images was applied to the model. This involved mirroring the model about the wind tunnel floor to give an equivalent model which was entirely three-dimensional and could be used in the analysis. The resulting three-dimensional model with new test section dimensions of 0.5m x 1m is shown in Figure 3.19.

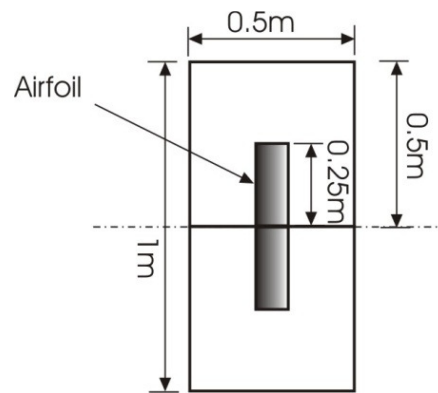


Figure 3.19 – Schematic showing method of images used to simulate three-dimensional model.

3.3.10.1 Tunnel Solid Blockage

Solid blockage is again estimated using a vertical distribution of alternating sources and sinks. The equation in three-dimensions is derived by considering the effects of these images on the model, leading to the following equation:

$$\varepsilon_{sb} = \frac{\Delta V}{V_u} = \frac{K_1 \tau_1 (\text{wing volume})}{C^{3/2}} \quad (3.33)$$

where,

K_1 and τ_1 are from Figures 10.2 and 10.3 respectively in Barlow *et al.* (1999)

C = cross-sectional area of wind tunnel.

3.3.10.2 Wake Blockage

Some important conclusions were drawn by Maskell (1965), which led to the development of a general analysis for wake blockage. Firstly, the wake does not vary significantly across the model span. In addition, a single correction can be used for models with different aspect ratios due to the tendency towards axial symmetry of the

wake. Also, a streamwise pressure gradient is induced on the model by the wake, which increases the drag experienced by the model.

The concepts upon which the correction for wake blockage is based are similar to the two-dimensional case where the wake is represented by a source and a sink is added downstream to preserve continuity. However, in the three-dimensional case, a doubly infinite array of sources and sinks must be considered, which extend vertically and horizontally, respectively. Once again, it is only necessary to consider the horizontal velocity induced by the sink system, which gives the incremental velocity due to wake blockage as:

$$\varepsilon_{wb} = \frac{\Delta V}{V_u} = \frac{S}{4C} C_{Du} \quad (3.34)$$

However, as described by Maskell (1965), it is necessary to consider the momentum effects outside of the wake when flow separation occurs. The presence of the wind tunnel walls creates a lateral constraint on the wake, resulting in a reduced wake pressure and therefore lower model base pressures than would occur in an unbounded domain. Therefore, an additional term is added to equation (3.34) to account for the increase in velocity outside of the wake, responsible for the reduced wake pressure:

$$\varepsilon_{wb} = \frac{S}{4C} C_{Do} + \frac{5S}{4C} (C_{Du} - C_{Di} - C_{Do}) \quad (3.35)$$

The minimum drag possible, C_{Do} , is found by plotting a graph of C_{Lu}^2 against C_{Du} and finding the minimum which corresponds to C_{Do} . The slope of the linear section of the curve is used to determine the induced drag, C_{Di} . Figure 3.20 shows an illustration of the relative contribution of each component of drag, where the drag due to separation is C_{Ds} .

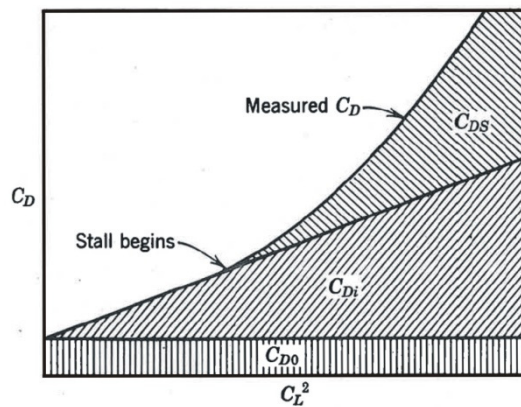


Figure 3.20 – Relative contribution of various sources of drag (Barlow et al., 1999).

3.3.10.3 Streamline Curvature

The idea behind corrections for streamline curvature is the same as for two-dimensional flow in that upwash is induced along the chord due to the presence of the wind tunnel walls. However, for the three-dimensional case the system of images is far more complicated and requires consideration of the bound vortex and trailing vortices associated with the wing as well as the infinite series of images related to the existence of the wind tunnel boundaries as shown in Figure 3.21.

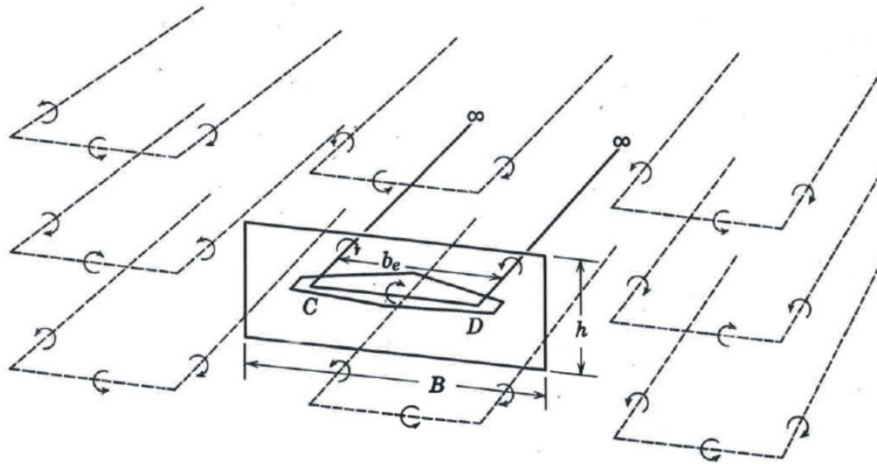


Figure 3.21 – Image system for a three-dimensional model in a closed rectangular test section (Barlow *et al.*, 1999). Note that the model in the current study is mounted vertically.

The amount of correction required is found by determining the value of τ_2 , which represents the increase in boundary-induced upwash (Barlow *et al.*, 1999). This parameter can be found from Figure 10.40 in Barlow *et al.*, (1999), which requires values of k (tunnel span/width = 0.5), λ (tunnel height/tunnel width = 1) and “tail length,” l_t , to be determined. Many aerodynamicists prefer to apply the streamline curvature correction to the angle of attack without adjusting the lift coefficient (Barlow *et al.*, 1999). In this case, the value for “tail length” is $l_t = 1/2c$.

For the current study the value of $\tau_2 = 0.1$ and the angle of attack correction for streamwise curvature, $\Delta\alpha_{sc}$, can be determined using equation

(3.36).

$$\Delta\alpha_{sc} = \tau_2 \delta \left(\frac{S}{C} \right) C_{Lu} \quad (3.36)$$

where,

δ = boundary correction factor from Figure 10.17 in Barlow *et al.*, (1999)

$$= 0.148$$

S = wing planform area, $b \times c$

C = test section area.

3.3.10.4 Downwash Correction

Trailing vortices are generated at the free end of both the model and its image. The method of images can be employed where the wind tunnel wall is represented as a streamline with stream function, $\psi = 0$. The sum of the stream functions of the wing tip vortices and their images is set equal to zero in order to find the associated spacing of the image vortices from the wind tunnel centre, which is shown in Figure 3.22.

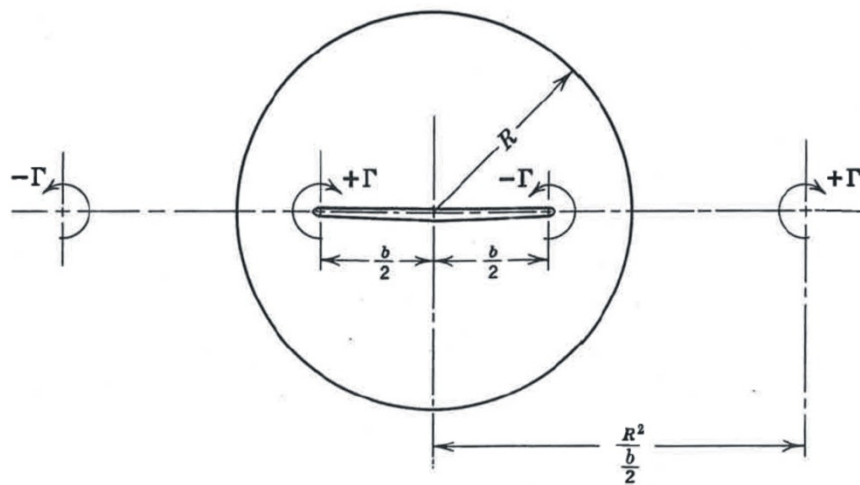


Figure 3.22 – Image vortex locations for a closed round jet (Barlow *et al.*, 1999).

Hence, the existence of the wind tunnel walls creates an apparent crossflow which reduces that caused by the wing tip vortices. This leads to results which indicate a smaller induced angle and induced drag than expected. The procedure for determining the required correction involves calculating the upwash for two vortices at a distance of $R^2/(b/2)$ as shown in Figure 3.22. This becomes:

$$w = \frac{\Gamma b}{8\pi R^2} \quad (3.37)$$

where,

b = airfoil span

R = half-width of wind tunnel.

$$\Gamma = \text{circulation}, \Gamma = \frac{SVC_L}{2b} \quad (3.38)$$

Thus, the induced angle, $\Delta\alpha_i$ is given by the following equation:

$$\Delta\alpha_i = \frac{w}{V} = \frac{S/C}{8} C_L \quad (3.39)$$

The induced drag augmentation due to the wind tunnel boundaries is:

$$\Delta C_{Di} = \Delta\alpha_i C_L = \frac{S/C}{8} C_L^2 \quad (3.40)$$

However, it is necessary to take into account the geometry of the test section in the analysis. Hence, the equations for the corrected angle of attack, α , and the corrected drag coefficient, C_D , incorporate the boundary correction factor, δ , defined in Section 3.3.10.3 as follows:

$$\alpha = \alpha_u + \delta \frac{S}{C} C_{Lu} \quad (57.3) \quad (3.41)$$

$$C_D = C_{Du} + \delta \frac{S}{C} C_{Lu}^2 \quad (3.42)$$

The factor of 57.3 is incorporated into equation (3.41) to convert from radians to degrees.

3.3.10.5 Summary

The summary of corrections for the three-dimensional case is similar to the two-dimensional case with some additional terms accounting for downwash. Also, the streamline curvature terms are significantly different. Hence, the overall equations are as follows:

$$\alpha = \alpha_u + (\tau_2 + 1) \delta \left(\frac{S}{C} \right) C_{Lu} \quad (57.3) \quad (3.43)$$

$$C_L = C_{Lu} (1 - 2\varepsilon) \quad (3.44)$$

$$C_D = C_{Du} (1 - 3\varepsilon_{sb} - 2\varepsilon_{wb}) + \delta \frac{S}{C} C_{Lu}^2 \quad (3.45)$$

For the unmodified half-span NACA 0021 airfoil at the highest angle of attack in the pre-stall regime ($\alpha = 14^\circ$), the corrections yield an overall increase in α of 4.5%, decrease in C_L of 0.5% and an increase in C_D of 7.9%.

3.3.11 Force Measurement Uncertainty Analysis

A conservative estimation of the uncertainty was carried out using the methods outlined by Bentley (2005). There are two main classifications of experimental uncertainties. These are

statistical uncertainties, determined from actual data, and measurement uncertainties, estimated for a specific experimental method. For the force measurements, the main sources of uncertainty were statistical uncertainties in freestream velocity measurement and force transducer data and measurement inaccuracies in freestream velocity measurement; force transducer output and angular alignment of the rotary table. Further analysis pertaining to the determination of the force transducer accuracy is discussed in further detail in Appendix A. It was found that the uncertainty for the x-direction was around 1% and in the y-direction around 2%.

For all sources of uncertainty, it was necessary to determine the standard deviation, σ . This could be done mathematically for the case of the wind tunnel and force transducer statistical uncertainties by applying the standard deviation formula to the measurement sets. As discussed in 3.3.5, a series of three data sets were collected for each angle of attack and the data was temporally averaged to determine an accurate value for the lift and drag coefficient. The same process was carried out to determine the wind tunnel velocity. Hence, the appropriate values to be used in the uncertainty analysis were the temporally averaged results, as experimental repeatability and hence accuracy was related exclusively to the variation in the average. The standard deviation was calculated according to Equation (3.46):

$$\sigma = \sqrt{\frac{\sum_{m=1}^n (x_m - \bar{x})^2}{n-1}} \quad (3.46)$$

where,

x_m = single measurement

\bar{x} = mean of data set

n = total number of measurements.

The standard deviation of the mean is equivalent to the uncertainty, U_i . The subscript, i , refers to the uncertainty of interest.

$$U_i = \frac{\sigma}{\sqrt{n}} \quad (3.47)$$

In the case of components not derived from actual data, the uncertainty was determined by estimating whether the distribution of readings was closer to a normal distribution or a rectangular distribution. It was assumed that all remaining sources of uncertainty followed a normal distribution since there was greater probability that the measurement would be closer

to the centre of the range. A rectangular distribution would assume that the measurement could lie anywhere in the range of uncertainty with equal probability. Subsequently, it was decided that uncertainty estimates could be assumed as worst case values, meaning that they existed at least two standard deviations from the mean. Hence, it was necessary that they should be reduced by a factor of $k_i = 2$.

The standard uncertainty is defined as:

$$u(x_i) = \frac{U_i}{k_i} \quad (3.48)$$

The next step in the analysis was to determine the sensitivity coefficient, c_i where:

$$c_i = \frac{\text{change in measurand}}{\text{change in input}} \quad (3.49)$$

The sensitivity coefficient takes into account the relative impact of each uncertainty on the measurement of interest since some uncertainties may appear small but still have significant effect on the results.

The sensitivity coefficient associated with the influence of wind tunnel velocity on force measurements was determined from data calculated using the XFOil code, which was developed by Drela and Youngren (2001). Lift and drag polars were obtained for a range of velocities from 23.5 - 26.5m/s, which encompassed the predicted uncertainties. Subsequently, a series of plots could be constructed of lift and drag coefficient against freestream velocity. The absolute value of the slope of each plot for each angle of attack was determined using Matlab. As a worst case estimate, the maximum uncertainty calculated for all angles of attack in the pre-stall regime was used as a sensitivity coefficient for these angles. The same process was used to determine the sensitivity coefficient for post-stall angles of attack. Since the values of this coefficient were relatively low, it was concluded that it would be feasible to use the pre-stall sensitivity coefficients as an approximation for all airfoils.

The sensitivity coefficient for the rotary table uncertainty was determined directly from the lift and drag coefficient versus angle of attack plots. For each airfoil, the plots were divided into a series of approximately linear sections and the slope for each was calculated using Matlab. The value of the slope was used as the sensitivity coefficient for the angles of attack contained within the given linear section. Each airfoil had a different

sensitivity coefficient for a given angle of attack relative to the other airfoils since the slope each lift and drag coefficient versus angle of attack plot varied.

With regards to the stall angle, it was ensured for each test run that this did not change and if uncertainties associated with the wind tunnel velocity and/or rotary table were significant enough to affect this, the entire measurement set was repeated. Hence, the sensitivity coefficient at the stall angle was deduced to be relatively similar to pre-stall sensitivity coefficients at other angles of attack. All uncertainties associated with the load cell had a sensitivity coefficient of 1.

The combined standard uncertainty, u_c , is then defined to incorporate the sensitivity coefficient, while simultaneously integrating all uncertainties into a single expression:

$$u_c = \sqrt{\sum_{i=1}^n |c_i u(x_i)|^2} \quad (3.50)$$

The confidence in each estimate of U_i is taken into account by determining the degrees of freedom, ν_i . For a statistical evaluation, the measurement certainty increases as more samples are collected and $\nu_i = n - 1$. For standard deviation estimates not derived from actual data, the degrees of freedom must be approximated according to Table 3.5:

Table 3.5 – Determining degrees of freedom for a given uncertainty approximation.

Accuracy of estimate	ν_i
Rough	3
Reasonable	10
Good	30
Excellent	100

Subsequently, the Welch-Satterthwaite formula is used to find the effective degrees of freedom, ν_{eff} for the entire uncertainty set:

$$\nu_{eff} = \frac{u_c^4}{\sum_{i=1}^n \frac{|c_i u(x_i)|^4}{\nu_i}} \quad (3.51)$$

The coverage factor, k , can then be calculated using the equation from Betts (1995):

$$k = 1.96 + \frac{2.5}{v_{eff}} + \frac{2.3}{v_{eff}^2} + \frac{2.2}{v_{eff}^3} + \frac{3.7}{v_{eff}^4} \quad (3.52)$$

Finally, the expanded uncertainty, U , is defined as:

$$U = k u_c \quad (3.53)$$

The value of U represents the total uncertainty associated with a particular measurement.

The statistical uncertainties associated with the wind tunnel and force transducer were dependent on the airfoil, quantity of interest, (i.e. lift or drag coefficient) and the angle of attack and are thus discussed in more detail in Section 4.4. Table 3.6 below summarises the values of parameters determined for the estimated uncertainties. Note that values for c_i are not included here as they are dependent on the angle of attack and quantity of interest.

Table 3.6 – Values of relevant parameters for measurement uncertainty analysis

Uncertainty	U_i	k_i	v_i
Freestream velocity accuracy	± 0.96 m/s	2	30
Force transducer accuracy	$\pm 1\%$	2	10
Rotary table accuracy	$\pm 0.2^\circ$	2	30

The uncertainty in the freestream velocity was estimated through consideration of the combined uncertainty associated with the Baratron pressure transducer and the data logger, which are quoted as 0.08% and 0.07% of full scale, respectively by the manufacturers. This is then multiplied by the measured pressure and converted to an uncertainty in velocity which is displayed in Table 3.5.

3.4 Surface Pressure Measurements

Surface pressure measurements can be interpreted to identify transition points, separation points, separation bubbles and pressure distributions. Various techniques, both qualitative and quantitative in nature, were considered including oil flow visualisation, liquid crystals, pressure sensitive paint, china clay technique and hydrated magnesium silicate (talcum powder) combined with methylated spirits or light oils. After careful consideration of the major advantages and disadvantages of each method, it was decided that the most feasible technique for determining the flow features in this study was static

pressure taps. Further details pertaining to the factors that were taken into account to come to this conclusion are discussed in Appendix C.

Surface pressures were converted into nondimensionalised form by dividing by the dynamic pressure, giving the pressure coefficient, C_p .

$$C_p = \frac{p - p_\infty}{q} \quad (3.54)$$

where,

p = pressure at airfoil surface

p_∞ = freestream static pressure

q = dynamic pressure, $q = 1/2\rho U_\infty^2$ (3.55)

(measured directly by Pitot-static tube)

3.4.1 Pressure Taps

Static pressure ports were incorporated into three of the airfoils under investigation to observe the surface pressures. These included both of the unmodified profiles (NACA 0021 and NACA 65-021) and one model with tubercles (A8W30 configuration – see Section 3.2). The small thickness of the airfoils increased the complexity of incorporating pressure taps into the existing models. Hence, it was decided that it would be more feasible to manufacture airfoils using a casting technique whereby the pressure taps could be moulded into the design during fabrication.

The casting technique required the fabrication of female moulds on a CNC milling machine. Holes were drilled into the top mould at the mid-span location to incorporate 1.5mm O.D. copper tubing. This tubing has an inner diameter of 1mm which is a compromise between minimising the likelihood of blockage and minimising the uncertainties for the pressure taps. The copper tubing was bent at 90° to form an L-shape and then attached to vinyl tubing which extended outside of the base of the mould. The vinyl tubing was not bent as this would risk the possibility of kink formation and hence limit the ability to take pressure readings. Polyester resin was poured into both top and bottom moulds and spanwise strips of carbon fibre were distributed throughout the resin for strengthening and stiffening. The moulds were then held tightly together with clamps until the resin had set. Care was taken to ensure that the holes did not become blocked during this process and that the copper tubes were perpendicular to the surface. When the

polyester resin had set, the tubes were filed until they were flush with the airfoil surface and all burrs had been removed.

3.4.2 Scanivalve

Pressures at the airfoil surface were received by a Scanivalve mechanical pressure multiplexer, model number: 48D3-1404A. This was connected to a controller as shown in Figure 3.23. The Scanivalve used in this study consists of 48 input pressure ports and a central output port which can be connected to a Baratron pressure transducer. A stepper motor is used to rotate a grooved disc which enables individual selection of the pressure ports.

The Scanivalve controller drives the stepper motor and was built in-house by the Electronics Department at the School of Mechanical Engineering. This controller can be set to “manual” mode or “auto” mode, depending on the application. Manual mode allows the valve to be stepped one position at a time using the front panel button. An additional front panel button returns the stepper motor to the “home” position (port 0) regardless of its current position. Auto mode is to allow an external input to step the valve. For this setting, the input is a 5V pulse from a data logger. The pulse should have 50% duty cycle and should not exceed 2Hz. Each pulse causes the Scanivalve to advance one position. For the “auto” setting, the “home” position is identified when the output from the controller is 5V. For all other positions, this output is 0V.

The freestream static pressure was measured using a Pitot-static tube. The Scanivalve and Pitot-static tube were connected to a Baratron pressure transducer and the voltage output from the pressure transducer was transmitted to the computer via a National Instruments USB 6009 data logger. A Labview program was written to interface with the data logger. As shown in Figure 3.24, when the output from the controller was 5V, a measurement cycle would be initiated.

This consisted of a digital input received by the controller which prompted the stepper motor to advance one position. Subsequently, a time delay was included to allow the pressure to stabilise at a given location before the commencement of data acquisition. Measurement duration was 30s, which was followed by another time delay to ensure that

there was no chance of uncertainties caused by advancement of the Scanivalve to the next position.

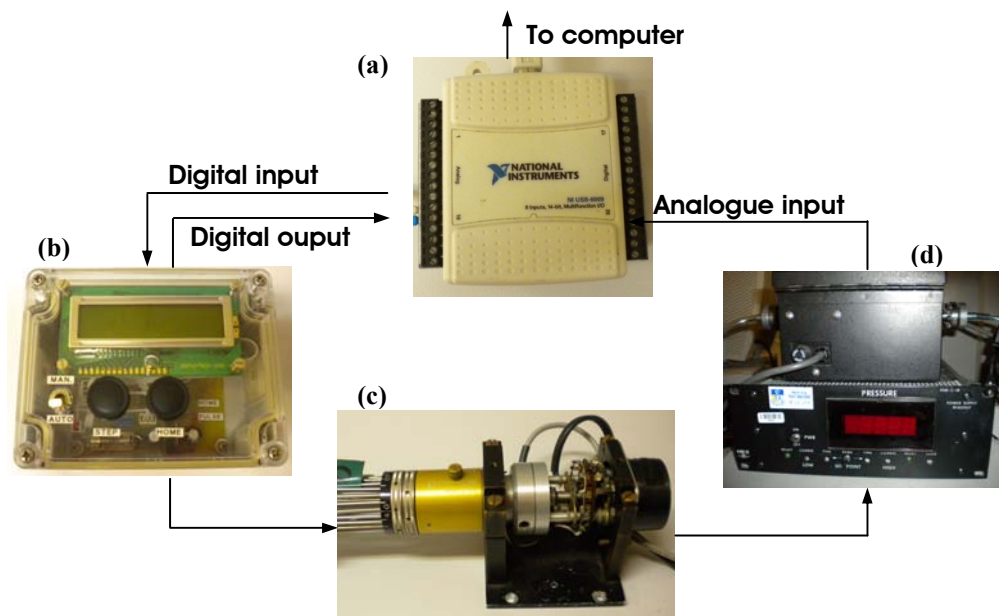


Figure 3.23 - Block diagram of Scanivalve pressure multiplexer and associated hardware, (a) data logger, (b) Scanivalve controller, (c) Scanivalve and (d) Baratron pressure transducer

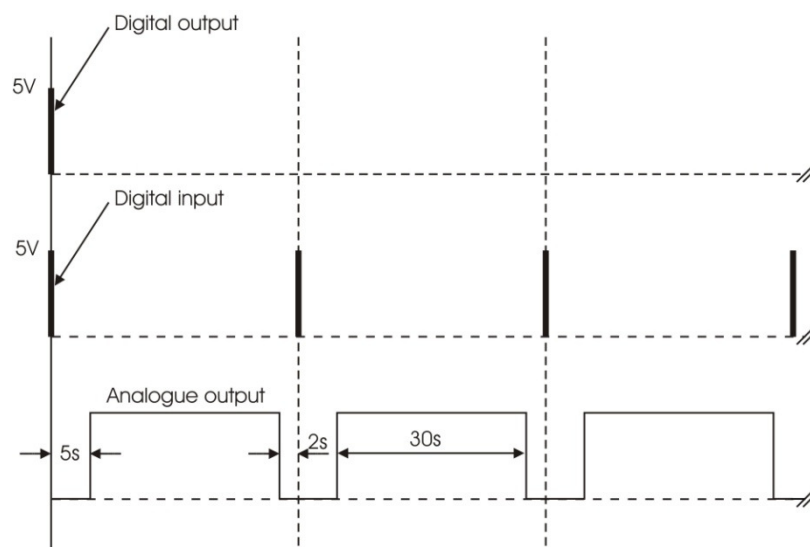


Figure 3.24 – Timing diagram in reference frame of controller.

3.4.3 Pressure Tap Locations

The chordwise pressure tap locations for the unmodified airfoils are shown in Table 3.7 and illustrated in Figure 3.25. These chordwise locations were the same for the modified airfoils but in this case, rows of pressure taps were incorporated at three spanwise positions; trough, peak and midway between a trough and a peak as shown in Figure 3.26. An additional pressure tap was included on the tubercle peak at $x/c = 0.06$ in front of

pressure tap 0. Pressure tap 1 did not exist at the tubercle trough. Thus there were 13 pressure tap locations for each of the unmodified airfoils and 36 locations for the modified airfoil. Unfortunately three pressure taps became blocked during the fabrication process for the modified airfoil and were deemed unusable. Table 3.8 summarises the pressure tap positions for the modified airfoil and indicates the unusable positions with “x”.

Table 3.7 – Pressure tap positions for unmodified airfoil.

Pressure tap	Position (x/c)
0	0
1	0.05
2	0.1
3	0.15
4	0.2
5	0.25
6	0.3
7	0.4
8	0.5
9	0.6
10	0.7
11	0.8
12	0.9

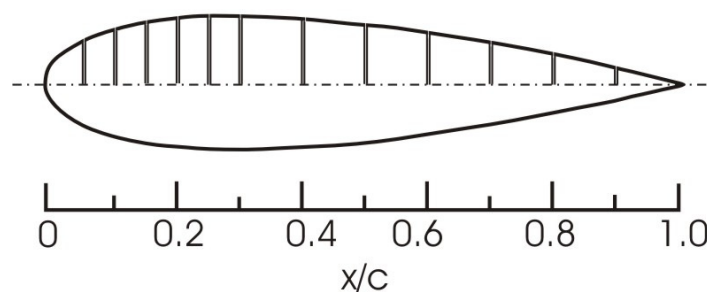


Figure 3.25 – Pressure tap locations for unmodified airfoils.

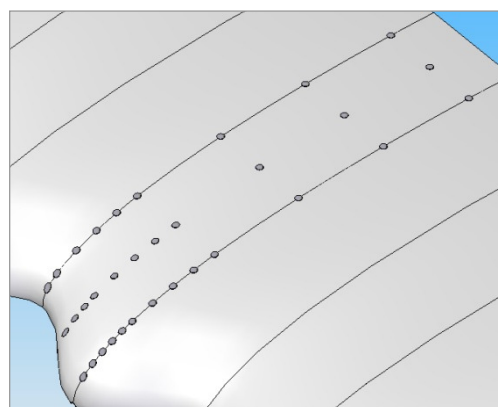


Figure 3.26 – Modified airfoil showing three rows of pressure taps.

Table 3.8 – Pressure tap positions for modified airfoil.

Pressure tap	Position (x/c)	Pressure tap	Position (x/c)	Pressure tap	Position (x/c)
T0	x	M0	0	P0	-0.06
T1	0.1	M1	x	P1	0
T2	0.15	M2	0.1	P2	0.05
T3	0.2	M3	0.15	P3	0.1
T4	x	M4	0.2	P4	0.15
T5	0.3	M5	0.25	P5	0.2
T6	0.4	M6	0.3	P6	0.25
T7	0.5	M7	0.4	P7	0.3
T8	0.6	M8	0.5	P8	0.4
T9	0.7	M9	0.6	P9	0.5
T10	0.8	M10	0.7	P10	0.6
T11	0.9	M11	0.8	P11	0.7
		M12	0.9	P12	0.8
				P13	0.9

3.4.4 Determining Lift and Form Drag From Pressure Distributions

The lift and drag coefficients can be calculated from the pressure distribution by determining the line integral around the closed curve outline, C , of the airfoil. The aerodynamic force coefficients are defined as follows:

$$C_N \approx \oint_C C_p d \frac{x}{c} \quad (3.56)$$

$$C_{Cf} \approx \oint_C C_p d \frac{y}{c} \quad (3.57)$$

where,

C_N = normal coefficient

C_{Cf} = chordwise component of form drag coefficient

$dx = ds \sin \theta$

$dy = - ds \cos \theta$

c = airfoil chord.

A discrete element on the airfoil surface with a length of ds experiences surface pressure, p , and wall shear stress, τ_w , as shown in Figure 3.27.

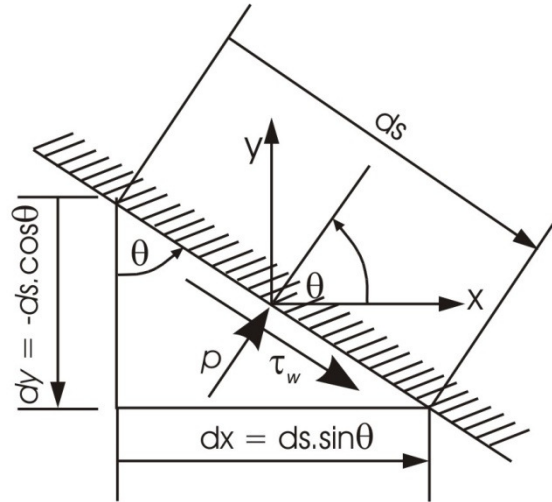


Figure 3.27 – Coordinate system and stress definitions.

Values of the normal coefficient, C_N , and chordwise component of the form drag coefficient, C_{Cf} , were found through numerical integration using the trapezoidal rule. These forces were then transformed by an angle equal to the angle of attack, α , to give the lift coefficient, C_L , and the form drag coefficient, C_{Df} .

$$C_L \approx C_N \cos \alpha - C_{Cf} \sin \alpha \quad (3.58)$$

$$C_{Df} \approx C_N \sin \alpha + C_{Cf} \cos \alpha \quad (3.59)$$

3.4.5 Pressure Tap Uncertainty Analysis

The uncertainty analysis involved the same process discussed in Section 3.3.11. Since the wind tunnel set up is the same and the only major change is the fact that pressure is measured instead of force, there are many common sources of uncertainty. The only difference is that uncertainties associated with the load cell are replaced with uncertainties related to pressure measurement. These uncertainties include: statistical uncertainties in pressure data and measurement uncertainties in pressure output. The former is calculated by finding the standard deviation of the mean for three data sets to determine the uncertainty in the mean value. The latter is determined by considering the combined errors associated with the Baratron pressure transducer and the data logger as discussed in 3.3.11.

The statistical uncertainties related to wind tunnel fluctuations and pressure measurement fluctuations differed depending on the measurement set being analysed and thus are discussed in more detail in Section 5.5. For uncertainty components not derived from the actual data sets, the uncertainty analysis parameter values are summarised in Table 3.9. Similarities in the value of uncertainty, U_i , can be noted between the force and pressure measurements. However, the sensitivity coefficient, c_i , is quite different as it relates to the variation of pressure readings in response to a small change in one of the system components such as velocity. Note that values for c_i are not included here as they are dependent on the angle of attack.

Table 3.9 - Values of relevant parameters for uncertainty analysis.

Uncertainty	U_i	k_i	v_i
Freestream velocity accuracy	± 0.05 m/s	2	30
Pressure measurement accuracy	0.08%	2	100
Rotary table accuracy	$\pm 0.2^\circ$	2	30

3.5 Hydrogen Bubble Visualisation

Hydrogen bubble visualisation is a relatively simple and cost-effective technique which can be used to highlight the flow patterns for a wide variety of fluid mechanics phenomena (Smits & Lim, 2000). For the current study it was considered to be an effective method for highlighting the streamwise vortices, identifying approximate flow separation locations and predicting local pressure and velocity variations.

3.5.1 Water Channel

Hydrogen bubble visualisation experiments were carried out using a free surface closed-return water channel at the School of Mechanical Engineering at the University of Adelaide. Figure 3.28 shows a schematic diagram of the water channel, which has a working section 2m in length and cross-section 500mm \times 500mm. The base and sides of the working section are manufactured from clear acrylic, allowing the flow to be viewed from all directions. The water channel flow is driven by a frequency-controlled centrifugal pump that gives steady operating conditions for velocities up to 450 mm/s.

Fluid from the pump enters the upstream settling section via a perforated cylindrical section which provides a uniform distribution of the flow to the supply section. The flow then passes through a series of flow conditioning sections before entering the working section. These include two perforated metal plates, a honeycomb flow straightener, three 58% open area nylon mesh screens and a 4:1 three-dimensional contraction. These flow conditioning sections are used to minimise the turbulence intensity and maximise uniformity of the free stream flow in the channel. The measured turbulence intensity at a free-stream flow rate of 70 - 84mm/s is approximately 2% (ER Hassan 2011, personal communication).

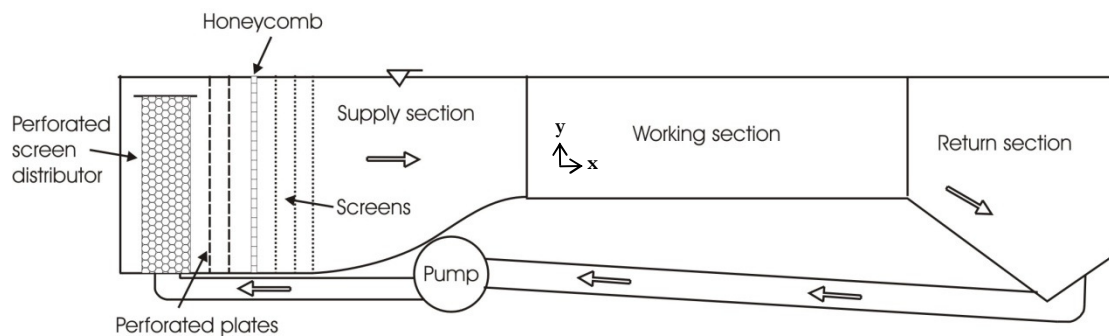


Figure 3.28 – Water tunnel facility used for hydrogen bubble visualisation.

3.5.1.1 Channel calibration

The free-stream velocity of the flow in the water channel was calibrated against the pump frequency for the water channel. This was achieved through the use of particle image velocimetry (see Section 0) and confirmed with dye visualisation. Data for a series of pump frequencies spanning the operating range of the facility were acquired for a small cross-section (100mm x 100mm) in the centre of the water channel. The viewing plane was perpendicular to the channel floor and parallel with the free stream. For verification, small packets of dye were injected into the centre of the test section at the upstream end. Video footage of the experiment was then used in conjunction with a length scale determined from a target image to determine the freestream velocity for each pump frequency investigated.

3.5.1.2 Mean Freestream Flow

The mean freestream flow velocity for a given pump operating frequency is determined by averaging the flow velocity vectors obtained using the PIV technique. Initially, a temporal average is determined from a series of image pairs collected over a given period of time. The resulting vector field is then spatially averaged to give the mean velocity

which consists of a horizontal component, \bar{u} , and a vertical component, \bar{v} . The vertical component is expected to be very small relative to the horizontal component. Figure 3.29 shows the freestream velocity as a function of the pump frequency for both dye and PIV measurements (ER Hassan 2011, personal communication) and these data sets are reasonably consistent.

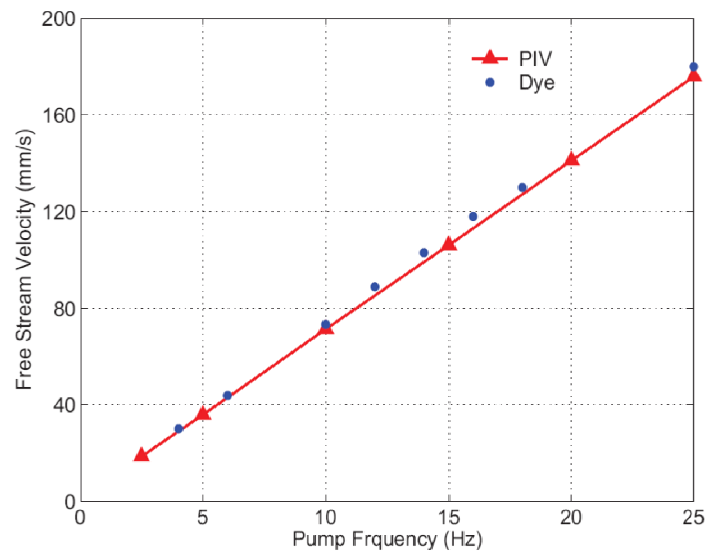


Figure 3.29 – Independent dye visualisation and particle image velocimetry (PIV) for water tunnel calibration (ER Hassan 2011, personal communication).

3.5.2 Hydrogen Bubble Method

Typically, the hydrogen bubble size is approximately one half of the wire diameter, thus by using a very small wire diameter, the bubble size can be chosen so that the rate at which the bubbles rise is almost negligible compared to the local velocity (Smits & Lim, 2000). The advantage of hydrogen bubbles over dye is that over time the water does not become unusable due to excessive colouring. In comparison with smoke visualisation, hydrogen bubble visualisation can be set up more quickly and does not have such stringent requirements of low turbulence intensity to be effective (Smits & Lim, 2000).

Hydrogen bubble visualization was carried out in the closed-return water channel at the University of Adelaide described in Section 3.5.1. The airfoil was mounted vertically as shown in Figure 3.30 and the wing tip was positioned approximately 2mm from the channel floor. This is within the range of the suggested maximum gap of $0.005 \times \text{span}$ (Barlow *et al.*, 1999).

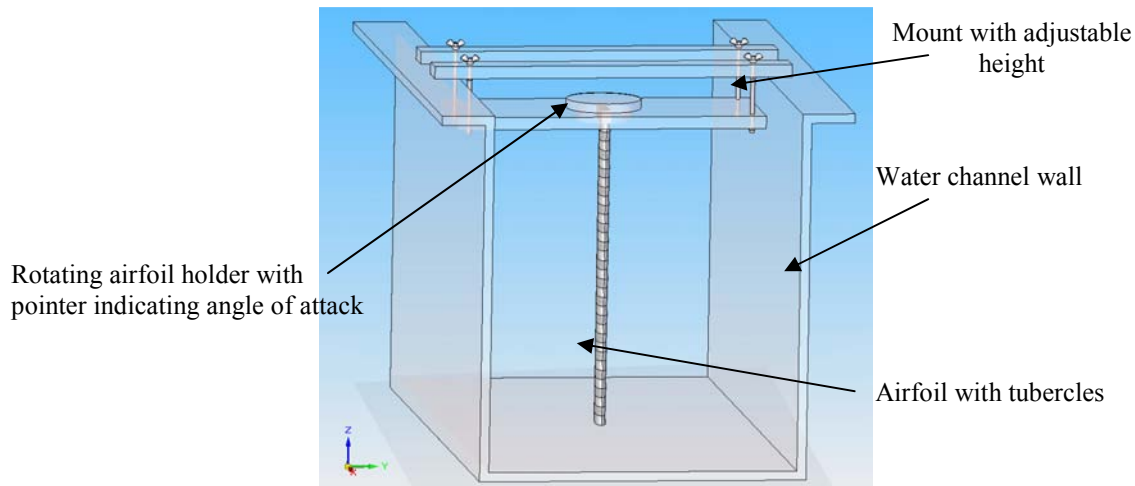


Figure 3.30 – Mount used in water tunnel for hydrogen bubble visualisation experiments.

The water channel velocity was selected to give optimum flow conditions for visualization with the hydrogen bubble method. Thus, velocities of $U_\infty = 70\text{mm/s}$ and 84mm/s were utilized, corresponding to Reynolds number based on the airfoil chord length of $Re = 4370$ and 5250 , respectively. These Reynolds numbers are substantially lower than those of the wind tunnel experiments discussed in Section 3.3. In spite of this, the large-scale vortical structures generated by the tubercles are expected to be fundamentally the same for both cases. There is some precedence for this in studies by Erm (2003), where it was found that both flow patterns and normalized surface pressure measurements on delta wings are very similar for Reynolds numbers differing by over an order of magnitude. Furthermore, a study by Thompson (1990) found very little qualitative difference in separated vortex flow patterns around an F/A-18 aircraft for Reynolds numbers spanning four orders of magnitude. The Reynolds number for the wind tunnel was not reduced to match that of the water tunnel since this gave rise to an undesirable increase in the free-stream turbulence intensity. A lower freestream velocity would also lead to a significant reduction in the forces on the wings, increasing the signal-to-noise ratio and hence uncertainty of the measurements. Moreover, the intention of the hydrogen bubble visualisation was to investigate the nature of the flow itself, rather than replicating wind tunnel conditions. Additionally, viscous forces are more dominant at low Reynolds numbers, increasing the size of vortical structures associated with a given flow condition, which enhances the results from flow visualisation.

Hydrogen bubble streaklines were generated by passing a low current through a sinusoidally-kinked platinum wire with diameter of $40\mu\text{m}$. Both a vertical wire and a horizontal wire were assembled in a mount and connected to electrodes which were wired to

a power supply which supplied the current necessary for electrolysis. The mounts were constructed in such a way as to minimise interference with the flow. The supports were positioned to the side of the airfoil where possible or otherwise at a spanwise location far removed from the viewing area. These characteristics can be seen in Figure 3.31, where the supports are angled away from the flow.

The flow was illuminated with a thin light sheet (~10mm thick) generated using an overhead projector. Images were digitally recorded via a SONY DCR-TRV900E Mini-DV video camera, which was connected to a laptop computer. Footage was recorded from different orientations to highlight specific features. The side view showed the separation point; the top view showed variations in streakline spacing alluding to local pressure and velocity variations and the angled top view enabled identification of vortex structures. In all cases, the flow was visualized as close as possible to the mid-span location to minimize 3-D flow effects.

NOTE:
This figure/table/image has been removed
to comply with copyright regulations.
It is included in the print copy of the thesis
held by the University of Adelaide Library.

Figure 3.31 – Examples of generic hydrogen bubble wire designs, (a) horizontal wire probe, (b) vertical wire probe (Smits & Lim, 2000).

3.6 Particle Image Velocimetry

Particle image velocimetry (PIV) is a laser-based technique which can be used to generate a single plane velocity field from images of a particle-laden flow. The advantages of the

technique are that it is non-intrusive and that it allows simultaneous measurement of velocities in a plane rather than single point measurements (Raffel, Willert & Kompenhans, 1998). A typical PIV set-up requires a laser source for illumination, an optics train for light sheet generation, seeding particles to trace the flow, a digital camera for recording the images, a computer for image storage and a software package or custom-written computer code to process the data. It is imperative that the timing between the two lasers and the camera can be controlled and easily adjusted and this is often achieved using a pulse delay generator.

The basic principle behind the technique is to measure the displacement of tracer particles during a known interval of time, which is the time delay between image acquisitions (Raffel *et al.*, 1998). The tracer particles are sized on the order of micrometres to ensure that they will follow the motion of the fluid elements faithfully. This is verified through calculation of the Stokes number (Melling, 1997). Illumination is provided by pairs of laser pulses which have the high energy required to produce adequate light scattering from the particles to be effectively collected by the CCD (charged couple device) camera sensor. The laser pulse duration must be short enough to ensure that the motion of the particles is “frozen” during the pulse exposure and that there is no image blurring (Adrian, 1991).

The particle images captured by the camera are transferred to a computer and then subdivided into interrogation windows (Raffel *et al.*, 1998). A spatial cross-correlation using a discrete Fourier transform is carried out for each interrogation window in a given image pair (Willert & Gharib, 1991). This provides an estimate of the particle displacement in each interrogation window. The associated velocity vector can then be determined through knowledge of the time delay between the images and the system magnification (Raffel *et al.*, 1998). The main limitation in the current set-up is that the image pair acquisition rate is limited by the frequency of the pulsed laser, which is fixed at 10Hz. This places a limitation on the temporal resolution of the measurements and thus the dynamic nature of turbulent flows may not be captured with this constraint.

3.6.1 Specific Considerations for Airfoils with Tubercles

The primary aim of the PIV experiments was to investigate the characteristics of the longitudinal vortices generated in the troughs between tubercles. Hence it was concluded

that the most useful information could be obtained by measuring the flow field in a plane perpendicular to the vortex axis. Several spanwise planes were investigated including $0.2c$, $0.4c$, $0.6c$, $0.8c$ and $1c$ as shown in Figure 3.32. The freestream velocity was selected to give optimal resolution of the vortex structures and it was found that $U_\infty = 32\text{mm/s}$ gave the best results. This corresponds to a Reynolds number based on the airfoil chord length of $Re \sim 2230$.

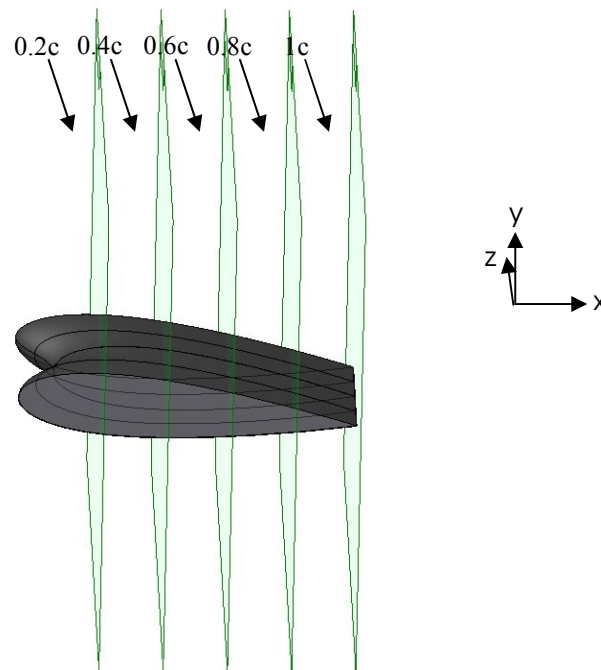


Figure 3.32 – Section of airfoil at $\alpha = 5^\circ$ with tubercles showing particle image velocimetry measurement planes from a perspective viewpoint.

The airfoil used in the PIV experiments was the largest amplitude and wavelength tubercle (A8W30) configuration since it was believed that the most significant vortex structures would be generated by this configuration. Larger vortices would enable improved resolution of the flow features as well as a higher expected circulation. Since the pattern of the sinusoidal tubercles is periodic, it was not necessary to measure the velocity for the entire airfoil span. Therefore a compromise was made between resolving the flow patterns and ensuring that the area under investigation was sufficiently large to give an accurate representation of the overall flow behaviour. Based on these considerations, the field of view shown in Figure 3.33 was chosen, giving an area of interest of $40\text{mm} \times 40\text{mm}$.

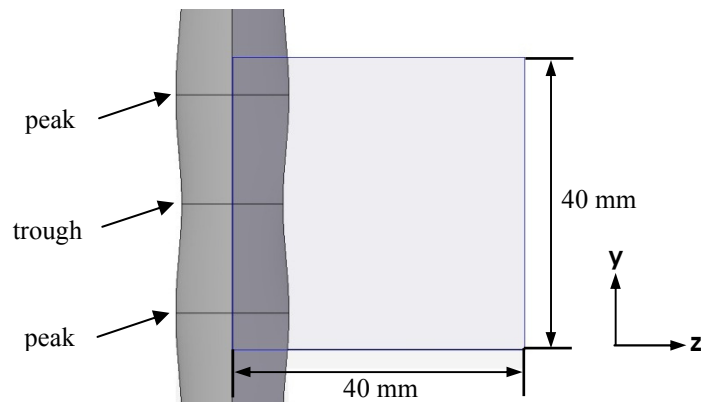


Figure 3.33 – Typical field of view for PIV experiments.

3.6.2 Thebarton Water Channel

Particle image velocimetry (PIV) experiments were undertaken in the free surface closed-return water channel shown in Figure 3.34. This water tunnel is named according to its location for the remainder of the thesis and is thus referred to as the “Thebarton water tunnel.” The working section of this flow facility is 350mm x 500mm and it is also made entirely of clear acrylic. There are two pumps available but since the flow velocity for the PIV experiments was relatively low, only one pump was used. The maximum steady flow operating velocity with one pump operating is approximately 140mm/s. Consistent with the water channel described in Section 3.5.1, the flow passes through a perforated cylindrical section, settling chamber and a series of flow conditioning sections.

For this facility, the flow conditioning sections consist of five 58% open area nylon mesh screens and a 1.35:1 contraction. The measured turbulence intensity at a freestream velocity of 32mm/s is approximately 3% based on a temporal average of 500 image pairs.

It was considered unnecessary to measure the boundary layer profile for the water tunnel facilities since the planes of interest for both hydrogen bubble visualisation and PIV were located at the centre of the test section. The maximum spanwise extent of the viewing planes was 100mm.



Figure 3.34 – Thebarton water tunnel used for PIV experiments.

The time delay parameters used for the PIV water tunnel calibration were based on approximate dye visualisation measurements and are shown in Table 3.10.

Table 3.10 – Time delay used for particle image velocimetry measurements of freestream velocity.

Frequency (Hz)	Time delay (μs)
10	21,400
20	10,700
30	7500
40	5500
50	4400

For each data set, a total of 500 image pairs were collected. The velocity fields obtained from these image pairs were then temporally and spatially averaged as described in Section 3.5.1.2. Figure 3.35 shows the freestream velocity as a function of the pump frequency for the PIV measurements.

It can be seen that there exists a linear relationship between the pump velocity and the freestream velocity as expected. The unexpected occurrence that the plot does not pass through the origin is related to flow short-circuiting through the other parallel pipe section. This indicates that flow does not begin to move in the circuit until the pump has reached a certain rotational speed.

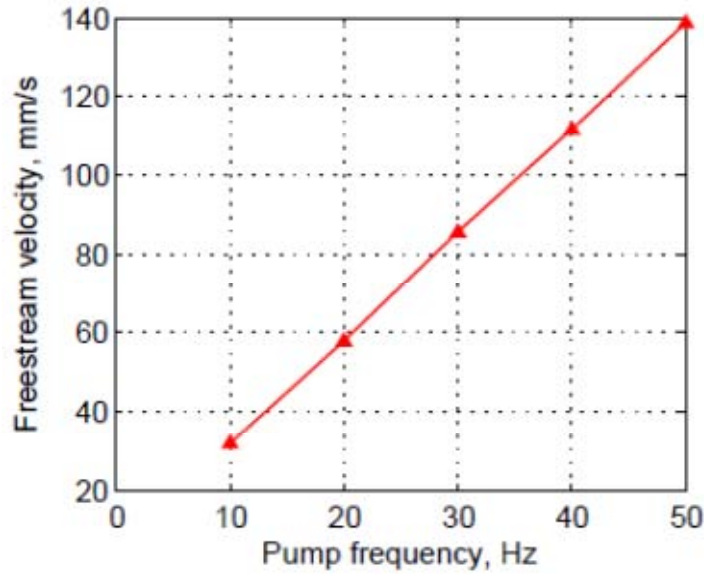


Figure 3.35 – Particle image velocimetry calibration for Thebarton water tunnel.

3.6.3 Tracer Particles

The water channel was uniformly seeded with polyamid seeding particles (PSP) which had mean diameter, $d_p = 50\mu\text{m}$ and a density of $\rho_p = 1030\text{kg/m}^3$. These particles have a narrow size distribution and can effectively scatter light. The density of the seeding particles was chosen to be very close to that of water to ensure that the particles would follow the flow as closely as possible. A measure for gauging how well a particle will follow the flow path over a distance, L , is the Stokes number. For a particle to follow the flow faithfully, the Stokes number, Stk , for a spherical particle should meet the condition $Stk \ll 1$. The Stokes number is defined as follows:

$$Stk = \frac{\tau U_c}{L_c} = \frac{\rho_p U_c d_p^2}{18\mu L_c} \quad (3.60)$$

where,

τ = particle relaxation time

L_c = characteristic length

ρ_p = particle density

U_c = characteristic velocity

d_p = particle diameter = $50\mu\text{m}$

μ = dynamic viscosity $\sim 10^{-3}\text{Pa}\cdot\text{s}$.

The characteristic length scale for a typical vortex structure was estimated to be approximately half of a tubercle wavelength, giving $L_c \sim 15\text{mm}$. This can be justified by

considering that two counter-rotating vortices were expected to occur between a given pair of tubercle peaks. A conservative estimate for the characteristic velocity is $U_c \sim U_\infty = 32\text{mm/s}$.

The calculated Stokes number is $\text{Stk} \sim 0.0003$ which is $\ll 1$ as required.

The particle settling velocity, v_s can also be calculated using Stokes' law which is defined as:

$$v_s = \frac{g(\rho_p - \rho_f)d_p^2}{18\mu} \quad (3.61)$$

where,

$$\rho_f = \text{fluid density} \sim 1000 \text{ kg/m}^3.$$

The calculated settling velocity is $v_s = 4.1 \times 10^{-5}\text{m/s}$. Therefore, for the maximum time delay used in the experiments, $\Delta T = 32\text{ms}$ (see Section 3.6.7), the particles would fall approximately 0.0013mm due to the gravitational force acting on them. This is equivalent to approximately 0.03 pixels (px), which means that particle settling has a negligible impact on the results.

Tracer particles were added to the flow in such a way that they were uniformly dispersed and could be introduced gradually. Hence, a small quantity of particles was added to a bottle of water and the contents were thoroughly mixed. Firstly, the bottle was held horizontally and rotated about its axis to begin the mixing process in order to minimise coagulation of the particles in the next stage. The following process involved vigorous shaking until mixing had occurred.

The resulting solution was added incrementally to the centre of the water channel, upstream of the pump, which was operating at full capacity. The channel was run at high speed for a considerable time before experiments were conducted to ensure that uniform mixing had taken place.

The optimum number of particles was determined by finding a balance between the conflicting requirements of spatial resolution and accuracy (Hart, 1999). As the number

of particles in the system is increased, spatial resolution improves since more particles exist within the interrogation region. However, at a certain point, it becomes difficult to differentiate between each particle in a given image pair and consequently, correlation accuracy is compromised.

3.6.4 Particle Image Size

The particle image diameter, d_e , describes the image size as recorded on the CCD array of the camera. The image size has a significant impact on the accuracy of PIV measurements. If the image size is too small, then particle displacements tend to be biased towards integral values (Raffel *et al.*, 1998). This leads to an effect called “peak-locking” which can be observed on a histogram diagram similar to that in Figure 3.36, as clusters of vectors instead of an even distribution as expected.

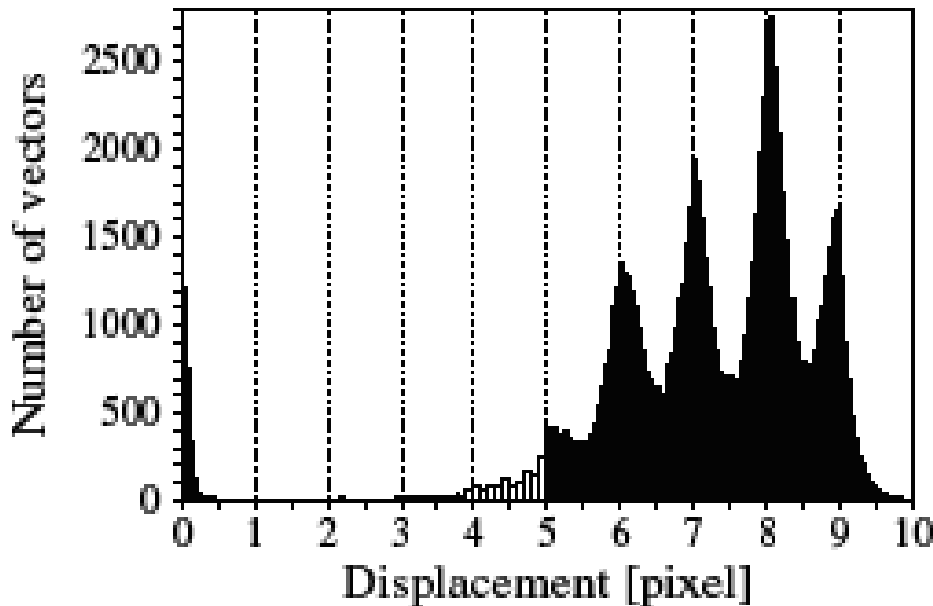


Figure 3.36 – Histogram of PIV data showing the “peak-locking” effect (Raffel *et al.*, 1998).

When the particle image diameter is too large, however, the random uncertainty increases due to irregularities in the electronic images (Prasad, Adrian, Landreth & Offutt, 1992). The optimum image diameter is slightly greater than $d_e = 2$ pixels according to Raffel *et al.* (1998).

The particle image diameter can be estimated from the following equation:

$$d_e = \sqrt{M^2 d_p^2 + d_{diff}^2} \quad (3.62)$$

Where for the present experiments,

$$M = \text{magnification factor, } M = D_i/D_o = 0.23$$

$$D_i = \text{diagonal of sensor frame} = \sqrt{(9.1)^2 + (9.2)^2} = 12.94 \text{ mm}$$

$$D_o = \text{diagonal of object plane} = \sqrt{(39.6)^2 + (40)^2} = 56.29 \text{ mm}$$

$$d_{diff} = \text{diffraction limited image diameter, } d_{diff} = 2.44 f_{\#} (M + 1) \lambda$$

$$\lambda = \text{wavelength of illuminating light} = 532 \text{ nm}$$

$$f_{\#} = \text{f-number, } f_{\#} = f/D_a = 11-16$$

$$f = \text{focal length}$$

$$D_a = \text{aperture diameter.}$$

Thus, particle image diameter is calculated to be $d_e \sim 0.025 \text{ mm}$. According to the calibration undertaken using PivView, 1mm is represented by 25.43 pixels. This means that the particle image size is ~ 0.6 pixels. To increase the particle image size on the CCD array, it is feasible to defocus the particle image (Raffel, 1998). This method was used successfully to obtain an acceptable value for d_e . This was confirmed by the absence of peak locking.

3.6.5 Lasers

The illumination source was a dual-cavity Quantel Brilliant B Nd:YAG laser, which has a fixed flashlamp pulse frequency of 10Hz. The laser emits a collimated beam of monochromatic coherent light of wavelength 1064nm which is frequency-doubled to give a beam at $\lambda = 532 \text{ nm}$. The diameter of the beam is 9mm and the doubling crystal was adjusted to ensure that the beam was at its maximum intensity. The energy of each pulse was controlled by changing the delay between the flash lamp and Q-Switch (Δ_{f-q}). A power meter was used to measure the energy output of each cavity at various values of Δ_{f-q} and the results are shown in Figure 3.37. This information could be used to gauge the difference in Δ_{f-q} for a given energy requirement for each laser. Typical values of Δ_{f-q} used in the experiments varied between 350 and 370 μs , corresponding to energy per laser pulse between 100 and 130mJ. The laser pulse duration was approximately 5ns (Quantel, 2002).

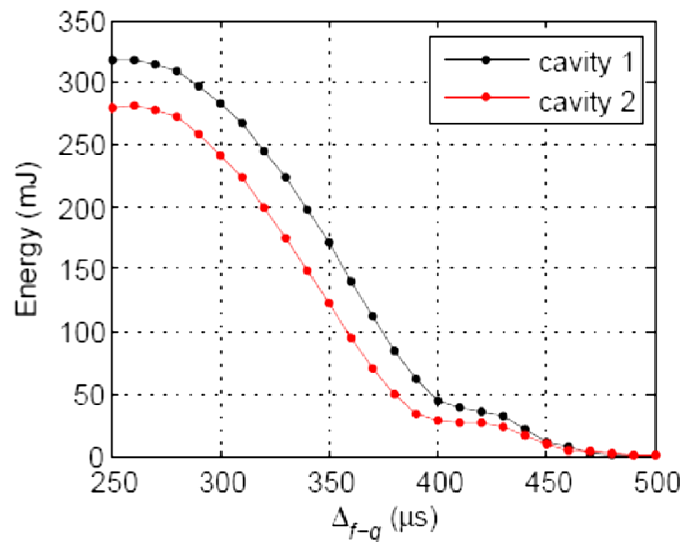


Figure 3.37 – Energy output from laser cavity as a function of Flash lamp – Q switch delay.

3.6.6 Light Sheet Optics

To create a sheet of light with the desired thickness, it was first necessary to reduce the laser beam diameter and then to spread the beam into a sheet. This was achieved by passing the beam through a series of optical elements as shown in Figure 3.38. The first optic was a convex spherical lens, S1 of focal length, $f = 100\text{mm}$. This was followed by a spherical concave lens, S2 with focal length, $f = -50\text{mm}$. The spacing between these two lenses was slightly greater than 50mm, which gave a beam that was converging by a small amount. It was thus possible to achieve a beam diameter reduction greater than the expected factor of two for this lens combination. Following the beam reducing lens pair was a cylindrical lens, C1 of focal length, $f = -6.25\text{mm}$ which spread the beam into a sheet. This was the smallest focal length cylindrical lens available and was chosen to give maximum sheet spreading angle which was desired due to space constraints. In order to direct the laser sheet to the region of interest, a high energy mirror with a 532nm-compatible coating was used. The plane of interest was perpendicular to both the freestream and the airfoil chord as discussed in Section 3.6.1. The final light sheet thickness was approximately 2mm, which was chosen as a compromise between maximising the time that particles would be inside the sheet and minimising cross-correlation uncertainties. These uncertainties would result if particles were in close proximity to one another but on different planes and thus one particle could be mistakenly correlated with another particle rather than with itself. The light sheet was regularly checked using burn paper to ensure that the thickness remained consistent.

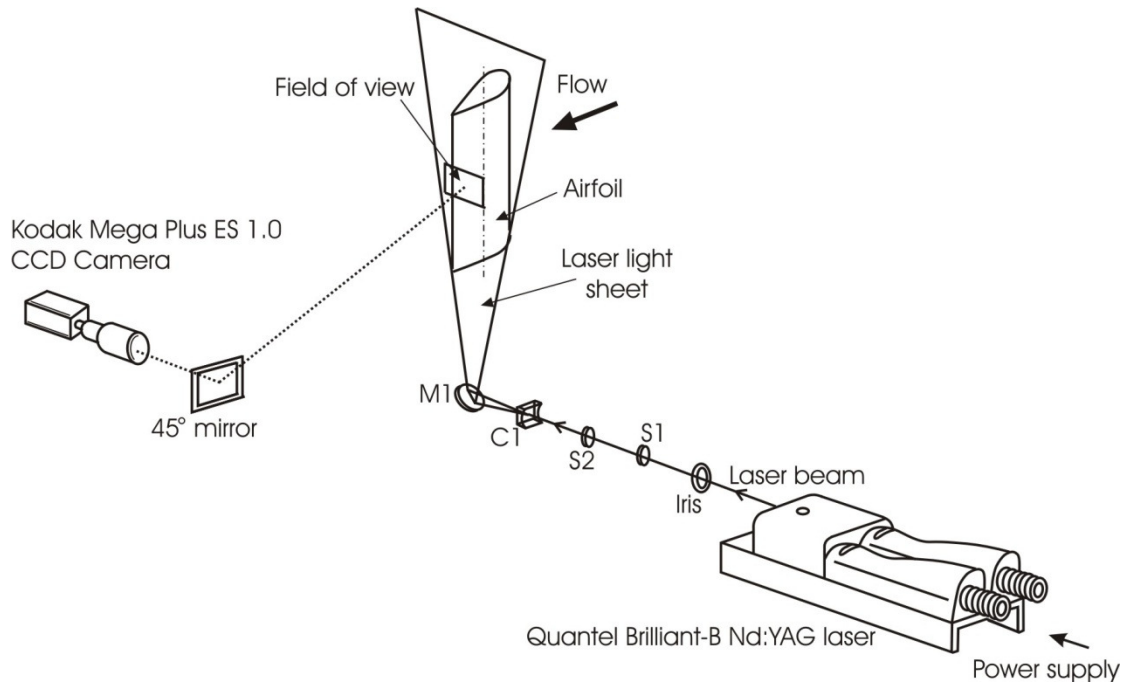


Figure 3.38 – Optics set-up for particle image velocimetry experiments (not to scale).

3.6.7 Time Delay Calculations

The time delay between illumination pulses must be long enough to ensure sufficient resolution of the particle displacements between images and short enough to minimise the probability of particles leaving the light sheet between subsequent illuminations. For a highly three-dimensional flow, a large number of particles have an out-of-plane velocity component which places an upper limit on ΔT . For the measurement planes under investigation as shown in Figure 3.32, the largest velocity component was the freestream component which was an out-of-plane velocity. Hence, to limit the out-of-plane loss of correlation, it was desirable to choose a suitable value of ΔT to ensure that the out-of-plane displacement of the particles would not exceed 30%, as recommended by Keane and Adrian (1990). Thus:

$$\frac{W\Delta T}{\Delta Z_0} \leq 0.3 \quad (3.63)$$

where,

W = out-of-plane component of velocity = 32mm/s

ΔZ_0 = light sheet thickness = 2mm.

The calculated upper limit for ΔT is 0.02s or 20ms, assuming that the maximum out-of-plane velocity component is equal to the freestream velocity. This was a typical value for

ΔT used in the experiments, however there was some optimisation required at certain chordwise positions to improve the resulting correlation between images. A smaller value of ΔT was used when there was a high level of vorticity and hence large particle displacement. However, in some cases when the vorticity was low, ΔT needed to be increased to achieve acceptable values of particle displacement. The value of ΔT could also be increased for stronger amounts of vorticity since the corresponding out-of-plane motion was lower. The location of the investigated image planes and their corresponding value of ΔT is shown in Table 3.11.

Table 3.11 – Summary of measurement planes and associated time delay, ΔT .

Chordwise position of laser sheet	Time delay, ΔT		
	$\alpha = 5^\circ$	$\alpha = 10^\circ$	$\alpha = 15^\circ$
0.2c	30ms	20ms	-
0.4c	30ms	20ms	32ms
0.6c	30ms	20ms	32ms
0.8c	30ms	20ms	20ms
1c	30ms	20ms	-

3.6.8 Timing and Synchronisation

Correct synchronisation between the laser pulses and the camera is an important component of the PIV method. For a given image pair, each image corresponds to a pulse from one of the two laser cavities and hence it is necessary to trigger the camera shutter to be open and close at the appropriate times. In addition, the time delay between pulses must be set accurately and it is preferable that this is easily adjustable.

The triggering of the laser pulses was regulated by a Stanford DG535 digital pulse delay generator. The associated timing diagram is shown in Figure 3.39. Laser 1 acted as a trigger for the system and fixed the sampling rate at 10Hz. A short time delay (A) in addition to the camera delay of $20\mu\text{s}$ was employed before triggering the camera to record the first image frame to take into account Δ_{f-q_1} . The transfer pulse delay (TPD) was set to ensure that the image was recorded towards the end of the first frame (Raffel *et al.*, 1998), taking into account that a buffer of $\delta = 2\mu\text{s}$ was necessary to allow for camera jitter. Typical values for TPD are between $250\mu\text{s}$ and $350\mu\text{s}$ and an optimal value was found to

be $270\mu\text{s}$, since for lower values there was some smearing of the images. There was then a delay of $5\mu\text{s}$ (transfer pulse width, TPW) before the second frame was exposed. A time delay, ΔT as calculated in Section 3.6.7 corresponded to the duration between laser pulses and hence the time delay necessary before triggering of the flashlamp for laser 2 (B) was dependent on both ΔT and Δ_{f-q_2} .

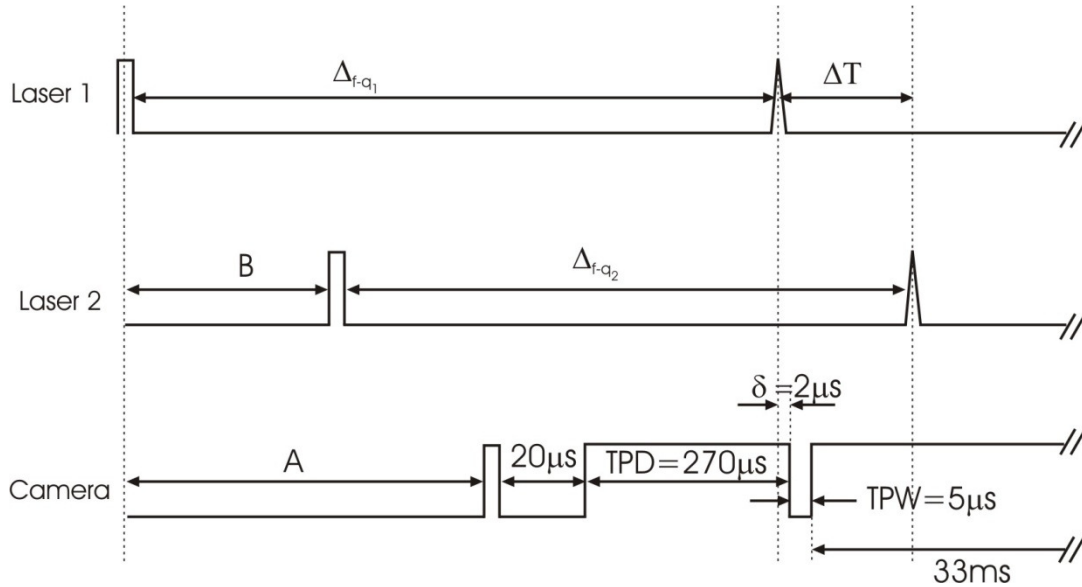


Figure 3.39 – Timing diagram for laser/camera synchronisation.

The equations for calculating A and B are shown below:

$$A = \Delta_{f-q_1} + \delta - \text{TPD} - 20\mu\text{s} \quad (3.64)$$

$$B = \Delta T + \Delta_{f-q_1} - \Delta_{f-q_2} \quad (3.65)$$

The calculated values of A and B were then entered into the signal generator to regulate the time delay of laser 2 and the camera respectively.

3.6.9 Imaging System

The PIV images were recorded using a Kodak Megaplug ES 1.0 10-bit CCD camera, which has a CCD array of $1008 \text{ pixels} \times 1018 \text{ pixels}$, having dimensions of 9.1 mm by 9.2 mm and the capability of capturing images up to a rate of 30Hz . The camera was run in “trigger double exposed mode” which allowed the capture of image pairs at a given rate set by the camera “trigger.” The camera was fitted with a Nikon 70-300mm f/11-16D zoom lens and mounted on a two-degree of freedom traverse. Thus, a desired target area could be imaged effectively and fine adjustments of positioning and zoom could be made

efficiently and accurately. All laser diagnostic images were saved as uncompressed 16 bit TIFF files. Image acquisition was facilitated by XCAP-Plus (for windows) software.

3.6.10 PIV Image Processing

To process the raw PIV image pairs, the software package PivView v1.75 was used. This software enables selection of image pre-processing parameters such as filtering and background image subtraction. It also provides image evaluation and post-processing capabilities such as selection of interrogation window size, correlation technique, peak fit method and outlier detection method.

3.6.10.1 Image Pre-Processing

In order to remove low level signals and to amplify the light scattered by particles, dynamic thresholding was applied to the raw images before cross-correlation. The lower limit defined the value below which the image intensity was cropped, and the upper limit increased the number of pixels at maximum intensity. Selection of the upper and lower limits was through an iterative process of optimising the resulting cross-correlation through minimising outliers (spurious vectors within an otherwise homogenous displacement field). Typically the lower threshold was 5% and the upper threshold was 99.5%.

3.6.10.2 Evaluation of Particle Displacement

To accurately resolve particle displacements, a sub-region is selected and then correlated to determine the peak correlation. More specifically, the 1008 x 1018 pixel images from the CCD camera were divided into interrogation windows having size 32 x 32 pixels. The overlap between these windows was set to 50% as a compromise between increasing spatial resolution while avoiding bias uncertainties caused by excessive overlap.

The correlation peaks were detected using “two-pass interrogation” and “double correlation” which are advanced techniques proposed by Westerweel, Dabiri, and Gharib (1997) and Hart (2000), respectively. The “two-pass interrogation” involves an initial correlation to determine the integer part of the particle image displacement. The interrogation windows are then offset by the amount corresponding to the integer part of the mean particle displacement (Westerweel *et al.*, 1997). The correlation analysis is subsequently repeated and according to simulations and experiments undertaken by Westerweel *et al.* (1997), the noise level of the measurement is reduced. This can be

explained by considering that the number of in-plane particles that are lost outside of the interrogation window is reduced.

The “double correlation” method is based on the assumption that adjacent interrogation windows should have similar locations of particle displacement peak but differing locations of random noise peaks. Hence, by multiplying the correlation data from adjacent interrogation windows, the strength of the correlation peak is predicted to increase while the relative random noise will decrease (Hart, 2000). This method is only effective for vector fields which do not have large velocity gradients.

Various peak fit algorithms are available which enable identification of the correlation peak to sub-pixel accuracy. According to Raffel *et al.* (1998), a robust method which is most frequently implemented is the Gaussian peak fit. This is because properly focussed particle images should resemble Airy intensity functions which are Gaussian. The correlation between two Gaussian functions is also Gaussian (Raffel *et al.*, 1998) and hence this peak fit method is often most suitable.

3.6.10.3 Preliminary Outlier Detection and Replacement

Outliers are defined as spurious vectors which are the result of detection of a correlation peak which is caused by noise or artifacts rather than matched image pairs (Raffel *et al.*, 1998). Basic methods for the detection and replacement of erroneous vectors are available in PivView. The methods used in this study considered both the “maximum particle displacement” and the “maximum displacement difference” relative to neighbouring displacement vectors to identify outliers. The maximum particle displacement was set to 10 pixels, which was a conservative estimate, given that the maximum in-plane particle displacement should not exceed 30% of the interrogation window size (Keene and Adrian, 1990) and experiments were tailored to meet this criterion. The maximum displacement difference is calculated by considering the magnitude of the vector difference between a given vector and its eight surrounding neighbours. If the difference in displacement is greater than the specified threshold value (typically 5 pixels) for more than four neighbours then the vector is considered an outlier. Methods of advanced outlier detection are discussed in Section 3.6.11.1.

Once the outliers had been identified, they were replaced with vectors corresponding to the second highest correlation peak. If this vector was also recognised to be an outlier then it was disabled. Generally, the number of outliers identified in this preliminary evaluation was 1-2% of the population but this varied depending on the flow case under investigation and the associated out-of-plane motion of the particles. A more advanced method of outlier detection was instigated at the post-processing stage of the analysis.

3.6.11 Post-Processing Techniques

Further processing techniques that are not available in the PivView software package were applied to the data in the next stage of the analysis using the technical computing language Matlab. Two methods were used for further processing of the data to minimise errors in the velocity-vector field. The first involved temporally averaging a total of 2085 image pairs. Due to the large number of image pairs available, outliers were not replaced and instead were omitted from the averaging process.

For the second method, detected outliers were replaced with a weighted average of valid surrounding vectors as explained in Section 3.6.11.2. Subsequently, an adaptive Gaussian window interpolator was implemented as described in Section 3.6.11.3. This technique reduces the amount of random noise associated with the velocity-vector field as discussed by Agui and Jiminez (1987). It was then possible to calculate the temporal average of the improved velocity-vector fields. Comparison could then be made between each image pair and the overall average of 2085 image pairs.

3.6.11.1 Normalised Median Test

This more advanced method of vector validation was introduced by Westerweel and Scarano (2005) and is an adaptation of the original median test proposed by Westerweel (1994). The more recent method involves normalisation of the residual of a given displacement vector by the median residual of its surrounding neighbours. The result is then compared to a threshold value and discarded if it exceeds this value.

Considering a 3x3 grid, the central displacement vector denoted by $\vec{V}_0(v_0, w_0)$ has eight surrounding neighbours $\{\vec{V}_1(v_1, w_1), \vec{V}_2(v_2, w_2), \dots, \vec{V}_8(v_8, w_8)\}$ which have an associated local median, \vec{V}_m (Westerweel, 1994). The residual is defined as $r_i = |\vec{V}_i - \vec{V}_m|$

(Westerweel, 1994) and is determined for each vector $\{\vec{V}_i \mid i = 1, 2, \dots, 8\}$. It is then possible to determine the median residual, r_m from the data set $\{r_1, r_2, \dots, r_8\}$ and this is used to normalise the residual of \vec{V}_0 . The resulting equation is as follows:

$$r_0^* = \frac{|\vec{V}_0 - \vec{V}_m|}{r_m + \varepsilon} \quad (3.66)$$

Here, ε is a compensating factor to ensure a minimal normalisation level. A suitable value for this parameter is $\varepsilon = 0.1\text{px}$ since this corresponds to a typical rms noise level for PIV data (Westerweel, 2000).

Westerweel and Scarano (2005) propose that a threshold value of $r_0^* = 2$ is an appropriate choice, where all vectors exceeding the threshold value are considered to be outliers. When r_0^* is defined to be below or above 2, this leads to a more or less stringent criterion, respectively. It should be noted that the horizontal and vertical components of the velocity vectors, w and v , are considered separately in this analysis. Thus, the final value of the normalised residual is found by calculating the root sum square of the residuals pertaining to the horizontal and vertical components of the displacement vector.

$$r_0^* = \sqrt{(r_{0H}^*)^2 + (r_{0V}^*)^2} \quad (3.67)$$

3.6.11.2 Outlier Replacement

Following identification and removal of the spurious vectors in a velocity vector field, analysis of instantaneous velocity fields required that the missing data should be replaced. The reason for this is that in order to perform integration or differentiation, it is necessary that data exists at each grid point in a data array. Hence, an estimation of the expected value was determined by using a weighted average of the valid data surrounding a given spurious vector. Adjacent neighbours only were considered in the evaluation, which led to a 3x3 array size with the outlier positioned at the centre. Each outlier, $\vec{V}_0(v_0, w_0)$, was replaced by the estimated value, $\vec{V}'_0(v'_0, w'_0)$:

$$v'_0 = \frac{\sum_{i=1}^3 \sum_{j=1}^3 w_{i,j} v(y_i, z_j)}{\sum_{i=1}^3 \sum_{j=1}^3 w_{i,j}} \quad (3.68)$$

The weighting coefficients, w_{ij} were determined by considering the relative distance between each grid point and the vector to be replaced. The weighting coefficient is inversely proportional to the distance between grid points as shown in the array, w_{ij} :

$$w_{i,j} = \Delta \begin{bmatrix} \frac{1}{\sqrt{2}} & 1 & \frac{1}{\sqrt{2}} \\ 1 & 0 & 1 \\ \frac{1}{\sqrt{2}} & 1 & \frac{1}{\sqrt{2}} \end{bmatrix} \quad (3.69)$$

where,

Δ = horizontal/vertical grid spacing.

In the case of an adjacent outlier, the weighting coefficient, w_{ij} was set to zero. However, since the number of outliers for a given instantaneous image was generally 1-2%, the number of adjacent outliers was minimal. Equation (3.68) and (3.69) were also used to find the horizontal velocity component of the estimated vector, w_0' .

Interpolated vectors were not included in the statistics for a given sample set and the main function of replacing outlying vectors was to ensure that the vector field was continuous for a given instantaneous image. For a time-averaged set of images, the existence of a large number of image pairs made it highly unlikely that there should be any missing data in the velocity vector field. Therefore it was possible to perform integration and differentiation without outlier replacement when the data were averaged temporally.

3.6.11.3 Adaptive Gaussian Window Technique

This technique acts to smooth the data when applied to regularly spaced data on a rectangular grid (Fouras & Soria, 1998). According to this method, each vector in a velocity field is replaced with a weighted average of the surrounding vectors (Agui & Jimenez, 1987). This procedure was applied to all regions of the vector field which were not boundaries. Each vector, $\vec{V}_{i,j}(v_{i,j}, w_{i,j})$, was replaced with the smoothed value, $\tilde{\vec{V}}_{i,j}(\tilde{v}_{i,j}, \tilde{w}_{i,j})$, which was calculated using the adaptive Gaussian window according to the following relationship:

$$\tilde{v}(y_i, z_i) = \frac{\sum_{k=1}^3 \sum_{m=1}^3 \alpha_{k,m} v(y_k, z_m)}{\sum_{k=1}^3 \sum_{m=1}^3 \alpha_{k,m}} \quad (3.70)$$

where,

$$\alpha_{k,m} = \exp\left(\frac{-\{[y_i - y_k]^2 + [z_j - z_m]^2\}}{H^2}\right) \quad (3.71)$$

Both in-plane velocity components ($\tilde{v}(y_i, z_i)$ and $\tilde{w}(y_i, z_i)$) were calculated using the appropriate form of Equation

(3.70). The parameter, H , determines the width of the Gaussian window and the optimum value is on the order of 1.24Δ , according to Agui and Jimenez (1987).

3.6.12 Dynamic Velocity Range

It is important to establish that the measured velocity is much larger than the minimum resolvable velocity due to the high signal-to-noise ratio associated with PIV. In addition, a large velocity range allows accurate measurements for flow fields in which the velocity is highly variable from one region to another (Adrian, 1997). The dynamic velocity range, VR , is determined by considering the ratio between the maximum in-plane velocity, \vec{V}_{\max} , and the minimum resolvable velocity, σ_u :

$$VR = \frac{\vec{V}_{\max}}{\sigma_u} \sim \frac{\vec{V}_{\max}}{r_o \sigma_s / \Delta T} \quad (3.72)$$

where,

r_o = conversion factor between pixel units at CCD array to mm = 0.04mm/px

σ_s = uncertainty in particle displacement

ΔT = time delay = 20 - 32ms

The parameter, σ_s , was determined by first approximating the average number of particles, N_I , present in an interrogation window, where a worst case estimate is $N_I = 6$. The uncertainty for a given particle displacement, $\sigma_s = 0.07\text{px}$, was then found from Figure 6b in Willert and Gharib (1991). The results from this figure were obtained by simulating fluid motion using a random pattern of dots which were shifted over the range of possible displacements.

Considering the randomly chosen case of $0.4\bar{c}$, $\alpha = 5^\circ$, the maximum velocity was $\vec{V}_{\max} = 2.6\text{mm/s}$, the corresponding dynamic velocity range was $DVR \sim 30:1$. Overall, the dynamic velocity range for the cases investigated was $20:1 \leq DVR \leq 65:1$.

3.6.13 Dynamic Spatial Range

A large spatial range enables measurements to be made of small scale variation embedded in larger scale motion (Adrian, 1997). Dynamic spatial range, DSR is defined as the ratio between the characteristic object size (in this case, the wavelength between tubercles, λ) and the minimum resolvable length scale, l_{yz} :

$$DSR = \frac{\lambda}{l_{yz}} \sim \frac{\lambda}{l_c / MN_{IW}} \quad (3.73)$$

where,

l_c = height or width of CCD array = 9.1mm

M = magnification factor = 0.23 (see Section 3.6.4)

N_{IW} = number of interrogation windows across image = 31.

Hence, the smallest resolvable length scale was $l_{yz} \sim 1.27\text{mm}$ and the dynamic spatial range was $DSR \sim 24:1$. This was considered acceptable to resolve the streamwise vortices associated with the tubercles since the vortex size, L_c was estimated to be around 15mm as discussed in Section 3.6.3.

3.6.14 Vorticity Estimation

Vorticity, ω , is a vector quantity and is defined as the curl of the velocity vector field:

$$\begin{aligned} \vec{\omega} &= \vec{\nabla} \times \vec{V} \\ &= \left(\frac{\partial w}{\partial y} - \frac{\partial v}{\partial z} \right) \vec{i} + \left(\frac{\partial u}{\partial z} - \frac{\partial w}{\partial x} \right) \vec{j} + \left(\frac{\partial v}{\partial x} - \frac{\partial u}{\partial y} \right) \vec{k} \end{aligned} \quad (3.74)$$

The streamwise vorticity of interest, ζ_x , can be estimated from the data collected for the velocity components, v and w in the cross-streamwise, cross-chordwise plane. Thus the streamwise vorticity is given by:

$$\omega_x = \frac{\partial w}{\partial y} - \frac{\partial v}{\partial z} \quad (3.75)$$

The data obtained from particle image velocimetry measurements are discrete and hence, to obtain an appropriate estimation of vorticity, numerical methods must be employed. These numerical methods provide an estimate for the differential terms in Equation (3.75).

3.6.14.1 Numerical Schemes for Vorticity Estimation

The chosen numerical scheme for vorticity estimation was the central difference scheme since it is adequate for most applications (Etebari and Vlachos, 2005). Other schemes were considered but since the areas of interest were in close proximity to the boundaries of the velocity field their large computational stencil caused inaccuracies. The central difference scheme is defined as follows:

$$\left(\frac{df}{dx}\right)_i \approx \frac{f_{i+1} - f_{i-1}}{2\Delta} \quad (3.76)$$

3.6.15 Circulation Estimation

An estimate of the circulation enables quantification of the strength of a vortex structure. The fundamental definition of circulation about a closed path, C , is given by the following equation:

$$\Gamma = \oint_C \vec{V} \cdot d\vec{l} \quad (3.77)$$

Circulation in two dimensions can thus be calculated through integration of the velocity integral, Γ_{vel} :

$$\Gamma_{vel} = \oint_C (vdy + wdz) \quad (3.78)$$

Alternatively, Stokes' theorem can be used to relate the circulation to the curl of the velocity vector, where the surface, S is enclosed by the path, C . The vector \vec{n} is normal to the plane of integration.

$$\Gamma = \iint_S (\vec{\nabla} \times \vec{V}) \cdot \vec{n} dS \quad (3.79)$$

In two dimensions, this equation can be simplified to the following:

$$\Gamma_{vor} = \iint_S \omega_z dS \quad (3.80)$$

Hassan, Lau and Kelso (2007) conducted numerical experiments on the velocity field of the Oseen vortex and studied various vorticity estimation schemes. Simulations were carried out for differing values of added noise magnitude, ε_u and resolution Δ/L , where Δ is the grid spacing and L is the length scale. It was found that the most accurate method of circulation estimation was the velocity integral, Γ_{vel} . Therefore, this method was used exclusively for the current study.

3.6.15.1 Numerical Schemes for Circulation Estimation

Once again the vorticity was determined through numerical integration using the central difference scheme. Hence, the region enclosed by the path of integration could be defined by a vorticity threshold or contour, ω_t , which corresponded to 10% of the maximum vorticity. A further constraint was applied which ensured that the radius, d , of the region of interest did not exceed a user-defined value. The value of d was in the range $14\text{mm} \leq d \leq 24\text{mm}$ for all cases but is specified more specifically in Section 6.5. These parameters were optimised to define the boundary of each vortex as accurately as possible. Details of the method and the associated uncertainty analysis are given in Hassan *et al.* (2007).

3.6.16 PIV Uncertainty Analysis

Quantification of the uncertainty in velocity is important as its magnitude impacts the accuracy of derived quantities such as vorticity and circulation. The uncertainty analysis necessary for the particle image velocimetry measurements is much more complex than the previous uncertainty analyses discussed in Sections 3.3.11 and 3.6.5. This is a consequence of a much more complicated system with a large number of inter-dependent variables. Hence, the uncertainty analysis employed does not consider the sensitivity coefficients and degrees of freedom as introduced in Section 3.3.11.

The uncertainty in velocity consists of both a systematic component and a random component. The systematic uncertainty is dominated by the perspective error, which is related to the use of a single image plane. The random component is related to various components of the experimental apparatus.

The perspective uncertainty is caused by the fact that the position of a given particle within the laser light sheet is unknown. For example, as shown in Figure 3.40, the particle may exist at the front or back of the light sheet or somewhere in between.

Consequently, there is an uncertainty in the actual position of the particle of δ_p . Considering the worst case scenario with the possible particle positions at the front and back of the light sheet and the range of the distance, x , corresponding to the maximum and minimum widths of a vortex from the centreline for the cases investigated, the relative uncertainty in velocity lies in the range 11.0 – 20.3%. However, in the majority of cases, the distance between particle positions would be much smaller than indicated in

Figure 3.40. More details about the calculation process for the perspective error are provided in Section 6.8.1.

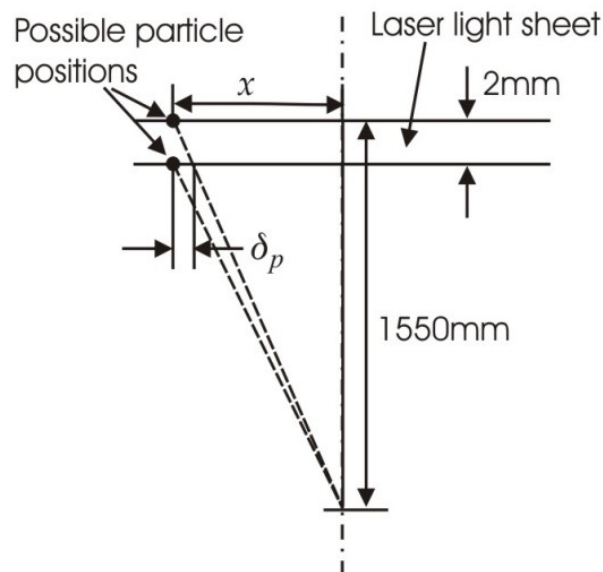


Figure 3.40 – Schematic of perspective error (not to scale).

The uncertainties due to the experimental apparatus are discussed in more detail in Section 6.8.2. The overall relative uncertainty in velocity calculated using this method is in the range of 0.2 - 0.4%. The uncertainty of the vorticity and circulation are derived from this quantity. The bias and random vorticity uncertainties are determined separately through application of the uncertainty propagation analysis of Fouras and Soria (1998) with reference to Lau (2010). Since the bias uncertainty in vorticity outweighs the random uncertainty, the range of vorticity uncertainty is dependent on the grid spacing, Δ and a suitable length scale, L . It is found that the vorticity uncertainty is influenced most significantly by the Δ/L ratio which is dependent on the number of vectors identified across a given vortex. The uncertainty is in the range of 1-15%, where the largest value corresponds to the $0.2\bar{c}$, $\alpha = 10^\circ$ case. The bias and random uncertainties in circulation are estimated from figures provided in Hassan *et al.*, (2007). Hence, the uncertainty in circulation is found to be such that $\varepsilon_r < 0.01\%$, except for the $0.6\bar{c}$, $\alpha = 15^\circ$ and $0.8\bar{c}$, $\alpha = 15^\circ$ cases, where $\varepsilon_r = 3\%$ and 7% respectively.

3.6.17 Summary

The parameters used in the particle image velocimetry experiments are summarised in Table 3.12 which is shown on the following page.

Table 3.12 – Summary of PIV recording parameters.

Parameter	Setting
Flow magnitude and orientation	$U_{\infty} \sim 32\text{mm/s}$ perpendicular to light sheet
Number of image pairs averaged	2085
Maximum in-plane velocity	$U_{\text{max}} \sim 1.9 - 6.4\text{mm/s}$ (case dependent)
Field of view	40mm x 40mm
Interrogation volume	1.55mm x 1.55mm x 2mm
Dynamic spatial range	DSR $\sim 24:1$
Dynamic velocity range	20:1 < DVR < 65:1
Observation distance	$z_o = 1.55\text{m}$
Recording method	double frame/double exposure
Ambiguity removal	frame separation (frame-straddling)
Recording medium	full frame interline transfer CCD (1008 x 1018 pixel)
Recording lens	Nikon 70-300mm, $f_{\#}$ 11-16
Illumination	Nd:YAG laser, 100-130 mJ/pulse
Pulse delay	$\Delta T = 20\text{-}32\text{ms}$
Seeding material	polyamid particles, $d_p = 50\mu\text{m}$, SG = 1.03

3.7 Acoustic Measurements

Acoustic measurements were carried out in the wind tunnel described in Section 3.3.1. The tonal noise characteristics for all airfoils under investigation were measured. Microphones were located outside of the working section and were fixed in the same positions for all experiments. Single point measurements were deemed acceptable since the aim of the investigation was to identify the magnitude and frequency of tonal noise rather than the source location.

It was considered necessary to use two microphones at different directional locations from the noise source. This would verify that any tonal noise reductions measured for the modified airfoils were legitimate and were not the result of redistribution of sound energy in a different direction. Hence, as shown in Figure 3.41, one microphone was positioned at a perpendicular distance of 280mm from the trailing edge of the airfoil, opposite an

acrylic window. The other was located near the atmospheric reference gap at the downstream end of the working section at a perpendicular distance of 400mm and a downstream distance of 280mm from the working section exit.

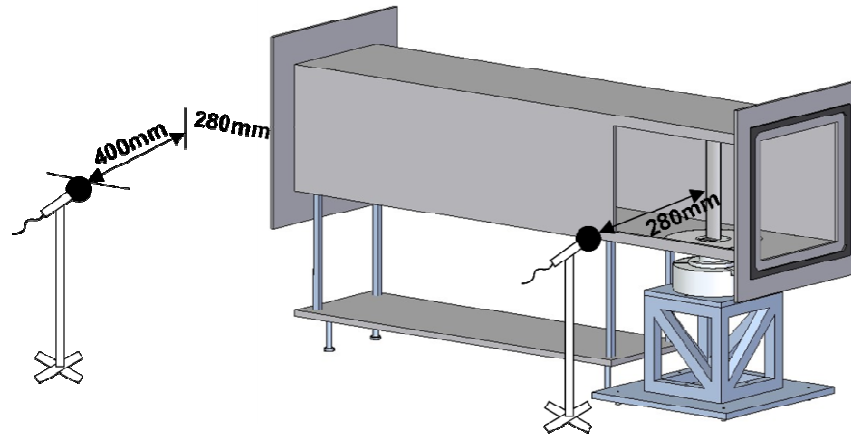


Figure 3.41 – Schematic of microphone positions.

3.7.1 Anechoic Wind Tunnel Measurements

Further acoustic results were obtained using the anechoic wind tunnel at the University of Adelaide to verify that the former results were not affected by the duct acoustics of the test section. This anechoic wind tunnel is shown in Figure 3.42 and consists of an 8m cubic room that is anechoic down to 200Hz, enclosing a free jet in the centre of which models can be tested. A centrifugal fan drives the air flow and is housed in an acoustic enclosure, consisting of a plywood box, lined with acoustic foam. The air inlet of the enclosure is fitted with louvers, specially designed to minimise noise emission while providing a low pressure drop to minimise system flow losses. The fan is attached to the silencer via a connecting flange that is fitted with a rubber vibration isolation strip and acoustic lining to further reduce noise radiation. The silencer is followed by the settling drum in which there are honeycomb and wire mesh screens to reduce the turbulence intensity. A contraction is fitted to the settling chamber and has dimensions of 75mm (height) and 275mm (width), giving a contraction ratio of 3.67. A thorough design process was followed to ensure high flow quality and is outlined in more detail by Leclercq, Doolan and Reichl (2007).

The flow uniformity along a vertical line at the centre of the exit plane is within 0.3% of the mean freestream velocity and the boundary layer thickness is 6mm on the top and

bottom walls of the contraction (Leclercq *et al.*, 2007). The turbulence intensity is approximately 0.4% at a freestream velocity of 25m/s (Leclercq *et al.*, 2007).

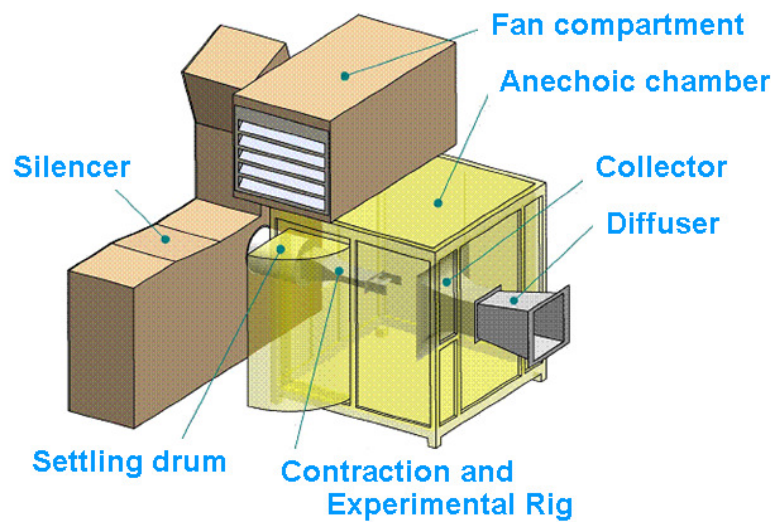


Figure 3.42 – Anechoic wind tunnel facility.

In order to reduce three dimensional effects, end-plates were manufactured for the model and a circular cut-out section with a “running fit” tolerance allowed the angle of attack to be adjusted as shown in Figure 3.43. For these measurements, a single microphone was positioned outside of the flow stream at a height of 650mm above the airfoil trailing edge and 50mm posterior to the trailing edge.

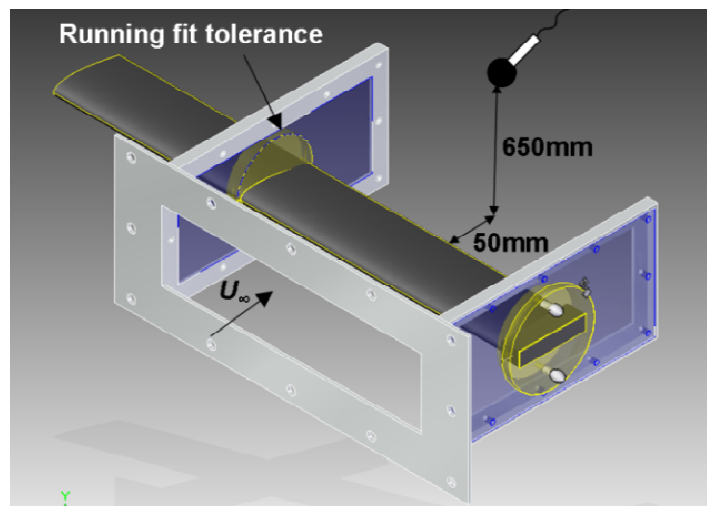


Figure 3.43 - Mount for anechoic wind tunnel.

To account for the downwash and flow curvature of the airflow around the model associated with the finite size of the open jet, a correction factor was applied to determine

the true angle of attack, α_* (Brooks, Marcolini, & Pope, 1986). The true angle of attack was reduced by approximately a factor of three as a result of these calculations.

$$\alpha_* = \alpha_i / \zeta \quad (3.81)$$

where,

$$\zeta = (1 + 2\sigma)^2 + \sqrt{12\sigma} \quad (3.82)$$

$$\sigma = (\pi^2 / 48)(c/H)^2 \quad (3.83)$$

c = airfoil chord

H = height of wind tunnel jet.

For both wind tunnel configurations, the free-stream velocity was measured using a Pitot-static tube according to the method described in Section 3.3.4. The Reynolds number based on the free-stream velocity of $U_\infty = 25\text{m/s}$ and airfoil chord length was $Re \sim 120,000$.

Acoustic data were measured in the wind tunnels using half-inch Brüel & Kjær condenser microphones attached to a Brüel & Kjær power supply and amplifier. The signals were processed using an Ace spectrum analyzer, which gave an output of the power spectral density. A stable averaging process was used, with a bandwidth of 1.6 Hz and a total of 100 averages per measurement, which took approximately 30 seconds to acquire. The frequency range of 200Hz - 2.5kHz was selected, based on preliminary measurements with the baseline NACA 0021 airfoil which indicated that all tones existed in this range. The angle of attack, α , was increased by one degree increments from $\alpha = 0^\circ$ to $\alpha = 12^\circ$. Some further measurements were taken in the stall regime but it was found that all tones occurred at $\alpha \leq 8^\circ$, and were absent when the wings were stalled.

3.7.2 Acoustic Measurement Uncertainty Analysis

The bandwidth of 1.6Hz is considered the uncertainty of the frequency measurements. Other sources of uncertainty include the freestream velocity and angle of attack. Data pertaining to the change in frequency with freestream velocity were not available and the tonal frequency varied significantly with angle of attack. In addition, the sound pressure level of the tonal noise varied from one measurement set to another. Hence, it was decided that a comprehensive uncertainty analysis would not be undertaken. Its absence

can be justified by the fact that the aim of the measurements was to demonstrate the absence and/or significant reduction of tonal noise for airfoils with tubercles when compared to an unmodified airfoil. The range of frequencies and sound pressure levels were considered to be of more importance than their exact values for a particular angle of attack.

3.8 Airfoil Structural Resonance Frequency Measurements

To verify that the tonal frequencies measured in the acoustic tests were not resonances unique to the particular airfoil and mounting arrangement used in the experiments, impact testing was performed. This involved using an instrumented hammer to strike the airfoil at different locations while simultaneously measuring the response using an accelerometer. The impact hammer tip was selected to ensure that the excited frequencies covered the entire frequency range of this investigation. The frequency range of interest was determined earlier from the acoustic tests described in Section 3.7.1 to be 200Hz - 2.5kHz. Thus, according to the impact hammer specifications, a plastic tip of medium hardness. To measure the structural response to excitation, a piezoelectric accelerometer was used. The accelerometer was attached to the airfoil via a thin layer of bee's wax which has little effect on the performance for temperatures less than 40°C (Hansen & Snyder, 1997). This method of attachment avoided damage to the structure under investigation and allowed the accelerometer to be conveniently moved to several locations.

Through calculation of the transfer function between the force and acceleration signal, peaks in the frequency spectrum could be identified and these peaks correspond to the resonance frequencies. In order to determine the transfer function, it was necessary to convert from the time to the frequency domain using a Fast Fourier Transform (FFT). The measured force and response signals are transients and it was important to select an appropriate window type and window width for each of them.

The force signal is a short-duration pulse which appears as a single compression spike on a time-history plot of the signal. Traditionally, the force window is a rectangular window of adjustable width, which should be set to the minimum duration required to capture the force pulse. The Ace spectrum analyser used in this analysis provides an improved force

window which compensates for a known deficiency of the response window. Rather than having a simple rectangular shape, the improved force window is of truncated exponential shape.

The response signal is a sum of exponentially decaying sinusoids. Thus, the response window has a decaying exponential shape and is weighted to essentially zero by the end of the window. The minimum decay necessary to entirely capture the signal is applied to minimise the artificial damping which can be introduced by the window. Such damping can reduce measurement resolution through obscuring closely-spaced modes. In addition, the width of the window is set to the minimum duration required for the signal to decay back to approximately zero.

A total of 5 averages per measurement were taken and each average was previewed to verify the integrity of the measurement. The force pulse is expected to be a single compression spike. However, if the test object is struck incorrectly, the impact hammer may hit more than once, leading to errors. The measurement parameters are summarised in Table 3.13 for both the vertical airfoil mount (used in the hard-walled wind tunnel) and the horizontal airfoil mount (used in the anechoic wind tunnel).

Where possible, parameters were kept constant, however it was necessary to reduce the width of both the force and response windows for the horizontal mount since there was more damping in the system due to the additional end constraint. The accelerometer positions and striking locations for the three tests undertaken are shown in Figure 3.44 and summarised in Table 3.14 for both the vertical and horizontal mounts.

Table 3.13 – Measurement parameters for resonance frequency testing (transfer function).

	Vertical airfoil mount	Horizontal airfoil mount
Frequency range	0 – 4 kHz	0 – 4 kHz
Bandwidth	2.5 Hz	2.5 Hz
No. of Averages	5	5
Trigger input	-0.5 V	-0.5 V
Force window width	0.01s	0.005 s
Response window width	0.2 s	0.03 s

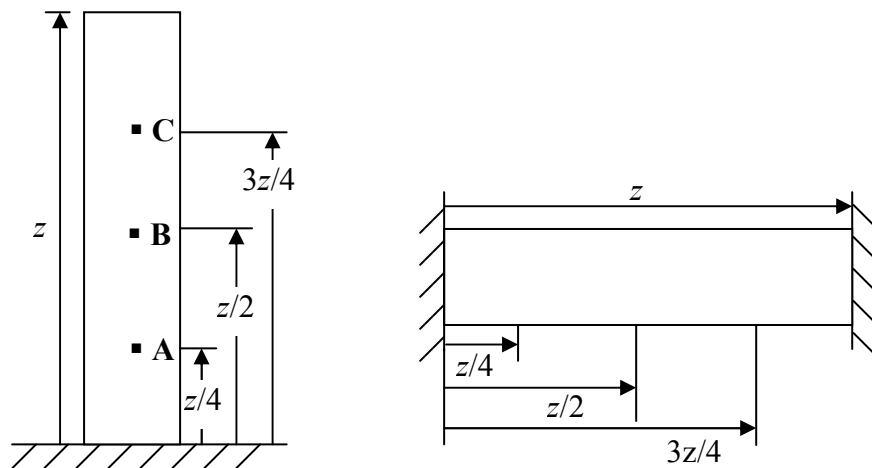


Figure 3.44 – Schematic showing accelerometer positions for vertical mount (left) and horizontal mount (right).

Table 3.14 – Summary of position combinations for accelerometer and impact hammer

<u>Test</u>	<u>Position</u>	
	Accelerometer	Impact Hammer
1	B	A
2	B	C
3	A	B

In order to verify the results, a reciprocity test was carried out where the accelerometer and striking positions were interchanged. With this configuration, it was expected that the response should be the same for both cases.

A more efficient but less accurate method was carried out to compare with the results using the impact testing method. This method involved measuring the auto power spectrum and taking a series of averages in “free run” mode (i.e. no trigger). The airfoil was tapped continuously in different random locations for the duration of each measurement. The frequencies with maximum amplification represent the resonance frequencies of the airfoil. A possible inaccuracy associated with this method is that since the force input is not evenly distributed as a function of frequency, it is possible to get false resonances, especially if the structure is not lightly damped. Thus it was used for

comparison only. The measurement parameters used for this test are specified in Table 3.15.

Table 3.15 - Measurement parameters for resonance frequency testing (auto power spectrum).

Parameter	Setting
Frequency range	0 – 4 kHz
Bandwidth	2.5 Hz
Window	Hanning
Overlap	50%
No. of averages	100

The measurements for the three different accelerometer/impact hammer configurations were compared and frequencies which were amplified in all three cases were considered. Values in Table 3.16 represent averages of the resonance frequencies for the three vertical airfoil mount configurations investigated. The resonance frequencies are represented by the peaks in the transfer function as shown in Figure 3.45. Results for the vertical mount in Figure 3.45 (a) indicate that the transfer function peaks correspond with the auto power spectrum values for two of the NACA 0021 resonance frequencies. One of the tones was not detected, which implies that the auto power spectrum method is less reliable. There did not appear to be any clear resonances for the airfoil in the horizontal mount in the frequency range of interest, which can be seen in Figure 3.45 (b). Results for the *A2 λ 7.5* tubercle configuration follow the same trends and the measured structural resonance frequencies are similar. This is expected as the fundamental structure of the two airfoils is the same and they are both milled from the same grade of aluminium.

Table 3.16 - Hard-walled wind tunnel (vertical airfoil mount).

Airfoil tested	Resonances (Hz)
0021	1328, 1890, 2128
<i>A2λ7.5</i>	1299, 1889, 2067

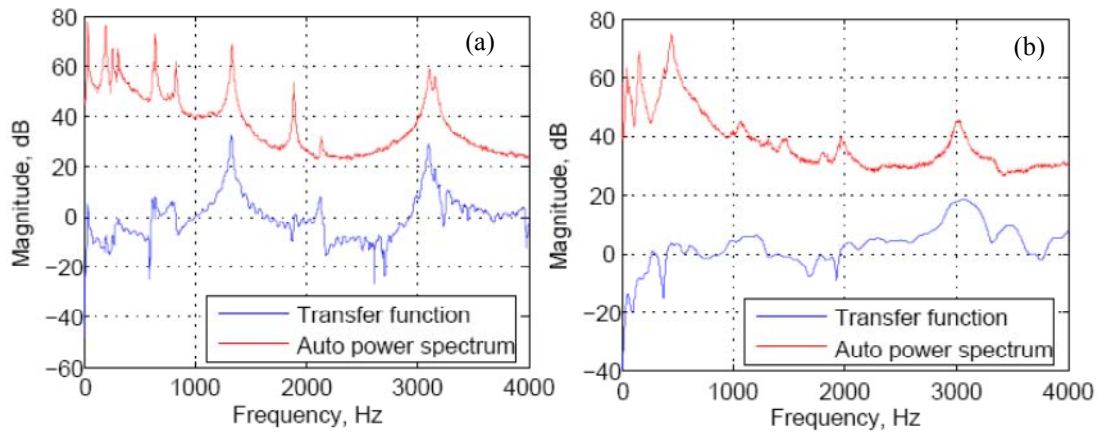


Figure 3.45 – Structural resonance frequency measurements for unmodified NACA 0021 airfoil. (a) Vertical mount (b) horizontal mount.

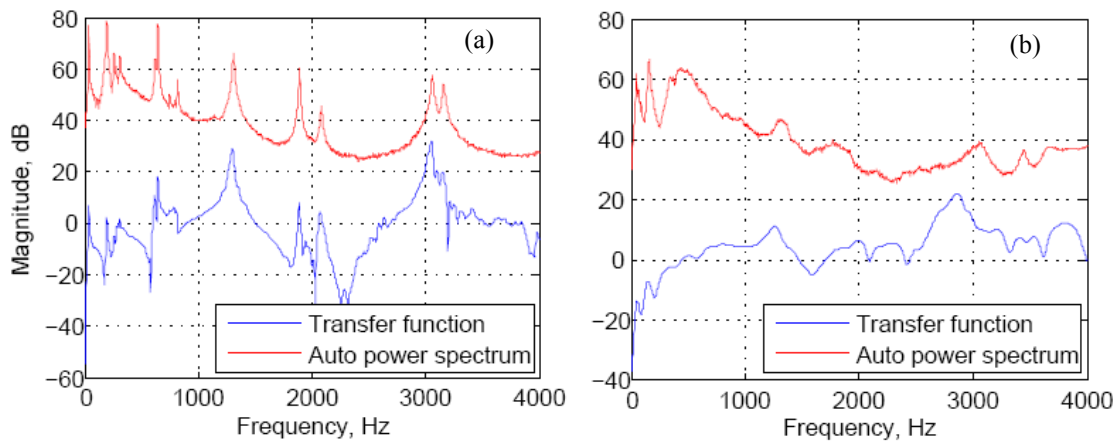


Figure 3.46 - Structural resonance frequency measurements for NACA 0021 airfoil with A227.5 tubercle configuration. (a) Vertical mount (b) horizontal mount.

An uncertainty analysis was not undertaken for these measurements since the resonance frequencies of the airfoils were found to be far different from the frequencies measured for the acoustic tones. The magnitude of the tonal noise was ignored as this is dependent on the force used to strike the airfoil with the impact hammer. Further information pertaining to the coherence and signal-to-noise ratios for the impact hammer and accelerometer signals is provided in Appendix D.

Chapter 4

Lift and Drag Forces



4.1 Introduction

The time-averaged lift and drag forces are presented in this chapter in non-dimensionalised form as a function of the angle of attack. These results provide a quantitative measure of aerodynamic performance, which enables identification of the optimal tubercle configuration for a given airfoil profile. In addition, the effects of variation in tubercle amplitude and wavelength are examined by comparing the relative lift coefficient, drag coefficient and stall angle. These performance indicators are also used to assess the viability of an alternative modification involving angular waviness. The investigation was carried out at a chord Reynolds number of $Re = 120,000$ with the airfoils presented in Section 3.2. A comparison is made between results for the NACA 0021 and NACA 65-021 airfoils to investigate the effect of profile shape on performance enhancement potential with tubercles. Dimensionless parameters such as the amplitude-to-wavelength (A/λ) ratio and the effective tubercle height to boundary layer thickness (h_{eff}/δ) ratio were used to highlight trends in order to more effectively predict performance.

In addition to quantifying the effects on performance of tubercles and waviness, further information could be gathered from the lift curve plots which indicate the existence of separation bubbles. In particular, it is observed that the NACA 65-021 airfoil generates

negative lift at low angles of attack and hence the effect of boundary layer trips on this phenomenon are also investigated.

A further aim of this chapter is to compare the lift and drag performance for models with and without modifications having different span lengths. This allows quantification of the three-dimensional effects and hence indicates whether tubercles perform more effectively on semi-span models compared to full-span models. This provides further information about the dominant performance enhancement method associated with leading edge tubercles and waviness.

4.2 Full-Span Airfoils

4.2.1 Comparison with Published Data

There is little published data available for comparison with the results for these specific airfoil profiles at low Reynolds numbers. Miklosovic *et al.* (2007) reported the lift and drag coefficients versus angle of attack for a NACA 0020 airfoil, however the Reynolds number was approximately double the one in the present work. It can be seen in Figure 4.1 and Figure 4.2 that the NACA 0021 airfoil in the present study has a lower stall angle and a higher drag, which is expected for a similar airfoil profile at a lower Reynolds number. However, the general trends are similar, particularly with regards to the abrupt stall characteristic as well as a slightly increasing lift-curve slope for angles of attack, α , between 5° and 8° .

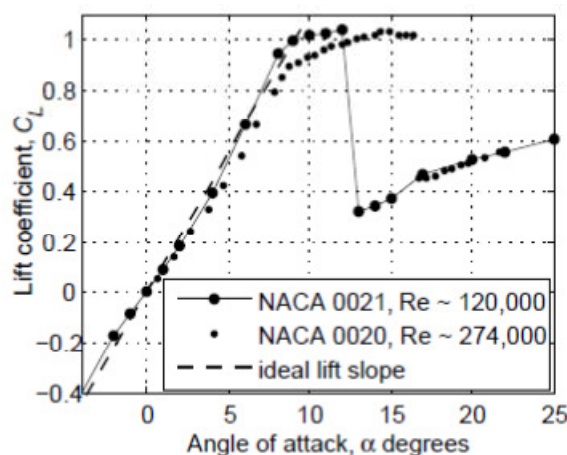


Figure 4.1 - Lift coefficient vs. angle of attack for NACA 0021 compared with experimental data for NACA 0020 (Miklosovic, 2007).

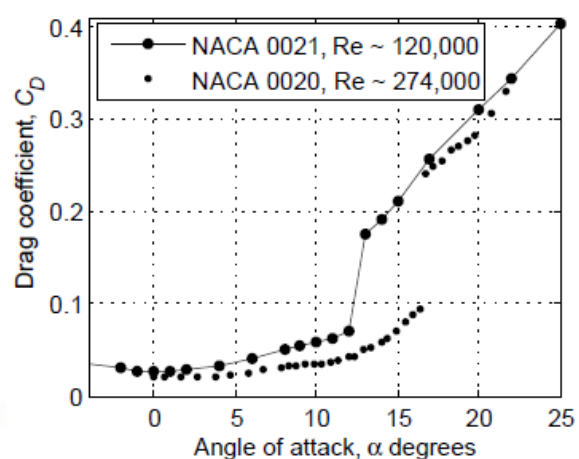


Figure 4.2 - Drag coefficient vs. angle of attack for NACA 0021 compared with experimental data for NACA 0020 (Miklosovic, 2007).

Comparison with the ideal lift-curve slope shows that the measured data approach this ideal slope and at one point exceed the theoretical value. The latter is attributed to either experimental uncertainty or the existence of a separation bubble which increased the apparent camber of the airfoil at this angle of attack (Mueller & Batill, 1982; Simons, 2002). This issue is discussed further in Chapter 5 where the surface pressure characteristics are investigated to determine whether such separation bubbles exist.

The repeatability of the measurements can be gauged from Figure 4.3 and Figure 4.4, where results from three independent tests are plotted on the same set of axes for comparison. It can be seen that there is negligible difference in lift for the three test runs. There is a slight variation in drag but it is not significant and the overall trends are the same. For example, the root-mean-squared deviation from the mean at an angle of attack of $\alpha = 10^\circ$ is 0.4% and 5% for the lift and drag coefficients, respectively. The same conclusions can be drawn from the fourth test (0021 foam), where the wing-tip was extended using closed-cell foam to minimize the gap between the airfoil and the test section ceiling. This implies that end effects were not significant and the airfoils can be considered two-dimensional.

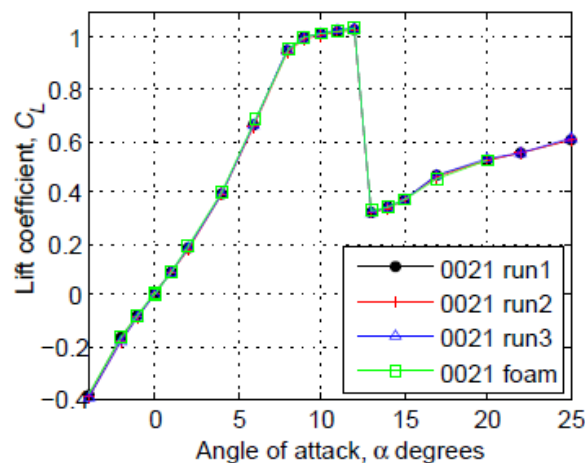


Figure 4.3 - Repeatability and influence of gap on lift coefficient for NACA 0021, $Re = 120,000$.

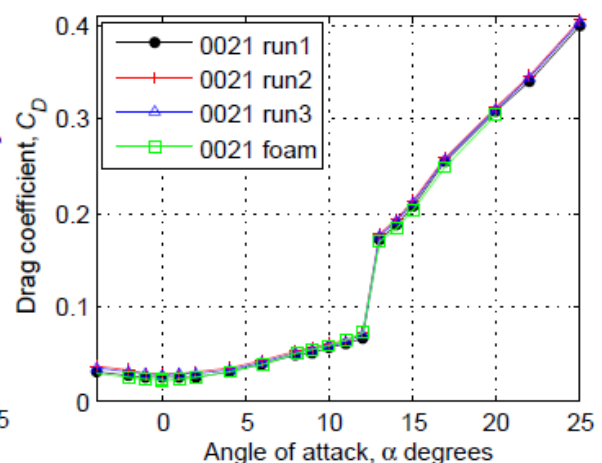


Figure 4.4 - Repeatability and influence of gap on drag coefficient for NACA 0021, $Re = 120,000$.

4.2.2 Negative Lift Characteristic of the NACA 65-021 Airfoil

At angles of attack between $0 \leq \alpha \leq 4^\circ$, the smooth NACA 65-021 airfoils produce a lift force in the opposite direction to that expected for a symmetrical airfoil at a positive angle

of attack. Figure 4.5 shows that this behaviour occurs for both the unmodified airfoil and the airfoils with tubercles. In Figure 4.5 and Figure 4.6, both the modified and unmodified airfoils demonstrate sudden increases in lift coefficient and decreases in drag coefficient at $\alpha = 5^\circ$ and 8° , respectively. The presence of the tubercles appears to reduce the angle of attack at which this occurs. The sudden increase in lift also occurs for the NACA 0021 but is not as pronounced and unusual. However, it is attributed to the same phenomenon of a separation bubble as discussed in Section 4.2. It can also be seen in Figure 4.6 that the drag associated with the modified airfoils is relatively higher as the stall angle is approached. Post-stall, however, the airfoils with tubercles experience a lower drag.

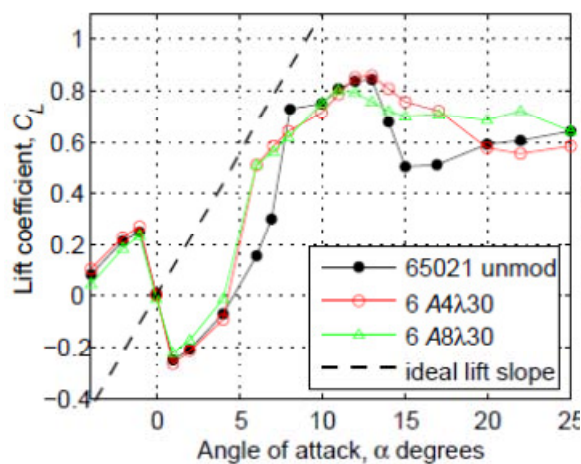


Figure 4.5 - Lift coefficient plotted against angle of attack for NACA 65-021, $Re = 120,000$.

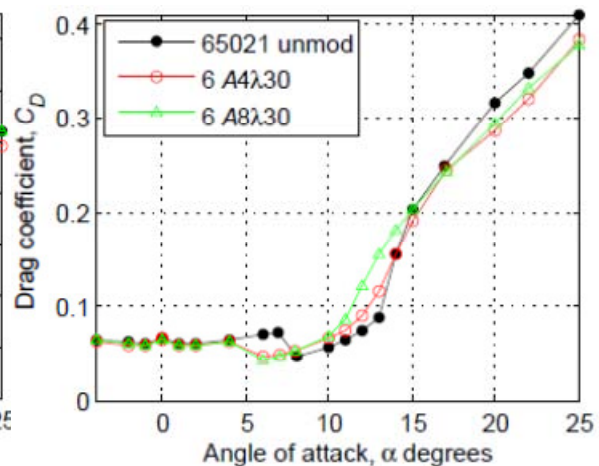


Figure 4.6 – Drag coefficient plotted against angle of attack for NACA 65-021, $Re = 120,000$.

It is evident that the magnitude of the negative lift force is the same for both a clockwise and anti-clockwise rotation of the airfoil, which negates the possibility that the phenomenon was due to model asymmetry as suggested by Mueller and Batill (1982). These researchers noticed the same negative lift effect for a NACA 66₃-018 airfoil at $Re \sim 130,000$ but attributed it to surface irregularities resulting from a surface finish done by hand after milling.

Marchaj (1979) also observed negative lift generation where a comparison was made between a NACA 63-018 and a NACA 64-018 airfoil at $Re = 2,600,000$. It was found that the airfoil section with maximum thickness further aft (NACA 64-018) experienced negative lift characteristics, whereas the other airfoil section had a linear lift curve slope which passed through the origin. This author attributed the negative lift to a significant thickening of the boundary layer at the trailing edge on the top surface of the airfoil,

which occurred due to the large trailing edge angle (Marchaj, 1979). This boundary layer thickening led to a larger effective curvature on the bottom surface of the airfoil relative to the top surface and hence, negative lift.

The negative lift behaviour was ameliorated through use of 0.4mm boundary layer trips placed on the suction and pressure surfaces. The height and position of the trips were optimized to give the lowest possible drag and maximum lift, while maintaining a linear relationship between C_L and α in the pre-stall regime. The roughness height was first estimated as discussed in Section 3.3.8 and then verified by experiment. Figure 4.7 and Figure 4.8 show that the 0.4mm trip satisfies the requirements specified above most accurately. These results show that the trip is sufficient to eliminate all of the separation bubbles responsible for the reverse lift and sudden lift increases. An ideal lift slope is provided in Figure 4.7 for comparison.

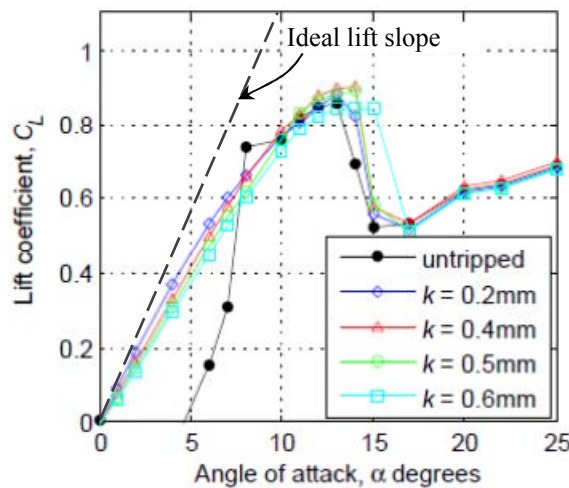


Figure 4.7 – Effect of trip height on lift coefficient for NACA 65-021 ($d = 5\text{mm}$), $Re = 120,000$.

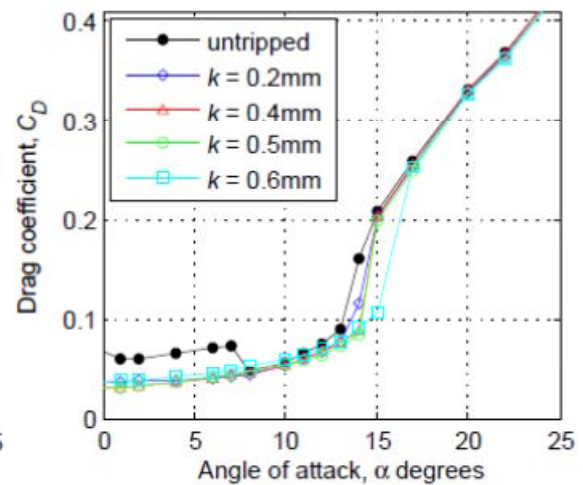


Figure 4.8 – Effect of trip height on drag coefficient for NACA 65-021 ($d = 5\text{mm}$), $Re = 120,000$.

The effectiveness of the boundary layer trips was also found to be dependent on their chordwise position. It was difficult to choose a standardized trip position for all airfoils since those with tubercles have a variable chord length along the span. Also, variation in the angle of attack of the airfoils led to different boundary layer characteristics. However, it was found that small variations in trip location gave negligible effects on C_{Lmax} . Figure 4.9 and Figure 4.10 show the variation in lift and drag performance, respectively for a trip height of 0.4mm. The distance, d , was measured from the leading edge to the front of the boundary layer trips. The figures indicate that the best position in which to place the

boundary layer trips is at 7% of the chord from the leading edge, which corresponds to a distance of 5mm.

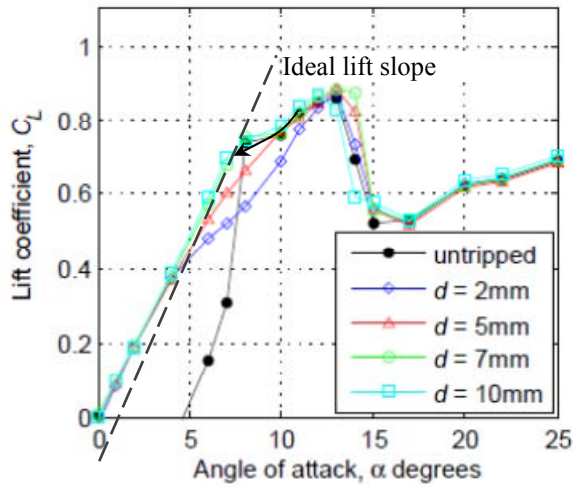


Figure 4.9 – Effect of trip position on lift coefficient for NACA 65-021 ($k = 0.4\text{mm}$), $Re = 120,000$.

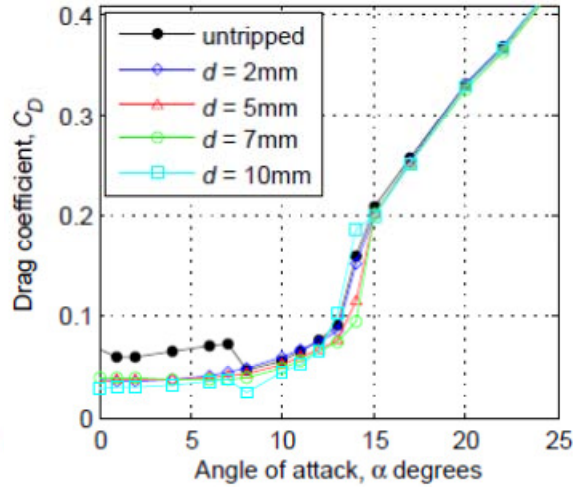


Figure 4.10 – Effect of trip position on drag coefficient for NACA 65-021 ($k = 0.4\text{mm}$), $Re = 120,000$.

Results in Figure 4.11 indicate that the negative lift characteristic is completely eliminated through use of boundary layer trips and that the slope of the lift curve is approximately linear for both modified and unmodified airfoils. Comparison between Figure 4.5 and Figure 4.11 reveals that the post-stall characteristics, C_{Lmax} and stall angles are almost identical with and without the presence of boundary layer trips for all NACA 65-021 airfoil models.

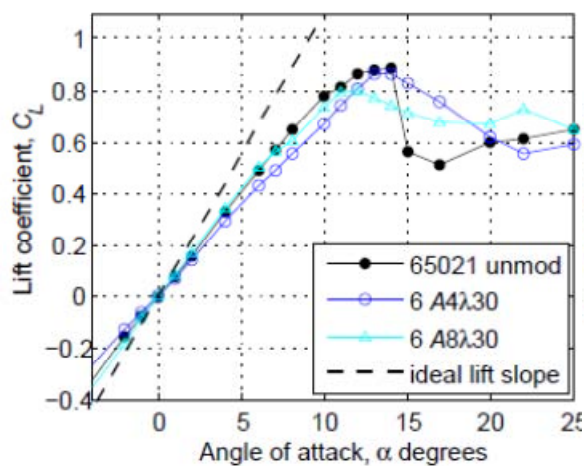


Figure 4.11 - Tripped lift coefficient plotted against angle of attack for NACA 65-021, $Re = 120,000$. Trip placed at $x/c = 0.07$.

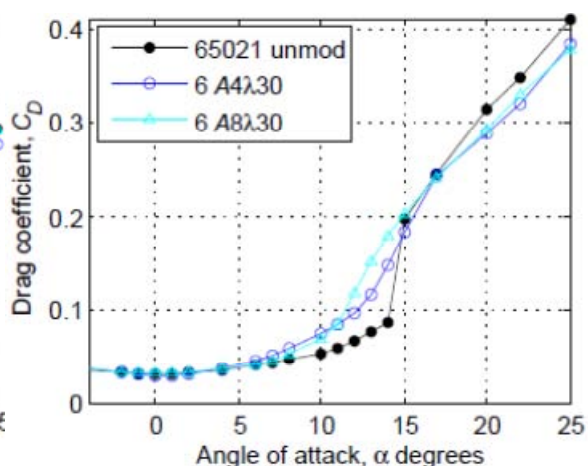


Figure 4.12 - Tripped drag coefficient plotted against angle of attack for NACA 65-021, $Re = 120,000$. Trip placed at $x/c = 0.07$.

The drag coefficient is reduced by the presence of the boundary layer trips for small angles of attack and is very similar for $\alpha > 10^\circ$, which can be seen in Figure 4.12. This implies that at angles of attack above $\alpha = 10^\circ$, the airfoil without trips experiences an early onset of a turbulent boundary layer, which negates the effects of the trips. These results are also consistent for both modified and unmodified airfoils. Comparison between Figure 4.6 and Figure 4.12 indicates that the relative differences in drag for various angles of attack for modified and unmodified models follow the same trends regardless of whether or not boundary layer trips are present. Comparison between Figures B5 and B7 in Appendix B show that the efficiency of the NACA 65-021 airfoil is noticeably improved through use of boundary layer trips.

4.2.3 Comparison of Airfoils and Effects of Tubercles

The lift and drag coefficients are plotted against the angle of attack for the NACA 0021 airfoils in Figure 4.13 and Figure 4.14. The tubercle configurations investigated are equivalent to those studied for the NACA 65-021 airfoil. It was deemed unnecessary to use a trip for the NACA 0021 airfoil however, since the lift coefficient versus angle of attack curve is relatively linear. There is a small increase in the slope of the lift plot for $5^\circ < \alpha < 8^\circ$, which results in a slope slightly greater than 2π , which is due to the presence of a separation bubble on the suction surface. This is discussed in more detail in Chapter 5.

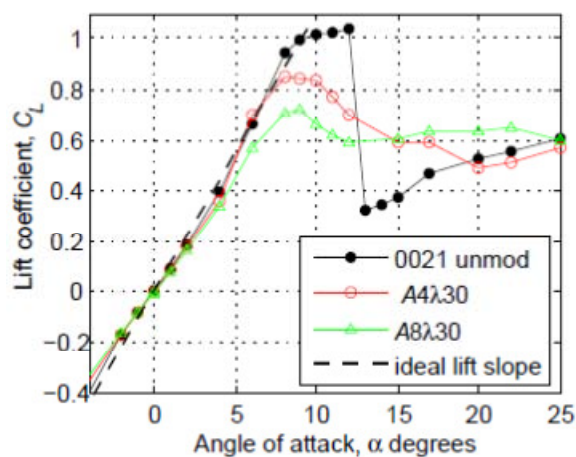


Figure 4.13 - Tubercle amplitude variation and the effect on lift coefficient for NACA 0021, $Re = 120,000$.

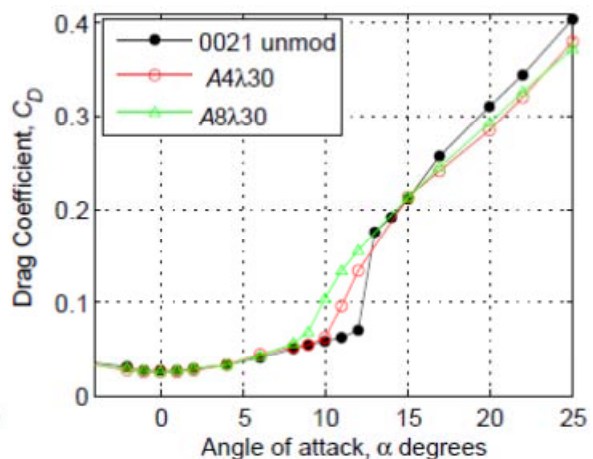


Figure 4.14 - Tubercle amplitude variation and the effect on drag coefficient for NACA 0021, $Re = 120,000$.

In comparison with the tripped and untripped NACA 65-021 airfoil results shown in Figure 4.11 and Figure 4.5 respectively, the NACA 0021 airfoil produces a larger amount of lift but stalls much more abruptly at a lower angle as displayed in Figure 4.13. It can be seen in Figure 4.14 that the drag characteristics for the two airfoils are similar and differences are associated with the fact that stall occurs at a lower angle of attack for the NACA 0021 airfoil, thus causing an earlier onset of increased drag for this airfoil. The efficiency of the NACA 0021 airfoil is greater than the NACA 65-021 which can be seen through comparing Figures B1 and B5 in Appendix B.

Examining the lift coefficient plots for the NACA 65-021 airfoil in Figure 4.5 and Figure 4.11 reveals that the maximum lift coefficient and stall angle are comparable for the modified and unmodified airfoils. In the case of the NACA 0021, the airfoils with tubercles perform less effectively in terms of maximum lift coefficient and stall angle, as shown in Figure 4.13. For both airfoil profiles, however, the stall characteristics are much more gradual with leading edge tubercles and the amount of lift generated in the post-stall regime is also greater. At low angles of attack, there is very little difference in drag between the various leading edge tubercle configurations as evident in Figure 4.6, Figure 4.12 and Figure 4.14. However, the width of the low drag zone is reduced for airfoils with tubercles due to the fact that these airfoils begin to stall at a lower angle of attack. For these airfoils, stall is more progressive and begins behind the troughs at a lower angle of attack. Nevertheless, as the angle of attack is increased beyond the unmodified airfoil stall point, the rate of increase in drag for the modified airfoils is lower. This leads to lower drag for airfoils with tubercles at high angles of attack. These results are consistent for both the NACA 65-021 and NACA 0021 airfoils. In terms of efficiency, the unmodified airfoils achieve the maximum efficiency pre-stall but the modified airfoils are more efficient post-stall, which is evident in Figures B1 and B5 in Appendix B.

4.2.4 Performance Effects of Variation in Tubercle Amplitude

The effect on the lift coefficient of changing the amplitude of tubercles is the same for both airfoil profiles under investigation as evident in Figure 4.11 and Figure 4.13. The airfoils with the smaller amplitude tubercles demonstrate a higher maximum lift coefficient and stall angle compared to the larger amplitude configuration. In addition, the post-stall characteristics are improved relative to the unmodified airfoil. On the other hand, airfoils with larger amplitude tubercles also have advantages such as a smoother

stall characteristic and increased post-stall lift relative to the smaller amplitude tubercle configuration.

The drag characteristics shown in Figure 4.12 and Figure 4.14 indicate that at low angles of attack there is very little difference in performance for the different leading edge configurations. However, there is an increase in drag associated with the earlier onset of stall for the airfoils with larger amplitude tubercles. In the post-stall regime, the amplitude does not have a significant effect on the drag characteristics.

Additional experiments were undertaken to determine the effect of further reduction in tubercle amplitude. Figure 4.15 and Figure 4.16 show that both lift and drag performance are improved as the tubercle amplitude is reduced. The lift performance of the airfoil with smaller amplitude tubercles ($A2\lambda7.5$) approaches that of the unmodified airfoil in the pre-stall regime. There is negligible difference in the drag coefficient for the $A2\lambda7.5$ airfoil in the pre-stall regime compared to the unmodified airfoil. However, a marked improvement is observed for both the lift and drag in the post-stall regime for the $A2\lambda7.5$ airfoil.

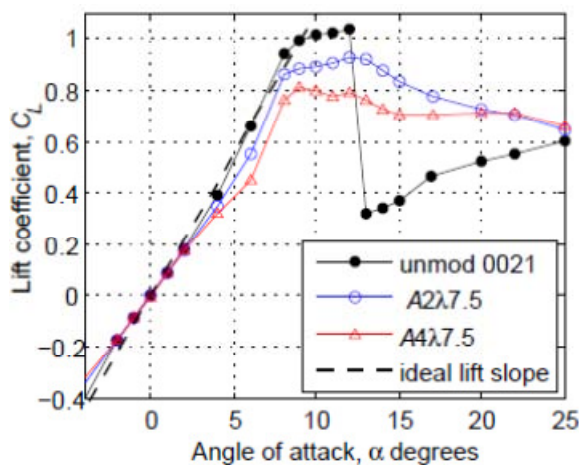


Figure 4.15 - Further amplitude reduction and the effect on lift coefficient for NACA 0021, $Re = 120,000$.

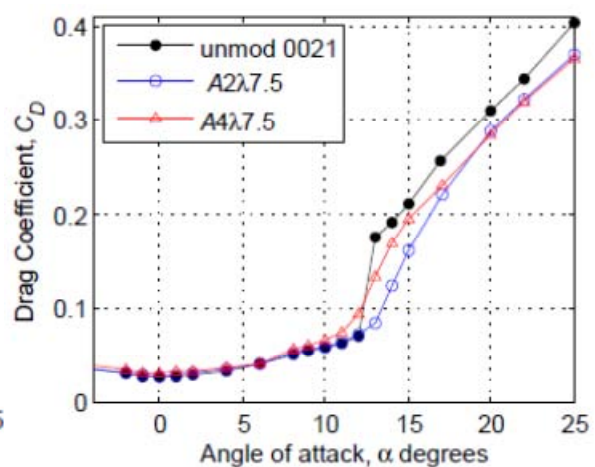


Figure 4.16 - Further amplitude reduction and the effect on drag coefficient for NACA 0021, $Re = 120,000$.

4.2.5 Performance Effects of Variation in Tubercle Wavelength

An investigation into the effects of wavelength variation on the performance of the modified airfoils was only carried out for the NACA 0021 airfoil due to budget limitations. Initial experiments suggested that as the wavelength of the tubercles is

reduced, the airfoil performance improves in terms of maximum lift coefficient, stall characteristics and drag. However, it was found that for a given tubercle amplitude, there is a limitation in the improvements that can be gained through reducing the wavelength.

Figure 4.17 shows that the largest wavelength tubercles ($A4\lambda60$) perform poorly and in fact demonstrate no advantage in comparison with the unmodified airfoil. Reducing the wavelength by a factor of four ($A4\lambda15$) allows the airfoil to reach a higher angle of attack before stalling and hence a larger lift coefficient. Although this airfoil ($A4\lambda15$) achieves a lower maximum lift coefficient in comparison with the unmodified airfoil, the post-stall lift characteristics are much more favourable. A further decrease in the wavelength by a factor of two ($A4\lambda7.5$), leads to a relative reduction in lift for the majority of attack angles, except $\alpha > 18^\circ$.

As explained in the previous section, a lower drag is experienced for a larger range of angles when stall occurs at a higher angle of attack. Hence, as shown in Figure 4.18 the $A4\lambda15$ airfoil not only demonstrates favourable lift characteristics but has a better overall drag performance considered across the whole range of angles shown, when compared to the unmodified airfoil. The fact that there appears to be an optimal wavelength for a given amplitude of tubercles is a positive discovery in terms of manufacturing complexity. As the distance between tubercles is reduced, the cutting tool size must also decrease and the number of protrusions for a given airfoil span will increase.

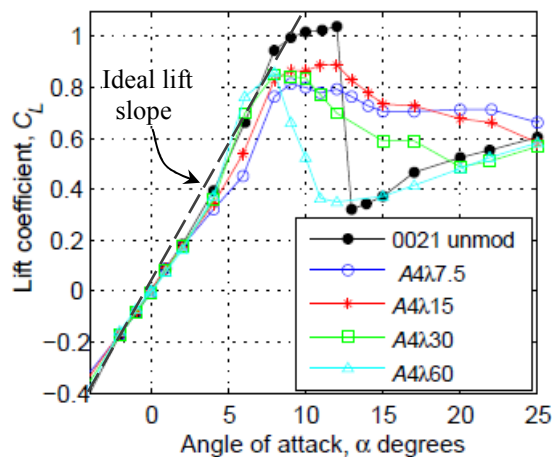


Figure 4.17 - Tubercle wavelength variation and the effect on lift coefficient for NACA 0021, $Re = 120,000$.

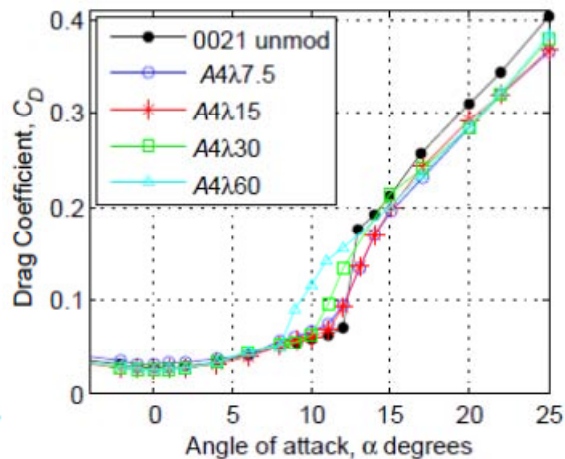


Figure 4.18 - Tubercle wavelength variation and the effect on drag coefficient for NACA 0021, $Re = 120,000$.

4.2.6 Wavy Airfoil Comparison

Incorporating waviness into the NACA 0021 airfoil leads to similar performance characteristics as leading edge protrusions. The effect of waviness on the lift coefficient is shown in Figure 4.19 and it is evident that the maximum lift coefficient for the various configurations is very similar. However, it can also be seen that the stall angle is increased and post-stall lift performance is improved for the wavy airfoil as the wavelength is decreased and the angle of waviness is increased. Hence, the most successful wavy configuration is the $\theta 4\lambda 15$ case which is compared to the best performing tubercle configuration, $A2\lambda 7.5$ in Figure 4.19. The maximum lift coefficient for both airfoils is almost equivalent but the wavy airfoil does not experience an increasing lift curve slope near the stall angle, which could be related to the absence of a separation bubble. Favourable lift characteristics can be observed for the wavy airfoil post-stall and it is predicted that a lift-generating mechanism similar to the one associated with tubercles is responsible for this behaviour. From the available lift data, it is not possible to conclude which wavy configuration offers the best potential lift performance as further optimisation of the wavy airfoil would be required.

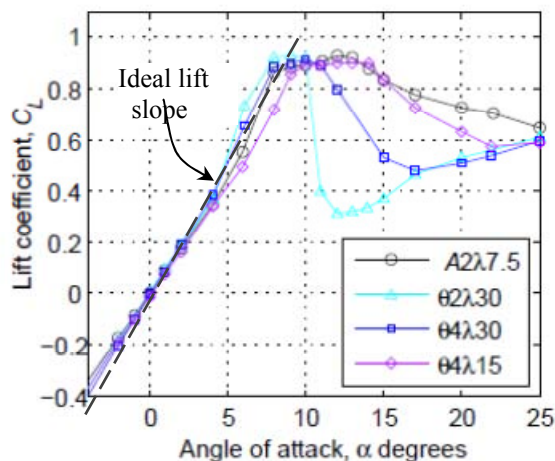


Figure 4.19 - Lift coefficient plot for various wavy airfoil configurations and comparison with the most successful tubercle configuration, $Re = 120,000$.

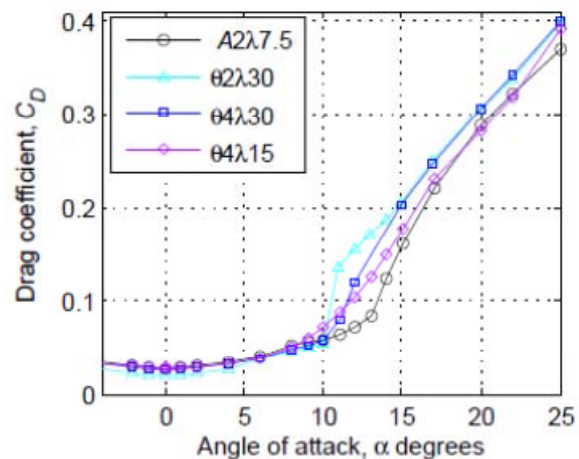


Figure 4.20 - Drag coefficient plot for various wavy airfoil configurations and comparison with the most successful tubercle configuration, $Re = 120,000$.

The overall drag performance of the $\theta 4\lambda 15$ wavy airfoil is also the most desirable when compared with the other wavy configurations. At low angles of attack, the $\theta 2\lambda 30$ configuration appears to experience the lowest drag, however the difference is relatively small and may be attributable to experimental uncertainty. Since this airfoil configuration

has sudden stall characteristics, there is a rapid increase in drag following stall and the amount of drag remains comparatively high for the remaining angles of attack post-stall. The airfoil with tubercles demonstrates superior drag characteristics near the stall angle but for other angles of attack the drag coefficient is similar to that of the $A4\lambda15$ wavy airfoil. The airfoil with tubercles is more efficient than the best-performing wavy configuration as shown in Figure B1 in Appendix B.

4.2.7 Amplitude-to-wavelength Ratio (A/λ)

It was shown in Section 4.2.5 that for a given tubercle amplitude, there is an optimum wavelength for a particular airfoil profile. Thus, it is informative to compare the performance of airfoils with the same A/λ ratio. These tubercle configurations also have the same mean tubercle sweep angle relative to the freestream flow and thus it is probable that this influences the strength of the streamwise vortices. While stall occurs at a lower angle of attack for the airfoil having larger amplitude and wavelength tubercles, the pre-stall lift and drag performance are almost identical for airfoils having the same A/λ ratio as shown in Figure 4.21 and Figure 4.22. The maximum lift coefficient, largest stall angle and lowest drag for this A/λ ratio are achieved by the airfoil with the smallest amplitude and wavelength tubercles. This is possibly because there is a more uniform boundary layer mixing, which leads to the greatest delay in separation.

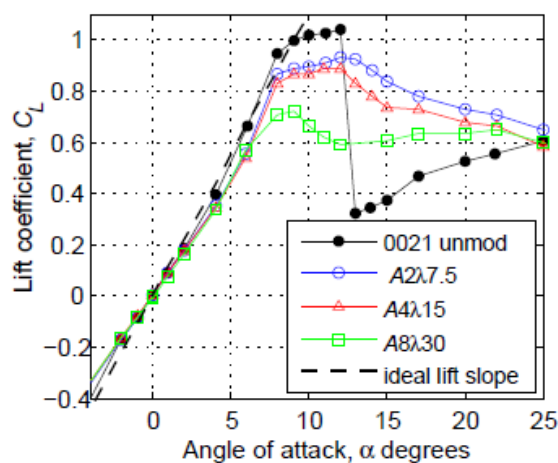


Figure 4.21 - Tubercle A/λ ratio and the effect on lift coefficient for NACA 0021, $Re = 120,000$.

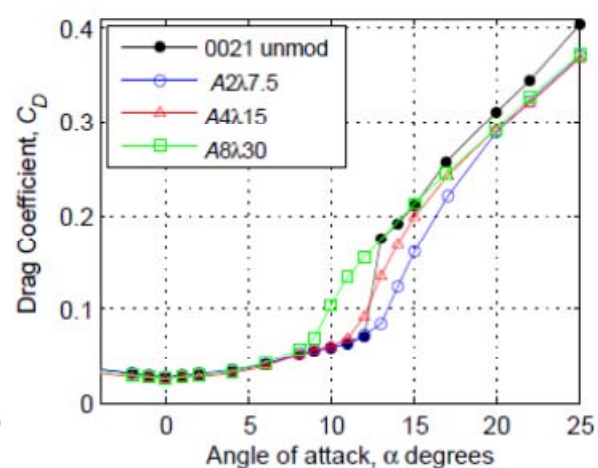


Figure 4.22 - Tubercle A/λ ratio and the effect on drag coefficient for NACA 0021, $Re = 120,000$.

Performance indicators including the maximum lift coefficient, stall angle and maximum lift to drag ratio have been plotted in Figure 4.23, Figure 4.24 and Figure 4.25 respectively for the NACA 0021 tubercle configurations. These plots indicate that there is

an optimum amplitude-to-wavelength ratio for the tubercle configurations tested which is $A/\lambda = 0.27$. The plots also highlight that the smallest amplitude and wavelength tubercle configuration demonstrates the most superior performance for this particular amplitude-to-wavelength ratio.

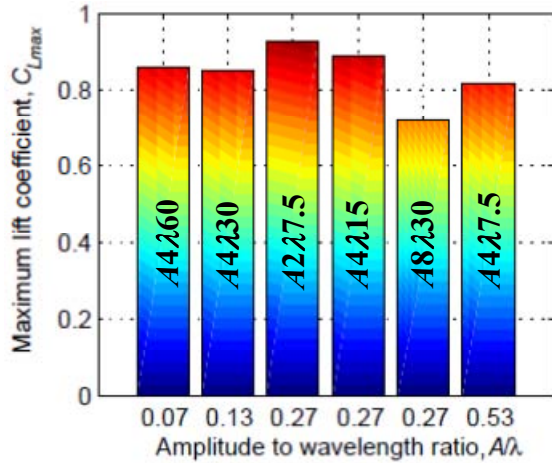


Figure 4.23 - The effect of amplitude-to-wavelength ratio on maximum lift coefficient, $Re = 120,000$.

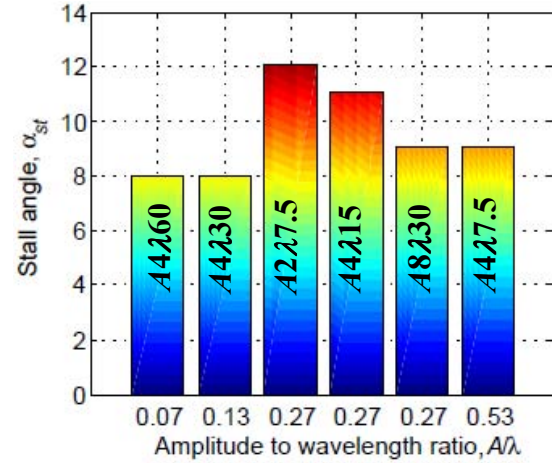


Figure 4.24 - The effect of amplitude-to-wavelength ratio on stall angle, $Re = 120,000$.

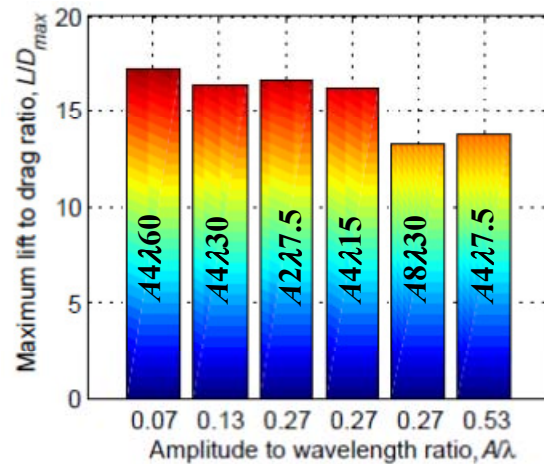


Figure 4.25 - The effect of amplitude-to-wavelength ratio on maximum lift to drag ratio, $Re = 120,000$.

4.2.8 Effective Device Height to Boundary Layer Thickness (h_{eff}/λ) Ratio

To determine the optimum tubercle amplitude for a given airfoil profile, the h_{eff}/δ ratio may be an important parameter. Finding the value of this parameter also facilitates comparison with studies on vortex generators. The effective height, h_{eff} , represents the height of the device as “seen” by the flow and calculated using $h_{eff} = A \sin \theta$. The

boundary layer displacement thickness, δ^* , is calculated at a chordwise distance corresponding to the tubercle amplitude of 2mm using the XFOIL code (Drela & Youngren, 2001). It is acknowledged that XFOIL will not replicate wind tunnel conditions exactly but it is used here since experimental data were not available. The boundary layer displacement thickness at a distance of 2mm from the leading edge for a NACA 0021 airfoil at $Re = 120,000$ and $\alpha = 10^\circ$ is $\delta^* = 0.06\text{mm}$ according to XFOIL calculations. For a laminar boundary layer, the ratio of boundary layer thickness to displacement thickness, $\delta/\delta^* \sim 2.9$ (Blasius, 1908). Neglecting pressure gradient effects near the leading edge of the airfoil, this gives $\delta \sim 0.2\text{mm}$. For the $A2\lambda7.5$ airfoil tubercle configuration at $\alpha = 10^\circ$, the value of $h_{eff} \sim A \sin \alpha \sim 2 \sin 10^\circ \sim 0.35\text{mm}$, giving $h_{eff}/\delta \sim 0.5$, which is consistent with conventional vortex generators (Lin, 2002).

Figure 4.26 to Figure 4.28 show the calculated ratio of effective tubercle height to boundary layer thickness corresponding to performance measures of maximum lift coefficient, stall angle and maximum lift to drag ratio. There is no clear correlation between the effective device height, h_{eff} , and airfoil performance, however, in general it seems that the smaller h_{eff} cases are more effective, with the most effective case overall being $A2\lambda7.5$. This is in contrast to the results for the wavy airfoils, where a larger effective height gave better performance characteristics. However, further optimization of the wavy parameters would be required to confirm this observation.

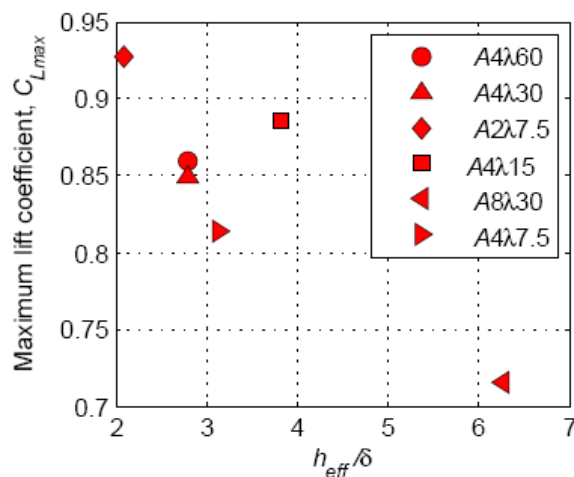


Figure 4.26 - Maximum lift coefficient and associated normalised effective tubercle height, $Re = 120,000$.

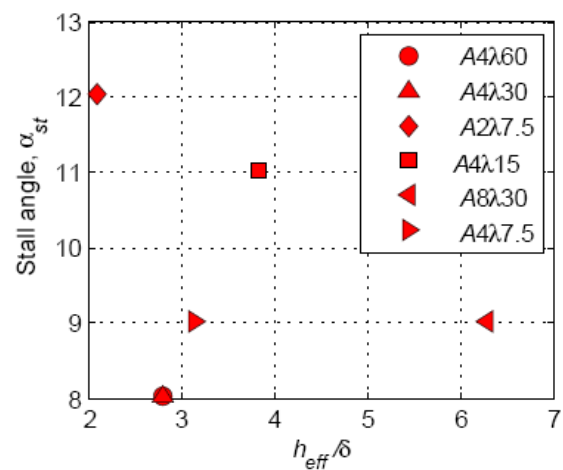


Figure 4.27 - Stall angle and associated normalised effective tubercle height, $Re = 120,000$.

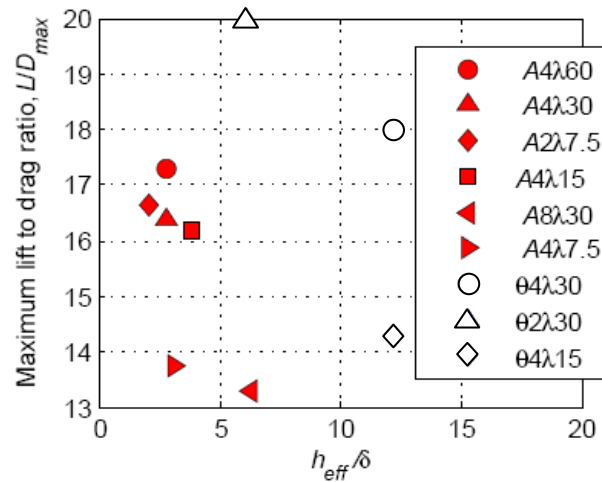


Figure 4.28 – Maximum lift-to-drag ratio and associated normalised effective tubercle height, $Re = 120,000$.

4.3 Half-Span Airfoils

Comparison of the full-span and half-span unmodified NACA 0021 airfoils shown in Figure 4.29 reveals that the half-span model generates a lower amount of lift and stalls at a higher angle of attack. Both of these characteristics are an expected consequence of downwash effects (Marchaj, 1979), whereby the effective angle of attack is reduced. Hence, the amount of lift generated for a given geometric angle of attack is lower than would be expected. In addition, the lift vector is tilted backward, leading to a further reduction in lift and creation of an additional drag component termed the “induced drag.”

Prandtl’s lifting line theory can be used to relate infinite-span lift data to finite-span data. To find the effective angle of attack for a finite-span model, it is necessary to subtract the downwash angle, $\Delta\alpha$, from the geometric angle of attack as shown in Equation (4.1).

$$\alpha' = \alpha - \Delta\alpha \quad (4.1)$$

where,

α' = actual angle of flow for finite-span airfoil

α = geometric angle of attack for semi-infinite span airfoil

$\Delta\alpha$ = angle induced by downwash from tip vortices, $\Delta\alpha = \left(\frac{C_L}{\pi AR}\right)\left(\frac{\pi}{180}\right)$.

Considering that the half-span model has one free end and one fixed end, the method of images is used to find the aspect ratio, giving $AR \sim 7$. It is evident from the “ideal 0021 unmod 3D” curve in Figure 4.29 that the lift curve slope of the half-span experimental results matches closely with the full-span results when the latter is plotted against α' from Equation (4.1). Moreover, there is good agreement with the ideal lift slope, which is also calculated using Prandtl’s lifting line theory according to Equation (4.2).

$$C_L \approx \frac{2\pi \left(\alpha + \frac{2h_{max}}{c} \right)}{1 + \frac{2}{AR}} \quad (4.2)$$

where,

α = angle of attack in Radians

h_{max} = camber

c = chord.

On the other hand, it is also evident that the finite-span model has an increasing lift-curve slope from $6^\circ \leq \alpha \leq 8^\circ$ and that the lift exceeds the ideal lift slope for a finite airfoil with aspect ratio, $AR \sim 7$. This indicates that the separation bubble identified in Section 4.2 is also present for the half-span NACA 0021 airfoil.

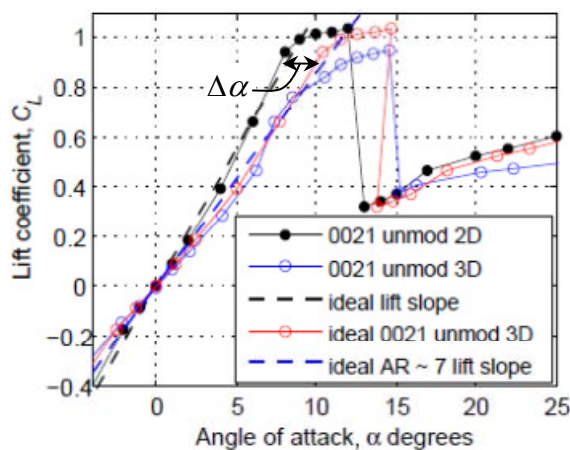


Figure 4.29 – Comparison of lift coefficient for full-span and half-span NACA 0021 airfoils, $Re = 120,000$.

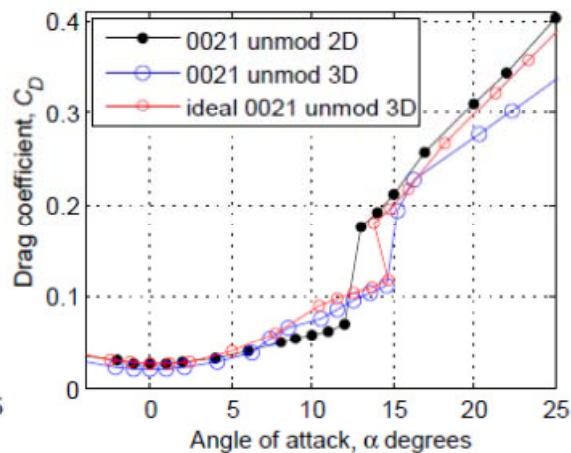


Figure 4.30 – Comparison of drag coefficient for full-span and half-span NACA 0021 airfoils, $Re = 120,000$.

Near the stall angle, the theoretical relation between the infinite and finite airfoil predicts a larger amount of lift for the finite airfoil than the experimental results as shown in Figure 4.29. Post-stall, the downwash angle, $\Delta\alpha$, appears to be under-predicted, giving the plot an unusual appearance near the stall angle and an over-estimation of the lift.

The induced drag component can be determined by taking into account the downwash velocity and constructing similar triangles for velocity and force. Hence, Equation (4.3) can be derived, giving the induced drag coefficient, C_{Di} :

$$C_{Di} = \frac{C_L^2}{\pi AR} \quad (4.3)$$

Subsequently, the drag coefficient for full-span data, C_{Do} , can be related to a finite-span drag coefficient, C_D using Equation (4.4).

$$C_D = C_{Do} + C_{Di} \quad (4.4)$$

Referring to Figure 4.30, there is negligible difference between the amount of drag generated by the full-span and half-span unmodified NACA 0021 airfoils at low angles of attack. As the angle of attack is increased, the amount of drag generated by the half-span airfoils is larger, presumably due to the induced drag component, which increases in magnitude as lift becomes higher. The extent of the low drag zone is greater for the finite-span airfoils because stall occurs at a higher angle of attack. The amount of drag predicted using Equation (4.4), shown by the “ideal 0021 unmod 3D” curve is very similar to the actual drag for the full-span case in the pre-stall regime. Post-stall, however, the predicted drag plot has an unusual appearance near the stall angle and an over-estimated drag due to under-prediction of the downwash angle, $\Delta\alpha$.

Results for the unmodified NACA 65-021 airfoil are shown in Figure 4.31 and Figure 4.32 and similar observations to those discussed above can be made. Some of the unusual characteristics associated with this airfoil are less pronounced for the half-span model such as the non-linearity of the lift curve slope, the magnitude of the negative lift and the relatively large changes in drag pre-stall.

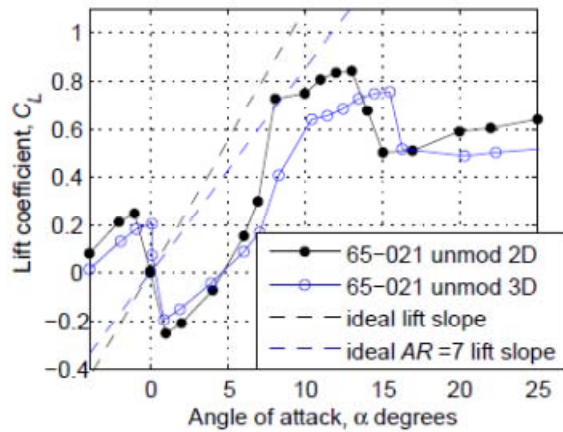


Figure 4.31 - Comparison of lift coefficient for full-span and half-span NACA 65-021 airfoils, $Re = 120,000$.

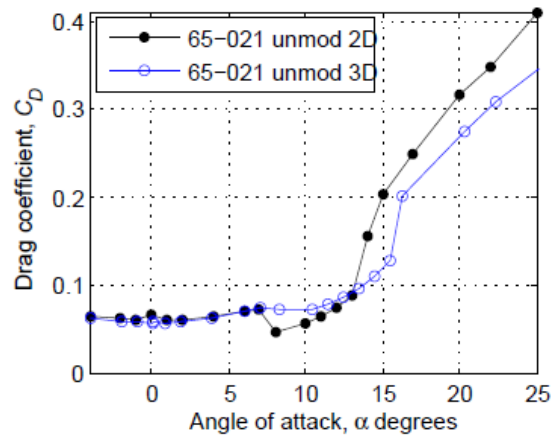


Figure 4.32 - Comparison of drag coefficient for full-span and half-span NACA 65-021 airfoils, $Re = 120,000$.

The fact that the amount of negative lift generated by the half-span airfoils is lower may indicate that three-dimensional effects reduce the extent of boundary layer thickening at the trailing edge.

4.3.1 Comparison of Results for Variation in Tubercle Amplitude

Figure 4.33 shows the differences in lift performance as the tubercle wavelength is kept constant while the amplitude is varied. It can be seen that for the half-span model, the maximum lift coefficient, stall angle and post-stall lift are higher for the smaller amplitude case, which is consistent with the full-span results. In addition, the difference in performance between the full-span and half-span models for the smaller amplitude tubercle configuration is more pronounced, which may be a consequence of the higher associated lift. However, in general, the variation in lift performance between full-span and half-span airfoils having these two tubercle configurations is comparable.

At low angles of attack, the difference in drag between the two tubercle configurations is negligible, which is evident in Figure 4.34. The smaller amplitude tubercle configuration then begins to experience a slightly higher amount of drag for the half-span case, which is related to the increase in the induced drag component associated with a higher lift. This explains the fact that the drag behaviour for the half-span model is slightly different from the full-span case.

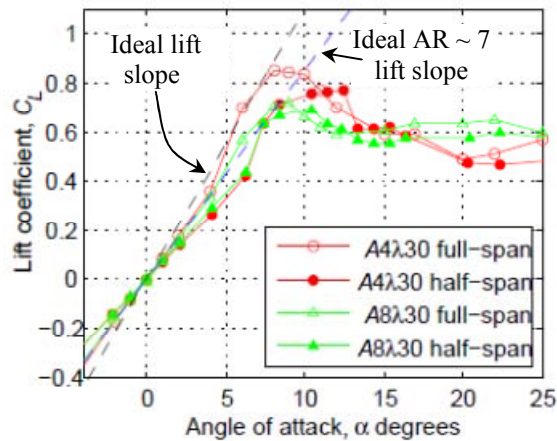


Figure 4.33 - Tubercle amplitude variation and lift performance for full-span and half-span NACA 0021 models, $Re = 120,000$.

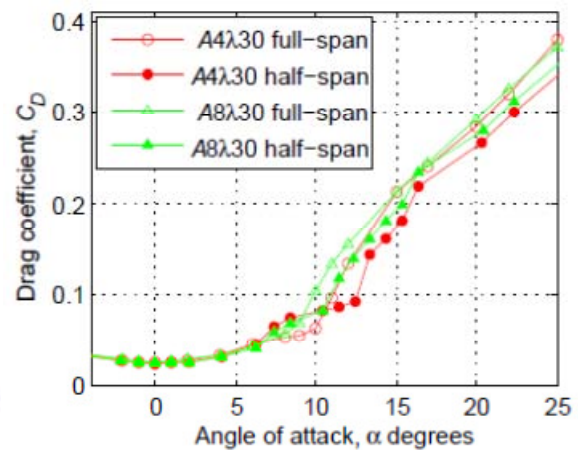


Figure 4.34 - Tubercle amplitude variation and drag performance for full-span and half-span NACA 0021 models, $Re = 120,000$.

By comparison, the larger-amplitude tubercle airfoil demonstrates higher drag near the stall angle. Post-stall, the drag associated with the smaller amplitude tubercles for the half-span model is lower than for the larger tubercles, which is consistent with the full-span results.

The half-span NACA 65-021 airfoils with tubercles are also found to have a lower maximum lift coefficient and higher stall angle when compared to the full-span cases, which is evident in Figure 4.35. The smaller amplitude configuration achieves the highest amount of lift at the largest angle of attack which is consistent with observations of the NACA 0021 airfoils as well as the full-span NACA 65-021 airfoils. Other performance variations for the half-span airfoils such as the reduction in negative lift and more gradual changes in lift and drag coefficient with angle of attack are consistent with the unmodified NACA 65-021 airfoil.

Figure 4.36 shows that the increase in drag attributed to the induced drag component appears to be negligible for the NACA 65-021 airfoils with tubercles in the pre-stall regime. The airfoil with small amplitude tubercles experiences the lowest drag for all angles of attack except $\alpha = 6^\circ$. At this angle of attack, there is a lower associated lift and it is possible that at this point, the airfoil has not yet recovered from the effects of the negative lift. After stall has occurred, the drag coefficient for the half-span models is lower, which was also observed for the NACA 0021 airfoils.

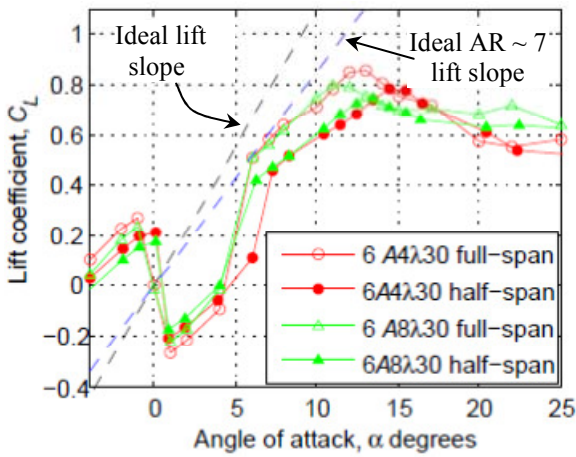


Figure 4.35 - Tubercle amplitude variation and lift performance for full-span and half-span NACA 65-021 models, $Re = 120,000$.

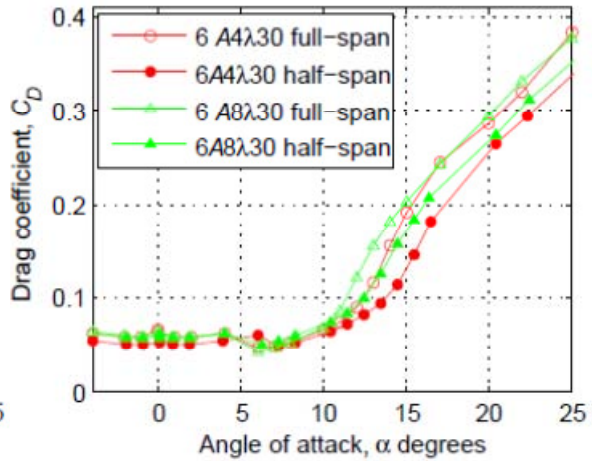


Figure 4.36 - Tubercle amplitude variation and drag performance for full-span and half-span NACA 65-021 models, $Re = 120,000$.

The efficiency of the half-span NACA 0021 airfoils is shown to be more consistently higher than the NACA 65-021 half-span airfoils as evident in Figure B3 and B9 of Appendix B.

Further reduction in tubercle amplitude leads to improved lift performance for half-span NACA 0021 airfoils as shown in Figure 4.37, which is consistent with trends observed for full-span airfoils. The tubercle configuration with the best lift performance for a half-span model is the $A2\lambda 7.5$ which has the smallest amplitude and wavelength tubercles. This configuration was also found to give superior performance for the full-span model.

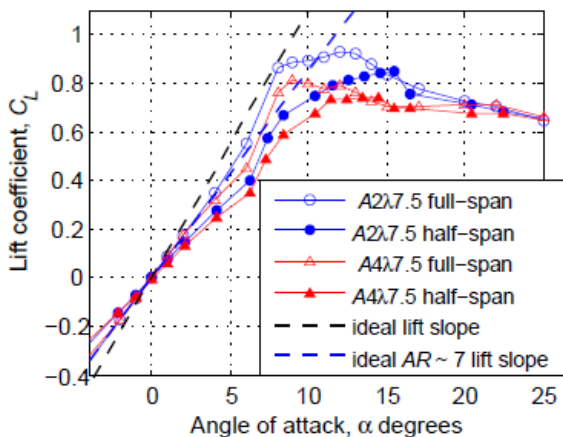


Figure 4.37 – Further reduction in tubercle amplitude and the effects on lift coefficient for NACA 0021 models, $Re = 120,000$.

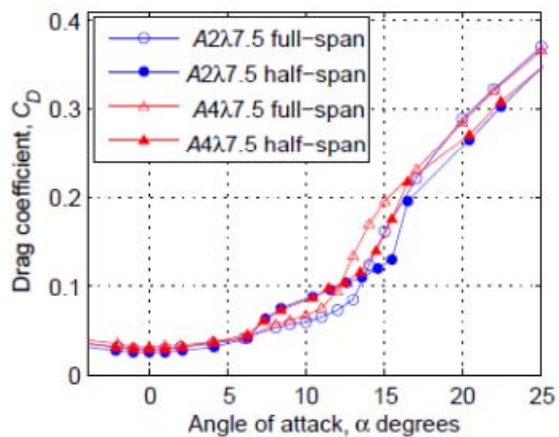


Figure 4.38 – Further reduction in tubercle amplitude and the effects on drag coefficient for NACA 0021 models, $Re = 120,000$.

The drag coefficient plot shown in Figure 4.38 for the half-span model with the smaller amplitude tubercle configuration reflects the increase in induced drag associated with higher lift generation. Consequently, the difference in drag between the two half-span models is negligible in the pre-stall regime rather than proving favourable for the small amplitude case as was observed for the full-span models. Post stall, the small amplitude tubercle configuration demonstrates improved performance.

4.3.2 Comparison of Results for Variation in Tubercle Wavelength

The results shown in Figure 4.39 and Figure 4.40 imply that three dimensional effects have negligible influence on the changes in performance which result from wavelength variation (note that figures have been stretched to lessen cluttering of the plots). This can be inferred by observing that for the half-span airfoil, the most successful tubercle configuration in terms of largest maximum lift coefficient, highest stall angle and lowest drag is the $A4\lambda15$ configuration. This is the same as the result for the full-span model. The relative difference between lift and drag for the various tubercle configurations is very similar when the half-span models are compared with the full-span models. However there is some increase in drag due to the induced drag component, which was discussed earlier in this section.

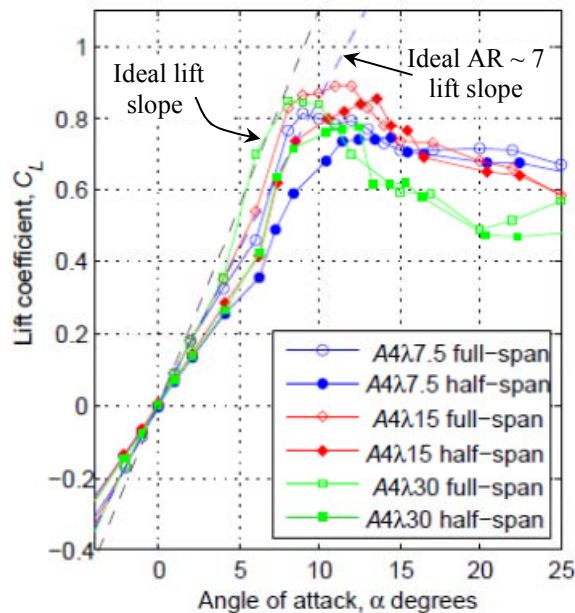


Figure 4.39 – Tubercle wavelength variation and lift performance for full-span and half-span NACA 0021 models, $Re = 120,000$.

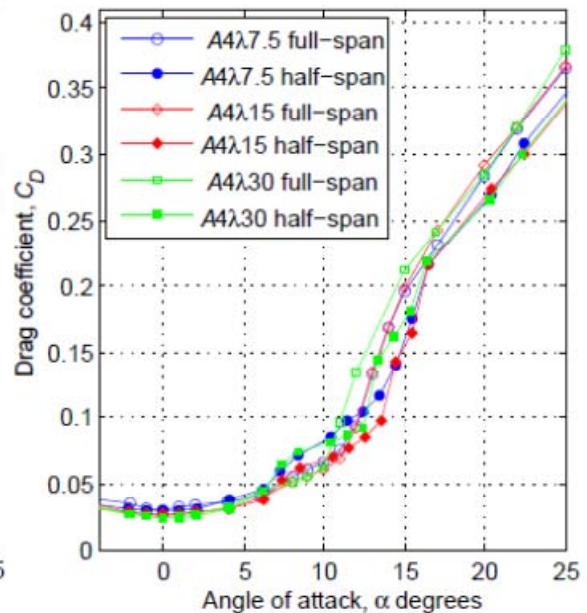


Figure 4.40 – Tubercle wavelength variation and drag performance for full-span and half-span NACA 0021 models, $Re = 120,000$.

4.3.3 Finite Effects on Wavy Airfoil Models

The wavy airfoils behave in a predictable manner when the span is reduced by half as depicted in Figure 4.41. Similar to the unmodified airfoils and the airfoils with tubercles, the stall angle is larger for the half-span models and the maximum lift coefficient is reduced. Additionally, the delay in stall angle increases the range of the low drag zone for the half-span models as shown in Figure 4.42. Note that both Figure 4.41 and Figure 4.42 have been stretched to make each plot more distinguishable. Comparison between the various wavy configurations shows that an increase in the lift curve slope occurs for the $\theta 2\lambda 30$ and $\theta 4\lambda 15$ cases for $6^\circ \leq \alpha \leq 8^\circ$. The associated induced drag component for these cases augments the total drag in this angle of attack range as shown in Figure 4.42. This implies that the mechanism which leads to increased lift generation adversely affects the drag.

Post-stall, the half-span models experience a lower drag which is consistent with the results for the unmodified airfoils and the airfoils with tubercles. Comparing the different wavy configurations indicates that the $\theta 4\lambda 15$ airfoil demonstrates the best lift and drag performance overall, which is the same for the full-span models.

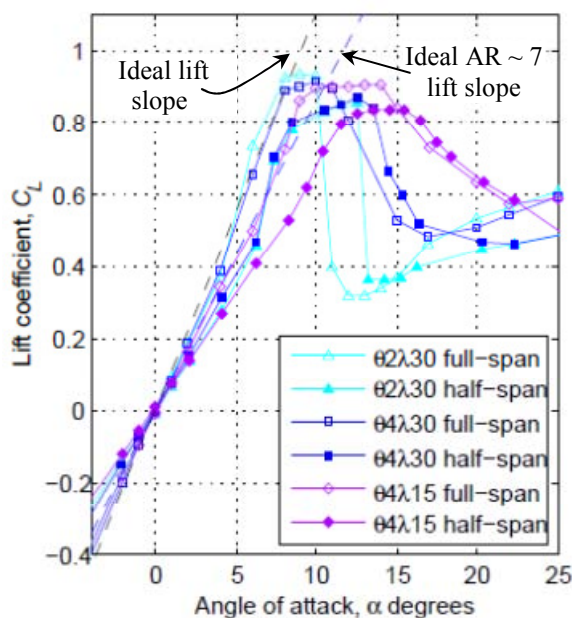


Figure 4.41 – Wavy airfoils and lift performance for full-span and half-span models, $Re = 120,000$.

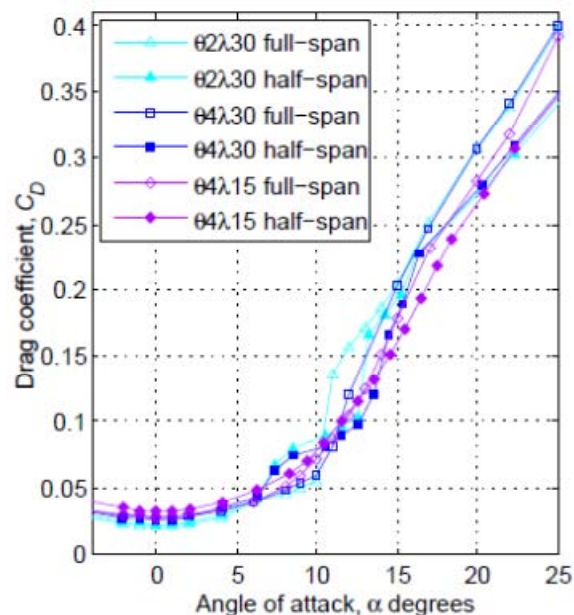


Figure 4.42 - Wavy airfoils and drag performance for full-span and half-span models, $Re = 120,000$.

4.4 Quantification of Three-Dimensional Effects

An investigation was carried out to verify that for the half-span experiments, the airfoil wing tip was located far enough away from the test section ceiling to ensure unimpeded development of the wing-tip vortices. This involved measuring the lift and drag performance for selected airfoils mounted with a gap of approximately one chord-length (0.85 span) between the wing tip and the test section ceiling. Results were collected for the unmodified NACA 0021 airfoil in addition to the best performing tubercle and wavy configuration, which are the $A2\lambda7.5$ and $\theta4\lambda15$, respectively. The lift and drag coefficients of the 0.85-span model were converted to equivalent half-span coefficients using Prandtl's lifting line theory according to Equations (4.1) and (4.3). Figure 4.43 to Figure 4.48 show that the curves generally match well and that differences are within uncertainty limits discussed in Section 4.5. In addition, Prandtl's lifting line theory is derived for an elliptical lift distribution so the results are not expected to match perfectly. On the other hand, it appears that the effects of the separation bubble are more significant for the half-span unmodified NACA 0021 airfoil and the half-span modified airfoil with $A2\lambda7.5$ tubercle configuration for $6^\circ \leq \alpha \leq 10^\circ$.

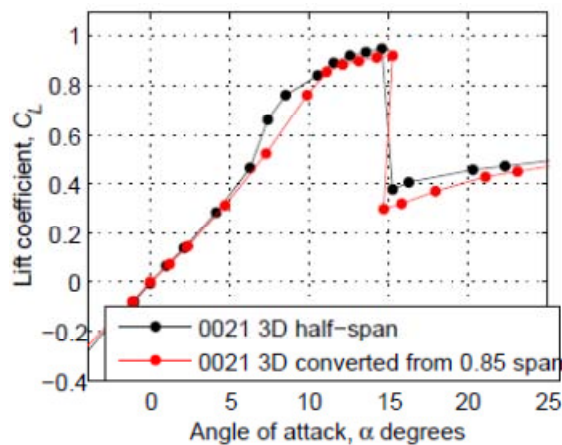


Figure 4.43 - Influence of wall proximity on three-dimensional effects affecting the lift force for unmodified NACA 0021 airfoil, $Re = 120,000$.

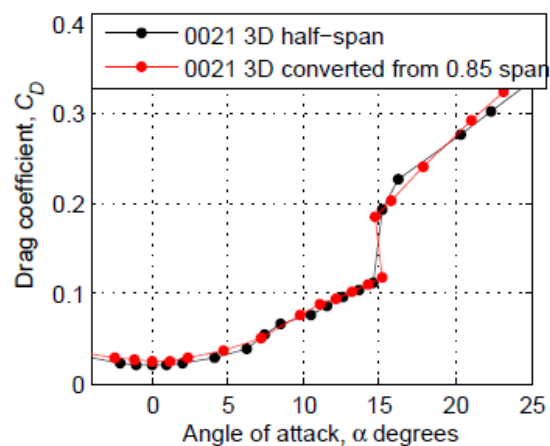


Figure 4.44 - Influence of wall proximity on three-dimensional effects affecting the drag force for unmodified NACA 0021 airfoil, $Re = 120,000$.

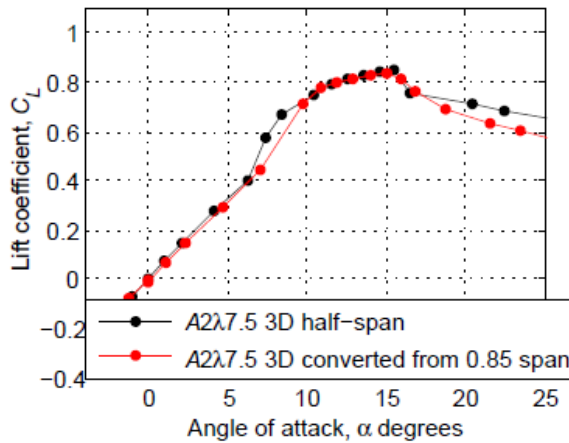


Figure 4.45 - Influence of wall proximity on three-dimensional effects affecting the lift force for $A2\lambda 7.5$ tubercle configuration, $Re = 120,000$.

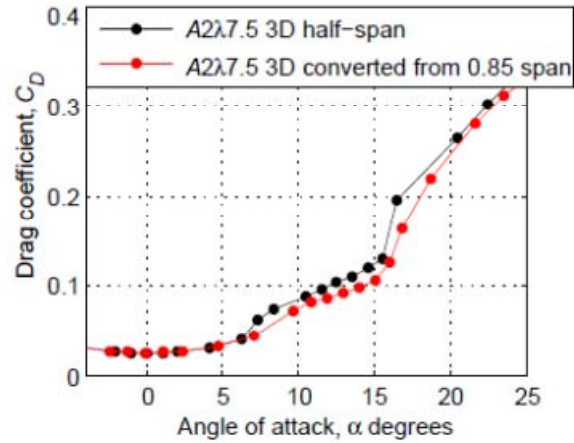


Figure 4.46 - Influence of wall proximity on three-dimensional effects affecting the drag force for $A2\lambda 7.5$ tubercle configuration, $Re = 120,000$.

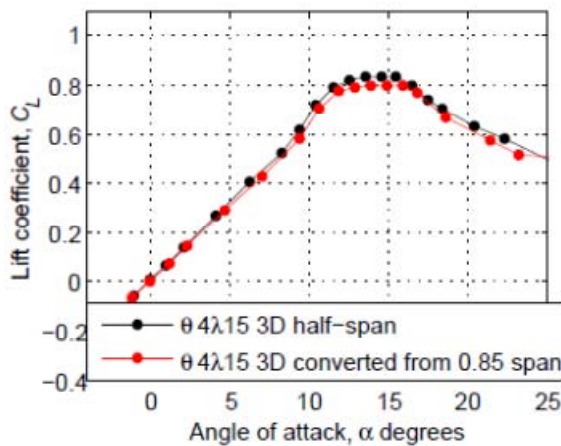


Figure 4.47 - Influence of wall proximity on three-dimensional effects affecting the lift force for $\theta 4\lambda 15$ wavy configuration, $Re = 120,000$.

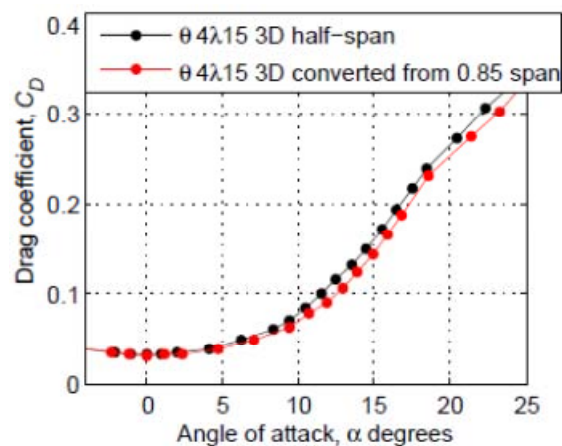


Figure 4.48 - Influence of wall proximity on three-dimensional effects affecting the drag force for $\theta 4\lambda 15$ wavy configuration, $Re = 120,000$.

Overall, it can be concluded that a gap of one chord length is sufficient to ensure that the test-section ceiling has negligible impact on the downwash effects associated with a finite-span model. Hence, a half-span model, with a larger wall clearance, can accurately demonstrate three-dimensional effects for the experimental set-up in this study.

4.5 Analysis of the Uncertainty Associated with Force Measurements

The uncertainty in force measurement was analysed for all airfoils investigated, however, since there was not a large variation in the uncertainty, not all cases are presented and discussed in this section. The focus here is on the uncertainty associated with full and half-span models of the unmodified airfoils as well as the best performing tubercle and wavy configuration (*A2 λ 7.5* and *θ 4 λ 15*, respectively). An uncertainty analysis for the tripped NACA 65-021 full-span model is also included.

According to Bentley (2005), the current international convention is that the uncertainty is evaluated such that there is a 95% confidence interval. The uncertainty distribution can be represented as a Gaussian function, and hence the 95% confidence interval is equivalent to ± 1.96 standard deviations about the mean. In this section, the 95% confidence interval convention is adopted for all uncertainty estimates and hence the plotted uncertainties reflect this condition. Figure 4.49 and Figure 4.50 show plots of the lift and drag coefficient against angle of attack and the associated uncertainty at each attack angle is indicated with errorbars.

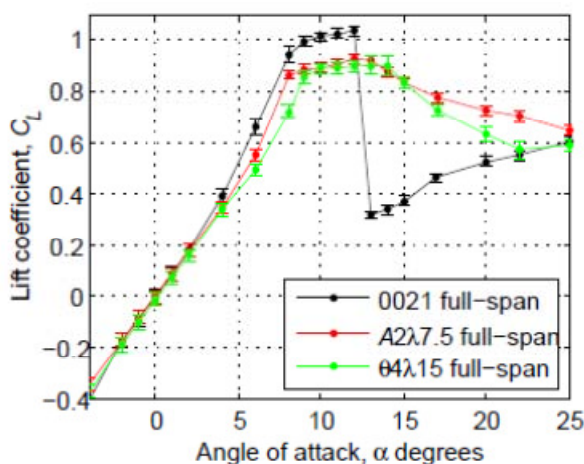


Figure 4.49 – Lift coefficient uncertainty analysis for NACA 0021 full-span models, $Re = 120,000$.

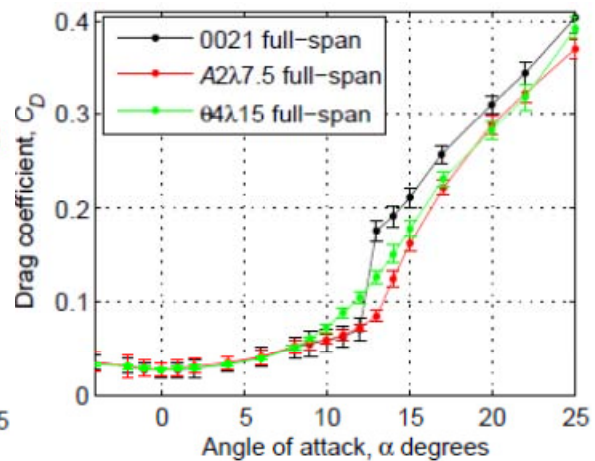


Figure 4.50 – Drag coefficient uncertainty analysis for NACA 0021 full-span models, $Re = 120,000$.

It is important to note that the uncertainties are relatively insignificant compared to the effects of incorporating tubercles or waviness. This verifies the observations described in Sections 4.2 - 4.4, since the performance differences between models which were

highlighted are not a result of uncertainty in the measurements. For low angles of attack, it can be seen that the difference in performance is smaller than the associated uncertainties, therefore accurate conclusions relating to performance variation cannot be drawn.

In order to visualise the relative contribution of each uncertainty to the overall uncertainty value, bar charts are shown for one pre-stall angle of attack ($\alpha = 6^\circ$) and one post-stall angle ($\alpha = 20^\circ$). The values indicated on the charts ($c_{iu}(x_i)$) have not been multiplied by the coverage factor to yield the standard uncertainty. However, their relative values can be compared to determine the most significant sources of uncertainty in both the pre-stall and post-stall regimes. The uncertainty sources highlighted in Section 3.3.11 will be abbreviated according to Table 4.1 below.

Table 4.1 – Nomenclature used in figures showing uncertainty in force measurements.

Statistical uncertainties in freestream velocity measurement	wstd
Inaccuracy of freestream velocity measurement	w
Statistical uncertainties associated with force transducer data	LCstd
inaccuracy of the force transducer	LC
Rotary table positioning uncertainties	rt

Figure 4.51 shows that the most significant pre-stall uncertainty in lift coefficient for all NACA 0021 airfoils is attributed to the rotary table positioning. The steep lift curve at pre-stall angles creates a high sensitivity to uncertainty, which explains the relatively high value of uncertainty.

Post-stall, the random wind tunnel uncertainty is the largest source of uncertainty in lift coefficient for the unmodified NACA 0021 airfoil and the $A2\lambda7.5$ tubercle configuration as evident in Figure 4.52. The associated uncertainty and sensitivity coefficient are constants as described in Section 3.3.11 and hence its prominence is related to the relative reduction of the other uncertainties. Note that the values are different in Figure 4.52 since *relative uncertainties* have been plotted. For the $\theta4\lambda15$ wavy configuration, there is a larger uncertainty associated with the standard deviation in measurements with the load cell. This could be explained by the existence of streamwise vortices post-stall, which cause larger data fluctuations, hence reducing the repeatability of the average force measurements.

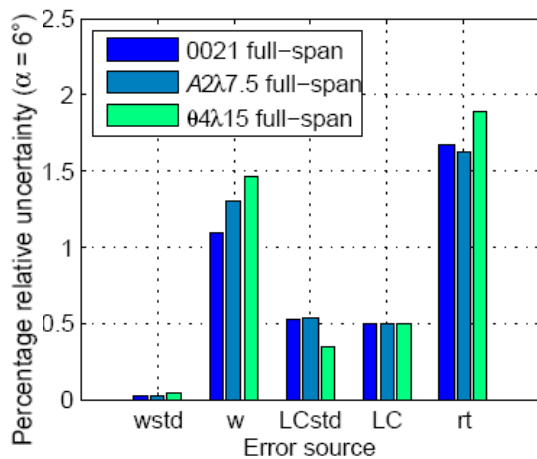


Figure 4.51 – Relative pre-stall contribution of uncertainties in lift coefficient for NACA 0021 airfoils, $Re = 120,000$.

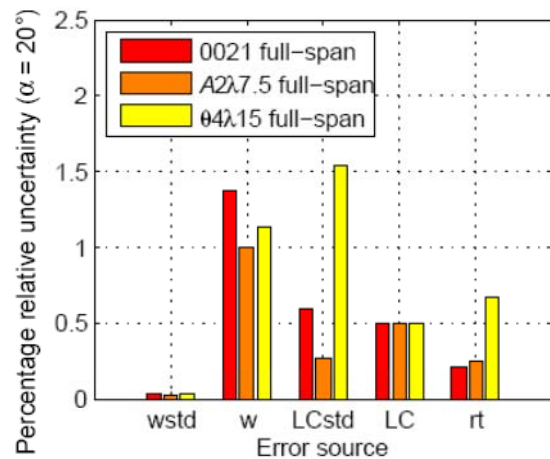


Figure 4.52 – Relative post-stall contribution of uncertainties in lift coefficient for NACA 0021 airfoils, $Re = 120,000$.

Similar bar charts have also been created to show the relative contribution of uncertainties to the drag coefficient. Figure 4.53 indicates that the standard deviation in the load cell measurements is the most significant source of uncertainty prior to stall for the unmodified NACA 0021 airfoil and the $A2\lambda7.5$ tubercle configuration. Since the measured drag is an order of magnitude lower than the lift, it is expected that the data fluctuations would have a greater impact on the calculated average force, adversely affecting repeatability of the measurements. Unexpectedly, this uncertainty is not significant for the $\theta4\lambda15$ wavy airfoil. In the post stall regime, as depicted in Figure 4.54, the relative uncertainties for all airfoils are generally similar however the contribution from the random uncertainty in the load cell measurements is the most significant.

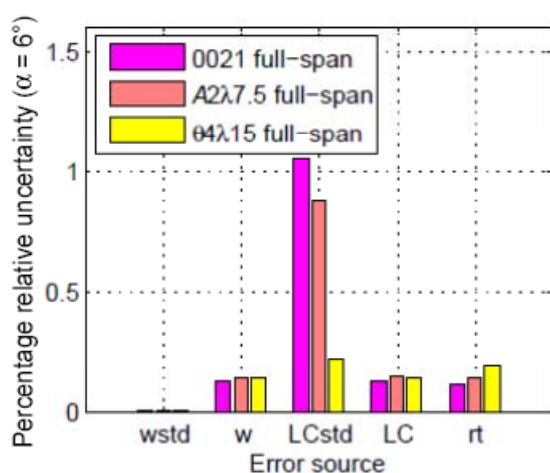


Figure 4.53 – Relative pre-stall contribution of uncertainties in drag coefficient for NACA 0021 airfoils, $Re = 120,000$.

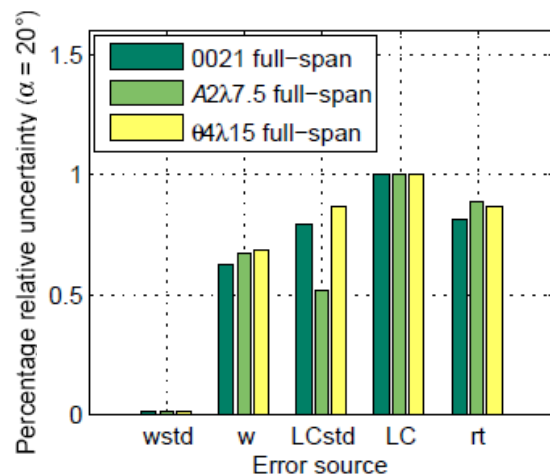


Figure 4.54 – Relative post-stall contribution of uncertainties in drag coefficient for NACA 0021 airfoils, $Re = 120,000$.

The overall uncertainty calculated for the half-span NACA 0021 airfoils is similar to that for the full-span models and hence will not be shown here. With regards to the relative contribution of uncertainties, the most significant changes were noted in the statistical uncertainty of the load cell. This is attributed to the increased unsteadiness associated with the presence of the wing tip vortex at the free end as well as the reduction in the measured forces, which led to a decrease in signal-to-noise ratio of the measurements.

Uncertainties were also calculated for the NACA 65-021 airfoils and errorbars are shown in Figure 4.55 and Figure 4.56 for three cases pertaining to the unmodified airfoil: full-span, full-span with boundary layer trips and half-span. It can be seen that there is a significant reduction of uncertainties at the majority of attack angles when boundary layer trips are utilised. This reflects the measurement uncertainty caused by instabilities in the boundary layer such as separation bubbles. It is also evident that these instabilities have a greater effect on the lift than the drag.

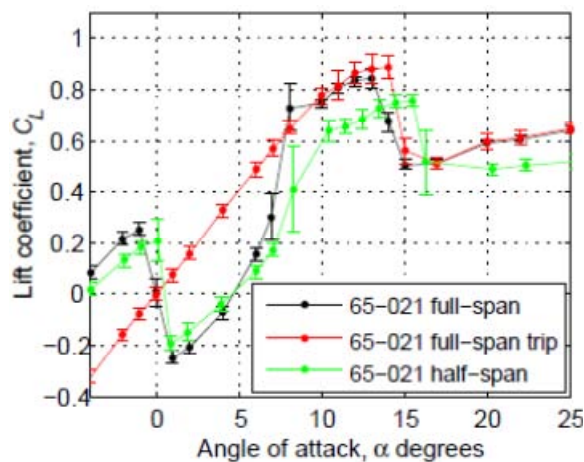


Figure 4.55 - Relative pre-stall contribution of uncertainties in lift coefficient for NACA 65-021 airfoils, $Re = 120,000$.

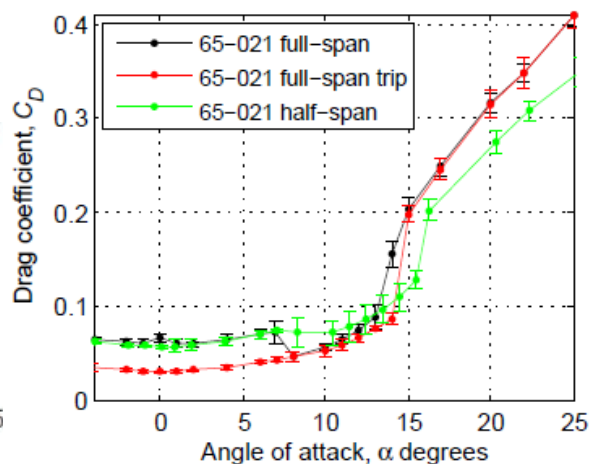


Figure 4.56 - Relative pre-stall contribution of uncertainties in drag coefficient for NACA 65-021 airfoils, $Re = 120,000$.

Since the largest uncertainties are observed for the lift coefficient of the NACA 65-021, an understanding of their relative contribution is beneficial. The angles of attack with the largest associated uncertainty are chosen in both the pre-stall and post-stall regimes and these angles correspond to $\alpha = 8^\circ$ and $\alpha = 17^\circ$. It can be seen in Figure 4.57 and Figure 4.58 that the dominant uncertainty for the half-span airfoil both before and after stall is the statistical load cell uncertainty most likely caused by a high level of turbulence in the airfoil's wake.

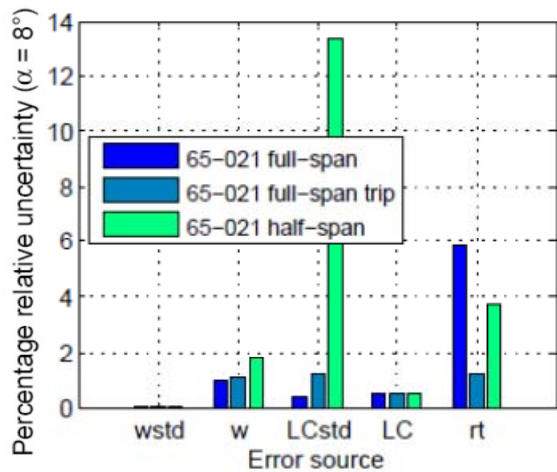


Figure 4.57 - Relative pre-stall contribution of uncertainties in lift coefficient for NACA 65-021 airfoils, $Re = 120,000$.

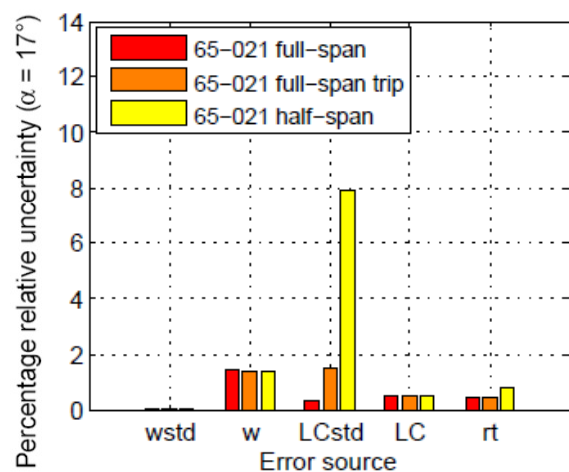


Figure 4.58 - Relative pre-stall contribution of uncertainties in lift coefficient for NACA 65-021 airfoils, $Re = 120,000$.

In the pre-stall regime, the rotary table positioning uncertainty is significant for the full-span airfoil because the slope of the lift coefficient plot is very steep around this angle, leading to a high sensitivity coefficient. Overall, the uncertainties are greatly reduced through incorporation of boundary layer trips, which leads to a much more linear lift curve slope as well as a reduction in instability at certain angles of attack.

4.6 Summary

The results indicate that the influence of tubercles varies depending on the airfoil profile under investigation. For a profile with maximum thickness located at 50% of the chord (NACA 65-021), tubercles have negligible effect on the lift performance in the pre-stall regime and are beneficial in the post-stall regime. On the other hand, for the NACA 0021, which has maximum thickness at 30% of the chord, increased lift performance in the post-stall regime comes at the expense of degraded lift performance in the pre-stall regime. However, it was found that through optimising the amplitude and wavelength of the tubercles, pre-stall lift performance approaches the values attained by the unmodified airfoil and post-stall performance is much improved.

For both of the airfoils investigated in this study, the maximum lift coefficient was achieved with the smallest amplitude tubercles. Reducing the wavelength improved the lift performance until a certain limit was reached, beyond which the performance was degraded for a given tubercle amplitude. Thus, it is expected that there exists an optimal

amplitude-to-wavelength ratio and, when this is coupled with the most successful amplitude, the best airfoil performance characteristics can be achieved. In this study the optimum tubercle configuration was the $A2\lambda7.5$, which demonstrated both superior lift and drag in comparison to the other models with tubercles. However, for applications where the post-stall lift characteristics need to be optimised, it was found that relative to the maximum lift coefficient, the most gradual stall was achieved by airfoils having the largest amplitude tubercles. Reducing the wavelength also improved the post-stall lift characteristics and, in fact, seemed to have a greater influence.

The results suggest that tubercles behave in a similar fashion to counter-rotating vortex generators, and that the optimum tubercle amplitude and wavelength bear strong similarity to the optimum vortex generator spacing and height. In addition, the device angle has been found to be an important performance parameter for both vortex generators (Lin, 2002) and tubercles. In the latter case, the device angle is defined as the mean tubercle sweep angle, which is governed by the A/λ ratio. Adequate spacing between device pairs of vortex generators has been identified as a necessary condition to minimize vortex interference (Ashill, Fulker, & Hackett, 2002). Since it was identified in Section 4.2.5 that there is a limitation to performance improvements that can be attained through reducing the wavelength between tubercles, it is postulated that the same phenomenon is responsible. Additionally, the vortex generating mechanism would become more prominent as the angle of attack and hence h_{eff} increases, which is a feasible explanation for the fact that the airfoils with tubercles produce more lift in the post-stall regime.

The relative performance of airfoils with tubercles compared to an unmodified airfoil is similar for full-span and half-span models with no sweep or taper. This implies that the presence of tubercles does not significantly affect the formation of wing-tip vortices for these airfoils. However, it should be noted that the effective aspect ratio of the airfoils of $AR \sim 7$ would lead to a relatively low induced drag component. Variation of the tubercle amplitude and wavelength leads to similar differences in performance for the half-span and full-span airfoils. In both cases, the most successful configuration is the one with the smallest amplitude and wavelength tubercles. It is believed that tubercles may offer more obvious benefits for airfoils with sweep and/or taper or rotating airfoils where there is a

much larger amount of span-wise flow. In comparison to previous studies where tubercles improved the lift performance of the airfoils under investigation, experiments were carried out at a much lower Reynolds number. Separation characteristics are more unpredictable at such low Reynolds numbers and the positive benefits to be attained with tubercles may be compromised.

The wavy airfoils demonstrated similar performance characteristics to the airfoils with tubercles, suggesting a similar affect on the flow. For the limited range of wavy airfoils available, the maximum lift coefficient was lower for the wavy airfoils compared to the unmodified NACA 0021 airfoil, however, analogous to the results with tubercles, the post-stall lift was favourable. In addition, the smallest wavelength configuration achieved the highest maximum lift coefficient. On the other hand, conversely to the results with tubercles, an increase in the effective device height realised by increasing the angle of waviness led to improved performance. Thus, the $\theta 4\lambda 15$ wavy configuration demonstrated the best overall performance.

Chapter 5

Surface Pressure Characteristics



5.1 Introduction

This chapter includes results from surface pressure measurements which were obtained using static pressure taps positioned at specific chordwise locations as discussed in Section 3.4.3. Different airfoils are investigated including the unmodified NACA 0021 and NACA 65-021 profiles as well as the NACA 0021 profile with the $A8\lambda30$ tubercle configuration. The selection of NACA 0021 airfoils enables a comparison to be made between one tubercle configuration and a baseline case. On the other hand, the NACA 65-021 airfoil is investigated to enhance understanding of the negative lift behaviour associated with this airfoil.

The measured chordwise pressure distributions are interpreted to reveal the existence of separation bubbles, which are responsible for the non-linearity of the pre-stall lift curve slope as well as the negative lift generation described in Section 4.2.2. A typical separation bubble is illustrated in Figure 5.1 and it can be seen that the laminar boundary layer separates to form a region of recirculation which is followed by reattachment of a turbulent shear layer. Since boundary layer flows and separation bubbles are complicated and difficult to predict at low Reynolds numbers (Simons, 1999) these measurements are important for understanding the unusual characteristics associated with the lift curves discussed in Chapter 4.

NOTE:
This figure/table/image has been removed
to comply with copyright regulations.
It is included in the print copy of the thesis
held by the University of Adelaide Library.

Figure 5.1 – Sketch of laminar separation bubble (Horton, 1968).

Pressure contour plots highlight the pressure distribution as a function of the angle of attack. This provides information about the chordwise movement of the minimum pressure point on the suction surface and the maximum pressure location on the pressure surface as the angle of attack is varied.

In addition, measurement of the chordwise pressure distribution at different spanwise locations on the airfoil with tubercles facilitates identification of the pressure variations associated with the presence of the leading edge protuberances. The chordwise pressure integral is calculated to obtain lift coefficient plots, which indicate lift performance at different spanwise cross-sections.

In this chapter, discussion will centre on gauge pressure. Positive pressure is therefore above the freestream static pressure and negative pressure is less than the freestream static pressure.

5.2 Unmodified NACA 0021 Airfoil

5.2.1 Analysis of Pressure Distribution

The pressure coefficient, C_p , is plotted as a function of the normalised chordwise position for the NACA 0021 airfoil in Figure 5.2 (a)-(h). Experimental measurements are compared to calculated values obtained using the XFOIL code (Drela & Youngren, 2001). The free transition model is specified using the standard e^n method, which predicts transition in situations where the growth of Tollmien-Schlichting waves via linear instability is the dominant mechanism for initiating transition (Drela & Youngren, 2001). This assumption is valid for the majority of applications involving airfoils (Drela & Youngren, 2001). For this analysis, the standard value of $n = 9$ is selected since this corresponds to the turbulence level associated with an “average wind tunnel.”

At angles of attack before stall, the experimental and XFOIL data are in good agreement. The suction and pressure peaks appear to be slightly lower for the experimental results due to limitations in spatial resolution associated with pressure tap positioning. In addition, the experimental results indicate that the pressure surface experiences a higher degree of suction after the initial pressure peak near the leading edge. Whereas XFOIL predicts that there is negligible suction on the pressure surface after $\alpha = 8^\circ$ as evident in Figure 5.2 (d), the experimental data show that there is a certain degree of suction present on the pressure surface at all angles of attack (negative C_p values). In addition, there is poor agreement between XFOIL and the experimental data with regards to the stall angle. This is attributed to using an inviscid solution for the wake trajectory in the XFOIL code to avoid unreasonably long calculation times (Drela & Youngren, 2001).

The existence of a separation bubble is reflected in both the experimental and XFOIL data and can be distinguished at $\alpha = 0^\circ$ by the departure of these results from the theoretical curve obtained using thin airfoil theory (Abbott and von Doenhoff, 1959) as shown in Figure 5.2 (a). The separation bubble region can also be identified as the section of the suction curve where the pressure gradient starts to decrease, almost reaching a value of zero. After the separation bubble, the pressure gradient increases rapidly and then reaches the value which would be predicted in the absence of the separation bubble.

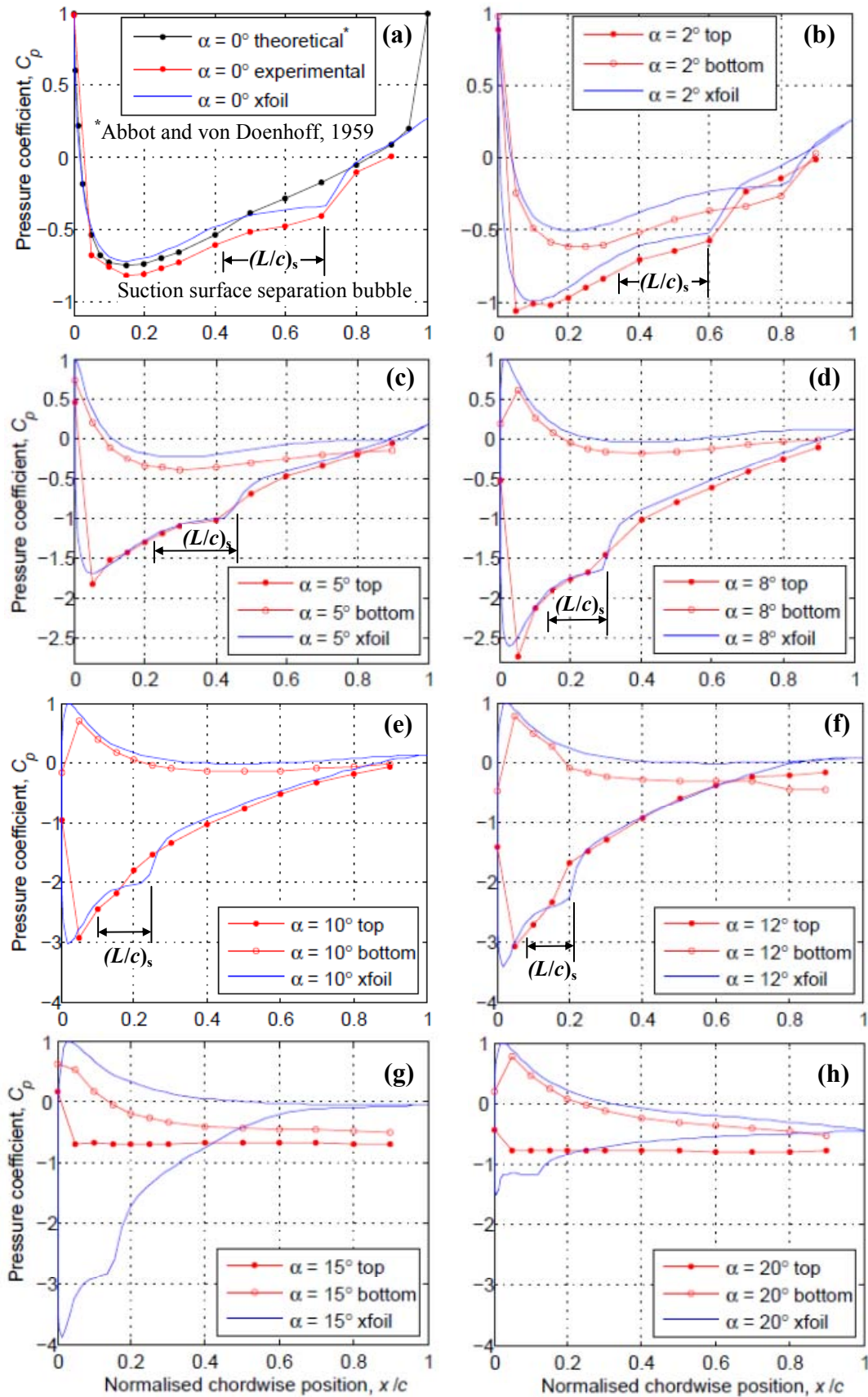


Figure 5.2 – Normalised pressure distribution plots for NACA 0021 unmodified airfoil, where “top” refers to suction surface and “bottom” refers to pressure surface, $Re = 120,000$. Separation bubble locations found from XFOIL skin friction data are indicated.

Since there is reasonable agreement between the pre-stall pressure distributions obtained experimentally and using the XFOIL code, it is possible to predict the non-dimensional location, x/c , and length, L/c , of the separation bubble more accurately by analysing the friction coefficient data generated by XFOIL. Plots of the friction coefficient against the normalised chordwise position for the suction surface are shown in Figure 5.3 and Figure 5.4. A summary of the separation bubble characteristics for the suction surface according to XFOIL data is provided in Table 5.1. For the angles of attack shown in Table 5.1, the flow does not separate downstream of the separation bubble and for $\alpha > 12^\circ$, separation occurs without reattachment.

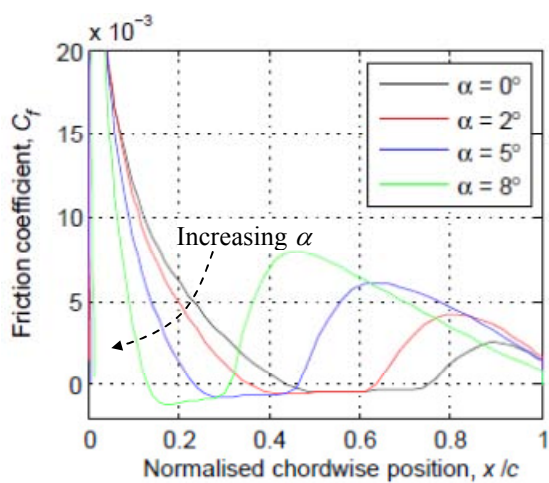


Figure 5.3 – Friction coefficient against chordwise position for NACA 0021 at low angles of attack (suction surface), $Re = 120,000$.

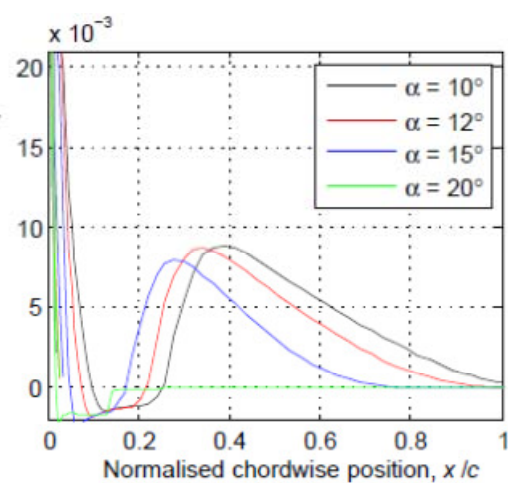


Figure 5.4 - Friction coefficient against chordwise position for NACA 0021 at high angles of attack (suction surface), $Re = 120,000$.

Table 5.1 – Chordwise extent of laminar separation bubble determined from the friction coefficient for the suction surface (NACA 0021), $Re = 120,000$.

Angle of attack, α	Chordwise extent of separation bubble	Normalised length of suction separation bubble, $(L/c)_s$
0°	$0.44 \leq x/c \leq 0.73$	0.29
2°	$0.36 \leq x/c \leq 0.62$	0.26
5°	$0.23 \leq x/c \leq 0.44$	0.21
8°	$0.14 \leq x/c \leq 0.30$	0.16
10°	$0.10 \leq x/c \leq 0.25$	0.15
12°	$0.08 \leq x/c \leq 0.22$	0.12

It should be noted that at higher pre-stall angles of attack, the XFOIL pressure distributions showed more prominent separation bubble effects than the corresponding experimental results. This characteristic is evident in Figure 5.2 (d-f) and it is possible that the extent of the separation bubbles for these angles of attack is not as significant as suggested by the XFOIL results.

The separation bubble on the suction surface is predicted to move towards the leading edge as the angle of attack is increased and there is a corresponding reduction in bubble length of 50% from $\alpha = 0^\circ$ to $\alpha = 12^\circ$. The apparent camber of the airfoil is increased by the presence of the separation bubble since it is large enough to cause the external flow to be diverted over the suction surface. As the bubble moves forward, there is an associated benefit of increased lift since an airfoil with maximum camber point close to leading edge develops a high maximum lift coefficient (Simons, 2002). Hence at high angles of attack, the slope of the lift curve can exceed theoretical predictions (Simons, 2002). This characteristic was highlighted in Section 4.2.1 with reference to the NACA 0021 force results, where it was found that the lift curve slope increased for angles of attack in the range $5^\circ \leq \alpha \leq 8^\circ$. Both the experimental and XFOIL data indicate the existence of a separation bubble at $\alpha = 5^\circ$ and $\alpha = 8^\circ$ as shown in Figure 5.2 (c) and (d).

The increase in lift curve slope beyond the theoretical maximum of $k = 2\pi$ can be explained in more detail through consideration of the lift coefficient for a cambered airfoil, given by Equation (5.1) and shown in Figure 5.5.

$$C_L = k \left(\alpha + \frac{2h_{max}}{c} \right) \quad (5.1)$$

It can be seen that when a separation bubble exists on an airfoil, the lift curve slope corresponds to that for a cambered airfoil. Hence, the data points exist on curves with differing values of $2h_{max}/c$. Connection of the data points corresponding to varying degrees of camber leads to an increasing lift curve slope as highlighted in Figure 5.5.

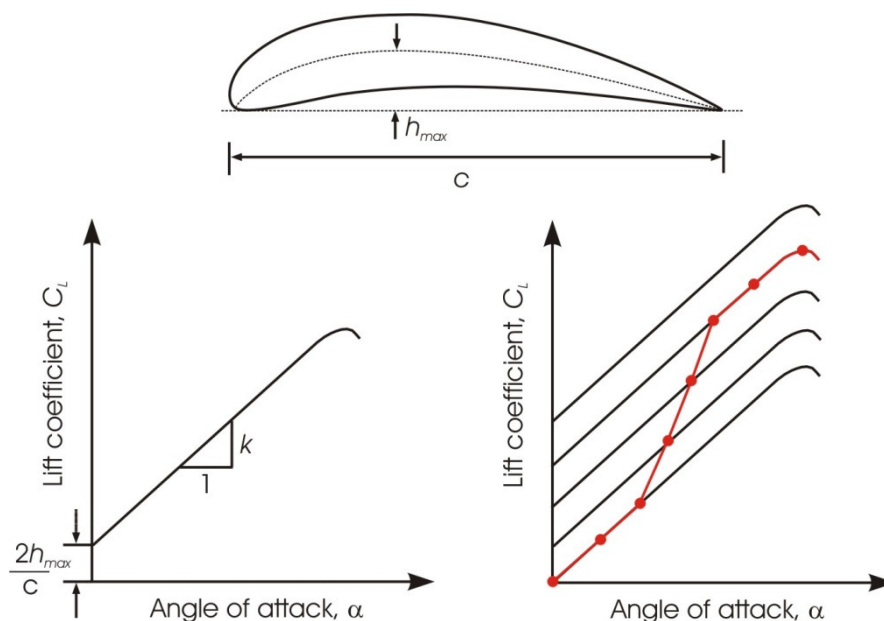


Figure 5.5 – Explanation for increase in lift curve slope beyond theoretical maximum.

A further implication of the presence of the separation bubble was the effect that it had on the stall characteristic of the NACA 0021 airfoil. The sudden loss in lift associated with the onset of stall can be explained by the “bursting” of the short separation bubble (Hoerner, 1985). Generally, thick airfoils such as the NACA 0021 experience a more gradual stall since boundary layer separation is initiated from the trailing edge and gradually proceeds towards the leading edge as the angle of attack is increased (Anderson Jr., 2007). However, when the boundary layer separation point is coincident with the edge of the separation bubble, the flow no longer reattaches. If the initial separation point is close to the leading edge then the airfoil immediately stalls, leading to the sudden loss in lift, which is also apparent in results presented in Section 5.2.2 (Figure 5.7). Data for the NACA 0021 was collected by Jacobs (1932) and also Swalwell and Sheridan (2001) where it was observed that this airfoil stalled more gradually for higher Reynolds numbers and also for flow regimes with a higher turbulence intensity.

The separation bubble characteristics on the pressure surface were also predicted from the friction coefficient data generated by XFOIL but are not shown here. A separation bubble was detected on the pressure surface for $\alpha = 2^\circ$ between $0.53 \leq x/c \leq 0.87$. For other angles of attack, the separation point moved closer to the trailing edge and at $\alpha = 12^\circ$, separation on the pressure surface no longer occurred.

5.2.2 Lift Coefficient Calculated from Pressure Distribution Data

Integration of the surface pressures around the airfoil surface using the trapezoidal rule enabled calculation of the lift coefficient as shown in Figure 5.6 and Figure 5.7, respectively. The trapezoidal rule used in this calculation is given by Equation (5.2), which is a standard formula for a non-uniform grid (i.e. the spacing between pressure taps varies in the chordwise direction). The integrals which are approximated in this equation were given in Equations (3.56) and (3.57). The numerical integration was undertaken in the anticlockwise direction beginning from the leading edge of the airfoil.

$$\int_a^b f(x) \approx 1/2 \sum_{k=1}^N (x_{k+1} - x_k)(f(x_{k+1}) + f(x_k)) \quad (5.2)$$

where,

$f(x)$ = Pressure coefficient, C_p , as a function of chordwise position

N = total number of pressure taps on both suction and pressure surfaces

x = chordwise position

a, b = stagnation pressure tap

The method was verified by inserting XFOIL pressure distribution data into the code and comparing the resulting output with lift and drag forces calculated using XFOIL. It can be seen in Figure 5.6 that the lift results matched exactly with those of XFOIL, which was expected since, according to the XFOIL documentation, the lift coefficient is obtained through direct surface pressure integration (Drela & Youngren, 2001).

On the other hand, the pressure drag coefficient is deduced by subtracting the skin friction drag from the total drag in XFOIL (Drela & Youngren, 2001). The surface pressure integration method was deemed to be subject to a large amount of numerical noise (Drela & Youngren, 2001). This was also noted in the current study, where the pre-stall drag was under-predicted, giving a result as much as three times lower in comparison to the force measurements. Therefore analysis of the pressure drag coefficient is not included here.

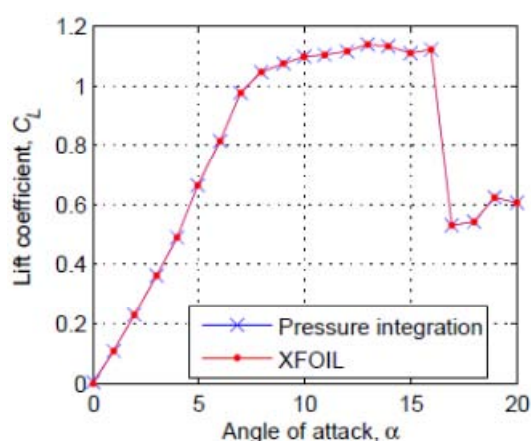


Figure 5.6 – Comparison between trapezoidal integration method and XFOIL for lift calculation, $Re = 120,000$.

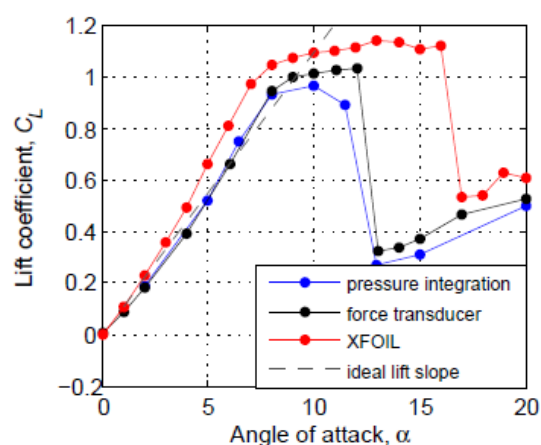


Figure 5.7 - Trapezoidal integration method for lift calculation using pressure distribution data, $Re = 120,000$.

For angles of attack up to $\alpha = 8^\circ$, the value of the lift coefficient calculated from the measured pressure distribution is in direct agreement with the force measurements as shown in Figure 5.7. However, as the stall angle is approached, the former method predicts a lower value for the lift coefficient than the latter. In addition, the integration method implies that stall occurs earlier than $\alpha = 12^\circ$. It is believed that the difference in results is due to a lack of spatial resolution of the pressure taps near the leading edge which was unavoidable due to manufacturing issues. As the angle of attack increases, the suction peak moves towards the leading edge. At angles of attack of $\alpha > 8^\circ$, the minimum value of this suction peak is not measured, hence leading to an under-prediction of the lift coefficient. Observation of the XFOIL results at $\alpha = 10^\circ$ and $\alpha = 12^\circ$ in Figure 5.2 (e) and (f) confirms that the spatial resolution of the suction peak is limited at high angles of attack. Variation between the force and pressure results could also be caused by manufacturing tolerance issues since the airfoils used in the former results were milled from aluminium, whereas those used in the latter results were moulded using polyester resin. An error analysis was not considered necessary for the lift plot derived from the pressure tapping data since it is only presented for comparison with the force measurements, where the latter are known to be more accurate.

The lift coefficient predicted by XFOIL is larger than the experimentally measured values and also exceeds the ideal lift slope as shown in Figure 5.7. This can be explained with reference to Figure 5.2 in Section 5.2.1 which indicates that there is

less negative pressure developed on the pressure surface after $x/c = 0.2$ for the XFOIL results in comparison with the experimental results. In addition, the separation bubbles have a greater influence on the pressure distribution characteristics for the XFOIL data, which suggests that the apparent camber would be greater, leading to lift in excess of that predicted by thin airfoil theory (Anderson Jr., 2007). Moreover, the XFOIL code predicts reattachment without further separation after the separation bubble on the suction surface, which is unlikely and also inconsistent with the hydrogen bubble visualisation results discussed in Section 6.1. It can also be seen that the stall angle is significantly higher for the XFOIL results compared to experimental data, which was also apparent for the comparison made by Miklosovic *et al.* (2007). This is not surprising since the accuracy of the XFOIL code is known to degrade as the stall angle is approached and at post-stall angles according to Drela and Youngren (2001).

5.2.3 Pressure Contours as a Function of Chordwise Position and Angle of Attack

Contour plots of the surface pressure distribution for the suction and pressure surfaces are shown in Figure 5.8 and Figure 5.9, respectively. It is evident from Figure 5.8 that as the angle of attack approaches the stall angle the suction peak moves towards the leading edge and there is a high concentration of negative pressure over a smaller area. On the pressure surface, positive pressure is present in a very small region near the leading edge, however a large proportion of the airfoil experiences negative pressure on this surface. Hence the majority of lift is generated due to the large amount of negative pressure on the suction surface and the positive pressure on the pressure surface has only a minor contribution as expected.

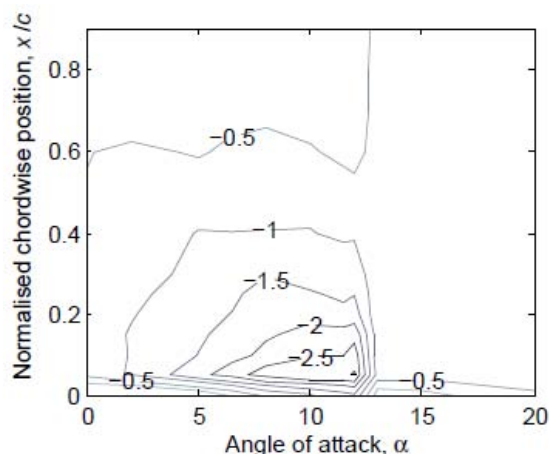


Figure 5.8 – Normalised pressure contours
for suction surface of NACA 0021,
 $Re = 120,000$.

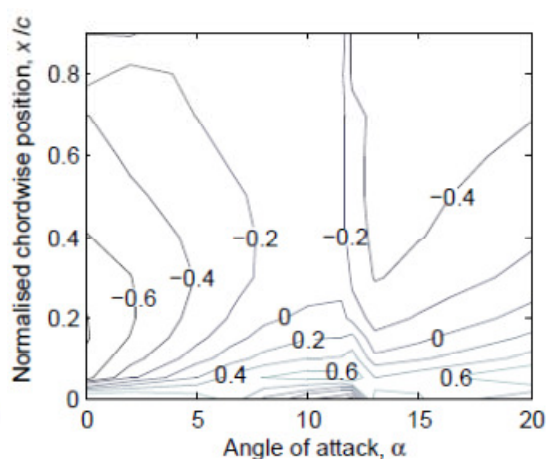


Figure 5.9 – Normalised pressure contours
for pressure surface of NACA 0021,
 $Re = 120,000$.

5.3 Unmodified NACA 65-021 Airfoil

5.3.1 Analysis of Pressure Distribution

Pressure distribution results for the NACA 65-021 airfoil verify the negative lift generation at low angles of attack as shown in Figure 5.10. At an angle of attack of $\alpha = 2^\circ$, the negative pressure generated on the pressure surface is in excess of the negative pressure on the suction surface as shown in Figure 5.10 (b). This results in an overall negative pressure differential. This phenomenon can also be observed from the data generated by the XFOIL code. Although, there are some minor discrepancies between the pressure distributions generated experimentally and numerically, the general shape is reasonably consistent. The most significant difference is evident for an angle of attack of $\alpha = 0^\circ$, where the XFOIL code predicts variations in the pressure distributions for the suction and pressure surfaces (the curve shown in Figure 5.10 (a) corresponds to the suction surface). This is unexpected for a symmetrical airfoil at $\alpha = 0^\circ$ and highlights the irregularity of the flow for this airfoil at low angles of attack and low Reynolds number. Nevertheless, both experimental and numerical methods predict a pressure differential directed from the suction surface towards the pressure surface at low angles of attack. This characteristic was not observed for the pressure distributions associated with the NACA 0021 airfoil.

The irregularity of the pressure distributions for the NACA 65-021 shown in Figure 5.10 implies the existence of separation bubbles, which were the expected cause of the negative lift generation. There is a noticeable difference in the distributions for $\alpha = 0^\circ$ to $\alpha = 4^\circ$ as shown in Figure 5.10 (a-c) when compared with $\alpha > 6^\circ$ depicted in Figure 5.10 (d-h). One major difference is the absence of the pressure and suction peaks at low angles of attack, which are present for $\alpha > 6^\circ$ up to the stall angle. The other significant difference in the pressure distribution at low angles of attack is the relative location of the curves for the suction and pressure surfaces of the airfoil which are inverted, leading to the negative pressure differential discussed earlier.

At an angle of attack of $\alpha = 8^\circ$, the experimental results indicate that a large amount of negative lift is maintained on the suction surface for a significant chordwise distance. In this instance, the XFOIL results are different from the experimental data in the case of the suction surface. The experimentally observed advantages in the pressure distribution at this angle of attack may explain the high lift generated as shown in Figure 5.17 of Section 5.3.3. In general, the XFOIL code predicts less negative lift on the suction surface, especially near the airfoil trailing edge, and more negative lift on the pressure surface along the majority of the chord for $6^\circ \leq \alpha \leq 12^\circ$. This leads to an overall under-prediction in lift in comparison to the experimental results, which is depicted in Section 5.3.3 (Figure 5.17). The chordwise location of the separation bubble as determined experimentally and through calculation using the XFOIL code is generally similar, despite the fact that the value of the pressure coefficient may be slightly different.

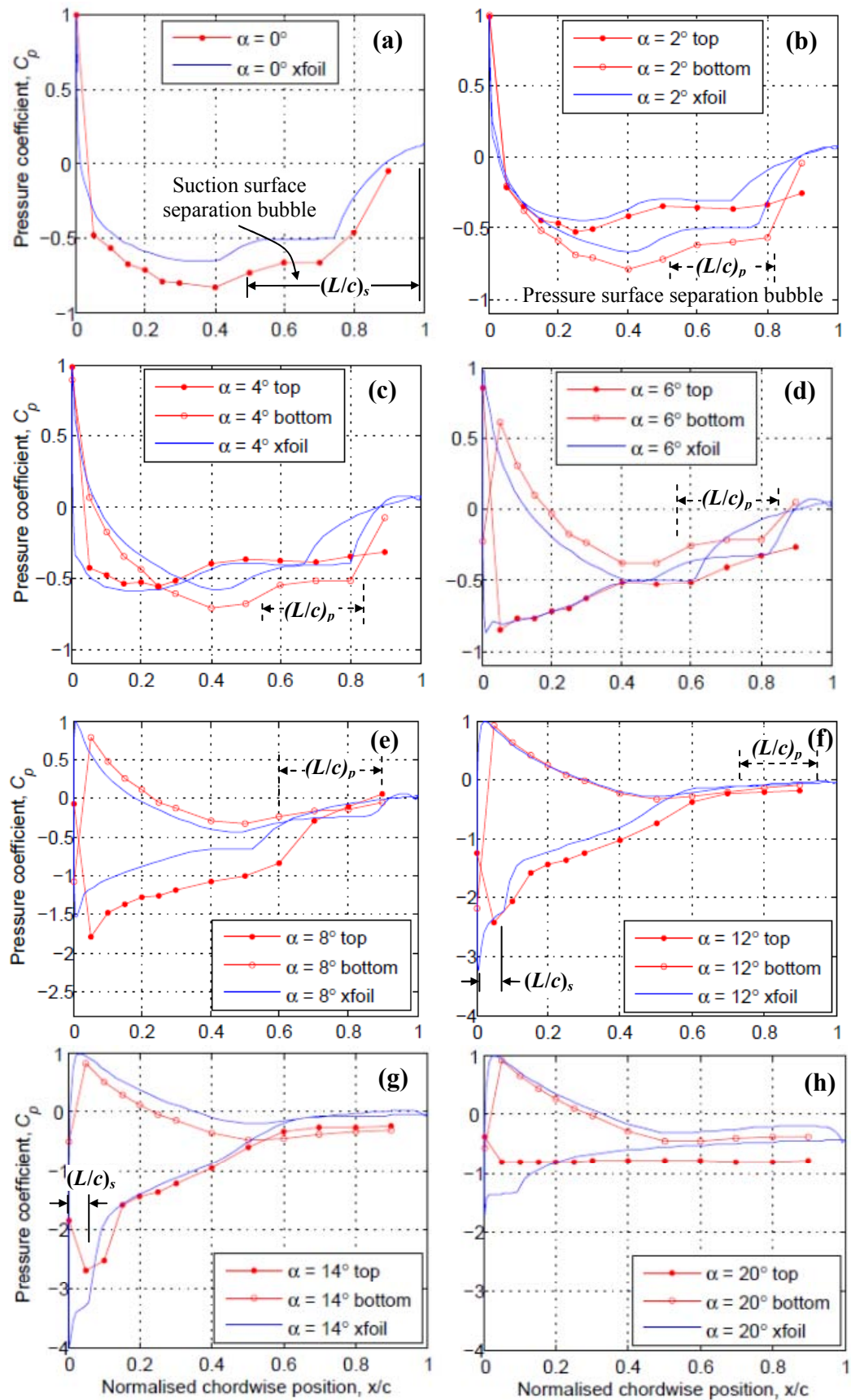


Figure 5.10 – Normalised pressure distribution plots for NACA 65-021 unmodified airfoil where “top” refers to suction surface and “bottom” refers to pressure surface, $Re = 120,000$. Separation bubble locations found from XFOIL skin friction data are indicated.

Predictions pertaining to the separation bubble characteristics were made through analysis of the friction coefficient data calculated using the XFOIL code. Conversely to the NACA 0021 airfoil, suction surface separation bubbles are only present at $\alpha = 0^\circ$, 12° and 14° for the NACA 65-021 airfoil. In the former case, the separation bubble covers almost half of the suction surface however at the high angles of attack the bubble is very short as shown in Figure 5.11 and Figure 5.12 and summarised in Table 5.2.

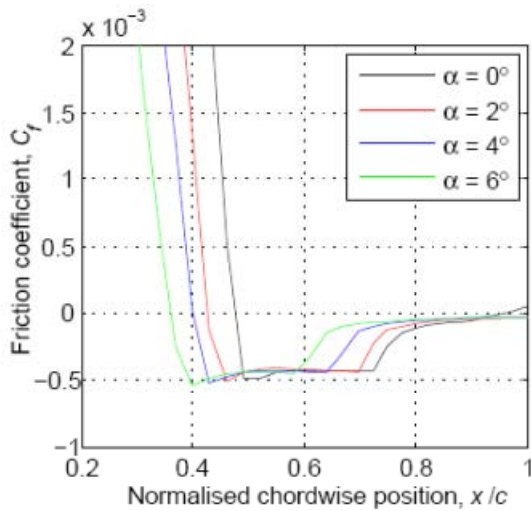


Figure 5.11 – Friction coefficient against chordwise position for NACA 65-021 at low angles of attack (suction surface), $Re = 120,000$.

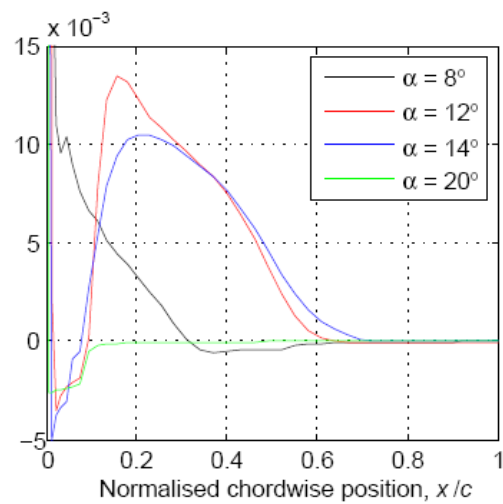


Figure 5.12 - Friction coefficient against chordwise position for NACA 65-021 at high angles of attack (suction surface), $Re = 120,000$

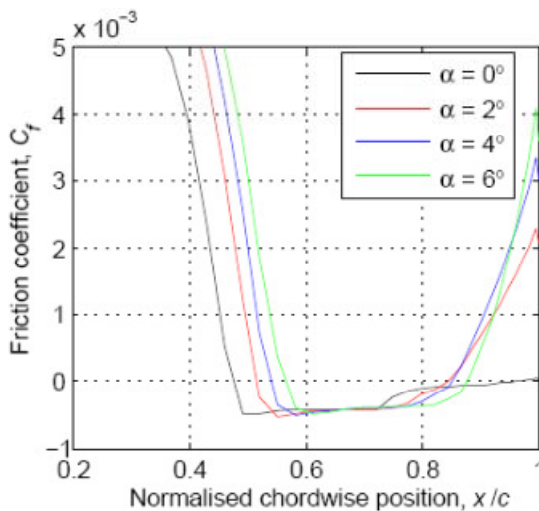


Figure 5.13 – Friction coefficient against chordwise position for NACA 65-021 at low angles of attack (pressure surface), $Re = 120,000$.

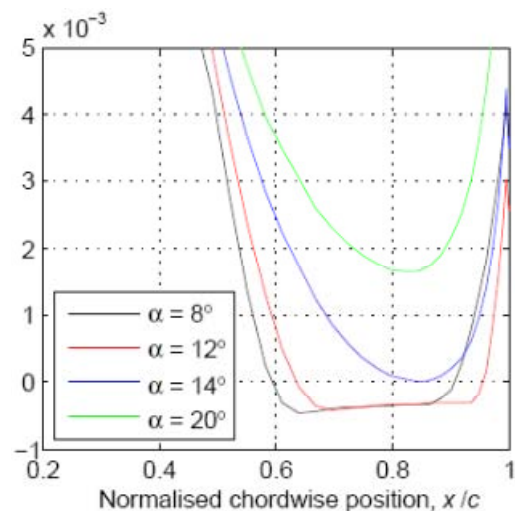


Figure 5.14 - Friction coefficient against chordwise position for NACA 65-021 at high angles of attack (pressure surface), $Re = 120,000$.

Another difference for the NACA 65-021 airfoil is that separation occurs without reattachment in the range $2^\circ \leq \alpha \leq 8^\circ$ according to XFOIL. This is reflected in the pressure distributions shown in Figure 5.10(b-e) where the pressure coefficient for the suction surface reaches a steady value at around $x/c = 0.4$ indicating that the flow is no longer attached (Marchaj, 1979; Simons, 1999). The experimental results show a similar behaviour for $2^\circ \leq \alpha \leq 6^\circ$ however, it appears that there is a separation bubble for $\alpha \leq 8^\circ$ and this is also suggested by the relatively high amount of lift at this angle of attack as shown in Figure 5.17.

For the majority of attack angles, a separation bubble is present on the pressure surface as shown in Figure 5.10 and summarised in Table 5.3. This separation bubble is relatively long compared to those associated with the NACA 0021 airfoil. It is also located closer to the airfoil trailing edge and as the angle of attack increased, it moves further aft but maintains the same length of approximately $L/c = 0.3$. The separation bubble remains until the angle of attack reaches $\alpha = 14^\circ$, at which point separation no longer occurs on the pressure surface.

Table 5.2 - Chordwise extent of laminar separation bubble and final separation location determined from friction coefficient for the suction surface (NACA 65-021), $Re = 120,000$.

Angle of attack, α	Chordwise extent of separation bubble	Normalised length of separation bubble $(L/c)_s$	Final separation location (x/c)
0°	$0.49 \leq x/c \leq 0.95$	0.46	-
2°	-	-	0.43
4°	-	-	0.43
6°	-	-	0.37
8°	-	-	0.34
12°	$0.02 \leq x/c \leq 0.08$	0.06	0.66
14°	$0.01 \leq x/c \leq 0.07$	0.06	0.75
20°	-	-	0.002

Table 5.3 – Chordwise extent of laminar separation bubble determined from the friction coefficient for the pressure surface (NACA 65-021), $Re = 120,000$.

Angle of attack, α	Chordwise extent of separation bubble	Normalised length of separation bubble $(L/c)_p$
0°	$0.49 \leq x/c \leq 0.96$	0.46
2°	$0.52 \leq x/c \leq 0.82$	0.30
4°	$0.55 \leq x/c \leq 0.84$	0.29
6°	$0.58 \leq x/c \leq 0.87$	0.31
8°	$0.61 \leq x/c \leq 0.90$	0.31
12°	$0.72 \leq x/c \leq 0.95$	0.23

5.3.2 Explanation for Negative Lift Phenomenon

The negative lift phenomenon observed for the NACA 65-021 airfoil is related to the presence of the separation bubble on the pressure surface which alters the effective camber. The change from negative to positive lift occurs because the model asymmetry increases with angle of attack. At a certain point, $\alpha = 6^\circ$, the counter-clockwise or positive circulation created by the separation bubble becomes less than the circulation created by model asymmetry which leads to overall negative circulation, which is desirable for positive lift generation.

Additionally, the explanation provided by Marchaj (1979) and discussed in Section 4.2.2 where the negative lift was attributed to thickening of the boundary layer on the suction surface is supported by the XFOIL results. The thickness of the boundary layer on the suction surface of the NACA 65-021 airfoil is substantially greater in comparison to that of the NACA 0021 for an angle of attack, $\alpha = 2^\circ$ as shown in Figure 5.15 and Figure 5.16, respectively. The boundary layer thickness on the pressure surface of the NACA 65-021 airfoil is relatively less significant, as depicted in Figure 5.14. At this angle of attack, $\alpha = 2^\circ$, negative lift was generated by the NACA 65-021 airfoil and this was confirmed by the force measurements, surface pressure integration and results from the XFOIL code as shown in Figure 5.17.

Use of boundary layer trips on the NACA 65-021 airfoil is believed to delay separation on the suction surface, reducing the boundary layer thickness and to eliminate the separation bubble on the pressure surface.

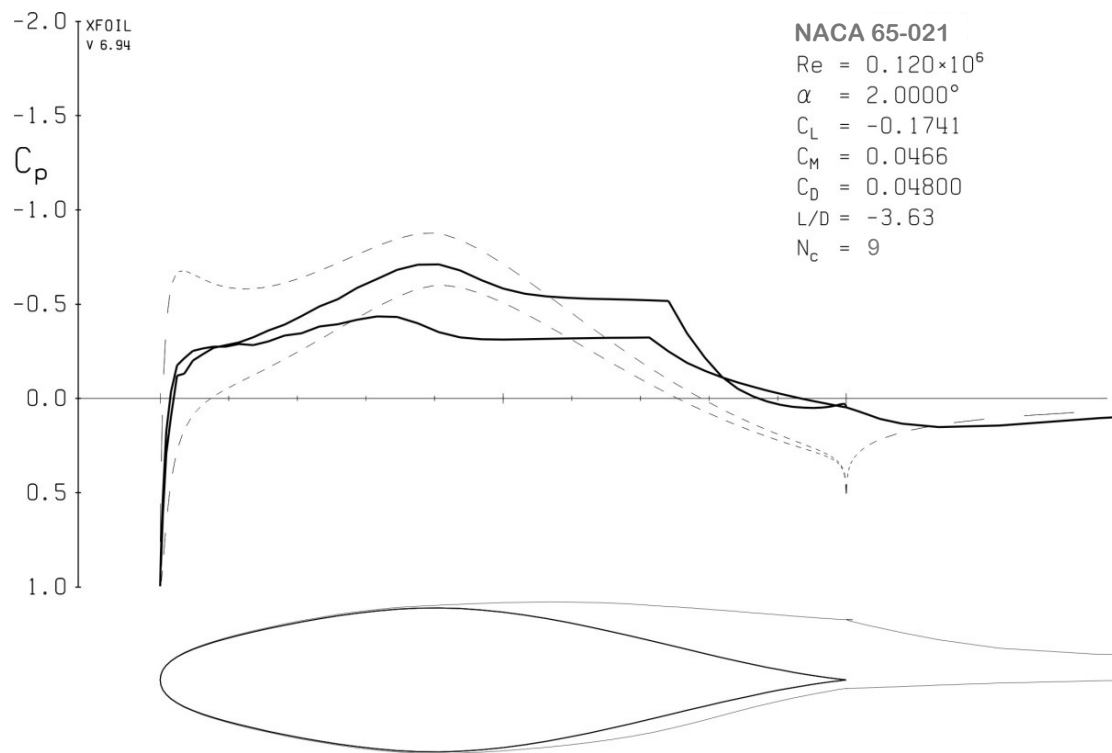


Figure 5.15 – Pressure distribution and boundary layer characteristics for NACA 65-021 airfoil at $\alpha = 2^\circ$ (dashed lines indicate the inviscid solution), $Re = 120,000$.

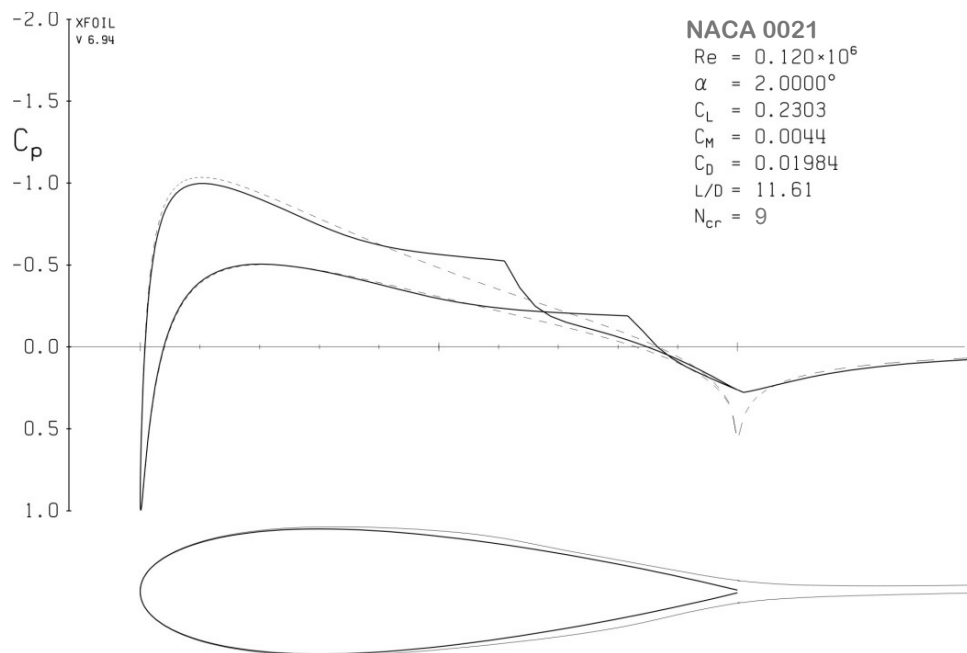


Figure 5.16 - Pressure distribution and boundary layer characteristics for NACA 0021 airfoil at $\alpha = 2^\circ$ (dashed lines indicate the inviscid solution), $Re = 120,000$.

5.3.3 Lift Coefficient Calculated from Pressure Distribution Data

The lift coefficient was determined from the surface pressure measurements using the same method as discussed in Section 5.2.2. The lift curve for the NACA 65-021 depicted in Figure 5.17 is highly non-linear due to the negative lift generated for angles of attack less than $\alpha = 4^\circ$. Results determined above this angle of attack also reflect that the lift generated is significantly less than that predicted by thin airfoil theory. This is attributed to the persistence of the long separation bubble on the pressure surface which extends over almost one third of the chord length as well as boundary layer thickening on the suction surface. The existence of a separation bubble is known to lead to deterioration in performance (Carmichael, 1981).

There is reasonable agreement between the lift results obtained from the force and pressure tap measurements. However, as observed for the NACA 0021 results, the maximum lift coefficient is under-predicted by the pressure integration method when compared to the force results due to spatial resolution limitations of the pressure taps. Results from XFOIL indicate a slight reduction in lift from $7^\circ \leq \alpha \leq 9^\circ$. This can be explained with reference to Table 5.2, which indicates that the separation point on the suction surface is relatively close to the leading edge at these angles of attack. For angles of attack in the range $10^\circ \leq \alpha \leq 15^\circ$, the positive lift curve slope is re-established. One possible mechanism for this is the formation of a small separation bubble, which trips the boundary layer to turbulence and hence delays separation and increases lift. Details of the separation bubble are provided in Table 5.2. A lift plateau was observed from the experimental results for $8^\circ \leq \alpha \leq 10^\circ$, as evident in Figure 5.17, which also occurred for the XFOIL results at a similar angle of attack. However, the large increase in lift predicted by XFOIL for $\alpha > 9^\circ$ was not observed for the experimental results for which lift only increased slightly for $\alpha > 10^\circ$. In spite of the large differences in lift for high angles of attack, the stall angles for the experimental measurements and the XFOIL results were consistent. As mentioned previously, XFOIL's performance is known to degrade near the stall angle and post-stall (Drela & Youngren, 2001).

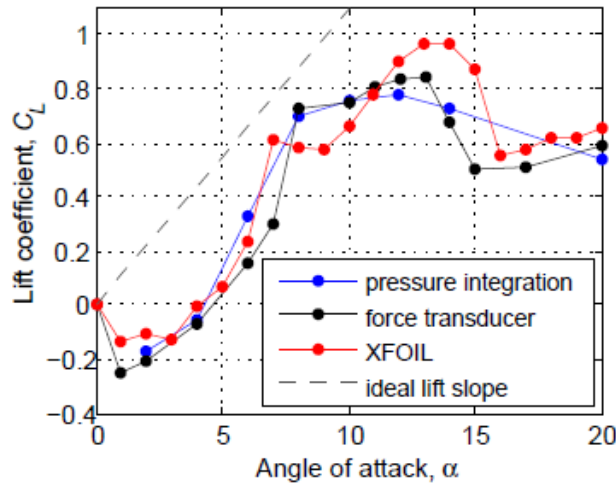


Figure 5.17 –Lift coefficient against angle of attack for different measurement methods (NACA 65-021), $Re = 120,000$.

5.3.4 Pressure Contours as a Function of Chordwise Position and Angle of Attack

The normalised pressure contours in Figure 5.18 plotted on the suction surface as a function of chordwise position and angle of attack reflect similar characteristics as shown in the NACA 0021 contours in Figure 5.8 of Section 5.2.3. The suction peak moves closer to the leading edge as the stall angle is approached and becomes more concentrated just prior to stall. There is a noticeable difference in the pressure distribution characteristics post-stall however, where the negative pressure on the suction surface is maintained at a relatively high value, reflecting the more progressive nature of the stall.

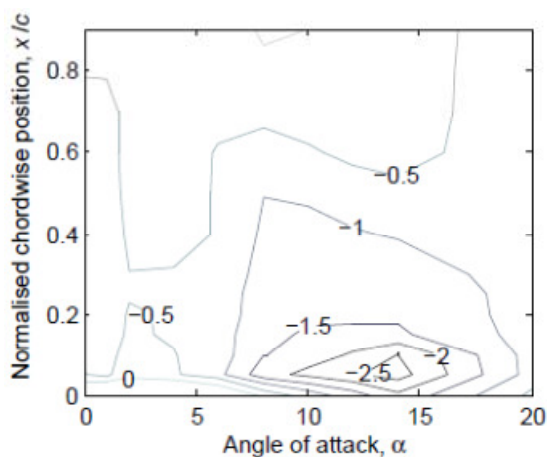


Figure 5.18 – Normalised pressure contours for suction surface of NACA 65-021, $Re = 120,000$.

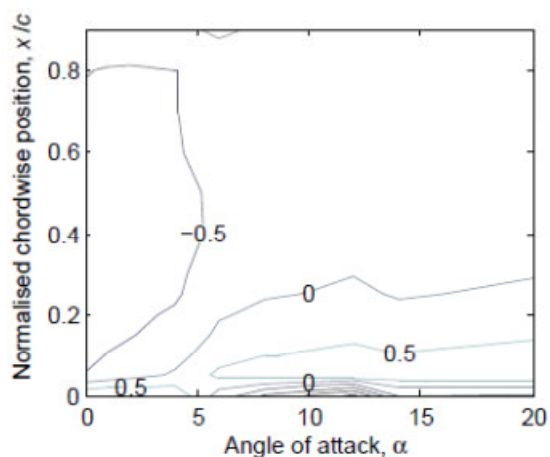


Figure 5.19 – Normalised pressure contours for pressure surface of NACA 65-021, $Re = 120,000$.

On the pressure surface there is much less variation in pressure for the NACA 65-021 airfoil as shown in Figure 5.19 compared to the NACA 0021 depicted in Figure 5.9 of Section 5.2.3. A possible reason for this is the existence of the long separation bubble near the trailing edge where the variation in pressure is expected to be small (Simons, 1999).

5.4 NACA 0021 with A8λ30 Leading Edge Tubercle Configuration

5.4.1 Analysis of Pressure Distribution

The surface pressure measurements taken at varying spanwise positions for the airfoil with tubercles yielded significantly different results as shown in Figure 5.20. For comparison, the pressure distributions for the unmodified NACA 0021 airfoil have been included in the plots. It is evident that the greatest amount of negative pressure is generated for the chordwise trough cross-section at all angles of attack prior to the onset of stall as shown in Figure 5.20 (b-d). This is consistent with results presented by Watts and Fish (2001), Fish and Lauder (2006) and Weber *et al.* (2010). The lowest magnitude of negative pressure is generated at the tubercle peak cross-section for these same angles of attack, $2^\circ \leq \alpha \leq 8^\circ$. For the cross-section between the tubercle peak and trough (mid-location), the amount of negative pressure generated is generally less than that for the trough and greater than that for the peak.

For the mid-location at angles of attack, $\alpha \leq 5^\circ$, the pressure distribution is similar to that measured for the unmodified airfoil (note the missing data point at $x/c = 0.05$, which was blocked during fabrication and rendered unusable). However, at the angle of attack just before stall, $\alpha = 8^\circ$, the amount of negative pressure measured for the modified airfoil is lower at this location. This is attributed to the presence of the streamwise vortices which have a larger affect with increasing angle of attack (Stanway, 2008). Results for $\alpha > 8^\circ$ for the suction surface should be regarded with caution since, upon repetition, the measurements yielded different values. This was most likely due to the effect of vorticity, which led to unsteadiness in the pressure characteristics.

On the pressure surface, the highest maximum value of the leading edge pressure peak is developed at the tubercle peak cross-section. The lowest minimum suction peak occurs at the trough cross-section and the pressure values for the middle cross-section lie somewhere between. The pressure peak for the middle cross-section is slightly lower than that measured for the unmodified airfoil. In general, there is minimal variation in the peak, mid and trough pressure distributions for $\alpha > 2^\circ$ after $x/c = 0.2$ on the pressure surface. This consistency is not present for the suction surface results, which implies that tubercles and their effects are more prominent for the suction surface. On the other hand, the negative pressure developed over the pressure surface is consistently less for the unmodified airfoil compared to all three cross-sections of the airfoil with tubercles, as shown in Figure 5.20. This would contribute to reduced lift for the airfoils with tubercles.

Direct comparison of the surface pressure results for the unmodified airfoil and the middle and peak tubercle cross-sections, suggests the absence of a separation bubble for the latter results. This is most evident in the pressure distributions for $0^\circ \leq \alpha \leq 5^\circ$ in Figure 5.20 (a-c), where the pressure gradient, dp/dx , remains relatively constant. However, it is apparent that a separation bubble exists for the trough cross-section. Based on results for the NACA 0021 and NACA 65-021 airfoils discussed previously, the position of the separation bubble is estimated by considering regions of reduced pressure gradient on the pressure distribution curve. Table 5.4 summarises the approximate separation bubble locations for the trough cross-section. It can be seen that, in general, the separation bubble moves towards the leading edge and maintains approximately the same length with increasing angle of attack up to the stall angle.

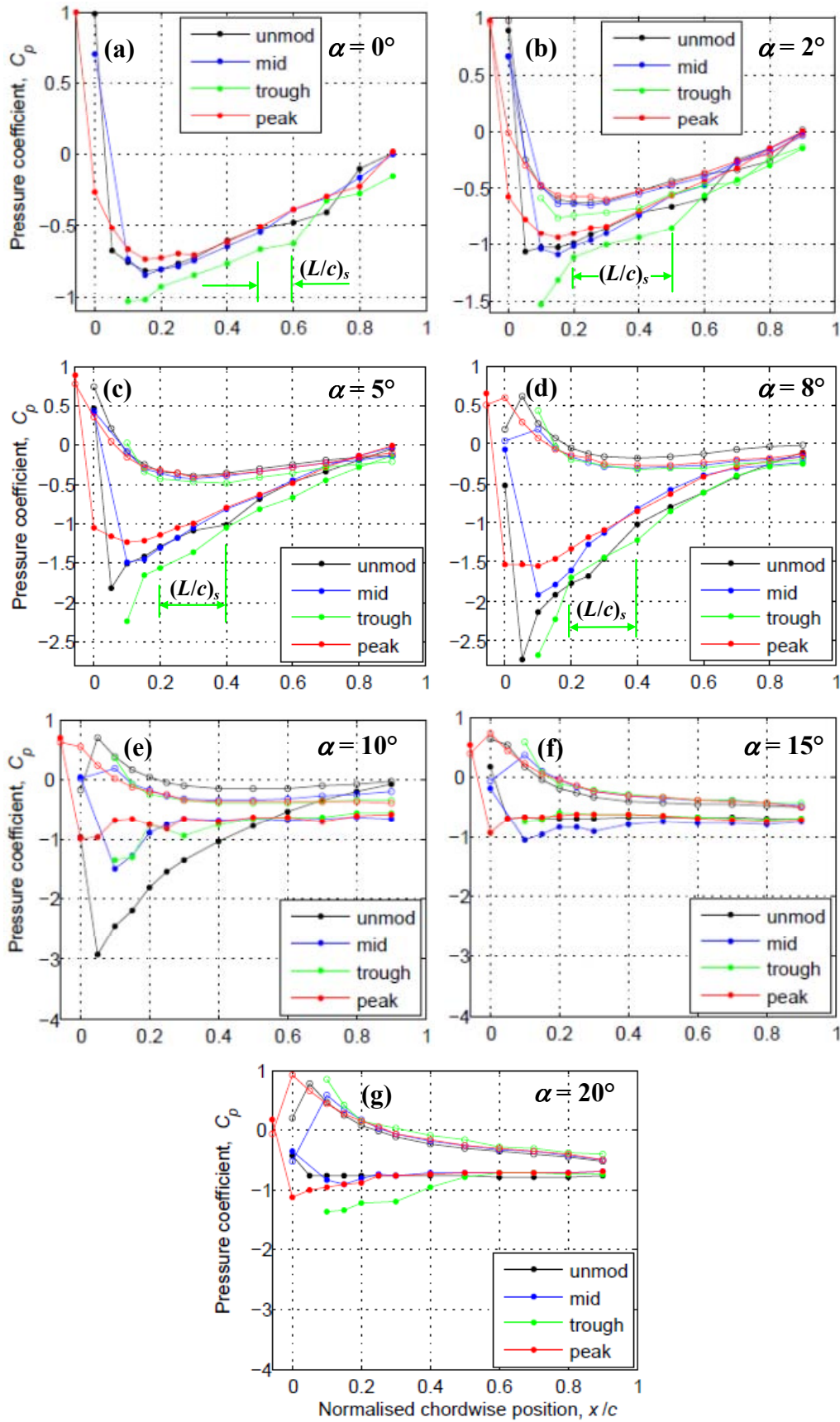


Figure 5.20 – Normalised pressure distribution plots for airfoil with A8230 tubercle configuration, where symbols are chosen as follows: “●” pressure surface “○” suction surface, $Re = 120,000$.

Table 5.4 – Location of separation bubbles for NACA 0021 airfoil with A8 λ 30 tubercles at trough cross-section on suction surface.

Angle of attack, α	Chordwise extent	Normalised length (x/c)
0°	$0.5 \leq x/c \leq 0.6$	0.1
2°	$0.2 \leq x/c \leq 0.5$	0.3
5°	$0.2 \leq x/c \leq 0.4$	0.2
8°	$0.2 \leq x/c \leq 0.4$	0.2

Results for the unmodified NACA 0021 airfoil are similar, except for the fact that the separation bubbles are restricted to troughs in the case of tubercles. This characteristic confirms that the flow is compartmentalised with tubercles and that “bursting” of the separation bubble would lead to localised stall at the trough cross-sections rather than stall of the entire airfoil. This is another explanation for the more gradual stall associated with airfoils with tubercles. Separation bubbles were also found to occur in the troughs for a wavy airfoil in the experiments conducted by Zverkov and Zanin (2008) described in Section 1.6.1.3.

5.4.2 Lift Coefficient Calculated from Pressure Distribution Data

Once more the trapezoidal integration method was used to determine the lift coefficient, as discussed in Section 5.2.2, for the NACA 0021 airfoil with A8 λ 30 tubercle configuration. However, in this case the results represent the amount of lift at a given two-dimensional cross-section and hence cannot be directly compared with the overall lift for the airfoil with tubercles.

Lift coefficient data calculated from the pressure distributions for the peak, mid-section and trough are plotted in Figure 5.21 along with results from the force measurements. It is evident that all lift curves determined from the surface pressure measurements show a reduced amount of lift for all angles of attack when compared to the force measurements in Figure 5.21. One possible reason for this is the limited spatial resolution near the airfoil leading edge, which leads to under-measurement of the magnitudes of the suction and pressure peaks. The unusable pressure tapings at

the trough and mid sections are also located near the leading edge and thus reduce the spatial resolution further at this critical location. Another possible reason is that the pressure distributions at the centre of the airfoil were not necessarily representative of the entire span and that a periodic flow pattern may have existed as suggested by Custodio (2008).

The maximum amount of lift for the three cross-sections was generated about the peak section until stall occurred. The minimum amount of lift before stall was generated about the trough cross-section. This is expected since the flow separates latest behind a tubercle peak and earliest behind a trough according to the hydrogen bubble results discussed in Section 6.1 and previous research (Johari *et al.*, 2008; van Nierop *et al.*, 2008). The lift curve for the middle cross-section was between that of the peak and trough before stall and a higher amount of lift was maintained in this location post-stall. This is perhaps due to positive effects related to the presence of the streamwise vortices which seem to be located in the region between the trough and peak according to the flow visualisation results presented by Custodio (2008).

The spanwise variation in lift for the peak, trough and mid-sections indicates that the amount of circulation is dependent on spanwise position and is greatest at a tubercle peak. The variation in circulation with spanwise location is believed to give rise to the formation of streamwise vorticity. A similar spanwise variation in circulation is predicted for the wavy airfoil since the relative angle of attack changes in the spanwise direction.

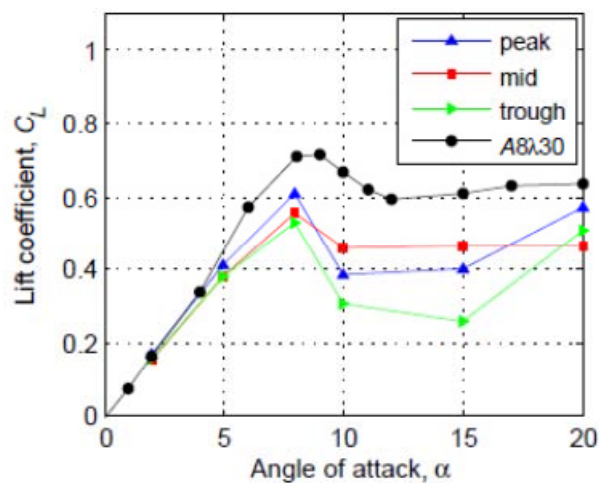


Figure 5.21 – Lift coefficient for A8230 evaluated from pressure distribution at “peak”, “mid” and “trough” tubercle positions compared to force results, $Re = 120,000$.

5.4.3 Pressure Contours as a Function of Chordwise Position and Angle of Attack

Pressure contours for the suction surface are shown in Figure 5.22 for the peak, trough and middle cross-sections. The axes are positioned with the origin corresponding to the leading edge at the middle cross-section.

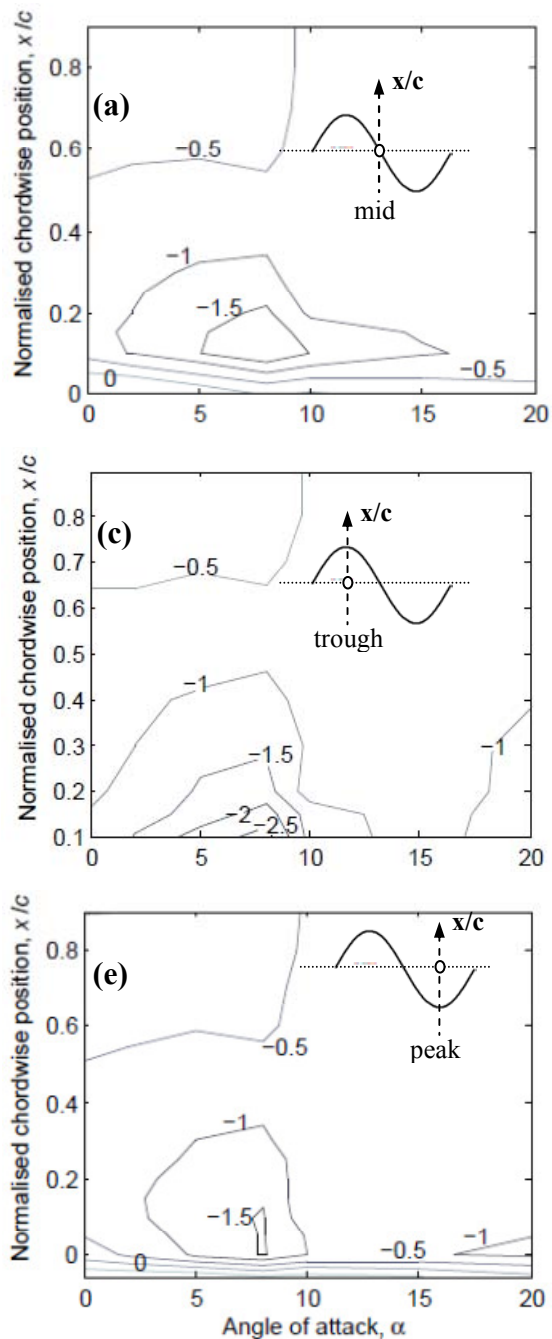


Figure 5.22 - Normalised pressure contours for suction surface of airfoil with A8 λ 30 tubercle configuration, $Re = 120,000$.

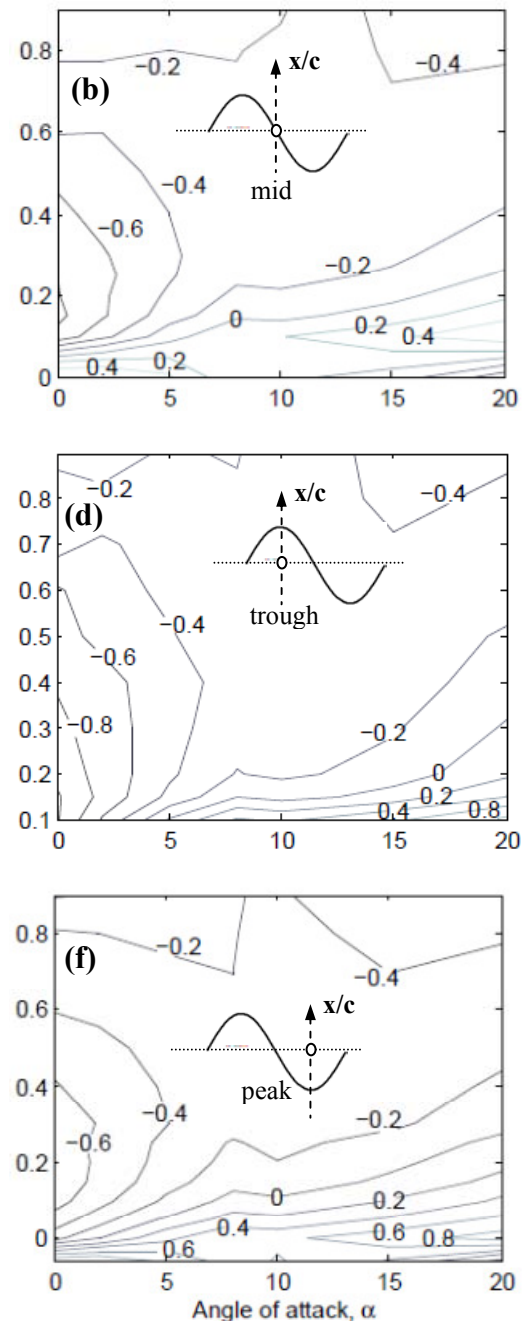


Figure 5.23 - Normalised pressure contours for pressure surface of airfoil with A8 λ 30 tubercle configuration, $Re = 120,000$.

It is confirmed that the greatest amount of negative pressure is developed at the trough region and that this occurs very close to the trough leading edge. The suction peak occurs at a similar chordwise location for all three cross-sections but seems to be slightly further aft for the middle section. In comparison to Figure 5.8, the negative pressure does not drop as rapidly after stall for the airfoil with tubercles, which is most notable at the middle cross-section. For the pressure surface, it can be seen that with increasing angle of attack, the trough cross-section experiences the most significant increase in pressure. The peak cross-section experiences the most consistent positive pressure with the largest magnitude.

5.5 Analysis of the Uncertainty Associated with Pressure Measurements

The uncertainty of the pressure tap measurements was analysed for each of the three airfoils at all angles of attack under investigation. The uncertainty was evaluated such that a 95% confidence interval was chosen as recommended by Bentley (2005) and explained in more detail in Section 3.3.11. The uncertainties associated with a given pressure tap location were found to differ and therefore it was important to consider each pressure tap location separately. However, results for all angles of attack are not included here and instead one pre-stall and one post-stall angle of attack are selected for analysis. As mentioned in Section 3.4.5, the pressure tap measurements include many of the same uncertainties as the load cell measurements leading to some similarities in the analysis. However, it was necessary to recalculate all sensitivity coefficients as well as including analysis on the uncertainties associated with the pressure measurement. Figure 5.24 and Figure 5.25 show error bars for a pre-stall and a post-stall angle of attack corresponding to those presented in the bar charts in Section 4.5 ($\alpha = 6^\circ$ and $\alpha = 20^\circ$).

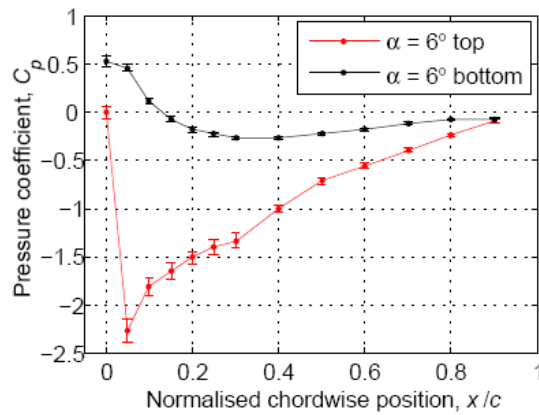


Figure 5.24 – Pressure coefficient uncertainty analysis for NACA 0021 at $\alpha = 6^\circ$, $Re = 120,000$.

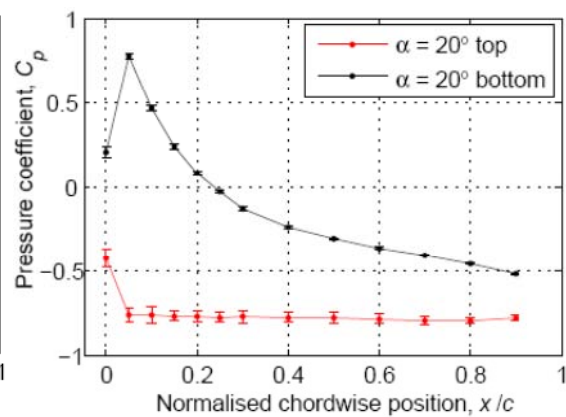


Figure 5.25 - Pressure coefficient uncertainty analysis for NACA 0021 at $\alpha = 20^\circ$, $Re = 120,000$.

It is evident that the largest uncertainties occur close to the leading edge of the airfoil and mainly on the suction surface. Hence, the pressure tap located at the suction peak ($x/c = 0.05$) was chosen for a more comprehensive analysis. This involved determining the contribution of each uncertainty component to establish the largest source of uncertainty. A second pressure tap located after the point of maximum thickness ($x/c = 0.6$) was also chosen for further analysis. The nomenclature from Section 4.5 was retained and additional uncertainty sources relating to pressure measurement accuracy were included, as shown in Table 5.5.

Table 5.5 - Nomenclature used in figures showing uncertainties in force measurements

Statistical uncertainties in freestream velocity measurement	wstd
Inaccuracy of freestream velocity measurement	w
Uncertainties associated with mean pressure value	pstd
Inaccuracy of the pressure output values	p
Rotary table positioning uncertainties	rt

Reference to Figure 5.26 reveals that the highest contribution to the uncertainty at $\alpha = 6^\circ$ for the pressure tapping at $x/c = 0.05$ is due to uncertainty in the mean value of the measured pressure. This is expected as there is a large pressure gradient in this region. Another significant contribution is from the uncertainty in angle of attack which is related to the large increase in the value of the negative pressure peak on the suction surface as the angle of attack increases. Further downstream at $x/c = 0.6$, the

relative uncertainty is slightly lower. The absolute uncertainty, however, is significantly lower.

In the post-stall regime at $\alpha = 20^\circ$, the random uncertainty associated with the wind tunnel velocity is the largest source of uncertainty for the pressure tapping at $x/c = 0.05$ as shown in Figure 5.27. This indicates that the value of the pressure peak is highly dependent on the Reynolds number at this location. At the pressure tapping further aft, the largest contribution to the overall uncertainty is from the uncertainty in the mean pressure, which is most likely related to the unsteadiness associated with the stalled condition.

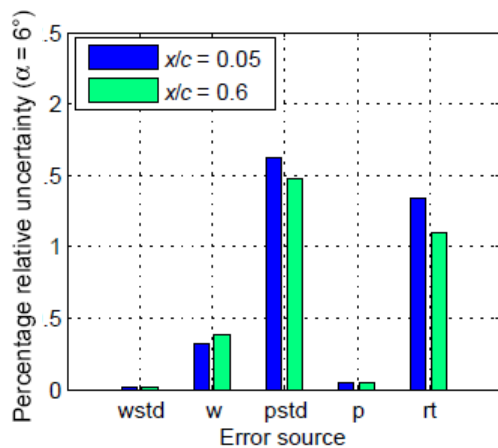


Figure 5.26 – Relative uncertainties pre-stall for pressure tappings located on airfoil suction surface (NACA 0021), $\alpha = 6^\circ$, $Re = 120,000$.

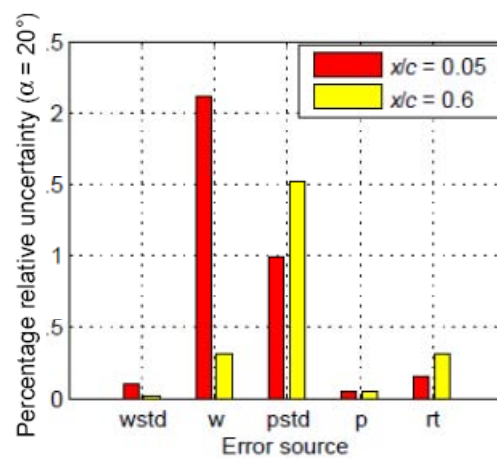


Figure 5.27 - Relative uncertainties post-stall for pressure tappings located on airfoil suction surface (NACA 0021), $\alpha = 20^\circ$, $Re = 120,000$.

Overall, the measurement uncertainty both pre-stall and post-stall is similar in magnitude to that of the force measurements. The largest contributing factors are also similar for both measurement techniques.

The pressure measurement uncertainties for the NACA 65-021 airfoil were analysed using a similar approach to that described for the NACA 0021 airfoil where a pre-stall and a post-stall angle of attack were chosen. These corresponded as closely as possible to the angles of attack chosen for the load cell uncertainty analysis, which led to the selection of $\alpha = 8^\circ$ and $\alpha = 20^\circ$. For the NACA 65-021 airfoil, the largest relative uncertainties occur near the leading edge on the suction surface for both angles of attack as shown in Figure 5.28 and Figure 5.29.

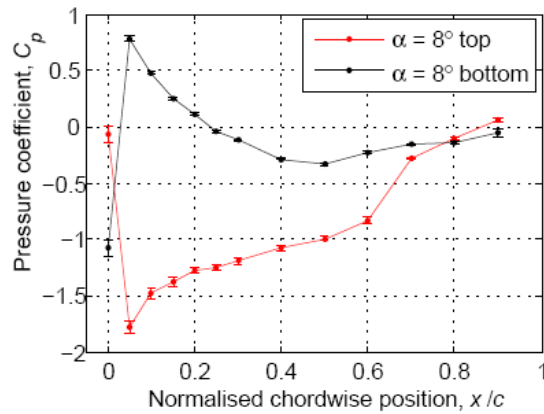


Figure 5.28 – Pressure coefficient uncertainty analysis for NACA 65-021 at $\alpha = 8^\circ$, $Re = 120,000$.

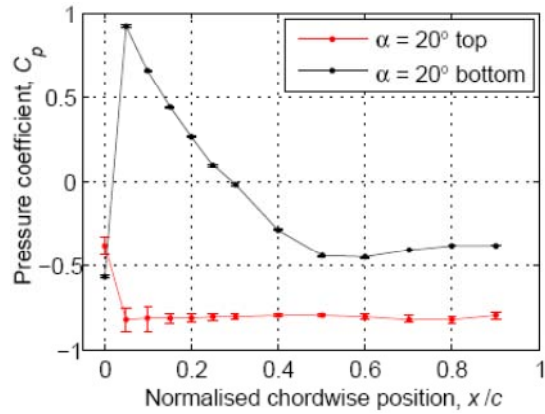


Figure 5.29 – Pressure coefficient uncertainty analysis for NACA 65-021 at $\alpha = 20^\circ$, $Re = 120,000$.

The relative uncertainties for the NACA 65-021 airfoil are depicted in Figure 5.30 and Figure 5.31. The largest source of uncertainty pre-stall is the uncertainty in airfoil angle of attack on the suction surface, which becomes more significant towards the trailing edge of the airfoil. Close to the leading edge, the negative pressure peak varies significantly with angle of attack and further aft, the flow behaviour is predicted to be highly variable due to an early onset of flow separation, as shown in Table 5.2. The uncertainty post-stall is also dominated by the uncertainty in airfoil angle of attack. This reflects that the measured pressure distribution changes significantly with angle of attack for this airfoil, especially close to the leading edge. In general, the uncertainties associated with the pressure tap measurements for the NACA 65-021 airfoil were much lower than those associated with the force measurements.

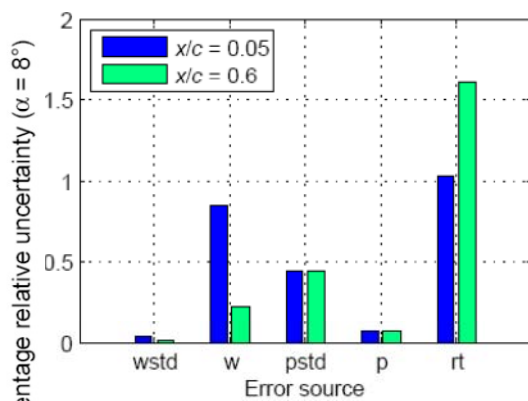


Figure 5.30 – Relative uncertainties pre-stall for pressure tapplings located on suction surface of airfoil (NACA 65-021), $\alpha = 8^\circ$, $Re = 120,000$.

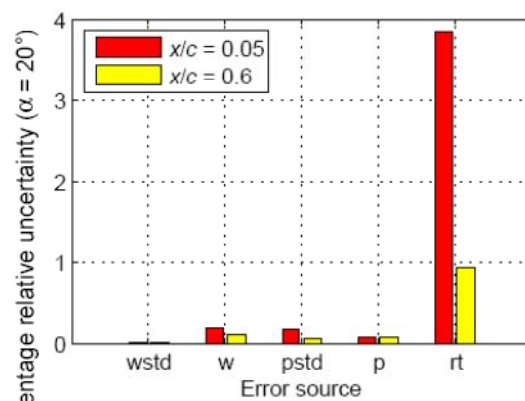


Figure 5.31 – Relative uncertainties post-stall for pressure tapplings located on suction surface of airfoil (NACA 65-021), $\alpha = 20^\circ$, $Re = 120,000$.

For the modified airfoils, there is a relatively low uncertainty prior to stall as shown in Figure 5.32. However, this changes dramatically in the post stall condition as depicted in Figure 5.33, where the uncertainties are so large that they overlap for some spanwise locations. These results highlight the large degree of unsteadiness associated with tubercles at high angles of attack which was also observed by Miklosovic (2007).

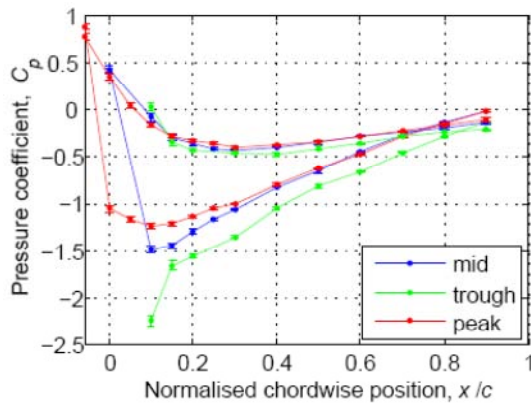


Figure 5.32 – Pressure coefficient uncertainty analysis for A8230 tubercle configuration at $\alpha = 5^\circ$, $Re = 120,000$.

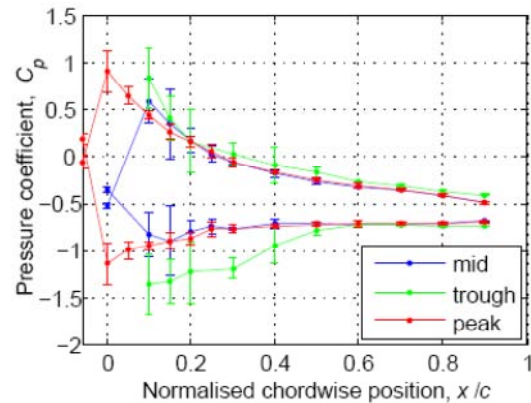


Figure 5.33 – Pressure coefficient uncertainty analysis for A8230 tubercle configuration at $\alpha = 20^\circ$, $Re = 120,000$.

The relative uncertainties are shown in Figure 5.33 and Figure 5.35, revealing the most significant contribution to the overall uncertainty. The location selected for analysis was the chordwise position closest to the leading edge at which there was a pressure tapping in each spanwise position corresponding to a tubercle peak, trough and midway between, $x/c = 0.1$. In the pre-stall regime, the standard deviation in mean pressure and uncertainty in angle of attack are the largest sources of uncertainty. However, post-stall the uncertainty in mean pressure increases markedly and far outweighs any other sources of uncertainty. This large uncertainty is not observed for the unmodified airfoil and is most likely associated with the presence of the streamwise vortices. It is also apparent that the largest uncertainty is associated with the pressure tapping in the trough between tubercles. Relative to the force measurements, the uncertainty in pressure were similar when comparing pre-stall values for airfoils with tubercles. However, post-stall the relative uncertainty associated with the pressure tap measurements was almost an order of magnitude higher.

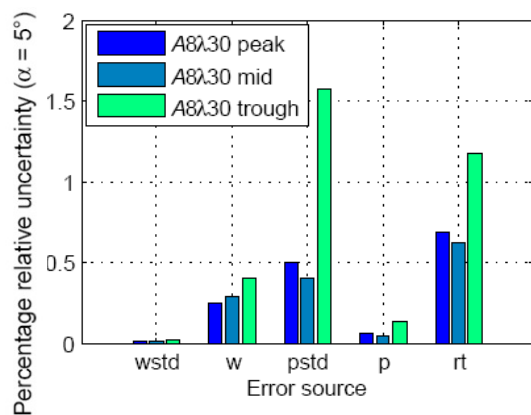


Figure 5.34 – Relative uncertainties pre-stall for tapping located at $x/c = 0.1$ on suction surface of airfoil, $\alpha = 5^\circ$, $Re = 120,000$.

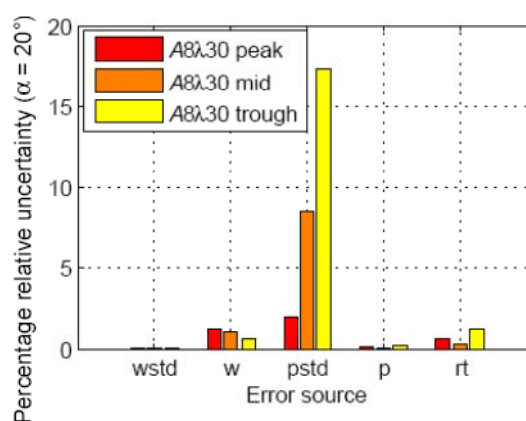


Figure 5.35 – Relative uncertainties pre-stall for tapping located at $x/c = 0.1$ on suction surface of airfoil, $\alpha = 20^\circ$, $Re = 120,000$.

5.6 Summary

The existence of a separation bubble was confirmed for all three airfoils involved in the surface pressure measurements. This enabled clarification of some of the unusual features observed in the force measurements presented in Chapter 4. Such features included lift in excess of the theoretical lift curve for the NACA 0021 unmodified airfoil. This characteristic was explained by the apparent camber created by the separation bubble on the suction surface, which increased for certain ranges of attack angle. Another unusual phenomenon noted in Chapter 4 was the generation of negative lift at low angles of attack for the NACA 65-021 airfoil. The explanation of this phenomenon was twofold. Firstly, a separation bubble was found to exist on the pressure surface which changed the effective camber leading to circulation in the opposite direction. As the angle of attack was increased, the asymmetry created by the orientation of the airfoil to the flow counteracted the effects of the separation bubble and the airfoil began to generate positive lift as expected. The second explanation for the negative lift was the thickening of the boundary layer on the suction surface, which can occur for airfoils with large trailing edge angles (Marchaj, 1979). This boundary layer thickening was clearly visible in XFOIL plots. A consequence of this phenomenon is the slowing down of flow on the suction surface relative to the pressure surface which would also create positive circulation, hence reduced or reversed lift.

Analysis of the pressure coefficient contours as a function of chordwise position and angle of attack indicated that the majority of lift is generated on the suction surface and that the minimum pressure point occurs before $x/c = 0.3$ for all airfoils investigated. It was also found that this minimum pressure location moved closer to the leading edge with increasing angle of attack and became more concentrated with a reducing pressure. The most severe stall was noted for the NACA 0021 airfoil since after the stall angle there was a large increase in pressure on the suction surface. This sudden stall was related to the presence of the separation bubble on the suction surface which eventually “burst.” The severity of the stall was moderated by the existence of tubercles on the NACA 0021 airfoil since separation bubbles were restricted to the troughs and hence bubble “bursting” did not lead to a catastrophic loss in lift because flow was still attached behind the peaks.

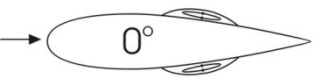
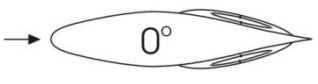
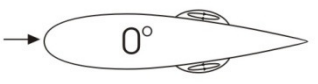
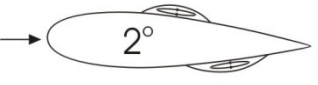
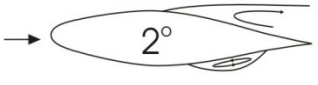
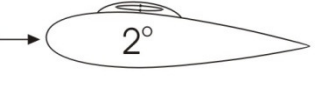

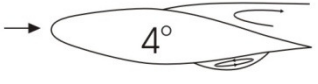

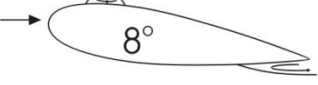
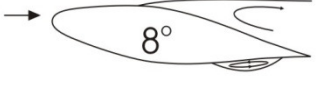

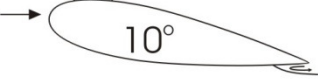





For the modified airfoil with tubercles, the greatest amount of negative pressure was generated for the trough cross-section at all pre-stall angles of attack. This was consistent with results presented by Watts and Fish (2001), Fish and Lauder (2006) and Weber *et al.* (2010), where the minimum pressure on the suction surface was observed in the troughs between tubercles near the leading edge. The least amount of negative pressure was generated at the tubercle peak cross-section pre-stall. The amount of negative pressure generated at the quarter-wavelength location was generally less than that for the trough and greater than that for the peak.

Through comparison with XFOIL, it was found that the lift coefficient could be feasibly calculated through numerical integration of the surface pressure measurements using the trapezoidal rule. Lift coefficient curves determined from the pressure distribution matched reasonably well with the force measurement results for the unmodified NACA 0021 and NACA 65-021 airfoils. Hence it was considered viable to plot the lift coefficient for the airfoil with the $A8\lambda30$ tubercle configuration at each spanwise location under investigation. The largest amount of lift was found to occur for the peak cross-section and the smallest amount for the trough. Prior investigations had alluded to these findings since it was found that the flow remains attached for longer behind a tubercle peak than behind a trough (Johari *et al.*, 2008; van Nierop *et al.*, 2008). Another characteristic which was observed was that the lift

curves for each cross-section were significantly lower than the overall lift measured with the force transducer. This is attributed to both a lack of spatial resolution in the measurements and also differences in chordwise pressure distribution along the span for different troughs, peaks and mid-sections.

Table 5.6 presents a series of schematic diagrams which provide a summary of the separation characteristics for the three airfoils analysed in this chapter. The diagrams illustrate how the flow patterns around the airfoils influence the lift and drag characteristics. In particular, the persistent separation on the pressure surface of the NACA 65-021 airfoil explains the reversed lift generated at the chosen Reynolds number of $Re \sim 120,000$. The diagrams also illustrate how the incorporation of tubercles can influence the flow pattern thereby altering the effective airfoil camber, hence the airfoil's lift characteristics.

Table 5.6 – Summary of separation characteristics.

NACA 0021	NACA 65-021	A8 λ 30 (trough)
		
		
		
		
		
		

Chapter 6

Analysis of Flow Patterns



6.1 Introduction

A visual representation of the flow patterns generated in response to the existence of tubercles on the airfoil leading edge is presented in this chapter. Analysis of these flow patterns allows for a deeper insight into performance enhancement mechanisms associated with tubercles. In addition, the overall behaviour of the flow can be studied to explain some features of the surface pressure and force results.

The first section of this chapter provides a general analysis of the flow patterns using hydrogen bubble visualisation which is a qualitative technique. Several viewing orientations are used in order to ensure the visibility of specific features. These features include the separation point, which is visible by observing the airfoil from the side. Qualitative predictions regarding local variations in pressure and velocity can be ascertained from the planform view based on the relative spacing of the streaklines. In addition, streamwise vortex structures can be visualised from an angled point of view.

Previous studies have shown that these streamwise vortices exist as counter-rotating pairs which are located in the troughs between tubercles (Stanway, 2008; Custodio, 2008). In this study, particle image velocimetry was used for a single tubercle configuration to investigate the velocity fields associated with the streamwise vortex structures. Data were obtained for several cross-sectional planes perpendicular to both the airfoil and the flow.

The velocity data were used in a custom-written Matlab code to determine the associated vorticity field about the airfoil. Calculation of the vorticity provided information pertaining to the trajectory of peak vorticity and the rate at which the vorticity diffuses as it moves in the downstream direction. Another custom-written code was implemented to determine the circulation associated with each vortex. This enabled quantification of the vortex strength at various streamwise locations along the airfoil surface.

6.2 Hydrogen Bubble Visualisation

Hydrogen bubble flow visualization images were used to highlight the characteristic flow features for airfoils with tubercles. The Reynolds numbers based on airfoil chord length investigated were $Re = 4370$ and $Re = 5250$. Justification of these flow regimes is given in Section 3.5.2. It was difficult to distinguish noticeable differences between the visualization results for the NACA 0021 and NACA 65-021 airfoils and thus the focus of the reported results is the illustration of important flow features associated with tubercles as well as comparison of different tubercle configurations.

Hydrogen bubble visualization with the A8 λ 30 airfoil is shown in Figure 6.1 (a) and reveals that streamwise vortices are formed in the troughs between tubercles. It can also be seen in Figure 6.1 (b) that the downwards turn of the flow (i.e downwash angle) behind a tubercle peak is greater than the behind a trough (Figure 6.1 (c)) which is consistent with calculations undertaken by van Nierop *et al.* (2008). This implies a greater degree of flow attachment behind a peak than behind a trough, which was in agreement with observations reported by Johari *et al.* (2007).

Additionally, Figure 6.1(d) indicates that near the leading edge, the streaklines converge in the troughs and this implies that the flow is accelerated in this region. By contrast, the streaklines appear to diverge in the troughs and converge behind the tubercle peaks as the flow approaches the trailing edge. This can be explained by the fact that, whilst the bubble streaks in Figure 6.1 (a) and Figure 6.1 (d) initially pass close to the tubercles, further downstream they move away from the surface, as indicated by Figure 6.1 (b) and Figure 6.1 (c). It is probable that downstream of the leading edge the surface flow in the troughs continues to converge along the entire airfoil chord due to the presence of the

streamwise vortices. The diverging flow far above the troughs is also consistent with the presence of these streamwise vortices.

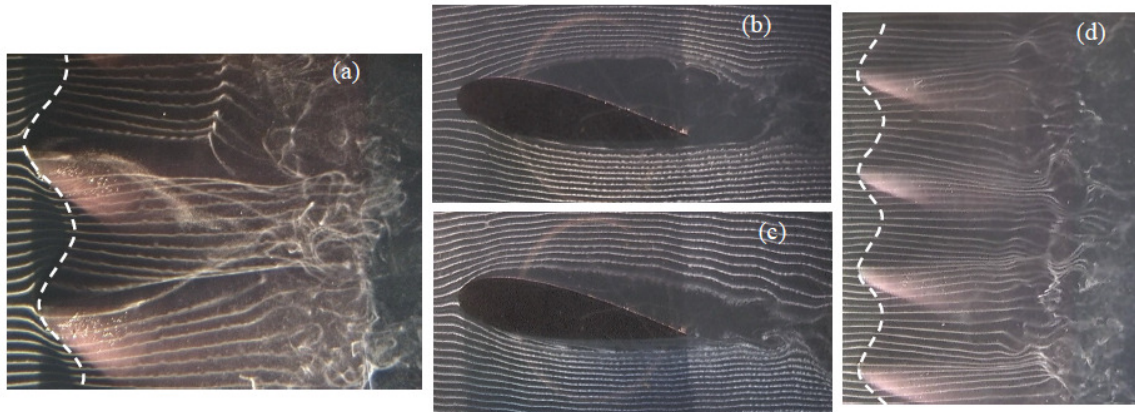


Figure 6.1 - Hydrogen bubble visualisation at $Re = 4370$, $\alpha = 10^\circ$, $A8\lambda30$ configuration (a) angled top view showing stream-wise vortices, (b) side view in plane of trough (c) side view in plane of peak and (d) top view depicting regions of acceleration. Dashed lines show the outline of the leading edge, flow is from left to right.

Figure 6.2 shows a comparison of the flow characteristics for various tubercle configurations as seen from an angled top view. In the case of the unmodified airfoil at $\alpha = 10^\circ$ shown in Figure 6.2 (a), there is no perturbation to the streaklines as they travel along the chord of the airfoil. However, it can be seen that for all airfoils with tubercles, a three-dimensional pattern of streaklines emerges, which shows the presence of streamwise vortices. For a smaller tubercle wavelength, the vortices are spaced more closely together and are therefore more likely to interact with one another. This can be seen in Figure 6.2 (b) and (c), where the deviation from laminar flow occurs further upstream with decreasing tubercle wavelength, as marked by the dashed red line. This leads to an apparent increase in turbulence, indicating increased momentum exchange as well as a more spatially uniform attachment of the flow to the airfoil surface.

Considering airfoils with the same amplitude-to-wavelength (A/λ) ratio and hence an equivalent maximum angle of the leading edge sweep, there is a similarity between Figure 6.2 (b) and (e), with respect to the appearance of the vortex structures and location of vortex breakdown. This observation may be the result of a similar vortex strength for these cases, which was mentioned by Custodio (2008). In summary, it is shown that the spacing influences the degree of mixing in the boundary layer and that the A/λ ratio affects the vortex strength. As the spacing between tubercles is reduced, they act more

like turbulence generators giving rise to more uniform boundary layer mixing and more uniform attachment of the boundary layer near the trailing edge. Eventually, reduction in spacing becomes detrimental to performance, whereby the interaction between nearby vortices increases and performance worsens as was found for vortex generators (Godard & Stanislas, 2006). This explains the deterioration in lift and drag performance for the $A4\lambda7.5$ airfoil (not shown in Figure 6.2) compared to the $A4\lambda15$ airfoil which was discussed in Section 4.2.5.

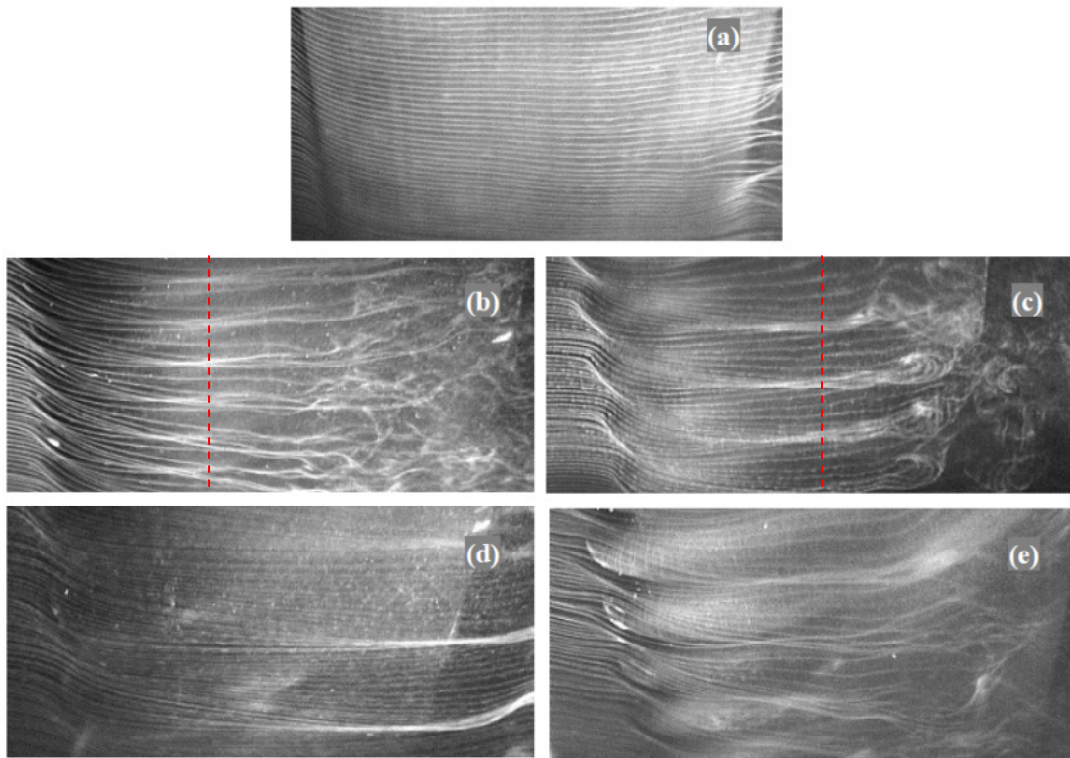


Figure 6.2 - Hydrogen bubble visualization of the NACA 0021, angled top view: (a) unmodified airfoil, (b) $A4\lambda15$ (c) $A4\lambda30$ (d) $A4\lambda60$ and (e) $A4\lambda130$ ($Re = 5250$, $\alpha = 10^\circ$), flow is from left to right.

6.3 Airfoil Selection for Particle Image Velocimetry (PIV)

For the PIV study, large streamwise vortices above the suction surface were required, with high vorticity and circulation. These specifications were important to ensure maximum spatial resolution and minimum uncertainty. Previous studies indicated that a higher amount of post-stall lift was achieved for larger amplitude tubercles (Johari *et al.*, 2007; van Nierop *et al.*, 2008; Custodio, 2008). This implies that the strength and perhaps size of vortices for larger amplitude tubercles is greater since the streamwise vortices are responsible for the increased generation of lift in post-stall conditions. In addition, the hydrogen bubble results discussed in Section 6.2 indicated that a larger A/λ ratio could

lead to generation of stronger vortices. Hence, the airfoil with the largest amplitude tubercles was chosen for the PIV experiments, which is the $A8\lambda30$ configuration. This is also the same configuration which was used in the pressure tap experiments, giving further opportunity for comparison.

6.4 Suitability of Ensemble Averaging

Observation of a time sequence of vorticity fields for a given case indicates that, while the counter-rotating vortices appear in every image, their characteristics vary with time. This can be seen in the image sequence shown in Figure 6.3, where the vorticity field in the range $-0.1 \leq \omega \leq 0.1$ is removed to improve the clarity of the image.

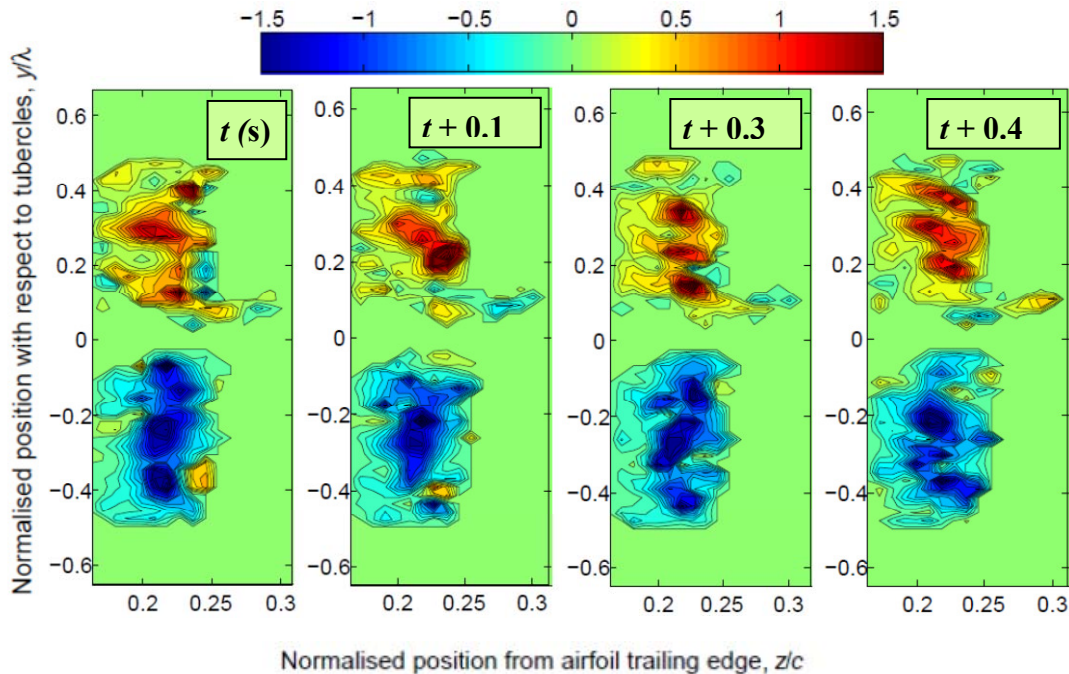


Figure 6.3 – An example of instantaneous vorticity contours for the $0.4c$ plane at $\alpha = 5^\circ$, where time spacing between images is $0.1s$, $Re = 2230$.

On the other hand, ensemble averaging of a large set of image pairs significantly reduces the uncertainty in the results as discussed in Section 3.6.11.2. Therefore, it is useful to analyse the velocity fluctuations, v' and w' , in the y and z directions for a given data set of 2085 image pairs to reveal the time dependent nature of the flow. Figure 6.4 (a-b) indicates that the highest magnitude of v' and w' occurs in the region of the streamwise vorticity peaks for the $0.4c$ plane at $\alpha = 5^\circ$. The magnitudes of both the root-mean-squared velocity fluctuations are approximately 16% of the peak average velocities. Note that the peaks in v'_{rms} and w'_{rms} occur at approximately the same locations as the peaks in

the mean vorticity pattern (Figure 6.6 (a)). This is consistent with the velocity fluctuation being caused by fluctuation in the location, size and strength of the streamwise vortices. This indicates that the nature of the vortices changes over time but their position remains relatively constant.

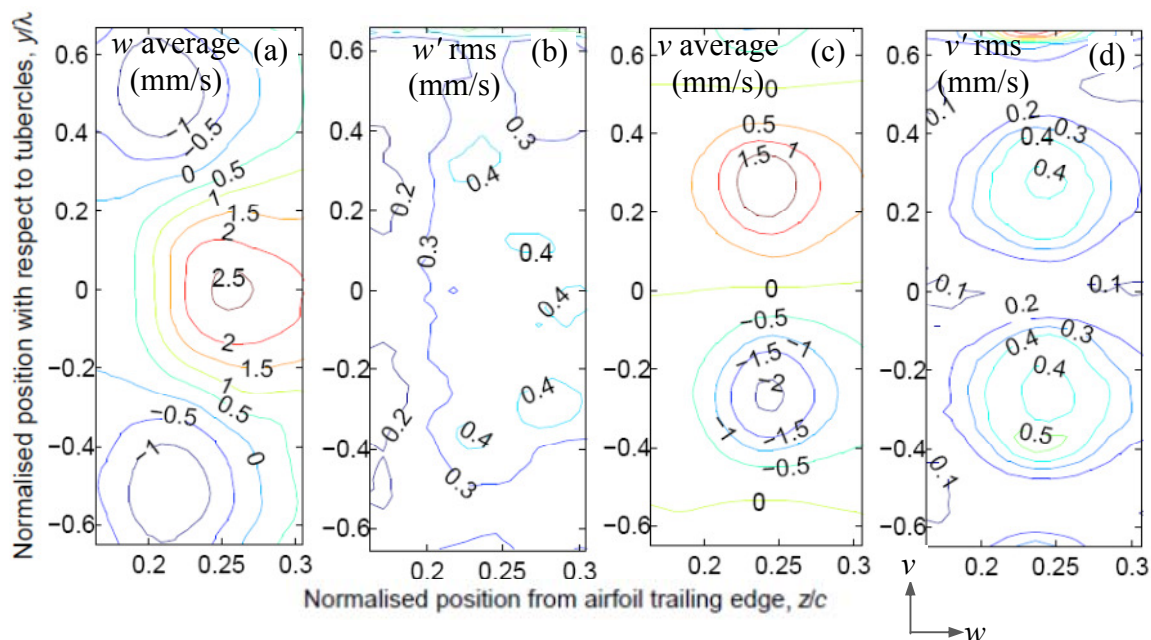


Figure 6.4 – Average velocity contours compared with velocity fluctuation contours, $0.4c$ plane at $\alpha = 5^\circ$, $Re = 2230$.

The above analysis was applied to other streamwise planes and it was found that unsteadiness and vortex movement increased towards the trailing edge. This was expected due to the occurrence of boundary layer separation and the increasing size of the separated zone along the chord. Nevertheless, it was found that the average velocity-vector field for all planes located on the airfoil chord (except at $\alpha = 15^\circ$) provided qualitatively accurate representation of the flow field.

6.5 Vorticity

The presence of counter-rotating pairs of streamwise vortices is depicted in Figure 6.5 for $x/c = 0.4$ at $\alpha = 15^\circ$, where the image origin is located at the trailing edge in the centre of the trough between the tubercles. In these and subsequent figures in this chapter, the images have been compressed laterally by approximately 30% to aid presentation. It can be seen that vorticity (Figure 6.5 (b)) presents the information in a clearer format and also indicates the region of maximum vorticity, which are difficult to identify in Figure 6.5

(a). Therefore, for the remainder of this section, the focus is on representation of the streamwise vortices through vorticity contour plots. The apparent discrepancy in the locations of the vortex cores in the vector field is most likely due to the convection of the vortices relative to the surrounding fluid. This concept is discussed in more detail in Smits and Lim (2000). Correspondence between the patterns can be achieved by subtracting the vortex convection velocity from the entire pattern.

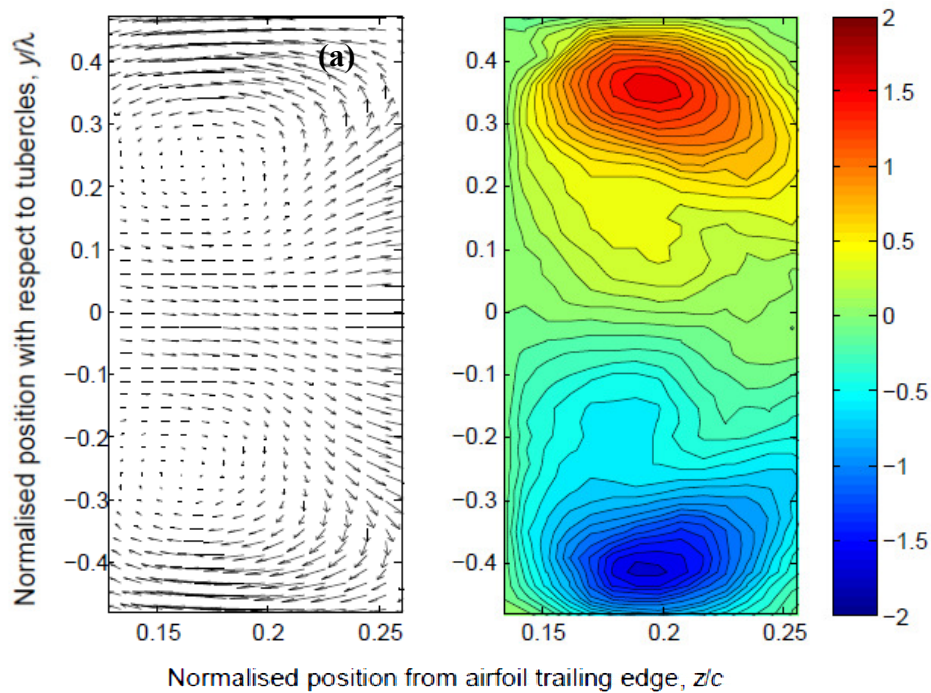


Figure 6.5 - Comparison between (a) velocity vector field and (b) vorticity contour plot at $\alpha = 15^\circ$, $x/c = 0.4$, $Re = 2230$.

A series of vorticity plots for an angle of attack of $\alpha = 5^\circ$ is shown in Figure 6.6 and each image corresponds to a unique chordwise plane. The x-axis corresponds to the distance from the airfoil trailing edge in the perpendicular direction, whereas the y-axis shows position relative to the tubercle peaks and troughs. The lower limit of the x-axis values is governed by the airfoil curvature and hence is nonzero in most cases.

It is evident that the positive and negative vorticity maxima exist approximately midway between the tubercle peak and the trough, regardless of chordwise location. These vortices, marked “P” in Figure 6.6, will henceforth be described as the primary vortices. With streamwise distance, the peak vorticity decreases and the size of the vortices increases which reflects spreading of the vorticity. It can also be observed that the primary vortices move closer to the surface as they approach the trailing edge. This

signifies that they followed the contour of the airfoil, which would be beneficial for the purposes of boundary layer momentum exchange. An additional feature present in Figure 6.6 (a) and (b) is the vorticity of opposite sign (or secondary vorticity) marked with an asterisk. This vorticity appears to be annihilated by the primary vorticity of opposite sign beneath it, so that it is absent (or nearly so) for chordwise planes further aft. The significance of this observation is discussed in Section 6.5.1. A possible mechanism responsible for the existence of this secondary opposite-sign vorticity is described in Section 6.7.

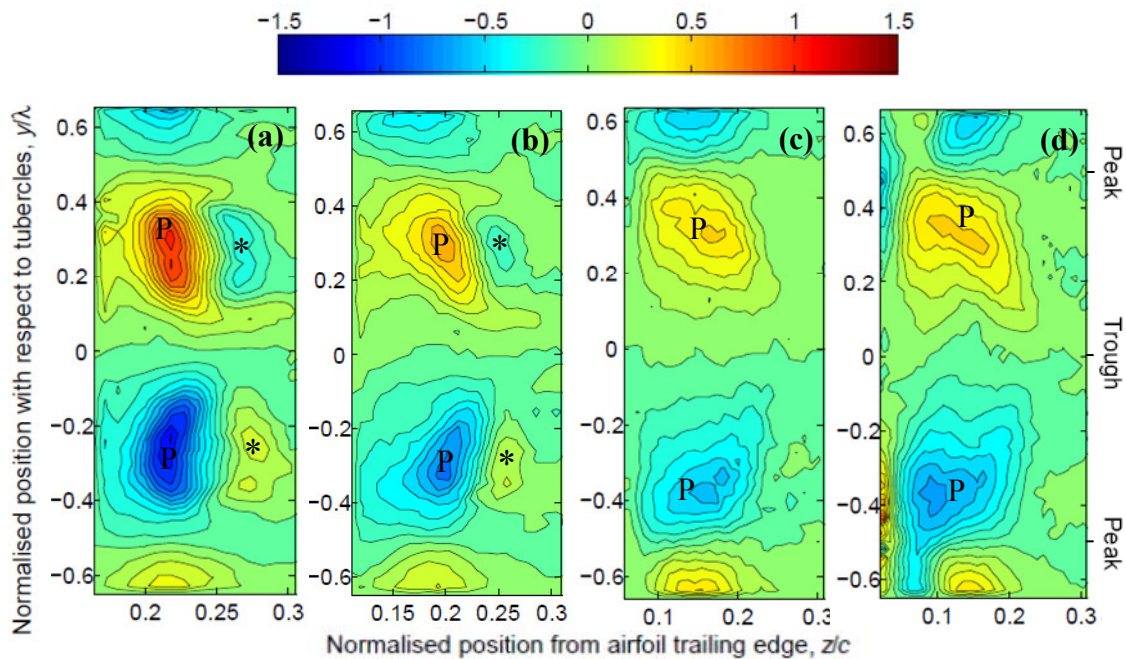


Figure 6.6 - Vorticity contours (1/s) for sequential chordwise planes at $\alpha = 5^\circ$, $x/c = 0.4$, (b) $x/c = 0.6$, (c) $x/c = 0.8$, (d) $x/c = 1$, $Re = 2230$. Asterisks mark secondary vortex structures.

Note generation of vorticity of opposite sign at the surface to the left of the streamwise vortices in (d).

Table 6.1 presents the positive and negative peak vorticity corresponding to the contour plots in Figure 6.6. The peak negative vorticity (clockwise flow rotation) is slightly stronger than the positive vortex peak. The position of positive vorticity remains almost equivalent for all four cases. However, the vorticity peaks appear to move towards the tubercle peaks in the streamwise direction. This is in contradiction to the predictions made by Custodio (2008) describing movement of the primary vortices towards the troughs between tubercles and their eventual coalescence.

Table 6.1 – Positive and negative peak vorticity for chordwise measurements planes ($\alpha = 5^\circ$).

Measurement Location (x/c)	Positive peak (1/s)	Location of positive peak [$z/c, y/\lambda$]	Negative peak (1/s)	Location of negative peak [$z/c, y/\lambda$]
0.4	0.92	[0.22, 0.30]	-0.97	[0.22, -0.24]
0.6	0.68	[0.20, 0.28]	-0.74	[0.20, -0.33]
0.8	0.55	[0.16, 0.30]	-0.56	[0.18, -0.34]
1	0.57	[0.11, 0.30]	-0.65	[0.08, -0.37]

When the airfoil angle of attack is increased to $\alpha = 10^\circ$, there is a corresponding increase in the magnitude of the vorticity, which is shown in Figure 6.7 and Figure 6.8. The image plane at $x/c = 0.2$ yielded successful results for this angle of attack only, however it can be seen from the edge effects in Figure 6.7 that it would have been more accurate to ensure that the vortices were captured closer to the centre of the imaging device. Consistent with the results at $\alpha = 5^\circ$, secondary vorticity of opposite sign are present for chordwise planes nearer to the airfoil leading edge and this is marked with an asterisk in Figure 6.7 and Figure 6.8 (a). However for $\alpha = 10^\circ$, this secondary vorticity is absent for the planes at $x/c = 0.6, 0.8$ and 1, which implies that it is annihilated in closer proximity to the leading edge in comparison with the results at $\alpha = 5^\circ$.

The magnitudes of both the positive and negative primary vorticity peaks decrease with downstream distance for the chordwise planes nearer to the leading edge ($x/c = 0.2 - 0.6$), as shown in Table 6.2. However, for the chordwise plane at the trailing edge ($x/c = 1$), the magnitudes are substantially higher. This supports the idea that annihilation of the secondary vorticity has taken place earlier and subsequent to this process, the vorticity peak increases in magnitude. Initially, the peak negative vorticity is greater than the positive peak however the diffusion of vorticity with downstream distance results in a relatively lower peak in negative vorticity. At the trailing edge, the primary vortices appear to have grown and diffused to the extent that vorticity annihilation is taking place between them.

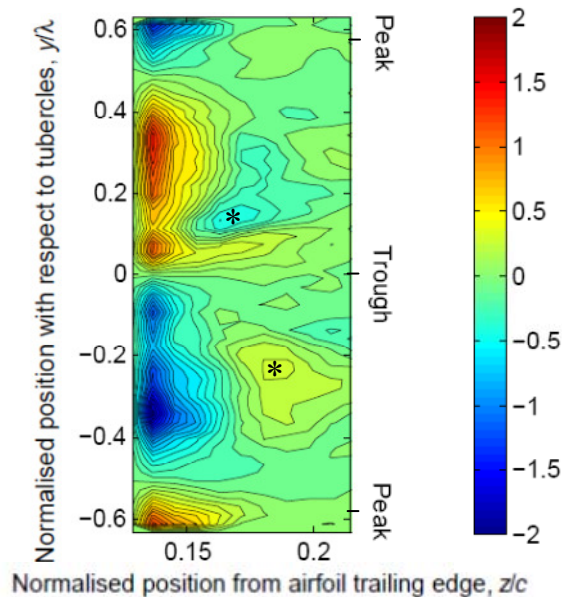


Figure 6.7 - Vorticity contours for $x/c = 0.2$ at $\alpha = 10^\circ$.

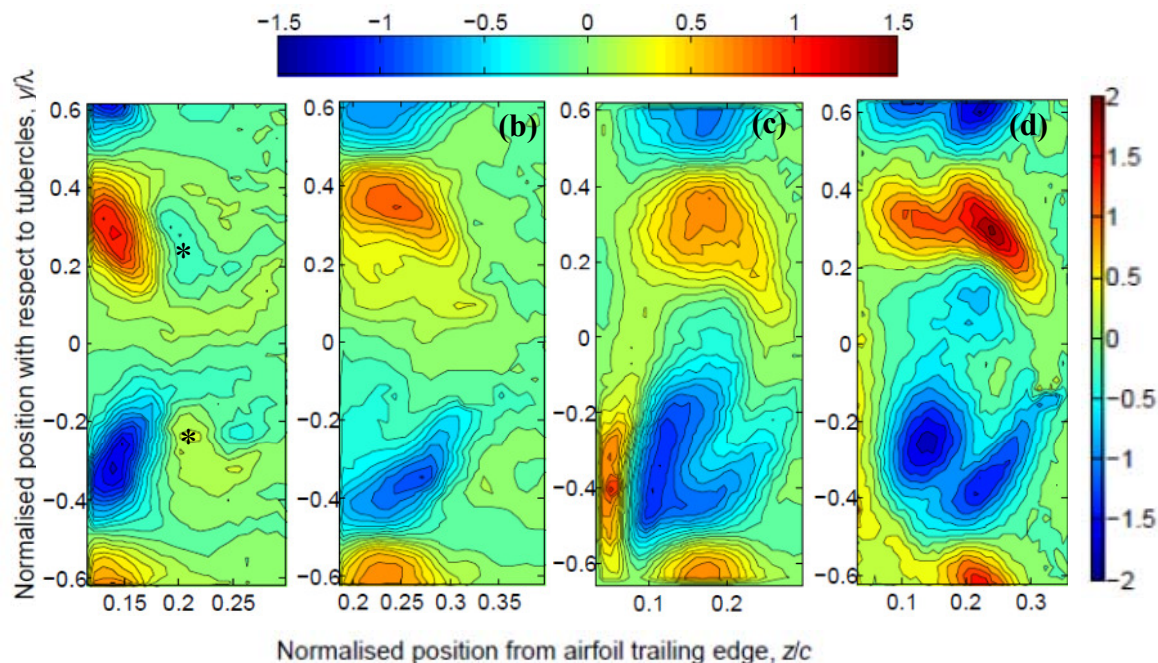


Figure 6.8 - Vorticity contours for sequential chordwise planes at $\alpha = 10^\circ$, (a) $x/c = 0.4$, (b) $x/c = 0.6$, (c) $x/c = 0.8$, (d) $x/c = 1$, $Re = 2230$. Asterisks mark secondary vortex structures. Note that a different vorticity scale is shown for the $x/c = 1$ plane.

Other interesting features include the apparent breakup of the primary vortices as well as the generation of vorticity of opposite sign near the foil surface in Figure 6.8 (c) and (d). It is possible that the vortices do not roll up into a tight, neat core and instead form several vortices which roll up together downstream. This could explain the appearance of Figure

6.3 and the unusual shapes of the primary vortices in figures such as Figure 6.8 (c) and (d).

Table 6.2 - Positive and negative peak vorticity for chordwise measurements planes ($\alpha = 10^\circ$).

Measurement Location (x/c)	Positive peak (1/s)	Location of positive peak [$z/c, y/\lambda$]	Negative peak (1/s)	Location of negative peak [$z/c, y/\lambda$]
0.2	1.47	[0.14, 0.32]	-1.86	[0.14, -0.34]
0.4	1.13	[0.14, 0.28]	-1.25	[0.14, -0.32]
0.6	0.91	[0.24, 0.35]	-0.92	[0.27, -0.35]
0.8	0.80	[0.18, 0.37]	-1.01	[0.11, -0.41]
1	2.05	[0.24, 0.29]	-1.74	[0.14, -0.24]

As the angle of attack is increased further to $\alpha = 15^\circ$, the primary vortices become more distinct and the magnitude of the vorticity becomes greater as shown in Figure 6.9. It should be noted that some of the data are unreliable near $[z/c, y/c] = [0.32, -0.05]$ in the negative vortex core for $x/c = 0.6 - 0.8$. This is attributed to a problem with the imaging apparatus which was not discovered during the experiments.

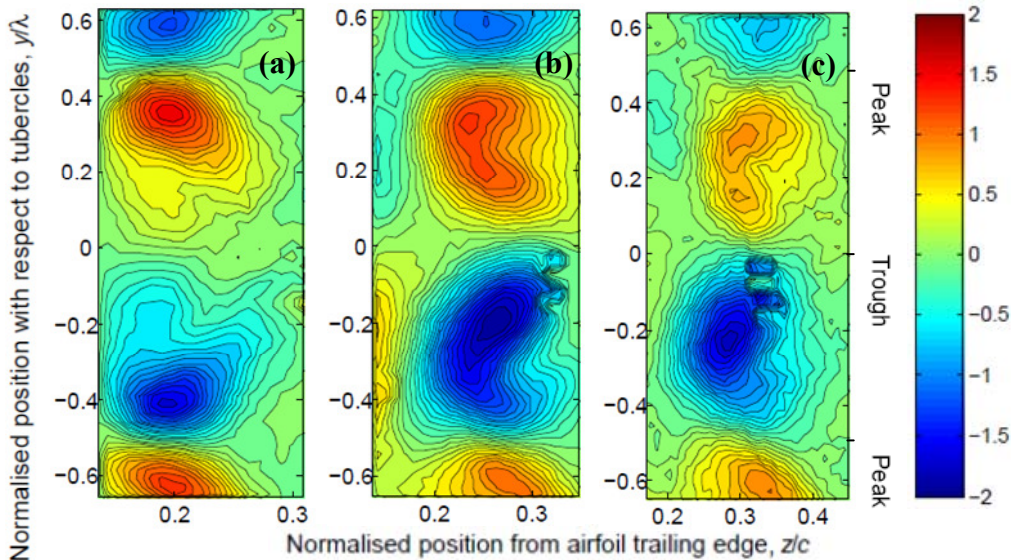


Figure 6.9 - Vorticity contours for sequential chordwise planes at $\alpha = 15^\circ$, (a) $x/c = 0.4$, (b) $x/c = 0.6$, (c) $x/c = 0.8$, $Re = 2230$.

It was decided that it would be inaccurate to replace velocity vectors in this region with a weighted average of their neighbours because there were six incorrect vectors adjacent to one another. Another difficulty was encountered when averaging the results for the $x/c = 1$ plane since the average results did not reflect the same characteristics that were

associated with a single image pair. This indicates that the flow was highly unsteady at this location which is expected since the region of separation would be largest at $\alpha = 15^\circ$ and would become progressively larger towards the trailing edge. Consequently, the temporally-averaged results for the $x/c = 1$ plane are not presented in this chapter.

There is evidence that vorticity of opposite sign is generated near the foil surface for $x/c = 0.6$, as shown in Figure 6.9 (b). It is possible that this surface vorticity is generated at other locations but was not captured in the images due to resolution limitations. Vorticity annihilation due to a combination of the proximity of the regions of positive and negative vorticity and the presence of the secondary vortices of opposite sign lead to an eventual decrease in peak vorticity. In addition, the vortex cores move towards one another as summarised in Table 6.3.

Table 6.3 - Positive and negative peak vorticity for chordwise measurements planes ($\alpha = 15^\circ$).

Measurement Location (x/c)	Positive peak (1/s)	Location of positive peak [$z/c, y/\lambda$]	Negative peak (1/s)	Location of negative peak [$z/c, y/\lambda$]
0.4	1.58	[0.19, 0.36]	-1.65	[0.19, -0.41]
0.6	1.37	[0.24, 0.32]	-1.89	[0.26, -0.20]
0.8	0.96	[0.30, 0.30]	-1.78	[0.29, -0.22]

6.5.1 Summary of Vorticity Characteristics

For all angles of attack investigated, pairs of counter-rotating streamwise vortices (primary vortices) were observed between the tubercle peaks. These vortices became larger and stronger with increase in the angle of attack. In the streamwise direction, the primary vorticity appears to have grown and diffused to the extent that, for $\alpha = 15^\circ$, vorticity annihilation between the primary vortices began to take place before the trailing edge. It was also noted that vorticity of opposite sign was generated near the airfoil surface for some cases and may have existed for all cases but could only be observed in images which were in close range of the trailing edge.

At angles of attack of $\alpha = 5^\circ$ and $\alpha = 10^\circ$, pairs of secondary vortices of opposite sign formed near the leading edge on the flow side of the primary vortices, and were advected

above the primary vortices and then were rapidly annihilated. The presence of these vortices appears to be a consistent feature for the lower angles of attack near the leading edge. Their location was also relatively constant and it appears that they were the result of a secondary vortex roll-up from the tubercles. Details of the surface flow pattern around the tubercles needs to be investigated in order to properly understand the origin of these vortices. A proposed flow pattern is discussed in Section 6.7.

6.6 Circulation

The regions enclosed by the path of integration are shown superimposed on the vorticity contour plots in Figure 6.10. It can be seen that the vorticity threshold of $\omega = 0.1$ and maximum radius (shown in Table 6.4) constraints provide reasonable bounds for defining the closed path of integration. This is further evident through comparison with Figure 6.6, where the boundary between positive and negative vorticity is more clearly defined.

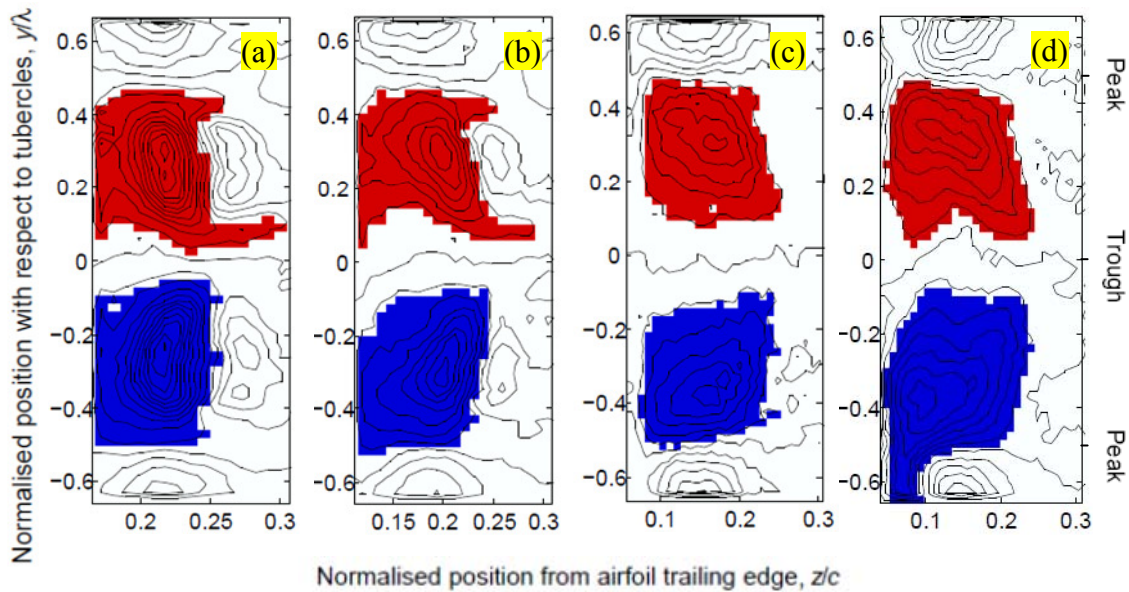


Figure 6.10 - Path of integration and enclosed region for $\alpha = 5^\circ$, where: (a) $x/c = 0.4$, (b) $x/c = 0.6$, (c) $x/c = 0.8$, (d) $x/c = 1$, $Re = 2230$. Red - positive vortex core, blue - negative vortex core.

Results from the integration for $\alpha = 5^\circ$ are shown in Table 6.4, where the magnitude of circulation is listed for both the positive and negative primary vortex cores. In both cores the circulation magnitude decreases between the $x/c = 0.4$ and $x/c = 0.6$ planes due to the presence of secondary vorticity with opposite sign adjacent to the primary vortices, which was indicated with an asterisk in Figure 6.6 (a) and (b). This annihilation process is further evidenced by the closely-spaced contours of vorticity between the primary and secondary

structures. At the $x/c = 0.8$ plane, the secondary structures are weak or absent altogether, indicating that annihilation is nearly complete. Subsequently, the circulation of the primary vortices increases for the $x/c = 0.8$ and $x/c = 1$ planes, which could be due to entrainment of wall vorticity generated beneath the adjacent primary vortices.

Table 6.4 - Circulation for chordwise measurements planes ($\alpha = 5^\circ$).

Measurement Location (x/c)	Radius of integration (mm)	Positive circulation, Γ_{vel} (mm^2s^{-1})	Negative circulation, Γ_{vel} (mm^2s^{-1})
0.4	14	26.8	-30.4
0.6	14	24.9	-29.6
0.8	14	30.8	-31.8
1	16	39.1	-51.4

The regions of integration for an angle of attack of $\alpha = 10^\circ$ are shown in Figure 6.11 and Figure 6.12. For this particular case, the maximum radius of the integration contour was increased to account for the “tail” associated with the positive vorticity evident in Figure 6.11 and Figure 6.12 (a). Also, for the locations downstream of the $x/c = 0.4$ plane, the area of interest defined by the minimum vorticity threshold became substantially larger. This increase in vorticity spreading coincides with the point at which the secondary vorticity has been substantially annihilated, which occurs by the $x/c = 0.6$ plane as shown in Figure 6.12(b).

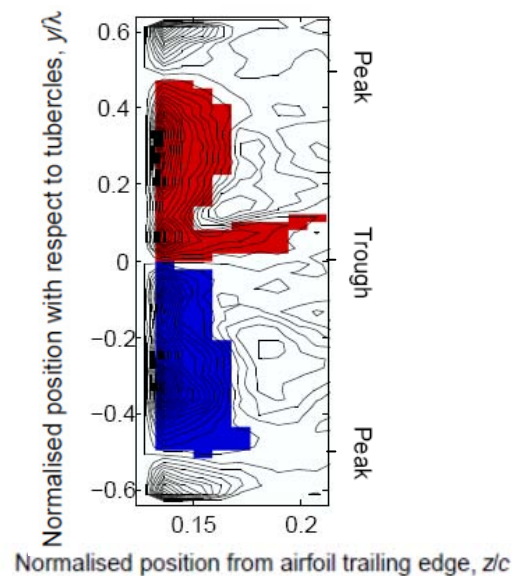


Figure 6.11 - Path of integration and enclosed region for $\alpha = 10^\circ$, $x/c = 0.2$ plane. Red - positive vortex core, blue - negative vortex core.

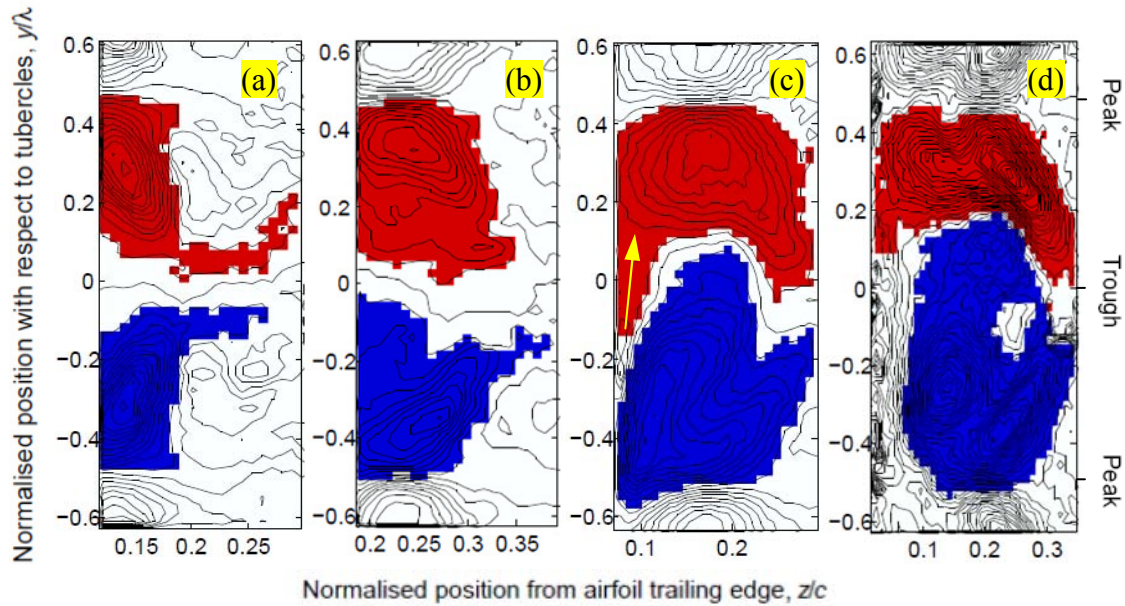


Figure 6.12 - Path of integration and enclosed region for $\alpha = 10^\circ$, where: (a) $x/c = 0.4$, (b) $x/c = 0.6$, (c) $x/c = 0.8$, (d) $x/c = 1$, $Re = 2230$. Red - positive vortex core, blue - negative vortex core. The yellow arrow indicates a possible pathway of vorticity entrainment.

Close to the leading edge, the circulation associated with the positive and negative primary vortex cores is relatively similar, however for $x/c = 0.8$ and $x/c = 1$ there is a substantial increase in negative circulation. This information is summarised in Table 6.5. Compared to the results for $\alpha = 5^\circ$, the circulation is only slightly greater at the higher angle of attack for the $x/c = 0.4$ plane but the difference in values becomes considerably larger for the planes further downstream. The rate at which the positive and negative values of circulation deviate from one another also increases with downstream distance.

Table 6.5 - Circulation for chordwise measurements planes ($\alpha = 10^\circ$).

Measurement Location (x/c)	Radius of integration (mm)	Positive circulation, Γ_{vel} (mm^2s^{-1})	Negative circulation, Γ_{vel} (mm^2s^{-1})
0.2	24	11.7	-12.0
0.4	24	27.5	-29.9
0.6	24	44.7	-38.3
0.8	24	58.7	-88.0
1.0	24	114.0	-178.8

The absence of the secondary vortex structures results in a larger area of integration at $\alpha = 15^\circ$ for all planes investigated, as shown in Figure 6.13. Consequently, a more gradual process of vortex spreading was observed to occur. On the other hand, it is noted that at the $x/c = 0.8$ plane, the magnitude of the positive circulation has decreased as shown in Table 6.6, which was not observed for the lower angles of attack. This is attributed to the closer proximity of the negative vortex which has a much larger associated circulation. The magnitude of the negative circulation continues to increase with downstream distance.

In terms of the potential errors introduced by the unreliable data present within the region of negative vorticity, an analysis was carried out where the circulation of this region was approximated and then replaced by an appropriate contour level. The choice of this contour level was based on the surrounding values of circulation. The resultant value of negative circulation was compared to that which was obtained when this region was maintained in its original state. The difference in the value of negative circulation was around 3% for $x/c = 0.6$ and 7% for $x/c = 0.8$ and hence deemed acceptable.

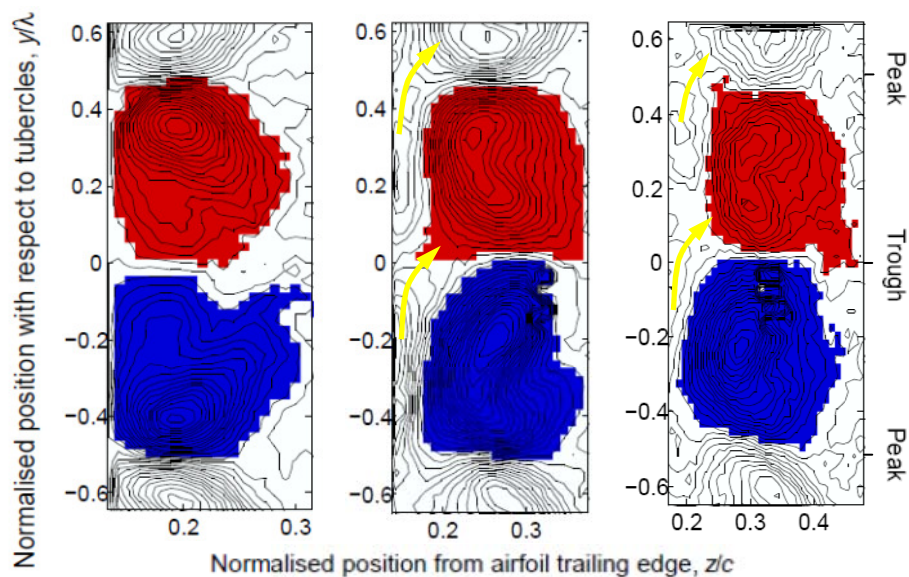


Figure 6.13 - Path of integration and enclosed region for $\alpha = 10^\circ$, where: (a) $x/c = 0.4$, (b) $x/c = 0.6$, (c) $x/c = 0.8$, (d) $x/c = 1$, $Re = 2230$. Red - positive vortex core, blue - negative vortex core. Yellow arrows indicate possible pathways of vorticity entrainment.

Table 6.6 - Circulation for chordwise measurements planes ($\alpha = 15^\circ$). Circulation values calculated without erroneous region are shown in brackets.

Measurement Location (x/c)	Radius of integration (mm)	Positive circulation, Γ_{vel} (mm^2s^{-1})	Negative circulation, Γ_{vel} (mm^2s^{-1})
0.4	18	66.8	-71.0
0.6	14	99.3	-127.7
0.8	18	76.0	-131.7

6.7 Discussion of Circulation

In summary, the circulation increased with angle of attack for both the positive and negative primary vortices as shown in Figure 6.14. Generally, the circulation also increased in the streamwise direction for all angles of attack. Minor variations in this increase are attributed to the presence of opposite-sign secondary vorticity, which was observed at low angles of attack on the “right” side of the primary vortex. Vorticity of opposite sign was also observed adjacent to the airfoil surface, which was most notable in Figure 6.8 (c) and (d) and Figure 6.9 (b). It is believed that this vorticity contributes to the increasing primary circulation. However, the averaging process would mask the associated mechanism as it is most likely time-dependent in nature.

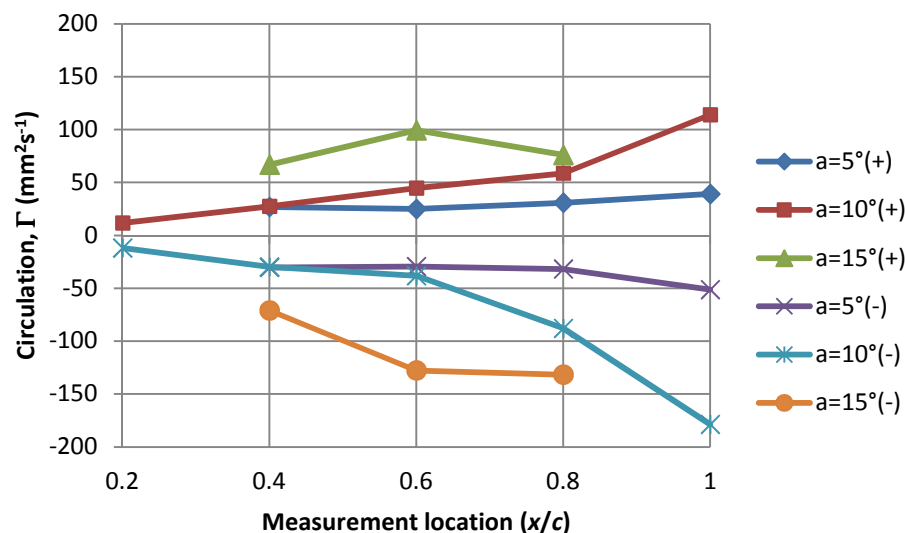


Figure 6.14 – Circulation variation with angle of attack and chordwise position.

According to Thompson (1869), in the absence of viscous stresses and density variations, the circulation of a vortex tube must remain constant. Therefore, since there is no density

variation, the increase in circulation of the primary vortices must be due to the presence of viscous stresses, in this case, at the wing surface.

Therefore, a proposed mechanism for the increase in circulation is shown in Figure 6.15, where the primary and wall vortices are indicated in Figure 6.15 (a). It can be seen in Figure 6.15 (b) that the negative wall vorticity near the surface is entrained by the negative primary vortex, which could describe one extreme pattern of the flow. The opposite extreme pattern is shown in Figure 6.15 (d), where positive wall vorticity is entrained by the positive primary vortices. The pattern shown in Figure 6.15 (c) is believed to represent the intermediate state. This mechanism may also involve vorticity transported to vortices formed behind adjacent tubercles. This is indicated in Figure 6.15 by the dashed arrows which show flow movement behind the tubercle peaks.

The entrainment of wall vorticity by the primary vortices would increase the associated circulation as found in the experimental results presented in Figure 6.14. The patterns of alternating symmetry presented by Custodio (2008) could represent a stable version of the proposed unsteady pattern shown in Figure 6.15. Due to the large component of uncertainty for the instantaneous images, it was not possible to verify this proposition.

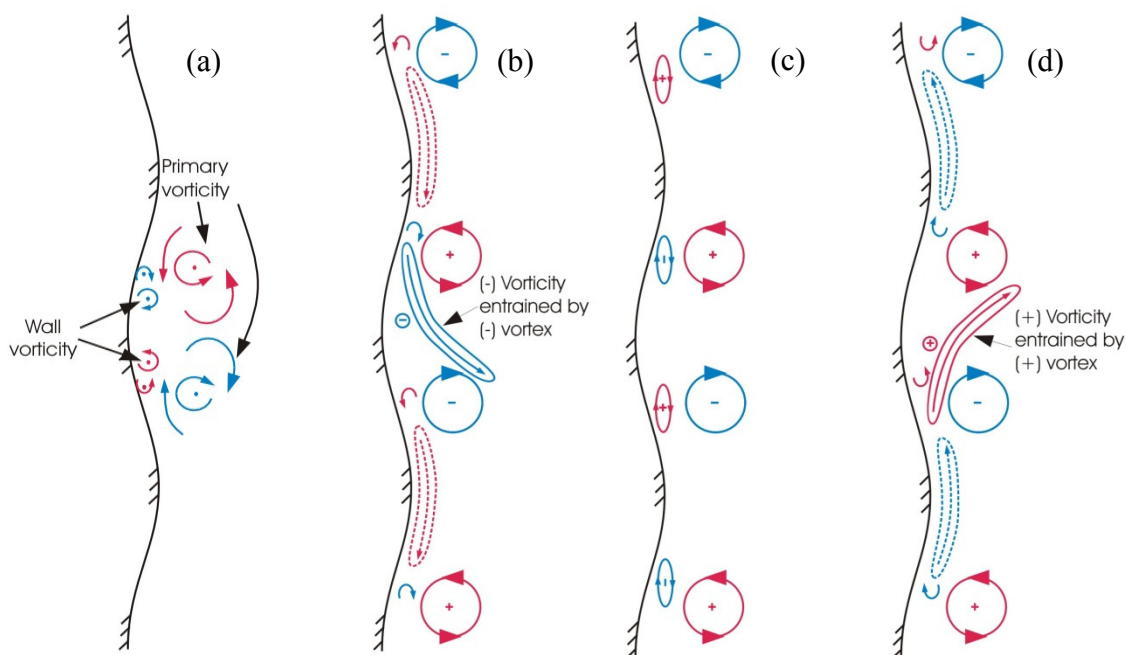


Figure 6.15 – Schematic showing wall vorticity close to the surface being entrained by the primary vortices at adjacent locations. Dashed arrows indicate transport of vorticity to adjacent troughs between tubercles

It is useful to study the relationship between the primary and secondary vorticity indicated in Figure 6.6, Figure 6.7 and Figure 6.8 in order to develop a possible explanation for the generation of streamwise vorticity. It is proposed that the flow topology resembles that which is referred to as an owl-face pattern of the second kind (Perry & Chong, 1987), as indicated in Figure E1 (c) of Appendix E, which was adapted from Tobak and Peake (1979) for slender, low-aspect-ratio wing. The roll-up of the primary vorticity is shown in Figure E1 (g) and this marks the point of initiation of the primary streamwise vortices. One possible vortex skeleton pattern for the pattern shown in Figure E1 is depicted in Figure E2 from Perry & Chong (1987) and illustrates the relative position of the primary and secondary vortices. This three-dimensional pattern confirms the flow visualisation observation in Section 6.2 that streamlines diverge some distance above the surface of the airfoil due to the presence of the primary vortices. Additionally, it can be seen that near the surface, the streamlines converge towards the troughs, which is consistent with the numerical results of Watts and Fish (2001) and the flow visualisation of Custodio (2008).

6.8 PIV Uncertainty Analysis

This analysis is carried out for a single instantaneous image and subsequently, the calculated uncertainty is converted to a value which characterises the uncertainty in the averaged results. The representative case of $x/c = 0.4$, $\alpha = 5^\circ$ was chosen at random to illustrate the process involved in determining the uncertainty. A representative displacement of $\Delta D \sim 0.9\text{px}$ was determined for this particular case.

6.8.1 Estimation of Systematic Uncertainty in Particle Displacement

As discussed in Section 3.6.16, the perspective uncertainty, δ_p , is relatively significant for 2D PIV as the position of the particle within the light sheet in the thickness direction is unknown. Equation (6.1) is used for calculating δ_p and is derived from Figure 3.40 and agrees with the relations presented in the literature (Reeves & Lawson, 2004):

$$\delta_p = m \left[\frac{x}{d_o} (\Delta z) \right] \quad (6.1)$$

where,

m = magnification = 0.23 (see Section 3.6.4)

x = distance from camera centreline to outer edge of vortex

d_o = distance between object and image planes = 1550mm

Δz = light sheet thickness = 2mm.

For the $x/c = 0.4$, $\alpha = 5^\circ$ case, the distance from camera centreline to outer edge of vortex was 15mm. Hence, the calculated value of the perspective uncertainty is $\delta_p = 0.11$. The corresponding relative uncertainty is $\varepsilon_p = \sigma_p / \Delta D = 0.12$. Perspective uncertainty can be reduced by using a stereoscopic PIV system (Reeves & Lawson, 2004), which would be a strong recommendation for future work.

6.8.2 Estimation of Random Uncertainty in Particle Displacement

The method for determining the random uncertainty in particle displacement is outlined below and accompanied by analysis for a particular case. The individual contributions to the uncertainty from various components of the experimental system are estimated. There are numerous potential sources of random uncertainty in applying the particle image velocimetry technique but it is most important to identify those which have the largest impact on the overall results. The following paragraphs outline typical sources of uncertainty for an instantaneous image pair, which contribute most significantly to the overall uncertainty. Calculation of the relative uncertainty enables both comparison between the various sources of uncertainty and also determination of the overall uncertainty.

The laser triggering mechanism suffers from a random variation in frequency known as “jitter” which reduces the accuracy of the time delay parameter, ΔT . According to manufacturer’s specifications (Quantel, 2002) the jitter time, δ_t , is estimated to be 250ns. Hence, the relative uncertainty due to jitter, ε_t , is $\varepsilon_t = \delta_t / \Delta T$, where ΔT is the time delay used in the experiments. The relevant time delay is $\Delta T = 30\text{ms}$, giving a relative uncertainty of $\varepsilon_t = 8.3 \times 10^{-3}$. The corresponding relative displacement uncertainty is equivalent since for a given velocity the displacement and time are directly proportional to one another.

The particle image diameter can impact on the accuracy of the cross-correlation procedure. According to the results from Monte Carlo simulations conducted by Raffel *et al.* (1998) shown in their Figure 5.23a, for an estimated worst-case scenario with $d_e = 1.5\text{px}$, the uncertainty is $\delta_e = 0.03$. Using a representative displacement of 0.9px , the relative uncertainty in displacement is $\varepsilon_e = \delta_e/\Delta D = 0.03$.

The uncertainty in particle displacement, ΔD , is a function of the seeding density and can be found from Figure 6b in Willert and Gharib (1991) as discussed in Section 3.6.12. A pessimistic estimate for the seeding density is 6 particles per interrogation window. This gives a value for $\delta_{\Delta D} \sim 0.07$ for a displacement of 0.9px . Hence, the relative uncertainty in displacement is $\varepsilon_{\Delta D} = \delta_{\Delta D}/\Delta D = 0.08$.

Sub-optimal levels of particle seeding can also have a negative impact on the results. The associated uncertainty, δ_N , can be determined with reference to Figure 5.29 in Raffel *et al.* (1998). Assuming a low seeding density of 5.2 particles per interrogation window as a worst case, the associated uncertainty is found to be $\delta_N \sim 0.036$. Therefore, the relative uncertainty is $\varepsilon_N = \delta_N/\Delta D = 0.04$.

A further consideration to take into account is the uncertainty related to the magnification scale used, which is determined from a target image having a grid with known spacing. A visual inspection of the target image and overlaid ruler scale enables estimation of the associated uncertainty, where $\delta_m = 2\text{px}$. The relative uncertainty is found by considering the total grid width, w_g as the denominator, giving: $\varepsilon_m = \delta_m/w_g = 2/1008 = 0.002$.

Regions of high velocity gradient will have a larger associated uncertainty because not all of the particle images present in the first interrogation window will also be present in the second. Through Monte Carlo simulations, Raffel *et al.* (1998) determined the uncertainty for various particle image densities and interrogation window sizes. Here, the positive vortex core is considered and the displacement gradient in both the horizontal ($\partial(\Delta D_z)/\partial y$) and vertical ($\partial(\Delta D_y)/\partial z$) directions can be determined. These values were found by plotting the particle displacements in the z and y directions along axes corresponding to the location of positive vortex peak, as shown in Figure 6.16.

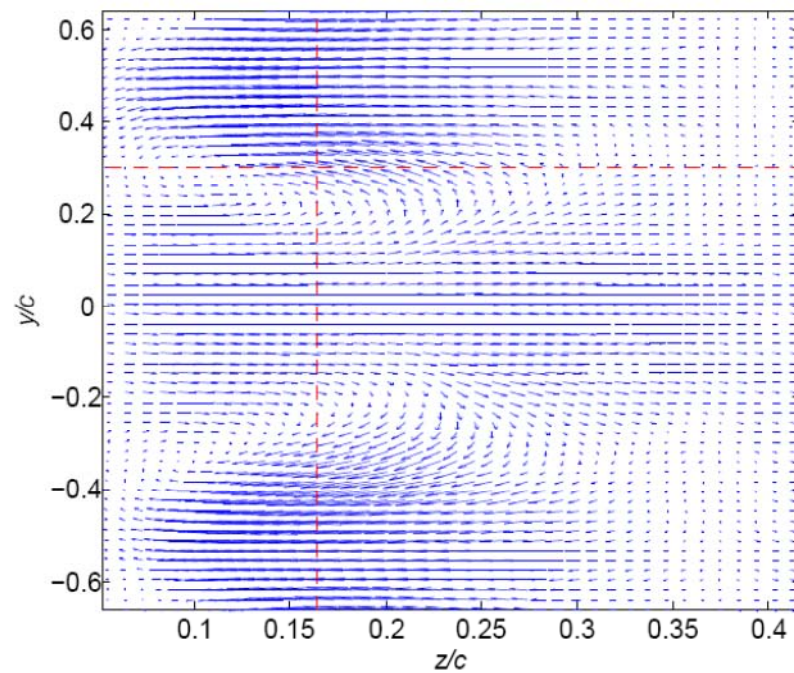


Figure 6.16 – Vector plot of velocity vectors for $0.4\bar{c}$, $\alpha = 5^\circ$ case, where the dashed red lines cross at the point of maximum positive vorticity, $Re = 2230$.

The maximum gradients were then determined from the maximum slope of any given tangent as depicted in Figure 6.17 and Figure 6.18. Figure 5.33 in Raffel *et al.* (1998) was then consulted and the plot corresponding to a particle image density, $N_I = 5$ and interrogation window size of 32×32 px is used to determine the uncertainty which is $\delta_g \sim 0.08$. The relative uncertainty is calculated as $\varepsilon_g = \delta_g / \Delta D = 0.09$.

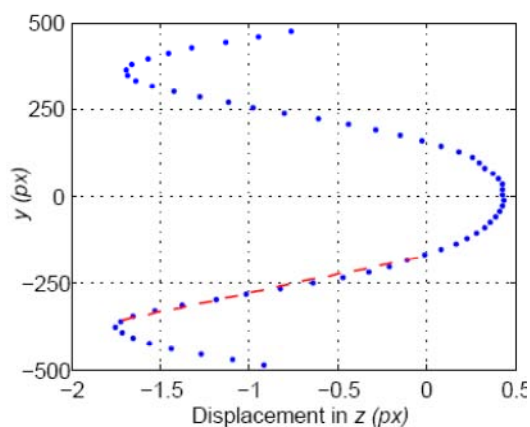


Figure 6.17 – Particle displacement in z with respect to y location, where dashed red line shows the associated maximum gradient, $Re = 2230$.

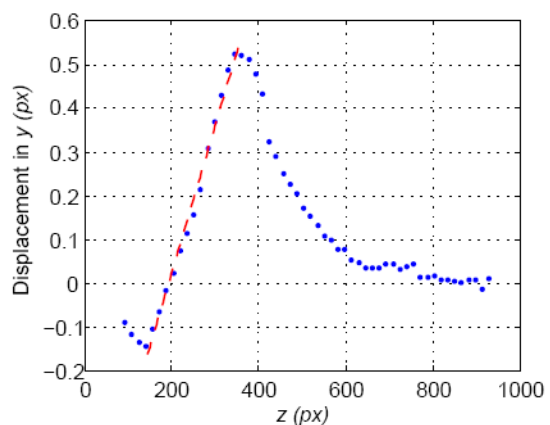


Figure 6.18 – Particle displacement in y with respect to z location, where dashed red line shows the associated maximum gradient, $Re = 2230$.

The overall uncertainty for a given image pair is determined by combining the relative uncertainties and this gives an estimate of the relative random velocity uncertainty, ε_u :

$$\varepsilon_u = \sqrt{\varepsilon_p^2 + \varepsilon_t^2 + \varepsilon_e^2 + \varepsilon_{\Delta D}^2 + \varepsilon_N^2 + \varepsilon_m^2 + \varepsilon_g^2} = 0.18 \quad (6.2)$$

The average uncertainty takes into account the total number of image pairs which were averaged. Therefore, assuming that the distribution of random errors in the velocity field is approximately Gaussian and that there exist at least 2000 valid vectors for each image pair, $\varepsilon_{u(av)} = \varepsilon_u / \sqrt{2000} = 0.004$. This value does not change if there are slightly more or fewer outliers.

6.8.3 Uncertainties in Vorticity Estimation

The uncertainty in the vorticity estimate can be broken down into two independent components: random uncertainty in vorticity, $\varepsilon_{\omega\text{-rand}}$, and bias uncertainty in vorticity, $\varepsilon_{\omega\text{-bias}}$. The former component is the ratio of noise transmission, λ_0 , from the velocity field to the vorticity field and is dependent on the random velocity error, ε_u , and the relative velocity sample spacing, Δ/L . The latter component considers the consistent over-estimation or under-estimation by a given vorticity scheme and is only dependent on the sample spacing, Δ/L . In order to determine these uncertainties, the uncertainty propagation analysis of Fouras and Soria (1998) is utilised with reference to Lau (2010). The random error in vorticity, $\varepsilon_{\omega\text{-rand}}$, is defined by Equation (6.3):

$$\varepsilon_{\omega\text{-rand}} = \frac{\varepsilon_u \times \lambda_0}{L} \quad (6.3)$$

where,

L is a suitable length scale.

The noise transmission ratio, λ_0 , depends on the chosen vorticity estimation scheme and is calculated using Equation (6.4):

$$\lambda_0 = \frac{K}{\Delta/L} \quad (6.4)$$

where,

K is a constant and for the central difference scheme, $K = 1$ (Etebari & Vlachos, 2001),

Δ is the grid spacing.

The length scale, L , is found through assuming that the vortex has a Gaussian distribution. This means that 95% of the vorticity lies in the range of ± 2 standard deviations. Hence:

$$\frac{\Delta}{L} = \frac{4}{n_v} \quad (6.5)$$

where,

n_v is the number of vectors across the diameter of a vortex and $n_v \sim 20$ (through visual inspection).

Hence, $\Delta/L = 0.2$, $\lambda_0 = 5$ and $L = 1.29/0.2 = 6.45$. Therefore, the random uncertainty in vorticity, $\varepsilon_{\omega-random}$, for the $0.4\bar{c}$, $\alpha = 5^\circ$ case is 0.2%.

The bias uncertainty, $\varepsilon_{\omega-bias}$, is found from Table C.4 in Lau (2010), which is based on numerical simulations of the Oseen vortex. The value of $\varepsilon_{\omega-bias}$ is 1.4% and this term dominates the total error which is therefore equivalent, i.e. ε_{ω} is 1.4%.

6.8.4 Uncertainties in circulation estimation

The random and bias components of the uncertainty in circulation $\varepsilon_{\Gamma-random}$ and $\varepsilon_{\Gamma-bias}$ are both dependent on the random velocity error, ε_u , and the relative velocity sampling spacing, Δ/L . According to Figure 2 and 3 in Hassan *et al.* (2007), the estimated random uncertainty in circulation, $\varepsilon_{\Gamma-random} < 0.002\%$ and the estimated random uncertainty, $\varepsilon_{\Gamma-bias} < 0.01\%$ for the $x/c = 0.4$, $\alpha = 5^\circ$ case, giving a total estimated uncertainty of $\varepsilon_{\Gamma} < 0.01\%$.

6.9 Summary

From the results presented in this chapter, it is clear that tubercles give rise to the formation of stream-wise vortices, which have been observed by several researchers (Fish & Battle, 1995; Miklosovic *et al.*, 2004; Custodio, 2008; Pedro & Kobayashi 2008). The hydrogen bubble flow visualisation results show that flow was accelerated in the troughs between tubercles, leading to a region of low pressure in the troughs at the leading edge, which is consistent with Watts and Fish (2001) and the results presented in Chapter 5 of this thesis. The flow from behind the peaks was entrained towards this apparent low-pressure region, giving rise to a pair of counter-rotating vortices behind each trough. In addition, the flow was observed to separate earlier behind the tubercle troughs than the peaks, which was explained by van Nierop *et al.* (2008) as the result of a smaller chord length at the trough and hence larger adverse pressure gradient. Hence the spanwise variation of pressure gradient suggested by van Nierop *et al.* (2008) is supported but the absence of streamwise vortices is refuted.

Comparison between the hydrogen bubble flow visualisation results for airfoils with varying tubercle configurations revealed similarities between the flow patterns for tubercles with the same amplitude-to-wavelength (A/λ) ratio and hence equivalent maximum angle of leading edge sweep. It is possible that the resemblance between flow patterns was the result of a similar vortex strength for these cases, which was mentioned by Custodio (2008). The visualisation results also showed that the wavelength of the tubercle configuration influenced the degree of mixing in the boundary layer and that the A/λ ratio may have affected the vortex strength. Reduction in the spacing between tubercles resulted in behaviour analogous to turbulence generators, where there was an apparent increase in boundary layer mixing and a more uniform attachment of the boundary layer near the trailing edge.

Overall, the peak vorticity and circulation of the primary streamwise vortices increased with angle of attack for a given measurement plane. It was found that at lower angles of attack ($\alpha = 5^\circ$ and $\alpha = 10^\circ$), secondary vorticity of opposite sign was present near the leading edge and the process of annihilation led to a small decrease in the primary vortex circulation in the downstream direction for these cases. In the

absence of secondary vorticity, the circulation of the primary vortices was found to increase in the downstream direction, most likely due to entrainment of wall vorticity by the primary vortices. For a given angle of attack, the positive and negative peak primary vorticity tended to decrease in the downstream direction whilst the region of vorticity expanded.

For locations nearer the leading edge, the vorticity and circulation associated with the positive primary vortex core was similar to that associated with the negative primary vortex core. However, towards the trailing edge, the magnitude of both the vorticity and circulation for the negative primary vortex core was generally higher for all angles of attack. The larger observed negative circulation for the $x/c = 0.8$ and $x/c = 1$ locations was due to the increased size of the region of integration as well as increased vorticity. It should be noted that the image sequences become more time dependent near the trailing edge and hence the average became a less accurate representation of the actual flow field. Increasing the number of averages did not significantly improve this issue and thus it would be necessary to analyse the images as a sequence in time to obtain meaningful results. Nevertheless, asymmetry in the flow may also have been responsible for the larger region of negative vorticity. It is possible that as the primary vortices moved further downstream along the airfoil chord, there was a transfer of wall vorticity between adjacent tubercle troughs. It has previously been suggested that alternate wavelengths of the tubercle pattern would demonstrate similar characteristics (Custodio, 2008). Hence, it would be useful to study several tubercle wavelengths with minimal wall effects. The proximity of the water tunnel walls may have influenced the results observed by Custodio (2008).

Chapter 7

Acoustic Measurements



7.1 Introduction

This chapter describes an experimental investigation into the effects of leading edge modifications on airfoil self noise at a Reynolds number of $Re \sim 120,000$. The ability of tubercle and wavy configurations to eliminate tonal noise is demonstrated for both a closed-section wind tunnel and an anechoic wind tunnel. For the anechoic wind tunnel, it is also possible to observe a reduction in the broadband noise level for certain frequency ranges for the modified airfoils. The influence of a given tubercle and wavy configuration on the generation of tonal noise is also explored for the NACA 0021 airfoil. This enables a correlation to be formed with regards to the importance of the amplitude and wavelength parameters on tonal noise elimination. In addition, the effect of the profile shape on noise reduction for airfoils with tubercles is investigated through comparison of results for the NACA 0021 and NACA 65-021 airfoils. The observed results are related back to the existing body of evidence in order to shed light on the airfoil tonal noise generation mechanism. The experimental arrangements are discussed in Section 3.7.

7.2 Calibration

Prior to the experiments, both microphones were calibrated using two different calibrators operating at 1000Hz. The post-calibration measured sound pressure level (SPL) signals for the 94dB and 114dB calibrators are shown in Figure 7.1 and Figure

7.2 for the microphone placed near the exit of the wind tunnel. It could be argued that calibration of the microphones was not absolutely necessary for the measurements taken in this study. This is because the quantity of interest was the relative difference between the noise generated by airfoils with tubercles and the noise generated by the unmodified airfoil. For this reason, the microphone positions were not specifically selected based on where tonal noise was expected to be loudest. On the other hand, since the microphone positions have been specified exactly in Section 3.7, and used for all airfoils tested, it was believed that the actual magnitude of the tonal noise may be of interest as well.

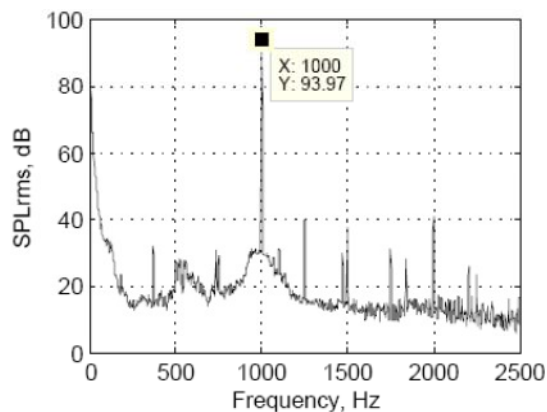


Figure 7.1 – Measured signal after calibration using 94dB calibrator.

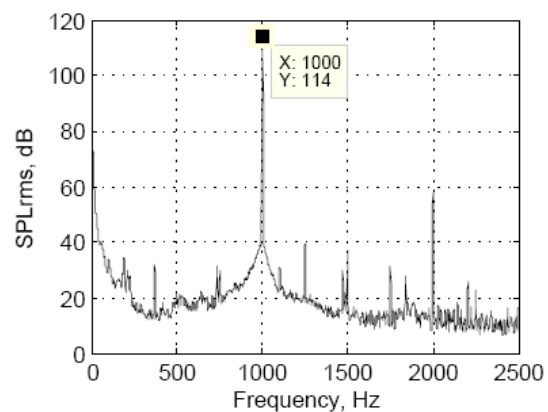


Figure 7.2 – Measured signal after calibration using 114dB calibrator.

7.3 Acoustic Measurements in Hard-Walled Wind Tunnel

Preliminary tonal noise measurements were conducted in the hard-walled wind tunnel (HWT) since it was observed that there was an audible difference in tonal noise between models with and without tubercles. Hence, it could be argued that the difference in noise levels was large enough to be measured. The influence of the duct on tonal noise propagation was monitored through comparing the results from two microphones positioned at different streamwise locations. Measurement of the duct modes was not considered pertinent to the investigation because the leading edge tubercles did not change the reflecting surface of the airfoil significantly. Therefore, significant differences in tonal noise for airfoils with and without tubercles were attributed to altered flow characteristics associated with the presence of tubercles.

Measurements were carried for an angle of attack range of $0^\circ \leq \alpha \leq 20^\circ$. For the hard-walled wind tunnel, tonal noise was only evident for $1^\circ \leq \alpha \leq 8^\circ$ for the NACA 0021 airfoil and $7^\circ \leq \alpha \leq 10^\circ$ for the NACA 65-021. The increase in the angle of attack at which the tonal noise occurred for the latter airfoil is possibly related to the fact that it has a higher stall angle. According to McAlpine *et al.* (1999), tonal noise would not occur if separation occurred sufficiently far from the airfoil trailing edge. This would be accompanied by an earlier onset of a turbulent boundary layer which was found to eliminate tonal noise in experiments performed with a boundary layer trip (Hersh & Hayden, 1971; Paterson *et al.*, 1971).

7.3.1 Noise Levels Associated with NACA 0021 Airfoil

At each angle of attack from $\alpha = 1^\circ$ to $\alpha = 8^\circ$, it is found that the unmodified NACA 0021 airfoil generated tonal noise as shown in Figure 7.3 and Figure 7.4. These results are obtained from the microphone nearest the airfoil as well as the microphone at the exit of the working section. As expected, the overall noise level detected by the microphone closest to the duct exit is higher, since for the microphone closest to the airfoil, there is a transmission loss associated with the acrylic window that the sound had to pass through. There are some slight variations in the two sets of results which can be attributed to the variation in sound directivity with frequency, however there is only one tone which was measured for one location and not the other. This is a secondary tone at $\alpha = 5^\circ$ with a frequency of 1863Hz and it was measured at the exit only. It is only present at one angle of attack and is therefore unrelated to potential noise sources from the wind tunnel itself.

The most significant tone occurred at $\alpha = 5^\circ$ with a frequency of 1675Hz and is just over 30dB above the equivalent broadband sound pressure level (SPL) at that frequency, as measured by the microphone near the window and can be seen in Figure 7.3. The microphone near the working section exit measured a tone of the same frequency to be just over 40dB above broadband as evident in Figure 7.4.

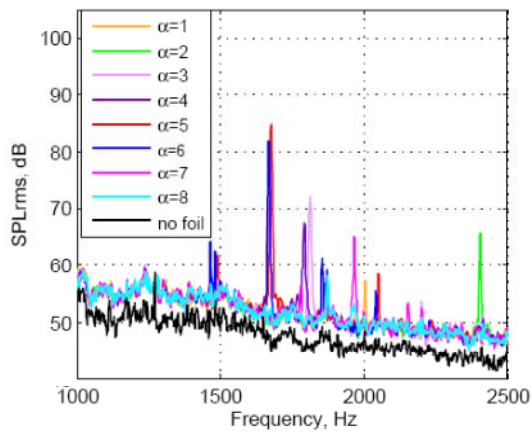


Figure 7.3 – Sound pressure level (SPL) against frequency, f , for NACA 0021 at angle of attack, $\alpha = 1-8^\circ$ (microphone at window), $Re = 120,000$.

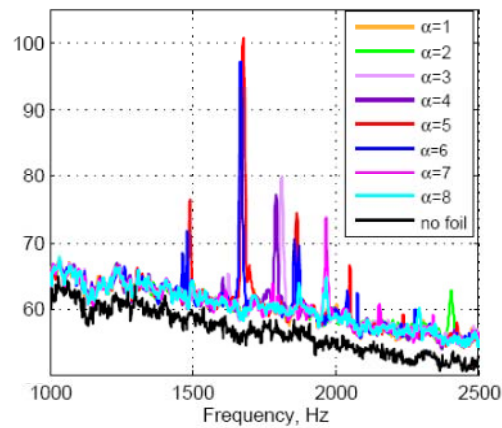


Figure 7.4 - Sound pressure level (SPL) against frequency, f , for NACA 0021 at angle of attack, $\alpha = 1-8^\circ$ (microphone at exit), $Re = 120,000$.

The results shown below in Figure 7.5 to Figure 7.8 were obtained using the microphone near the window due to its closer proximity to the airfoil and because it was located approximately 2m upstream from the other microphone, thus minimising the distance travelled by the sound. Since the highest amplitude tone was detected at $\alpha = 5^\circ$, the acoustic spectra comparison with the modified airfoils is made at this angle of attack. It should be noted that in their experimental study with a NACA 0018 airfoil, Nakano, Fujisawa and Lee (2006) found maximum tonal noise amplification at $\alpha = 6^\circ$, which is very similar to the current results.

Figure 7.5 is a plot of three separate runs at $\alpha = 5^\circ$ which were taken at different times but with exactly the same set-up. The measured SPL and frequencies of the tones show good repeatability. For a conservative estimate, the measurement with the lowest SPL at the main tone is used to compare with the results from the modified airfoils.

Figure 7.6 and Figure 7.7 present the effects on the acoustic spectra of changing the tubercle amplitude, whereas Figure 7.8 shows results for variation of the wavelength at $\alpha = 5^\circ$. Figure 7.9 shows the results for the wavy airfoils at $\alpha = 5^\circ$. In general, the airfoils with the smallest wavelength and largest amplitude tubercles (i.e. largest A/λ ratio) and all wavy airfoil configurations are the most effective at eliminating tonal noise at this angle of attack.

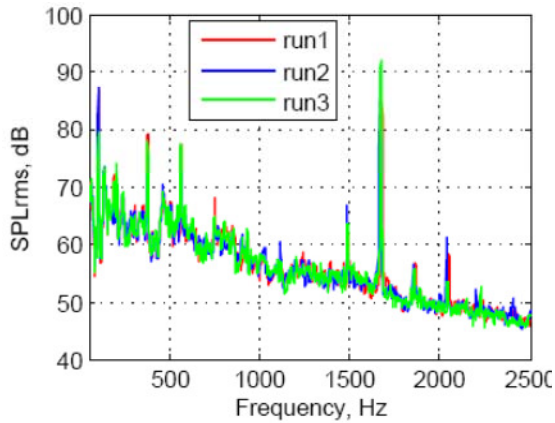


Figure 7.5 - SPL against frequency for unmodified NACA 0021 at $\alpha = 5^\circ$ for three separate runs (microphone at window), $Re = 120,000$.

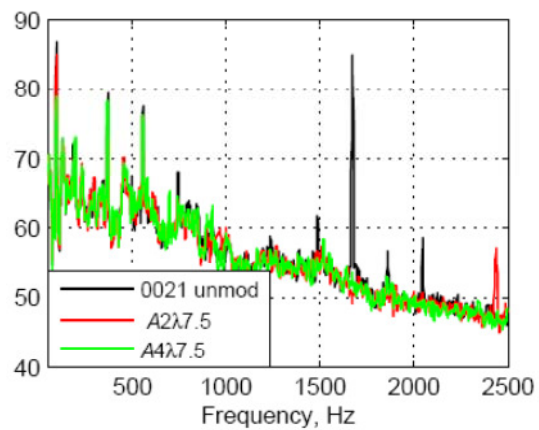


Figure 7.6 - SPL against frequency for variation of tubercle amplitude (small A) for NACA 0021 at $\alpha = 5^\circ$ (microphone at window), $Re = 120,000$.

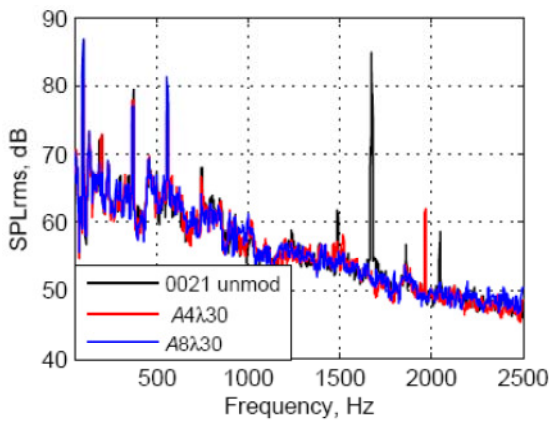


Figure 7.7 - SPL against frequency for variation of tubercle amplitude (large A) for NACA 0021 at $\alpha = 5^\circ$ (microphone at window), $Re = 120,000$.

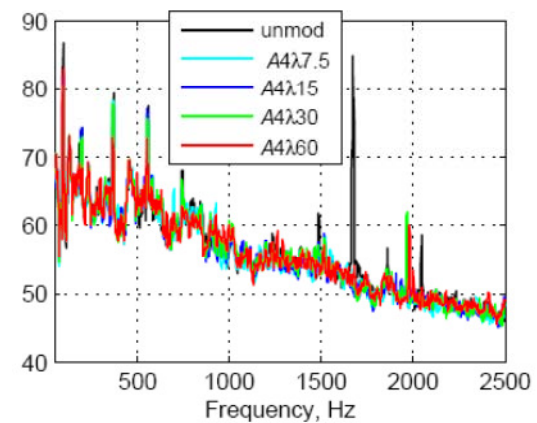


Figure 7.8 - SPL against frequency for variation of tubercle wavelength (small λ) for NACA 0021 at $\alpha = 5^\circ$ (microphone at window), $Re = 120,000$.

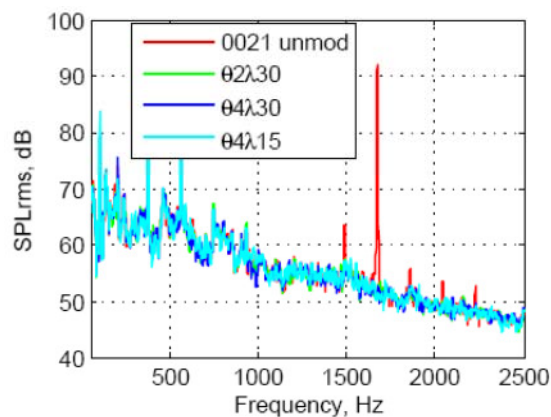


Figure 7.9 - SPL against frequency for wavy NACA 0021 variations at $\alpha = 5^\circ$ (microphone at window), $Re = 120,000$.

Interestingly, some tubercle configurations successfully removed tonal noise at the problematic frequency but then generated another tone at a higher frequency. In all cases, however, the amplitude of the new tone above the equivalent broadband SPL at that frequency was much lower than that of the original tone for the unmodified airfoil.

Results were also obtained for other angles of attack and are presented in a more condensed format. Figure 7.10 and Figure 7.11 consider the largest amplitude tone only and use the Strouhal number to represent the non-dimensional frequency. It can be seen that in general, the Strouhal number for the tonal noise is higher for airfoils with tubercles and the SPL is lower. Comparison between measurements taken with the microphone nearest the window (Figure 7.10) and that nearest the test-section exit (Figure 7.11) indicates that there is negligible variation in the Strouhal number for all angles of attack except $\alpha = 0^\circ$ where the tone was not recorded for the latter microphone. Some of the tones generated by the airfoils with tubercles were also not recorded by the microphone at the test-section exit. This was due to the directivity of the sound radiated from the duct exit, which varies with frequency. Hence at a given measurement location, some frequencies appeared to be louder and others quieter.

The sound pressure level results for other angles of attack are also shown in summarised form in Figure 7.12 and Figure 7.13. Two tubercle configurations were not included in the plots since they did not generate any detectable tonal noise. These are the largest amplitude case, $A8\lambda30$, and the smallest wavelength case, $A4\lambda7.5$, both of which have relatively large A/λ ratios. This implies that the A/λ ratio is important, however it is not possible to state that tonal noise would not be generated for a given A/λ ratio since tones were still present for the $A4\lambda15$ airfoil. Comparison between tubercle configurations which generate tonal noise reveals that the smallest wavelength case ($A2\lambda7.5$) has the highest frequency and lowest SPL amplitude at the two angles of attack at which it produces tonal noise. The largest wavelength tubercles ($A4\lambda60$) generate the lowest frequency tones at a greater number of attack angles and a higher SPL compared to the other airfoils. Note that the results in

Figure 7.10 and Figure 7.11 were obtained by subtracting the broadband SPL for the corresponding angle of attack and frequency. In addition, only the largest amplitude tone is considered and thus secondary tones are not plotted.

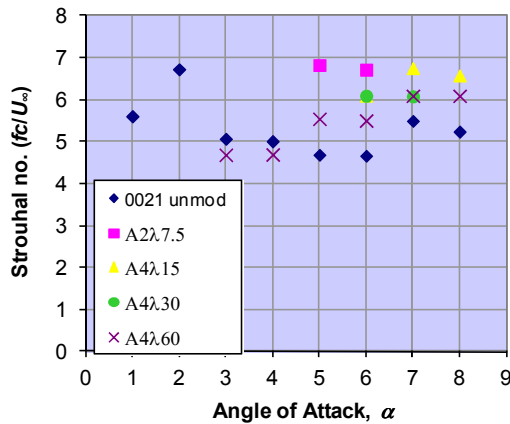


Figure 7.10 - Strouhal no. against angle of attack for NACA 0021 tubercle configurations with tonal noise (microphone at window), $Re = 120,000$.

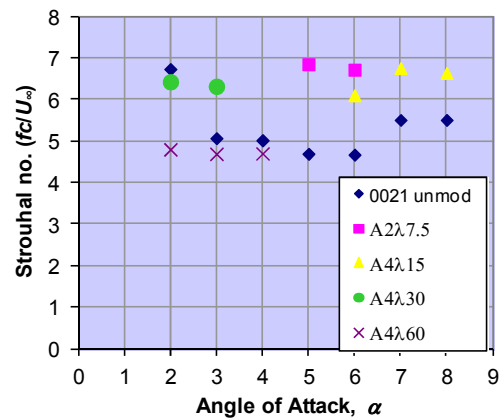


Figure 7.11 - Strouhal no. against angle of attack for NACA 0021 tubercle configurations with tonal noise (microphone at exit), $Re = 120,000$.

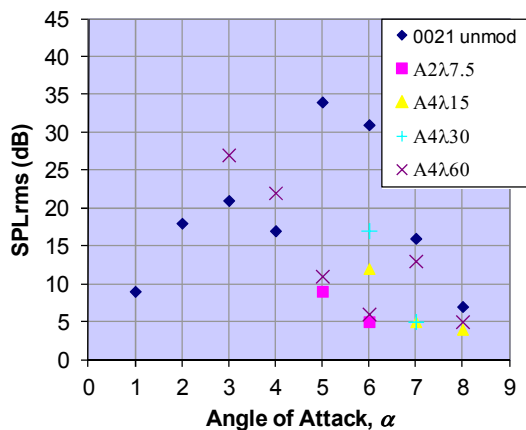


Figure 7.12 - SPL against angle of attack for tubercle configurations with tonal noise (microphone at window), $Re = 120,000$.

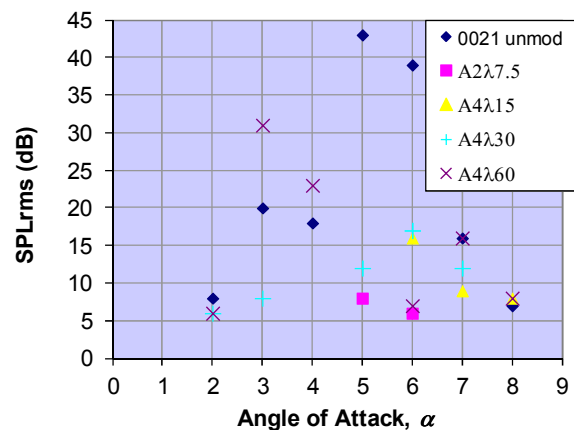


Figure 7.13 - SPL against angle of attack for tubercle configurations with tonal noise (microphone at exit), $Re = 120,000$.

7.3.2 Noise Levels Associated with NACA 65-021 Airfoil

Tonal noise for the NACA 65-021 occurred at a lower relative SPL level and at fewer angles of attack compared to the NACA 0021 airfoil. In addition, the frequency of the tonal noise was relatively higher for the NACA 65-021 which is consistent with the findings of Tam and Ju (2011) which suggest that an airfoil with a thicker trailing edge (NACA 0021) would generate a lower frequency tone for a given flow velocity. Figure 7.14 and Figure 7.15 show that tonal noise was measured by both the window

and exit microphones at $7^\circ \leq \alpha \leq 10^\circ$. Consistent with the measurements for the NACA 0021, the broadband SPL is higher at the exit of the working section as expected. Directivity of the noise is also observed where some tonal frequencies are louder at the test section exit and others are quieter when compared to measurements taken near the window. The largest magnitude tone has a SPL around 15dB above the broadband level and a frequency of $f = 2320\text{Hz}$ and was measured by both microphones at $\alpha = 8^\circ$.

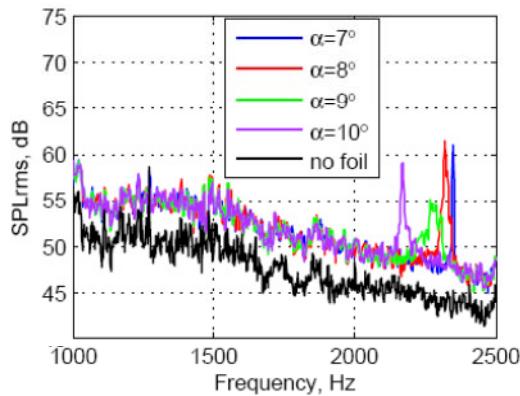


Figure 7.14 - SPL against frequency for NACA 65-021 at angle of attack, $\alpha = 7-10^\circ$ (microphone at window), $Re = 120,000$.

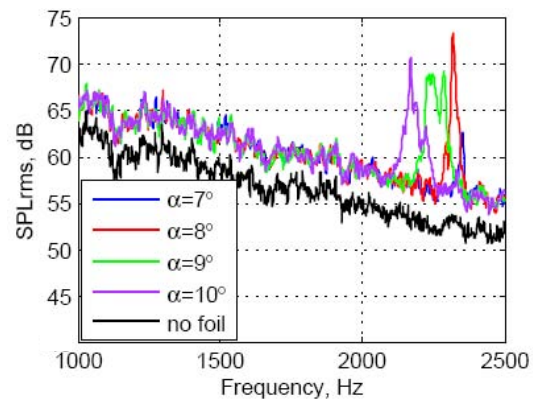


Figure 7.15 - SPL against frequency for NACA 65-021 at angle of attack, $\alpha = 7-10^\circ$ (microphone at exit), $Re = 120,000$.

Hence, the angle of attack, $\alpha = 8^\circ$, was chosen as a suitable point of comparison between the tonal noise associated with airfoils with and without tubercles as shown in Figure 7.16. Due to the unusual nature of the tone at $\alpha = 9^\circ$, the effect of tubercles at this angle of attack was also analysed and is depicted in Figure 7.17.

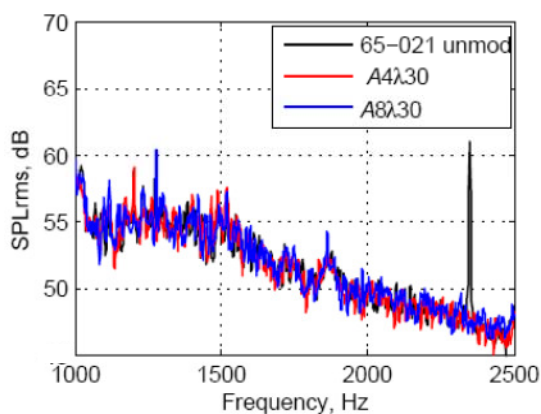


Figure 7.16 - SPL against frequency for NACA 65-021 at $\alpha = 8^\circ$ for variation tubercle amplitude (microphone at window), $Re = 120,000$.

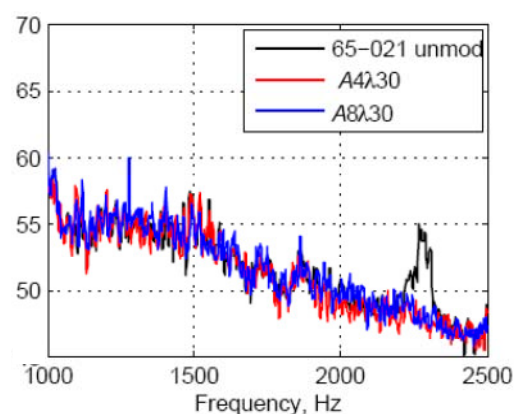


Figure 7.17 - SPL against frequency for NACA 65-021 at $\alpha = 9^\circ$ for variation tubercle amplitude (microphone at window), $Re = 120,000$.

It was found that for both tubercle configurations and angles of attack, the tonal noise is completely eliminated by the presence of the tubercles. This also occurred for all angles of attack in the range $7^\circ \leq \alpha \leq 10^\circ$.

For the NACA 65-021 airfoil, only tonal noise characteristics for the unmodified airfoil are presented in Figure 7.18 and Figure 7.19 since the airfoils with tubercles did not generate tones. Also, the secondary tones are not included in the figures since the largest amplitude tones were considered the most important for the analysis. Results for the two microphone positions are summarised in Figure 7.18 and indicate that the Strouhal number decreases with angle of attack. Also, there is much less variation in the value of the Strouhal number compared to the results for the NACA 0021 airfoil. The most unusual characteristics can be observed at $\alpha = 9^\circ$ since this tone is not specifically located at one distinct frequency as shown in Figure 7.17. In general, the SPL is higher at the duct exit, except for $\alpha = 9^\circ$ as shown in Figure 7.19. It can also be seen in Figure 7.19 that the tonal noise SPL is generally lower for the NACA 65-021 airfoil than the NACA 0021 airfoil.

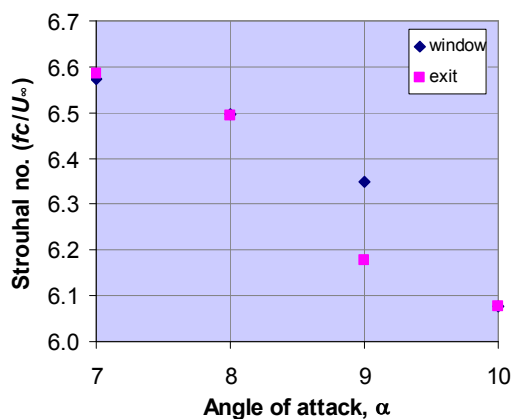


Figure 7.18 - Strouhal no. against angle of attack for NACA 65-021 unmodified airfoil with tonal noise, $Re = 120,000$.

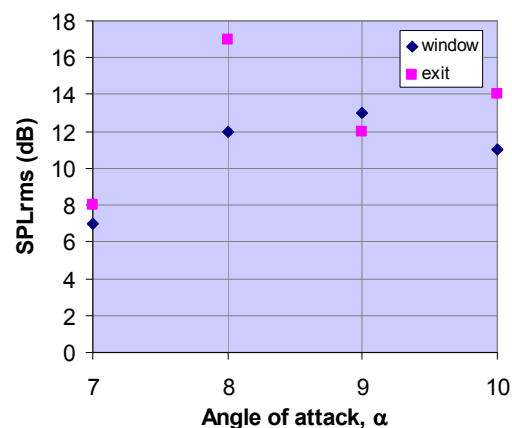


Figure 7.19 - SPL against angle of attack for unmodified NACA 65-021 with tonal noise, $Re = 120,000$.

7.4 Acoustic Measurements in Anechoic Wind Tunnel

Further acoustic measurements were conducted in the anechoic wind tunnel (AWT) to investigate whether the mechanism of tonal noise elimination for various tubercle configurations was influenced by the presence of the tunnel walls. In these experiments, the span was limited to the tunnel outlet width of 275mm. In addition, it was necessary

to apply corrections to the geometric angle of attack to account for the downwash and flow curvature effects. The experimental apparatus and corrections are discussed in more detail in Section 3.7.1.

7.4.1 Verification of the choice of frequency range

In order to increase the frequency resolution, it was beneficial to minimise the range of frequencies measured by the spectrum analyser. However, Figure 7.20 and Figure 7.21 are provided to verify that the chosen range of $0 \leq f \leq 2500\text{Hz}$ was sufficient to ensure that none of the tonal noise peaks were excluded from the measurements. Figure 7.21 shows that the airfoil with tubercles does not generate any tones beyond this frequency range.

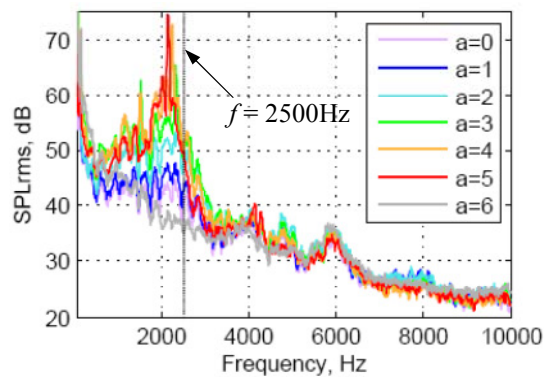


Figure 7.20 – SPL for NACA 0021 unmodified airfoil with larger frequency range, $50 \leq f \leq 10,000\text{Hz}$ in AWT, $\text{Re} = 120,000$.

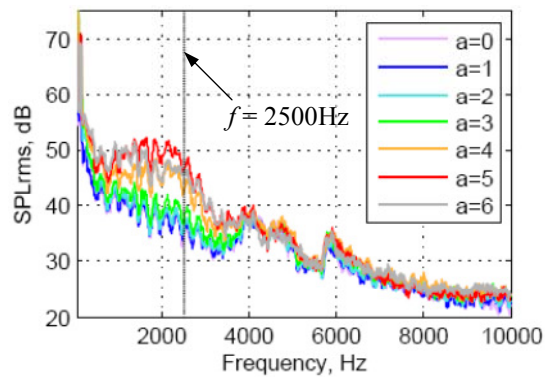


Figure 7.21 – SPL for A4λ7.5 tubercle configuration with larger frequency range, $50 \leq f \leq 10,000\text{Hz}$, in AWT $\text{Re} = 120,000$.

7.4.2 Noise Measurements for NACA 0021 Airfoil

Referring to Figure 7.22 (b-j), it can be seen that all tubercle and wavy configurations experience significantly reduced SPL at the tonal frequency and in most cases the tonal noise is eliminated altogether. Consistent with the results in the HWT, the most successful tubercle configurations for tonal noise elimination are those with a larger value of A/λ ratio as shown in Figure 7.22 (b), (c), (d) and (g). In addition, the results for all wavy configurations shown in Figure 7.22 (h-j) indicate that tonal noise is non-existent, which was also the case for the HWT. Also, the largest amplitude tone for the unmodified airfoil occurs at $\alpha = 5^\circ$, which can be seen in Figure 7.22 (a) and is in agreement with the results discussed in Section 7.3.1 for the HWT. However, the tonal frequency at this angle of attack is slightly higher in the AWT (2125Hz

compared with 1675Hz in the HWT). This is an interesting discrepancy and highlights the sensitivity of the tonal noise generating mechanism to changes in experimental parameters, even after appropriate corrections have been applied. Another difference between the sets of results is that tonal noise appeared over a much wider range of angles when testing in the HWT. A possible explanation for these differences is that the model solid blockage was greater in the case of the AWT, which would cause an increased freestream velocity in the vicinity of the model. In addition, the velocity profiles of the facilities were slightly different.

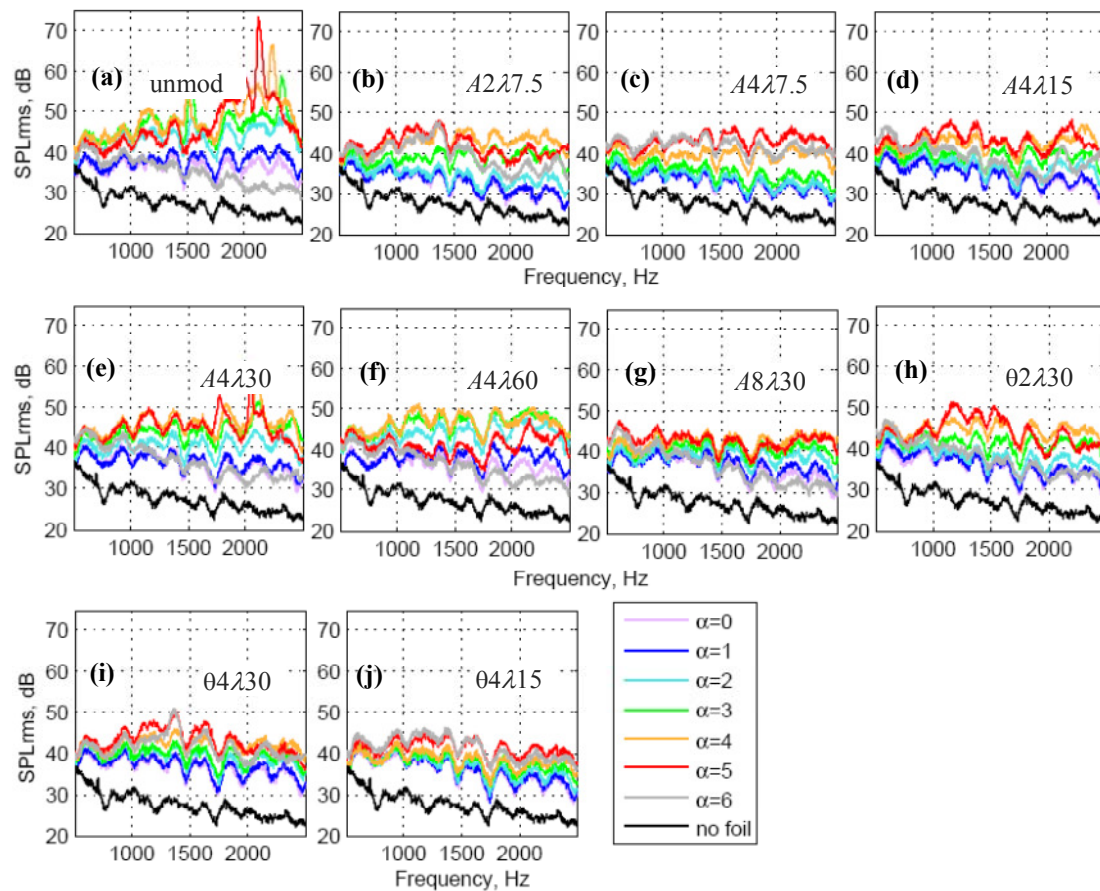


Figure 7.22 - SPL against frequency measured in anechoic wind tunnel (AWT) for
a) unmodified 0021 b) $A2\lambda7.5$ c) $A4\lambda7.5$ d) $A4\lambda15$ e) $A4\lambda30$ f) $A4\lambda60$ g) $A8\lambda30$ h) $\theta2\lambda30$ i) $\theta4\lambda30$
j) $\theta4\lambda15$, $Re = 120,000$.

A result not observable using the HWT is a small reduction in broadband noise, which occurred between 1500 and 2500Hz for all airfoils with tubercles. A higher broadband component appears to be directly related to the presence of the tones for the unmodified airfoil. It can be seen that the reduction in the broadband noise component is most significant for the $A4\lambda7.5$ and $A8\lambda30$ tubercle configurations and the $\theta4\lambda30$

and 0.4λ wavy configurations. These configurations also demonstrate the best performance in terms of noise reduction for the HWT as discussed in Section 7.3.1.

A summary of the relationship between the SPL of the tonal noise and the amplitude-to-wavelength ratio of tubercle and wavy configurations is depicted in Figure 7.23.

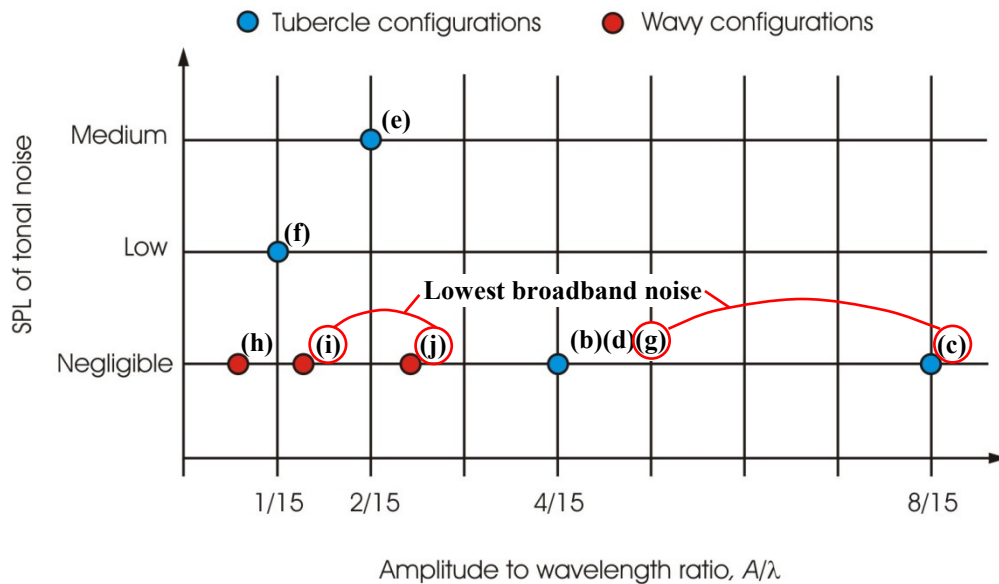


Figure 7.23 – Effect of amplitude-to-wavelength ratio on SPL of tonal noise.

Although the angles of attack at which tonal noise was measured varies for the AWT measurements, some general trends observed are similar, as is evident in Figure 7.24 and Figure 7.25.

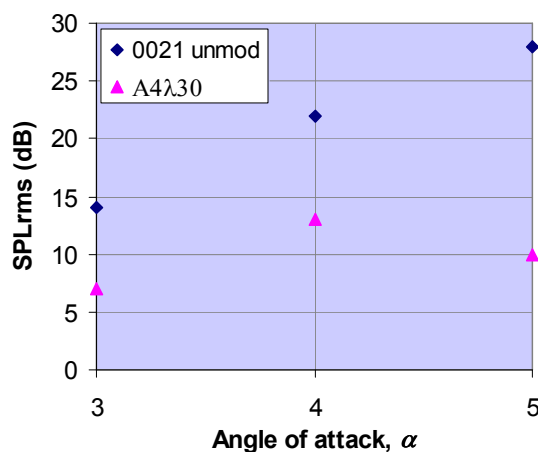


Figure 7.24 – SPL against angle of attack for NACA 0021 airfoils with tonal noise in AWT, $Re = 120,000$.

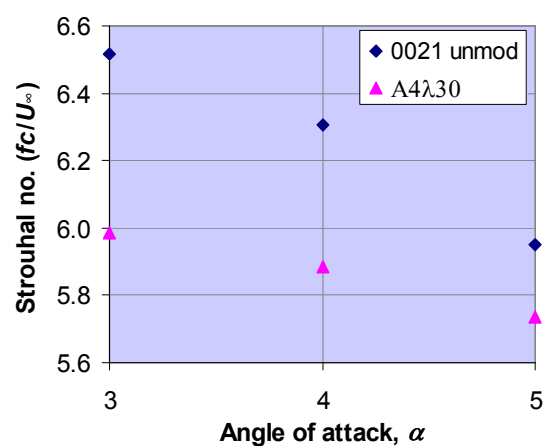


Figure 7.25 – Strouhal no. against angle of attack for NACA 0021 airfoils with tonal noise in AWT, $Re = 120,000$.

The Strouhal number decreases with angle of attack for both the unmodified airfoil and the airfoils with tubercles. In addition, the magnitude of the SPL above the broadband level is at a maximum for $\alpha = 5^\circ$ and the values are within 6dB of one another for the microphone near the window of the HWT. The higher level measured for the HWT is attributed to directivity.

7.4.3 Noise Measurements for NACA 65-021 Airfoil

Tonal noise occurs at only one angle of attack for the unmodified NACA 65-021 airfoil, which is $\alpha = 5^\circ$, having a frequency of $f = 2439\text{Hz}$ as can be seen in Figure 7.26 (a).

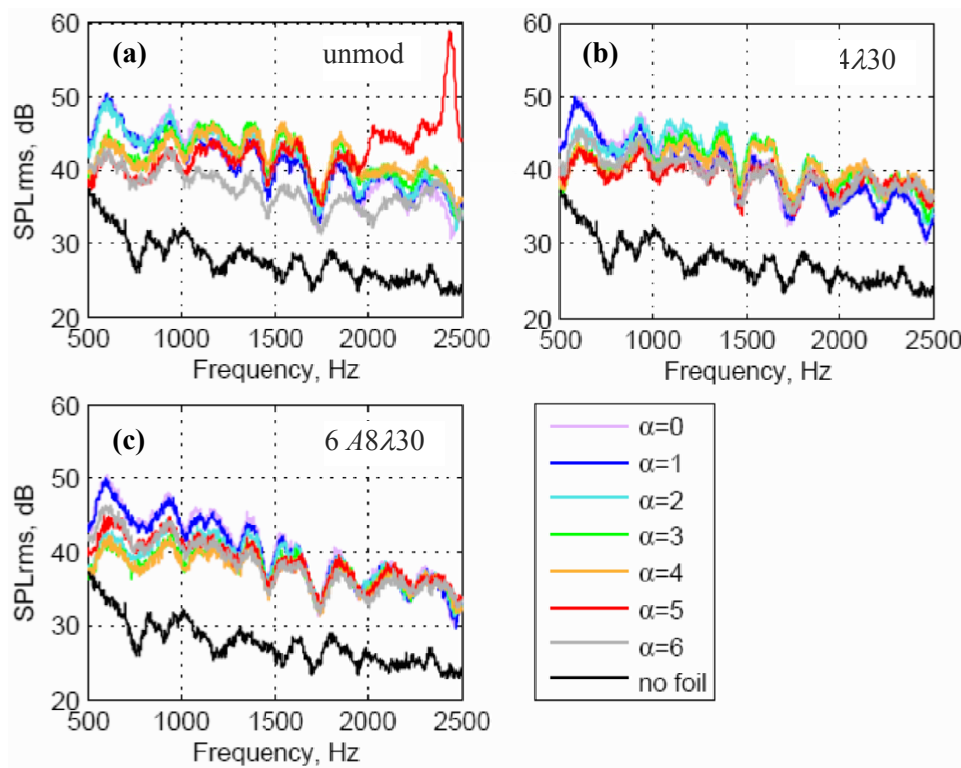


Figure 7.26 - SPL against frequency measured in AWT for a) unmodified 65-021 b) 6 A4230 c) 6 A8230, $Re = 120,000$.

The airfoils with tubercles do not generate this tonal noise and, in fact, there are no tones associated with these airfoils at any frequency. As noted for the NACA 0021 airfoil, the broadband component of the noise for the frequencies adjacent to the tone is reduced for both tubercle configurations of the NACA 65-021 airfoil. It can also be observed that, in general, the broadband component of the noise is slightly lower for the models with tubercles, especially in the lower frequency range $500 \leq f \leq 1000\text{Hz}$ and for $2^\circ \leq \alpha \leq 4^\circ$ as evident in Figure 7.26 (b) and (c). Overall, the broadband noise

reduction achieved with the larger amplitude tubercles is greater than for the smaller amplitude configuration.

The Strouhal number of the tonal noise for the NACA 65-021 airfoil is higher when measured in the AWT compared to the HWT as shown in Table 7.1. The maximum tonal noise also occurs at a different angle of attack. However, the SPL above broadband is in the same range.

Table 7.1 – Summary of tonal noise characteristics at $\alpha = 5^\circ$ for the NACA 65-021 airfoil

Experimental facility	Angle of attack, α	Frequency of main tone (Hz)	Strouhal no. (fc/U_∞)	SPLrms (dB)
AWT	5°	2439	6.8	14
HWT	8°	2320	6.5	15

7.4.4 Aeroacoustic Feedback Loop

It has been proposed that the tonal noise generation is a result of the existence of a self-excited feedback loop of aerodynamic origin (Tam, 1974; Arbey & Bataille, 1983; Desquesnes *et al.*, 2007). It is assumed that the instabilities in the boundary layer, which are convected at velocity, c_r , generate acoustic waves as they pass over the airfoil trailing edge (Arbey & Bataille, 1983). These acoustic waves propagate upstream until reaching the origin of the instabilities at point A shown in Figure 7.27. If the instabilities are in phase with the acoustic wave at this point, then it is believed that the former will be amplified. This concept is discussed in more detail in Section 2.3 and there are various interpretations of the location of the feedback loop. However, for the following analysis, the definition of Arbey & Bataille (1983) is adopted with the extension that the feedback loop may exist either on the suction or pressure surfaces.

NOTE:
 This figure/table/image has been removed to comply with copyright regulations. It is included in the print copy of the thesis held by the University of Adelaide Library.

Figure 7.27 – Schematic of feedback loop (Arbey & Bataille, 1983)

Equation

(7.1) from Arbey and Bataille (1983) can be used to find whether a relationship exists between the feedback loop length, L , shown in Figure 7.27 and the frequency of the tonal noise, f_s .

$$f_s = \frac{\left(\frac{c_r}{L}\right)(n + 1/2)}{\left(1 + \frac{c_r}{a_o - U_\infty}\right)} \quad (7.1)$$

where,

c_r = convection velocity of boundary layer instabilities $\sim 0.5 U_\infty$

L = length of feedback loop

$n = 1, 2, 3, \dots$

a_o = speed of sound = 343m/s

U_∞ = freestream velocity.

The analysis was carried out for the AWT results, where the maximum tonal noise occurred at an angle of attack of $\alpha = 5^\circ$ for both the NACA 0021 and the NACA 65-021 airfoils as discussed in Sections 7.4.2 and 0. The separation characteristics of these airfoils at $\alpha = 5^\circ$ are calculated using XFOIL and summarised in Table 7.2.

The feedback loop point should correspond to the position at which the flow is most receptive to external excitation (Tam, 2011). There is some debate as to the actual location of this point and a receptivity analysis would be necessary to determine it accurately. However, there are certain positions where boundary layer receptivity is likely to be greater, which include locations of separation and reattachment as well as the mid-point of the separation bubble. In this table, the parameters of feedback loop length, L , value of “ n ” and calculated frequency, f_s are included. The following subscripts are adopted: “ s ” = location of separation, “ m ” = middle of separation bubble and “ r ” = reattachment point. The values of these parameters were then substituted into Equation (7.1) to determine whether the solution for f_s was close to the measured tonal noise for an integer value of n . The closest solutions are highlighted in grey in Table 7.2 and

correspond to the separation point of the separation bubble on the suction surface for the NACA 0021 and the middle of the separation bubble on the pressure surface for the NACA 65-021.

Table 7.2 – Separation characteristics calculated using XFOIL at $\alpha = 5^\circ$

Airfoil profile	Frequency of tone	Surface	Separation characteristics	Parameters
NACA 0021	$f = 2125\text{Hz}$	Suction	Separation bubble for $0.23 \leq x/c \leq 0.44$, then attached flow to trailing edge	$L_s = 53.9\text{mm}$ $L_m = 46.6\text{mm}$ $L_r = 37.8\text{mm}$ $n_{s,m,r} = 9, 8, 6$ $(f_s)_s = 2120\text{Hz}$ $(f_s)_m = 2196\text{Hz}$ $(f_s)_r = 2068\text{Hz}$
		Pressure	Separation at $x/c = 0.62$	$L = 26.6\text{mm}$ $n = 4$ $f_s = 2034\text{Hz}$
NACA 65-021	$f = 2439\text{Hz}$	Suction	Separation at $x/c = 0.38$	$L = 43.4\text{mm}$ $n = 8$ $f_s = 2356\text{Hz}$
		Pressure	Separation bubble for $0.57 \leq x/c \leq 0.86$, then attached flow to trailing edge	$L_s = 30.1\text{mm}$ $L_m = 50.1\text{mm}$ $L_r = 9.8\text{mm}$ $n_{s,m,r} = 6, 10, 1$ $(f_s)_s = 2597\text{Hz}$ $(f_s)_m = 2403\text{Hz}$ $(f_s)_r = 1841\text{Hz}$

These results suggest that there is a possible correlation between the measured data and the feedback loop described by Arbey and Bataille (1983). However, there may also be resonances associated with the experimental facility which affect the results. In addition, since the measured frequencies of tonal noise differed between the HWT and AWT facilities, it appears that the equation used to calculate the actual angle of attack in the AWT from Brooks *et al.* (1986) could have an associated error.

7.5 Summary

The results of an experimental study investigating the noise characteristics of airfoils with tubercles have been presented in this chapter. It was found that for the NACA 0021 airfoil, the larger amplitude and smaller wavelength tubercles, having the largest A/λ ratio, were the most effective configurations for eliminating tonal noise. For the remaining cases, reduction in wavelength appeared to generally increase the frequency at which tonal noise was detected. There was a corresponding decrease in sound pressure level (SPL).

The tubercle configuration with the smallest wavelength ($A2\lambda7.5$) was found to be the most effective in terms of maximum lift coefficient, stall angle and minimum drag as reported in Chapter 4. However, for the noise measurements, the configuration with larger amplitude tubercles ($A4\lambda7.5$) was more effective in tonal noise elimination according to the hard-walled wind tunnel (HWT) results. Some tonal noise was still generated by the $A2\lambda7.5$ airfoil in the HWT but relative to the unmodified NACA 0021 airfoil, the frequency was higher and SPL significantly lower by at least 25dB. In terms of post-stall performance, results in Chapter 4 indicated that larger amplitude tubercles were associated with a more gradual stall and higher post-stall lift. Larger amplitude tubercles also eliminated tonal noise if the associated wavelength was small enough as demonstrated by the results for the $A4\lambda7.5$ and $A8\lambda30$ configurations.

Measurements undertaken in the anechoic wind tunnel (AWT) also found that the above tubercle configurations were the most effective for noise reduction. However, the benefits were recognised more in terms of broadband noise reduction since it was found that, in general, airfoils with tubercles did not generate tonal noise. Hence, the amplitude and wavelength parameters were found to be less important according to these measurements.

Tonal noise for the NACA 65-021 occurred at fewer angles of attack compared to the NACA 0021 airfoil and the SPL was relatively lower. For this airfoil the tonal noise was eliminated for all tubercle configurations tested using both the HWT and the AWT facilities. The results from the AWT also indicated a reduction in the broadband

component of the noise both in the location of the original tone and also in the lower frequency range $500 \leq f \leq 1000\text{Hz}$ for $2^\circ \leq \alpha \leq 4^\circ$. The most favourable noise reduction was achieved by the 6A8λ30 tubercle configuration.

An interesting discrepancy was found between the tonal frequencies measured in the HWT and the AWT for both the NACA 0021 and NACA 65-021 airfoils. However, results were consistent with regards to the angle of attack with maximum tonal noise for the NACA 0021. This was not the case for the NACA 65-021 airfoil. The most likely reason for the difference in results is related to the errors associated with Equation (3.81) which was used to determine the true angle of attack for the airfoil in the AWT according to Brooks *et al.* (1986). The only variables considered in this calculation are the dimensions of the wind tunnel outlet and the geometric angle of attack. The freestream velocity and blockage effects were not considered in the calculation which would lead to uncertainties. It was found that the tonal noise frequency was highly dependent on the angle of attack and a variation as small as $\Delta\alpha = 1^\circ$ could lead to a change in frequency as large as $\Delta f = 592\text{Hz}$ for the NACA 0021 airfoil, giving a corresponding change in Strouhal number, $\Delta St = 1.7$. Correspondingly, the SPL was very sensitive and the largest variation for the NACA 0021 airfoil was found to be $\Delta\text{SPL} = 17\text{dB}$ for an angle of attack variation of $\Delta\alpha = 1^\circ$. Hence the variation in results for the two wind tunnel facilities is not entirely unexpected. On the other hand, results were in unanimous agreement that tonal noise was either significantly reduced or completely eliminated for airfoils with leading edge tubercles and wavy airfoils.

It is believed that tonal noise reduction and potential elimination is facilitated by the presence of streamwise vortices generated by the tubercles and wavy geometry and that the spanwise variation in separation location is also an important factor. Both characteristics modify the stability characteristics of the boundary layer, altering the frequency of velocity fluctuations in the shear layer near the trailing edge. This affects the coherence of the vortex generation downstream of the trailing edge, hence leading to a decrease in trailing edge noise generation. It is also postulated that for the large-amplitude tubercles, the streamwise vortices are larger, and for the small-wavelength tubercles, the streamwise vortices are closer together. Both factors are believed to

decrease the coherence of the vortex-shedding process, thus reducing the tonal noise amplitude. The feedback model of tonal noise generation can potentially describe the results in the AWT and it appears that separation bubbles provide regions where the boundary layer is most receptive to acoustic disturbances.

Chapter 8

Conclusions



In this thesis, the effect of tubercles on the lift and drag performance, surface pressure characteristics, flow behaviour and noise generation has been investigated. It was found that performance changes, in terms of enhanced lift with minimal additional drag for an airfoil with tubercles, is limited to specific Reynolds number regimes. This is due to the existence of separation bubbles at low Reynolds numbers that change the separation characteristics associated with an airfoil. There are also other important parameters to consider when specifying the use of tubercles such as the airfoil profile under consideration and whether or not the wing is swept or tapered. In addition, it was found that the amplitude and wavelength of sinusoidal tubercle configurations were important parameters to consider when optimising performance. Analysis of the flow behaviour revealed that a pair of streamwise vortices was generated in the troughs between tubercles and that vorticity and circulation were highly dependent on streamwise location and airfoil angle of attack. In terms of the acoustic results obtained, airfoils with tubercles consistently reduced or eliminated tonal noise.

A suitable method by which to compare airfoils with and without tubercles was through force measurements of the lift and drag. For a Reynolds number of $Re \sim 120,000$, the results for a NACA 0021 airfoil indicated that in terms of maximum lift coefficient and minimum drag, it was not advantageous to utilise tubercles in the pre-stall regime. On the other hand, tubercles promoted gentler stall characteristics and increased post-stall lift. Results for the maximum lift coefficient were slightly more favourable for the NACA 65-021, whereby a given tubercle configuration could achieve comparable results

to an unmodified airfoil pre-stall. The post-stall benefits were still relevant for this airfoil profile, indicating that tubercles may be advantageous provided they are incorporated into an appropriate airfoil profile. On the other hand, the drag coefficient was slightly higher around the stall angle so this would need to be taken into account for design purposes.

For both of the airfoils investigated in this study, the maximum lift coefficient and minimum drag were achieved with the smallest amplitude and wavelength tubercles, the $A2\lambda7.5$ and $6A4\lambda30$ configurations. Considering all tubercle configurations tested, the smallest amplitude was consistently associated with the highest lift coefficients. On the other hand there was a limit for wavelength reduction beyond which the performance degraded for a given tubercle amplitude. This implies that consideration of an optimal amplitude-to-wavelength (A/λ) ratio is more relevant than analysing the parameters separately since the unmodified airfoil represents the limit to which the amplitude and wavelength can be reduced. Moreover, hydrogen bubble flow visualisation results suggested similarities between flow patterns for tubercles with the same A/λ ratio. Tubercle configurations with the same A/λ ratio have an equivalent mean sweep angle relative to the flow, which may result in generation of vortices with similar strength, as mentioned by Custodio (2008). The visualisation results also indicated that a reduction in spacing between tubercles resulted in an apparent increase in boundary layer mixing and a more uniform attachment of the boundary layer near the trailing edge. However, since the force results suggested a limit beyond which wavelength reduction would reduce the effectiveness of tubercles, it is likely that excessive interaction between nearby vortices would reduce the effectiveness of the tubercles.

In addition, tubercles can be considered analogous to vortex generators (Fish & Battle, 1995; Miklosovic *et al.*, 2004) so another important parameter which was identified was the effective device height, h_{eff} . Since the vortex-generating mechanism, and hence h_{eff} , would become more prominent as the angle of attack was increased, this could be considered an effective indicator of the vortex strength. It was also identified that although the pre-stall performance of large amplitude tubercles was inferior, the post-stall performance and more gradual nature of the stall were generally improved compared to smaller amplitude tubercles. This could also be explained in terms of vortex lift generation as mentioned by Custodio (2008), where the losses associated with vortex

formation pre-stall negated the benefits, however post-stall vortex lift promoted superior performance.

An alternative “wavy” geometrical modification was also investigated which consisted of sinusoidal surface undulations aligned perpendicular to the freestream flow. The best-performing wavy configuration ($\theta\lambda 15$) had the largest angle between the peak and trough cross-sections and the smallest wavelength. Thus, in the case of the wavy configuration, increasing the angle of waviness and hence effective device height was found to improve performance whereas for tubercles, the converse was observed. Further optimisation would be required to verify these results, however. The improved performance for the smaller wavelength wavy configuration was in agreement with the results for tubercles. The wavy airfoils also demonstrated increased lift in the post-stall regime analogous to tubercles. Hence, it is believed that a similar flow mechanism exists for airfoils with tubercle and wavy configurations and that counter-rotating streamwise vortices are generated in the troughs between tubercle peaks for both cases.

Comparison between full-span and half-span models with no sweep or taper indicated that there were no performance advantages for the half-span model. This led to the conclusion that the presence of tubercles does not significantly affect the formation of wing-tip vortices for rectangular planform airfoils. On the other hand, the relatively weak wing tip vortices associated with the large effective aspect ratio of the airfoils investigated could make the relative performance enhancement of full-span and half-span models difficult to detect. Nevertheless, it is inferred that tubercles offer more obvious benefits for airfoils with sweep and/or taper where there is a much greater amount of span-wise flow. There may also be more significant advantages of incorporating tubercles into low aspect ratio wings.

Relative to previous studies where tubercles improved the lift performance of the airfoils under investigation, experiments were carried out at a much lower Reynolds number. Separation characteristics are more unpredictable at such low Reynolds numbers and the positive benefits to be obtained with tubercles may have been compromised. One example of an unusual result at $Re \sim 120,000$ was the generation of negative lift at low angles of attack by the NACA 65-021 airfoil. Investigations based on surface pressure

tappings combined with numerical analysis using the XFOIL code (Drela & Youngren, 2001) enabled a reasonable explanation of this phenomenon to be developed. Two predominant mechanisms were identified which included the formation of a separation bubble on the pressure surface of the airfoil and also thickening of the boundary layer on the suction surface. The former mechanism led to an increased effective camber on the pressure surface of the airfoil which promoted circulation in the positive direction, hence negative lift, at low angles of attack. As the angle of attack was increased, this effect was counteracted by the model asymmetry and hence positive lift was generated. The latter mechanism caused flow to slow down on the suction surface relative to the pressure surface, which also created positive circulation. This result was also observed by Marchaj (1979), for experiments on airfoils with large trailing edge angles. At higher angles of attack, the effect was once again counteracted by the negative circulation produced by model asymmetry.

The negative lift phenomenon was eliminated through use of boundary layer trips on the suction and pressure surfaces of the airfoil. The presence of this surface roughness appears to delay separation of the boundary layer on the suction surface and also eliminate the separation bubble on the pressure surface. It was noted that the effectiveness of tubercles did not deteriorate when the boundary layer was tripped to turbulence, which implies that the boundary layer state did not significantly influence the flow control mechanism of tubercles.

The increasing lift curve slope and sudden stall observed for the NACA 0021 airfoil were explained in terms of the existence of a separation bubble on the suction surface of the airfoil. This suction separation bubble moved closer to the leading edge as the angle of attack was increased, creating a variation in the effective camber of the airfoil. The measured lift curve slope corresponded to a combination of lift curve slopes for airfoils with varying degrees of camber. The “bursting” of this separation bubble at the leading edge led to a dramatic loss of lift and increase in drag. The abrupt nature of the stall for a NACA 0021 was mitigated by the existence of leading edge tubercles since it was found that separation bubbles were restricted to the trough regions between tubercles. Hence, flow was still attached behind the tubercle peaks at the time of the trough separation bubble “bursting” and therefore the entire airfoil was not stalled at this point. Zverkov

and Zanin (2008) also observed that separation bubbles were restricted to the troughs for a wavy airfoil model.

Consistent with results presented by Watts and Fish (2001), Fish and Lauder (2006) and Weber *et al.* (2010), the greatest amount of negative pressure was generated for the trough cross-section of the *A8 λ 30* airfoil with tubercles at pre-stall angles of attack. The least amount of negative pressure generated pre-stall was at the tubercle peak cross-section and halfway between a peak and a trough the amount of negative pressure produced was generally less than that for the trough and greater than that for the peak. It was also observed that at this mid-section, the negative pressure peak was lower in magnitude than that for the unmodified airfoil with the same chord length. Despite the large amount of negative pressure which was developed at the trough cross-section, there was a correspondingly larger pressure on the opposite surface of the airfoil. Hence, the lift associated with a given cross-section could not be inferred through observation of the pressure distribution curves and thus it was necessary to use numerical methods for calculation.

Lift coefficient curves determined from the integration of the surface pressure measurements matched reasonably well with the force measurement results for the unmodified NACA 0021 and NACA 65-021 airfoils. Thus, the pressure distribution data for the *A8 λ 30* tubercle configuration were used to determine the effective lift at spanwise positions corresponding to a peak, trough and midway between. The greatest amount of lift was calculated for the peak cross-section and the least amount for the trough. This was expected since previous studies (Johari *et al.*, 2008; van Nierop *et al.*, 2008) and also hydrogen bubble visualisation results in this work found that flow remained attached for longer behind a peak than a trough.

The low pressure region observed in the troughs between tubercles is consistent with the surface flow diverging from the peaks towards the troughs. It is also consistent with a pair of counter-rotating streamwise vortices above the surface as noted by Custodio (2008). Results published by Pedro and Kobayashi (2008) and Stanway (2008) also indicated the presence of streamwise vorticity. However, quantitative results for the streamwise vorticity and circulation were not stated in these publications. Particle image velocimetry

results obtained in the current study provided this information for a range of airfoil attack angles and streamwise measurement planes.

For the region investigated, which encompassed a field of view slightly greater than one tubercle wavelength and spanned two tubercle peaks, a pair of counter-rotating streamwise vortices was identified for each case investigated. It was found that the peak vorticity and circulation of these primary vortices increased with angle of attack for a given measurement plane. The peak vorticity generally decreased in the downstream direction as the vorticity became distributed over a larger area. This suggests that the observed effectiveness of tubercles at higher angles of attack is related to the fact that the separation point and the location of peak vorticity come within closer proximity. This would lead to increased momentum exchange and delayed separation. Another reason that tubercles were more effective at higher angles of attack is that vorticity of opposite sign was not observed on the flow side of the primary vortices at $\alpha = 15^\circ$.

At angles of attack of $\alpha = 5^\circ$ and $\alpha = 10^\circ$, it was observed that secondary vorticity of opposite sign on the flow side of the primary vortex was present near the airfoil leading edge and a process of annihilation led to an initial decrease in circulation in the downstream direction for these cases. On the other hand, when this secondary vorticity was not present, the circulation was found to increase in the downstream direction. A proposed mechanism for this increase in circulation suggests the entrainment of wall vorticity which was generated below the primary vortex of opposite sign. Since the entrainment process could not occur for both primary vortices simultaneously, it was believed that it would be cyclic in nature. The unsteadiness associated with the measurements supports this theory.

A certain degree of asymmetry was also observed in the time-averaged images of the vortices, especially towards the trailing edge. It was evident that the negative vortex core generally had a larger associated peak vorticity and a greater magnitude of circulation. The latter observation was the result of a slightly increased mean vorticity as well as a larger area of integration. The area of integration was selected based on a minimum vorticity contour, which suggests that the negative vortex had a higher associated spreading rate. Asymmetry in the flow supports the proposition suggested above

concerning entrainment of vorticity. It also suggests the possibility of a transfer of vorticity between adjacent tubercle troughs as the vortices move further downstream along the airfoil chord. Previous researchers inferred that the flow patterns observed between pairs of adjacent tubercle peaks would be different and a greater similarity would be observed between alternate peaks of the tubercle pattern (Custodio, 2008). However, the proximity of the flow facility walls may have influenced the results observed by Custodio (2008). It was also observed in the present results that the image sequences became more time dependent towards the trailing edge and hence the average became a less accurate representation of the actual flow field.

Upon positive identification of the streamwise vortex structures for a NACA 0021 airfoil with tubercles using visualisation and particle image velocimetry techniques, it was possible to propose a mechanism through which tonal noise could be eliminated. The presence of the streamwise vortices changed the stability characteristics of the boundary layer and hence the frequency of velocity fluctuations in the shear layer near the trailing edge. Another factor which contributed to alteration of these characteristics was the varying locations of separation along the span-wise direction (Pedro & Kobayashi, 2008). Consequently, the amplification of certain instabilities in the boundary layer did not occur and the feedback mechanism proposed in various forms by different researchers (Tam, 1974; Arbey and Bataille, 1983; McAlpine *et al.*, 1999; Desquenses, 2007) was influenced.

Acoustic measurements in the hard-walled wind tunnel demonstrated that the NACA 0021 airfoil created tones with sound pressure level over 40dB above broadband. The larger amplitude and smaller wavelength tubercle configurations, which included the A8 λ 30 configuration, completely eliminated all tonal noise for the NACA 0021 airfoil. Other tubercle configurations drastically reduced the sound pressure level of the tonal noise and there was generally an associated shift towards higher frequencies, which demonstrated that alternative instabilities were being amplified.

With regards to the relationship between aerodynamic performance enhancement and tonal noise elimination a positive correlation was identified. The most effective tubercle configuration for the NACA 0021 profile in terms of maximum lift coefficient, stall angle

and minimum drag had the smallest wavelength ($42\lambda_{7.5}$). Measurements in the anechoic wind tunnel indicated that there was no tonal noise associated with this tubercle configuration and additionally, the broadband sound pressure level was generally lower for all angles of attack. The larger amplitude tubercles ($48\lambda_{30}$) were more effective in terms of having a more gradual stall and higher post-stall lift. Larger amplitude tubercles also eliminated tonal noise for all angles of attack and in general, reduced the broadband sound pressure level.

For the NACA 65-021 airfoil, tonal noise was generated at fewer angles of attack compared to the NACA 0021 airfoil and the sound pressure was relatively lower. For this airfoil the tonal noise was eliminated for all tubercle configurations tested using both the hard-walled wind tunnel and the anechoic wind tunnel facilities. It was also evident that there was a reduction in the broadband noise both in the location of the original tone and also in the lower frequency range $500 \leq f \leq 1000\text{Hz}$ for $2^\circ \leq \alpha \leq 4^\circ$. The larger amplitude tubercle configuration ($648\lambda_{30}$) achieved the most favourable noise reduction which was consistent with results for the NACA 0021 airfoil.

It was observed that for the same Reynolds number and airfoil, the frequency and sound pressure level of the acoustic tones differed in the hard-walled wind tunnel compared to the anechoic wind tunnel. Hence it is plausible that the angle of attack correction proposed by Brooks *et al.* (1986) for an open jet wind tunnel is not sufficient to allow direct comparison with an open return wind tunnel having a closed section duct attached to the outlet. It was found that frequency and sound pressure results were extremely sensitive to angle of attack and hence it was difficult to provide equivalent experimental conditions in both facilities. On the other hand, the important conclusion which was established for both sets of measurements was that airfoils with leading edge tubercles could eliminate tonal noise for both a NACA 0021 and a NACA 65-021 airfoil.

A comprehensive uncertainty analysis was carried out for the force, pressure and PIV experiments. This verified the interpretations that were made from the results since the uncertainty was not excessively large to distort the general characteristics of the measurements.

The most significant and novel findings in this thesis can be summarised as follows:

- Tubercle effectiveness increased with amplitude and wavelength reduction.
- Surface waviness influenced the flow in a similar manner to tubercles.
- The airfoil profile affected the performance of tubercles.
- Three-dimensional effects had negligible effect on performance enhancement with tubercles for a large aspect ratio rectangular planform wing at low Reynolds numbers.
- Improved performance with tubercles was Reynolds number dependent.
- The effectiveness of tubercles was not changed when the boundary layer was turbulent.
- The existence of tubercles led to the formation of counter-rotating vortices which increased in strength with angle of attack, increasing momentum exchange.
- An increase in circulation was observed to occur in the streamwise direction for the primary vortices and this was attributed to the entrainment of same sign secondary vorticity which was generated between the airfoil surface and adjacent primary vortices.
- Tonal noise was mitigated by the presence of tubercles and also for wavy airfoils.

Chapter 9

Recommendations for Future Work



There are numerous opportunities for future work on this topic since there are so many potential applications and a large number of variables to consider when selecting an optimum tubercle configuration. The possibilities outlined below adopt the general themes of varying the Reynolds number, changing the shape of the tubercles, selecting airfoils with different profile shapes, investigating the effect of sweep and/or taper, studying the dynamic stall behaviour and investigating situations where noise could be reduced. In addition, different methods of analysis can be employed in order to generate data with a different perspective. It would be useful to conduct an experimental three-dimensional analysis on airfoils with tubercles. In addition, there is a large scope for further theoretical work on the topic. Moreover, a numerical study could provide access to a large amount of data, provided the model was properly validated.

Investigation of the performance variation for a range of Reynolds numbers would show if there is a specific Reynolds number range in which tubercles are most effective. The current study considered one Reynolds number only, $Re \sim 120,000$ because the objective was to investigate the influence of other parameters on tubercle performance. However, since it was discovered that the Reynolds number seems to have a large impact on the success of tubercles, it is believed that this line of research needs to be pursued. Performance enhancement was achieved for model whale

flippers at Reynolds numbers in the range $505,000 \leq Re \leq 550,000$ in terms of increased maximum lift coefficient and stall angle with minimal drag penalties (Miklosovic *et al.*, 2004; Murray *et al.*, 2005; Pedro & Kobayashi, 2008). However, for Reynolds numbers, $Re < 300,000$ results presented here and in the literature indicate that airfoils with tubercles showed inferior performance (Stein & Marray, 2005; Miklosovic *et al.*, 2007; Johari *et al.*, 2007; Stanway, 2008). It would be useful to explore whether benefits could be obtained for a rectangular planform in the transitional Reynolds number range since this would highlight the relative importance of Reynolds number and three-dimensional effects.

Leading-edge modifications with alternative shapes could be investigated to ascertain if there is a more effective shape for performance enhancement. A sinusoidal arrangement of protrusions is only an approximation of the actual Humpback whale-flipper leading-edge morphology. Thus, it is not necessarily optimal and various other leading edge shapes could be incorporated into the leading edge, which achieve similar effects to tubercles. These could include but not be limited to: parabolic, circular or triangular protrusions. In addition a wavy airfoil, as introduced in Section 3.2 could be investigated in further detail.

Studying the effect of tubercles on a variety of airfoil profile shapes used in different applications would provide useful information as to range of applications for tubercles. In this study, two profile shapes were considered. Both were symmetrical and had a similar profile to a typical cross-section of the Humpback whale flipper. Analysis could be extended to airfoil profiles with varying degrees of camber and thickness and also wings with existing modifications such as trailing edge flaps. It would be useful to select a particular application, and airfoil parameters could be based on typical service operating conditions. Subsequently, an optimisation process could be carried out. A similar approach could be adopted for investigation of the effects of tubercles on different planform shapes. Research thus far has focussed on two planform shapes: a rectangular planform and a planform corresponding to a Humpback whale flipper (Miklosovic *et al.*, 2004; Johari *et al.*, 2007; Pedro & Kobayashi, 2008). Hence, there is still scope for investigation of the effect of tubercles on airfoils with different planform shapes such as lunate and elliptical.

Further investigation into the effects of sweep and taper on tubercle performance would deepen understanding of the importance of three-dimensional effects on the performance enhancement mechanism. While improved performance was observed for model whale flippers when the sweep angle was varied (Murray *et al.*, 2005), it should be noted that the shape of the Humpback whale flipper is complex. Moreover, there is a certain degree of sweep at the leading edge even when the root of the Flipper is perpendicular to the wind tunnel floor. Hence it is plausible that tubercles may only provide noticeable benefits for airfoils with a certain degree of sweep. The effect of varying the sweep angle could be investigated for less complex foils than the humpback whale flipper. Alternatively, an approximation of the Humpback whale flipper shape without sweep could be investigated. Taper is another inherent feature of the Humpback whale flipper and to this date, a study of tubercle performance for varying degrees of taper has not been attempted. It would also be useful to study the effects on induced drag and wingtip vortices for wings with tubercles. The current work found that there was little difference in the induced drag component with and without tubercles for a rectangular planform. Therefore, this investigation could be carried out for an alternative planform shape or for an airfoil having sweep and/or taper.

Determination of the optimum rate of height and spacing reduction towards the wing tip would also be instructive. Close examination of the Humpback whale flipper reveals that the height and spacing of the tubercles decreases towards the tip of the flipper (Fish & Battle, 1995). It would be useful to study different rates of amplitude and wavelength reduction and the corresponding benefits or adverse effects on the performance. This study would most likely be more applicable to foils with sweep and/or taper since the chord length reduces towards the tip for these cases.

Considering the gradual stall associated with airfoils having leading edge tubercles, a study on dynamic stall would be worthy and applicable to wind turbines and helicopters. In addition, the effect of tubercles on leading edge - turbulence interaction noise would also be interesting and useful for wind turbines.

Previous studies, including the current work have been limited to either rectangular planform shapes or scale models of the Humpback whale flipper. The former

approach enables a more fundamental understanding of the influence of tubercles on airfoil performance. However, the latter approach allows a direct assessment to be made of how a Humpback whale flipper would perform without tubercles. Hence, we are approaching the problem from two directions: from nature to engineering and from engineering to nature. At this stage, there are still many gaps to fill in between.

References

Abbott, IH & von Doenhoff 1959, *Theory of wing sections*, Dover Publications, New York.

Adrian, RJ 1997, "Dynamic ranges of velocity and spatial resolution of particle image velocimetry," *Measurement Science and Technology*, 8, pp. 1393–1398.

Adrian, RJ 1991, "Particle-imaging techniques for experimental fluid mechanics," *Annual Review of Fluid Mechanics*, 23, pp. 261-304.

Agui, JC and Jimenez, J 1987, "On the performance of particle tracking," *Journal of fluid mechanics*, 185, pp. 447-468.

Ahuja, KK, and Burrin, RH 1984, "Control of flow separation by sound," *Proceedings of the 9th AIAA Aeroacoustics Conference*, Williamsburg, Virginia, 15-17th October.

Alexander, D 2001, *Stock car driving techniques*, MBI Publishing, St. Paul, MN, USA.

Allen, HJ and Vincenti, WG 1944, "Wall interference in a two-dimensional-flow wind tunnel with consideration of the effect of compressibility," *NACA TR 782*.

Anderson, GW 1973, "An Experimental Investigation of a High Lift Device on the Owl Wing," Thesis submitted to Air Force Institute of Technology, Air University.

Anderson, Jr., JD 1997, *A history of aerodynamics and its impact on flying machines*, Cambridge University Press, Cambridge, UK.

Anderson Jr., JD 2007, *Fundamentals of aerodynamics: Fourth edition-*, McGraw-Hill, Singapore.

Anderson, BD 2008, "The physics of sailing," *Physics Today*, February.

Arbey, H and Bataille, J 1983, "Noise generated by airfoil profiles placed in a uniform laminar flow," *Journal of Fluid Mechanics*, 134, pp. 33-47.

Ashill, PR, Fulker, JL and Hackett, KC 2002, "Studies of Flows Induced by Sub Boundary Layer Vortex Generators (SBVGs)," AIAA Paper 2002-3162, 1st AIAA Flow Control Conference, St. Lois, MO, June 24-27th.

Barlow, JB, Rae Jr., WH and Pope, A 1999, *Low-Speed Wind Tunnel Testing*, 3rd Edition, John Wiley & Sons Inc., New York.

Bar-Sever, A 1989, "Separation control on an airfoil by periodic forcing," *AIAA Journal*, 27, pp. 820-821.

Bearman, PW and Owen, JC 1998, "Reduction of bluff body drag and suppression of vortex shedding by the introduction of wavy separation lines," *Journal of Fluids and Structures*, 12, pp. 123-130.

Bechert, DW, Bruse, M, Hage, W and Meyer, R 1997, "Biological surfaces and their technological application – laboratory and flight experiments and separation control," AIAA Paper 97-1960.

Bechert, DW, Bruse, M, Hage, W and Meyer, R 2000, "Fluid mechanics of biological surfaces and their technological application," *Naturwissenschaften*, 87, pp. 157-171.

Bentley, RE 2005, *Uncertainty in measurement: the ISO guide*, National Measurement Institute, Sydney.

Betts, PJ 1995, "The practical aspects of 95% confidence level in uncertainty estimation," *Proceedings of the Conference of the Meteorology Society Australia*, Sydney. November, pp. 221-225.

Blasius, H 1908, "Grenzschichten in Flüssigkeiten mit kleiner Reibung," *Z Math Phys*, 56, pp. 1–37. (English translation in *NACA-TM-1256*.)

Braslow, AL, Hicks, RM and Harris Jr., RV 1966, "Use of grit-type boundary-layer-transition trips on wind-tunnel models," NASA TN D-3579.

Bristow GV 2002, *Ace the technical pilot manual*, McGraw-Hill, New York, p. 21.

Brooks, TF, Marcolini, MA, and Pope, DS 1986, "Airfoil Trailing-Edge Flow Measurements," *AIAA Journal*, **24**, pp. 1245-1251.

Brooks, TF, Pope, DS and Marcolini, MA 1989, "Airfoil self-noise and prediction," NASA-RP-1218.

Carmichael, BH 1981, "Low Reynolds number airfoil survey, Volume 1," *NASA CR* 165803.

Carpenter, PW and Garrad, AD 1986, "The hydrodynamic stability of flow over Kramer-type compliant surfaces. Part 2. Flow-induced surface instabilities," *Journal of Fluid Mechanics*, **170**, pp. 199-232.

Carpenter, PW, Davies, C and Lucey, AD 2000, "Hydrodynamics and compliant walls: does the dolphin have a secret?" *Current Science* **79**, pp. 758-65.

Chapdelaine, M 2011, "A whale of a design: WhalePower bumps into engineering innovation," *Opportunity Green Insights*, 24th August.

Clauser, FH 1954, "Turbulent boundary layers in adverse pressure gradients," *Journal of Aeronautical Sciences*, **21**, pp. 91-108.

Compton, DA and Johnson, JP 1992, "Streamwise vortex production by pitched and skewed jets in a turbulent boundary layer," *AIAA Journal*, **30**, p. 640.

Corke TC, Jumper EJ, Post ML, Orlov D, McLaughlin TE 2002, "Application of weakly-ionized plasmas as wing flow-control devices," Presented at 40th AIAA Aerospace Sciences Meeting and Exhibit, Reno, AIAA Pap. No. 2002-0350.

Corke, TC and Post ML 2005, "Overview of plasma flow control: concepts, optimization and applications," Presented at 43rd AIAA Aerospace Sciences Meeting and Exhibit, 10 – 13th January, Reno, Nevada, AIAA paper no. 2005-563.

Corke, TC, Enloe, CL and Wilkinson, SP 2010, "Dielectric barrier discharge plasma actuators for flow control," *Annual Review of Fluid Mechanics*, 42, pp. 505–529.

Custodio, D 2007, "The effect of Humpback whale-like leading edge protuberances on hydrofoil performance," Thesis submitted to Worcester Polytechnic Institute, December.

Desquesnes, G, Terracol, M, Sagaut, P 2007, "Numerical investigation of the tone noise mechanism over laminar airfoils," *Journal of Fluid Mechanics*, 591, pp. 155-182.

Dewar, SW, Watts, P and Fish, FE 2006, Turbine and compressor employing tubercle leading edge rotor design, International patent WO 2006/042401 A1.

Dingle, L and Tooley, MH 2005, *Aircraft engineering principles*, Elsevier Butterworth-Heinemann.

Dolphin, WF 1988, "Foraging dive patterns of Humpback whales, *Megaptera novaeangliae*, in southeast Alaska: cost-benefit analysis," *Canadian Journal of Zoology*, 66, pp. 2432-2441.

Dowling, AP 1985, "The effect of large-eddy breakup devices on oncoming vorticity," *Journal of Fluid Mechanics*, 160, pp. 447-463.

Drela, M and Youngren, H 2001, "XFOIL 6.94 User Guide," *Aeronautical and Astronautical Engineering*, MIT, Cambridge, MA.

Edel, RK and Winn, HE 1978, "Observations on underwater locomotion and flipper movement of the Humpback whale *Megaptera novaeangliae*," *Marine Biology* 48, pp. 279-287.

Engineering Science Data Unit (ESDU) 2011, *Wind tunnel corrections for aerofoils*, viewed 2 January 2012,

<http://www.ihsesdu.com/cgi-bin/ps.pl?sess=unlicensed_1120103043554xml&t=index&p=index_wi#WIND_TUNNEL_CORRECTIONS_FOR_AEROFOILS>

Enloe, CL, McLaughlin, TE, Van Dyken, RD, Kachner, KD and Jumper, EJ 2004, "Mechanisms and responses of a single-dielectric barrier plasma actuator: geometric effects," *AIAA Journal*, 42, pp. 595–604.

Erm, LP 2003, "Measurement of flow-induced pressures on the surface of a model in a flow visualization water tunnel," *Experiments in Fluids*, 35, pp. 533-540.

Etebari, A. and Vlachos, P 2005, "Improvements on the accuracy of derivative estimation from DPIV velocity measurements," *Experiments in Fluids*, 39, pp. 1040–1050.

Fanmaster 2011, Altra-air fan 2.4m, viewed 29th January, 2012,

<<http://www.fanmaster.com.au/Altra-Air-Fan-2.4m.html>>.

Filippov, VM 2002, "Influence of plate nose heating on boundary layer development," *Fluid Dynamics*, 37, pp. 27–36. Translated from *Izvestiya Rossiiskoi Akademii Nauk, Mekhanika Zhidkosti i Gaza*, 1, 2002, pp. 32–42.

Fink, MR 1978, "Fine structure of airfoil tone frequency," Paper H3, Presented at the 95th meeting of the Acoustical Society of America.

Fish, FE and Battle, JM 1995, "Hydrodynamic design of the Humpback whale flipper," *Journal of Morphology*, 225, pp. 51-60.

Fish, FE and Lauder, GV 2006, "Passive and active flow control by swimming fishes and mammals," *Annual Review of Fluid Mechanics*, 38, pp. 193-224.

Fish, FE, Howle, LE and Murray, MM 2008, "Hydrodynamic control in marine mammals," *Integrative and Comparative Biology*, 48, pp. 788–800.

Fouras, A and Soria, J 1998, "Accuracy of out-of-plane vorticity measurements derived from in-plane velocity field data," *Experiments in Fluids*, **25**, pp. 409-430.

Gad-el-Hak, M 1990, "Control of low-speed airfoil aerodynamics," *AIAA Journal*, **28**, pp. 1537-1552.

Gad-el-Hak, M 1996, "Modern developments in flow control," *Applied Mechanics Reviews*, **49**, pp. 365-379.

Gad-el-Hak, M 2000, *Flow control: passive, active and reactive flow management*, Cambridge University Press, Cambridge UK.

Gaster, M 1987, "Is the dolphin a red herring?" *Proceedings of IUTAM Symposium on Turbulence Management and Relaminarisation*, Springer, New York, pp. 285-304.

Gault, DE 1949, "Boundary-layer and stalling characteristics of the NACA 63-009 airfoil section," NACA TN-1894.

Glauert, H 1933, "Wind tunnel interference on wings, bodies and airscrews," *ARC R&M* 1566.

Grundmann, S, Frey, M and Tropea, C 2009, "Unmanned aerial vehicle (UAV) with plasma actuators for separation control," Presented at 47th AIAA Aerospace Sciences Meeting, 5 - 8 January, Orlando, Florida, AIAA paper no. 2009-698.

Godard, G and Stanislas, M 2006, "Control of a decelerating boundary layer. Part 1: optimization of passive vortex generators," *Aerospace Science and Technology*, **10**, pp. 181-191.

Goeksel, B, Rechenberg, I, Greenblatt, D and Paschereit, C 2006, "Steady and unsteady plasma wall jets for separation and circulation control," Presented at 3rd AIAA Flow Control Conference, San Francisco, AIAA paper number 2006-3686.

Hain, JHW, Carter, GR, Kraus, SD, Mayo, CA and Winn, HE 1982, "Feeding behaviour of the Humpback whale, *Megaptera novaeangliae*, in the Western North Atlantic," *Fishery Bulletin*, 80, pp. 259-268.

Hansen, CH and Snyder, SD 1997, *Active control of noise and vibration*, E & FN SPON, London.

Hansen, MO 2000, *Aerodynamics of wind turbines*, James & James, London.

Hart, DP 1999, "Super-resolution PIV by recursive local-correlation," *Journal of Visualization*, The Visualization Society of Japan, **10**, pp. 1-10.

Hart, DP 2000, "PIV error correction," *Experiments in Fluids*, **29**, pp. 13-22.

Hassan, ER, Lau, TCW and Kelso, RM 2007, "Accuracy of circulation estimation schemes applied to discretised velocity field data," *Proceedings of the 16th Australasian Fluid Mechanics Conference Crowne Plaza, Gold Coast, Australia, 2-7th December*.

Hoerner, SF 1985 *Fluid Dynamic Lift*, Hoerner Fluid Dynamics, Bakersfield, CA, 2nd edition.

Hoffman, J and Johnson, C 2008, "Mathematical theory of sailing," KTH University, viewed 23rd November 2010,

<<http://www.csc.kth.se/%7Ecgjoh/theoryofsailing.pdf>>.

Horton HP 1968, *Laminar separation bubbles in two and three-dimensional incompressible flow*, PhD thesis, University of London, UK.

Houghton, EL, and Carpenter, PW 2003, *Aerodynamics for engineering students*, 5th edition, Butterworth-Heinemann, Burlington, MA, pp. 485, 503.

Howland, HC 1974, "Optimal strategies for predator avoidance: the relative importance of speed and manoeuvrability," *Journal of Theoretical Biology* 47, pp. 333-350.

Howle, LE 2009, "A report on the efficiency of a Whalepower corp. 5 meter prototype wind turbine blade," Available at: <http://www.whalepower.com/drupal/>

Hsiao, FB, Liu, CF and Shyu, JY 1989, "Control of wall-separated flow by internal acoustic excitation," *AIAA Journal*, 28, pp. 1440-1446.

Huang, LS, Maestrello, L and Bryant, TD 1987, "Separation control over an airfoil at high angles of attack by sound emanating from the surface," *Proceedings of the 19th AIAA Fluid Dynamics, Plasma Dynamics and Lasers Conference, Honolulu, Hawaii, 8-10th June.*

Jacobs, EN 1932, "The aerodynamic characteristics of eight very thick airfoils from tests in the variable density wind tunnel," *NASA Technical Report* 391.

Jeffrey, D, Zhang, X and Hurst, DW 2000, "Aerodynamics of Gurney flaps on a single-element high lift wing," *Journal of Aircraft*, 37, pp. 295-301.

Johari, H, Henoch, C, Custodio, D & Levshin, A 2007, "Effects of leading edge protuberances on airfoil performance," *AIAA Journal*, 45, pp. 2634-2642.

Johnston, JP and Nishi, M 1990, "Vortex generator jets – means for flow separation control," *AIAA Journal*, 28, pp. 989-994.

Johnson, SJ, van Dam, CP and Berg, DE 2008, "Active Load Control Techniques for Wind Turbines," *Sandia National Laboratories, Albuquerque, New Mexico.*

Joslin, RD and Miller, DN 2009, "Fundamentals and applications of modern flow control," *Progress in Astronautics and Aeronautics*, 231.

Jurasz, CM, and Jurasz, VP 1979, "Feeding modes of the Humpback whale, *Megaptera novaeangliae*, in southeast Alaska," *The Scientific Reports of the Whales Research Institute*, 31, pp. 69-83.

Katz J 2006, *Race-car aerodynamics*, 2nd edition, Robert Bentley Inc., Cambridge, MA.

Keane, RD and Adrian, RJ 1990, "Optimization of particle image velocimeters. Part 1: Double pulsed systems," *Measurement Science Technology*, 1, pp. 1202-1215.

Kingan, MJ and Pearse, JR 2009, "Laminar boundary layer instability noise produced by an aerofoil," *Journal of Sound and Vibration*, 322, pp. 808-828.

Khan, ZU and Johnson, JP 2000, "On vortex generating jets," *International Journal of Heat and Fluid Flow*, 21, pp. 506-511.

Khurana, KC 2009, *Aviation management global perspectives*, Global India Publications Pvt. Ltd., New Delhi.

Koumoutsakos, P and Mezic, I 2006, *Control of fluid flow*, Springer-Verlag, Berlin.

Kuethe, AM 1972, "Effect of streamwise vortices on wake properties associated with sound generation," *Journal Aircraft*, 9, pp. 715-719.

Lau, T 2010, "The flow around a fish-inspired heaving and pitching hydrofoil," *PhD Thesis submitted to Adelaide University*.

Leclercq, D, Doolan, C and Reichl, J 2007, "Development and validation of a small-scale anechoic wind tunnel," *Proceedings of the 14th International Congress on Sound and Vibration*, Cairns, July 9th-12th.

Leatherwood, S, Reeves, RR, Perrin, WF and Evans WE 1988, *Whales, dolphins, and porpoises of the eastern north pacific and adjacent arctic waters: a guide to their identification*, Dover, New York.

Lee, SK 2009, "Study of a naturally oscillating triangular-jet flow," *Ph.D Thesis submitted to School of Mechanical Engineering, Adelaide.*

Lee, BHK, Brown, D, Zgela, M, and Poirel, D 1990, "Wind tunnel investigation and flight tests of tail buffet on the CF-18 aircraft," Specialists' Meeting on Aircraft Dynamic Loads Due to Flow Separation, AGARD CP-483, Sorrento, Italy, April, pp. 1.1-1.26.

Liebeck, RH 1978, "Design of subsonic airfoils for high lift," *Journal of Aircraft*, 15, pp. 547-560.

Lin, JC, Selby, GV, Howard FG 1991, "Exploratory study of vortex-generating devices for turbulent flow separation control," AIAA Paper 91-0042, 29th Aerospace Sciences Meeting, Reno, NV, 7-10th January.

Lin, JC 2002, "Review of research on low-profile vortex generators to control boundary-layer separation," *Progress in Aerospace Sciences*, 38, pp. 389-420.

Lissaman, PBS 1983, "Low-Reynolds-number airfoils," *Annual Review of Fluid Mechanics*, 15, pp. 223-239.

Lord, WK, MacMartin, DJ, Tillman, TG 2000, "Flow control opportunities in gas turbine engines," *Proceedings of Fluids 2000*, Denver, CO, 19-22nd June, Paper number: AIAA 2000-2234.

Marchaj, CA 1979, *Aero-Hydrodynamics of Sailing*, Granada Publishing Ltd., London.

Maskell, EC 1965, "A theory of the blockage effects on bluff bodies and stalled wings in a closed wind tunnel," *ARC R&M* 3400.

McAlpine, A, Nash, EC and Lowson, MV 1999, "On the generation of discrete frequency tones by the flow around an airfoil," *Journal of Sound and Vibration*, 222, pp. 753-779.

McCormick, BW 1999, *Aerodynamics of V/STOL flight*, Dover Publications, New York, p. 8.

McKeon, BJ, Li, J, Jiang, W, Morrison, JF and Smits, AJ 2003, "Pitot probe corrections in fully developed turbulent pipe flow," *Measurement Science and Technology*, **14**, pp. 1449-1458.

Melling, A 1997, "Tracer particles and seeding for particle image velocimetry," *Measurement Science and Technology*, **8**, pp. 1406-1416.

Meyer, R and Bechert, DW 1999, "Wind tunnel experiments with artificial bird feathers for passive separation control on airfoils," Proceedings of IUTAM Symposium on Mechanics of Passive and Active Flow Control, Kluwer Academic Publishers, Netherlands, pp. 99-100.

Miklosovic, DS, Murray, MM, Howle, LE and Fish, FE 2004, "Leading edge tubercles delay stall on Humpback whale flippers," *Physics of Fluids*, **16**, pp. L39-42.

Miklosovic, DS and Murray, MM 2007, "Experimental Evaluation of Sinusoidal Leading edges," *Journal of Aircraft*, **44**, pp. 1404-1407.

Morris, MJ, Donovan, JF, Kegelman, JT, Schwab, SD, Levy, RL and Crites, RC 1993, "Aerodynamic Applications of Pressure Sensitive Paint," *AIAA Journal*, **31**, pp. 419-425.

Mueller, TJ and Batill, SM 1982, "Experimental Studies of Separation on a Two-Dimensional Airfoil at Low Reynolds Numbers," *AIAA Journal*, **20**, pp. 457-463.

Mueller, TJ and DeLaurier, JD 2003, "Aerodynamics of small vehicles," *Annual Review of Fluid Mechanics*, **35**, pp. 89-111.

Munson, Young and Okiishi 1990, *Fundamentals of Fluid Mechanics*, John Wiley & Sons, Inc., New York.

Murray, MM, Miklosovic DS, Fish, FE, Howle, LE 2005, "Effects of leading edge tubercles on a representative whale flipper model at various sweep angles," Proceedings of Unmanned Untethered Submersible Technology (UUST), Durham, NH, August.

Nakano, T, Fujisawa, S and Lee, S 2006, "Measurements of Tonal-Noise Characteristics and Periodic Flow Structure around NACA 0018 Airfoil," *Experiments in Fluids*, **40**, pp. 482-490.

Nakano, T, Fujisawa, N, Oguma, Y, Takagi, Y, Lee, S 2007, "Experimental study on flow and noise characteristics of NACA0018 airfoil," *Journal of Wind Engineering and Industrial Aerodynamics*, **95**, pp. 511–531.

Nash, EC, Lawson, MV and McAlpine, A 1999, "Boundary-layer instability noise on aerofoils," *Journal of Fluid Mechanics*, 382, pp. 27-61.

Nosenchuck DM, Brown GL, Culver HC, Eng, TI and Huang IS 1995, "Spatial and temporal characteristics of boundary layers controlled with the Lorentz force, Proceedings of the 12th Australasian Fluid Mechanics Conference, 1, pp. 93-96, Sydney, Australia, 10-15th December.

Ogilvie, G. 2010, "Pearse, Richard William – Biography," Dictionary of New Zealand Biography, Te Ara - the Encyclopedia of New Zealand, viewed 19th June 2012, <<http://www.TeAra.govt.nz/en/biographies/3p19/1>>

Ontario Power Authority 2010, "Energy efficient fans take their cue from the humpback whale," Available at:
http://archive.powerauthority.on.ca/Storage/122/16957_AgNews_July231.pdf

Pankhurst, RC and Holder, DW 1968, "Wind-tunnel technique," Sir Isaac Pitman & Sons Ltd., London.

Paterson, RW, Vogt, PG, Fink, MR and Munch, CL 1973, "Vortex noise of isolated airfoils," *Journal of Aircraft*, 10, pp. 296-302.

Pedro, HTC and Kobayashi, MH 2008, "Numerical study of stall delay on Humpback whale flippers," Proceedings of 46th AIAA Aerospace Sciences Meeting and Exhibit, 7-10th January, Reno, Nevada.

Perry, AE 1982, *Hot-wire anemometry*, Oxford University Press, New York.

Post ML, Corke TC 2004, "Separation control using plasma actuators: stationary and oscillatory airfoils," Presented at 42nd AIAA Aerospace Sciences Meeting and Exhibit, Reno, Nevada AIAA paper number 2004-0841.

Prasad, K, Adrian, RJ, Landreth, CC and Offutt, PW 1992, "Effect of resolution on the speed and accuracy of particle image velocimetry interrogation," *Experiments in Fluids*, **13**, pp. 105-116.

Presz, Jr. WM, Paterson, RW and Werle, MJ 1989, Airfoil shaped body, U.S. patent 4,830,315.

Quantel 2002, *Brilliant and Brilliant-B Nd:Yag Laser, Instruction manual issue no. 5*, Quantel, France.

Raffel, M, Willert, CE, and Kompenhans, J 1998, *Particle image velocimetry: a practical guide*, Springer, Berlin.

Reda, DC and Wilder, MC n.d., "Measurement of continuous surface shear stress vector distributions," Lecture Two, NASA - Ames Research Center, Moffett Field, CA.

Reeves, M and Lawson, NJ 2004, "Evaluation and correction of perspective errors in endoscopic PIV," *Experiments in Fluids*, **36**, pp. 701-705.

Reithmaier, L 1995, *Mach 1 and beyond: the illustrated guide to high-speed flight*, McGraw-Hill, New York, p. 63.

Roshko, A 1954, "On the wake and drag of bluff bodies," *Journal of Aerospace Science*, 22, pp. 124–132.

Roth, JR 2003, "Aerodynamic flow acceleration using piezoelectric and peristaltic electrohydrodynamic effects of a One Atmosphere Uniform Glow Discharge Plasma," *Physics of Plasmas*, 10, pp. 2117-2126.

Schlichting, H & Gersten, K 2000, *Boundary layer theory*, Springer-Verlag, New York.

Schmid, SJ and Selberg, BP 1993, "Analysis of the effect of surface heating on boundary layer development over an NU-0215 airfoil," *Proceedings of 11th AIAA Applied Aerodynamics Conference*, Monterey, California, 9-11th August, pp. 320-331.

Scruton, C, Walshe, DE 1963, *Stabilisation of wind-excited structures*, US Patent 3076533.

Seifert, A, Bachar, T, Koss, A, Shepshelovich, M and Wyganski, I 1993, "Oscillatory blowing, a tool to delay boundary layer separation," *AIAA Journal*, 31, pp. 2052-2060.

Seifert, A 2007, "Closed-loop active flow control systems: actuators," in King, R (Ed.): *Active Flow Control*, NNFM 95, Springer-Verlag, Berlin, pp. 85–102.

Simons, M 1999, *Model Aircraft Aerodynamics*, Special Interest Model Books, Dorset, UK.

Smits, AJ and Lim, TT (eds.) 2000, *Flow visualization*, Imperial College Press, London.

Soderman, PT 1972, "Aerodynamic effects of leading edge serrations on a two-dimensional airfoil," NASA TM X-2643.

Somers, DM and Tangler, JL 2000, "Wind-tunnel tests of two airfoils for wind turbines operating at high Reynolds numbers," National Renewable Energy Laboratory, Colorado.

Stafford, T 2010, Tubercle fin, viewed 29th January, 2012, <<http://www.quivermag.com/boards/tim-stafford-surfboards-2010-0>>.

Stanway, MJ 2008, "Hydrodynamic effects of leading edge tubercles on control surfaces and in flapping foil propulsion," Thesis submitted to Massachusetts Institute of Technology, February.

Stein, B and Murray, MM 2005, "Stall mechanism analysis of Humpback whale flipper models," Proceedings of Unmanned Untethered Submersible Technology (UUST), Durham, NH, August.

Swalwell, KE and Sheridan, J 2001, "The effect of turbulence intensity on stall of the NACA 0021 aerofoil," *14th Australasian Fluid Mechanics Conference*, Adelaide, 10-14th December 2001.

Swatton, PJ 2011, Principles of flight for pilots, John Wiley & Sons Ltd., Chichester, UK.

Tam, CKW 1974, "Discrete tones of isolated airfoils," *Journal of the Acoustical Society of America*, 55, pp. 1173-1177.

Tam, CKW and Ju, H 2011, "Aerofoil tones at moderate Reynolds number," *Journal of Fluid Mechanics*, **690**, pp. 536-570.

Tavoularis, S. 2005, *Measurement in fluid mechanics*, Cambridge University Press, New York.

Thompson, DH 1990, "Water tunnel flow visualisation of vortex breakdown over the F/A-18," *Flight Mechanics Report*, **179**, DSTO Aeronautical Research Laboratory, Melbourne.

Thompson, DH 1997, "Effect of the leading edge extension (LEX) fence on the vortex structure over the F/A-18," DSTO-TR-0489, Melbourne, pp. 1-57.

Torenbeek, E 1982, Synthesis of subsonic airplane design, Delft University Press, Delft, The Netherlands.

Torgerson, SD, Liu, T, Sullivan, JP 1996, "Use of pressure sensitive paints in low speed flows," 19th AIAA Advanced Measurement and Ground Testing Technology Conference, New Orleans, June 17-20, *AIAA Paper* 96-2184.

Traub, LW and Cooper, E 2008, "Experimental investigation of pressure measurement and airfoil characteristics at low Reynolds numbers," *Journal of Aircraft*, **45**, pp. 1322-1333.

Tritton, DJ 1977, Physical fluid dynamics, Van Nostrand Reinhold, New York, Section 22.7: The Coandă Effect.

Tuck, A and Soria, J 2004, "Active flow control over a NACA 0015 airfoil using a ZNMF jet," Proceedings of the 15th Australasian Fluid Mechanics Conference, 13–17th December, Sydney.

van Nierop, E, Alben, S & Brenner, MP 2008, "How bumps on whale flippers delay stall: an aerodynamic model," *Physical review letters*, PRL 100, 054502, February.

Walsh, MJ and Anders, JB 1989, "Riblet/LEBU research at NASA Langley," *Applied Scientific Research*, **46**, pp. 255-262.

Watts, P and Fish, FE 2001, "The influence of passive, leading edge tubercles on wing performance," Proceedings of the Twelfth International Symposium on Unmanned Untethered Submersible Technology UUST, Autonomous Undersea Systems Institute, Lee, NH, Aug. 2005.

Watts, P and Fish, FE 2002, Scalloped wing leading edge, U.S. patent 6,431,498 B1.

Watts, P and Fish, FE 2006, Scalloped leading edge advancements, U.S. patent application 2006/0060721 A1.

Weber, PW, Howe, LE and Murray MM 2010, "Lift, drag and cavitation onset on rudders with leading edge tubercles," *Marine Technology*, 47, pp. 27-36.

Weihs, D 1981, "Effects of swimming path curvature on the energetics of fish swimming," *Fishery Bulletin*, 79, pp. 171-176.

Werle, MJ, Paterson, RW and Presz Jr., WM 1987, "Trailing-edge separation/stall alleviation," *AIAA Journal*, 25, pp. 624-626.

Westerweel, J 1994, "Efficient detection of spurious vectors in particle image velocimetry data," *Experiments in Fluids*, 16, pp. 236-247.

Westerweel, J, Dabiri, D and Gharib, M 1997, "The effect of a discrete window offset on the accuracy of cross-correlation analysis of digital PIV recordings," *Experiments in Fluids*, 23, pp. 20-28.

Westerweel J 2000, "Theoretical analysis of the measurement precision in particle image velocimetry," *Experiments in Fluids*, 29, pp. S3-S12.

Westerweel, J and Scarano, F 2005, "Universal outlier detection for PIV data," *Experiments in Fluids*, 39, pp. 1096-1100.

Willert, CE and Gharib, M 1991, "Digital particle image velocimetry," *Experiments in Fluids*, 10, pp. 181-193.

Williams, MD 2009, "Wind tunnel analysis and flight test of a wing fence on a T-38," Masters of science in aeronautical engineering thesis, Airforce Institute of Technology, Ohio, USA.

Wilkinson, SP 2003, "Investigation of an oscillating surface plasma for turbulent drag reduction," Presented at 41st AIAA Aerospace Sciences Meeting and Exhibit, Reno, Nevada, AIAA paper number 2003-1023.

Yen, DT, van Dam, CP, Bräuchle, F, Smith, RL, and Collins, SD, “Active load control and lift enhancement using MEM translational tabs,” Fluids 2000, AIAA-2000-2422, Denver, CO, June.

Zaman, KBM, Bar-sever, A and Mangalam, SM 1987, “Effect of acoustic excitation on the flow over a low-Re airfoil,” Journal of Fluid Mechanics, 182, pp. 127-148.

Zibkoff, M 2009, Spoked bicycle wheel, U.S. patent application 2009/0236902 A1.

Zverkov, I and Zanin, B 2008, ‘Disturbances growth in boundary layers on classical and wavy surface wings,’ *AIAA Journal*, **46**, pp. 3149-3158.

Appendices

Appendix A – Force Transducer Calibration

It was necessary to perform a static calibration of the load cell to determine the uncertainty associated with the device. This involved using fishing wire wrapped around the airfoil and then extending this wire to the exit of the experimental rig, over a low friction pulley and connecting it to a mass, which was suspended in free space. The largest problems that presented themselves for this calibration were ensuring that load was applied exclusively to the axis being calibrated and that friction from the pulley was negligible.

When the airfoil was not pulled from the centre point, a cross-coupling would result on the load cell. This was solved by wrapping the line around the airfoil rather than tying a knot, where two lines then extended backward toward the mass instead of one. However, this introduced the problem of an uneven distribution of the force between the two lines due to friction. This friction could be reduced by applying silicon spray to the model surface.

The calibration process was carried out for the x-direction (F_x), y-direction (F_y) and pitching moment (M_z) using 8 masses and plotting the relationship between measured force and actual force. Masses were selected in the range of the expected lift and drag forces. It was found that the uncertainty in the x-direction was around 1% and in the y-direction around 2%. These values are considered in the uncertainty analysis discussed in Chapter 4.

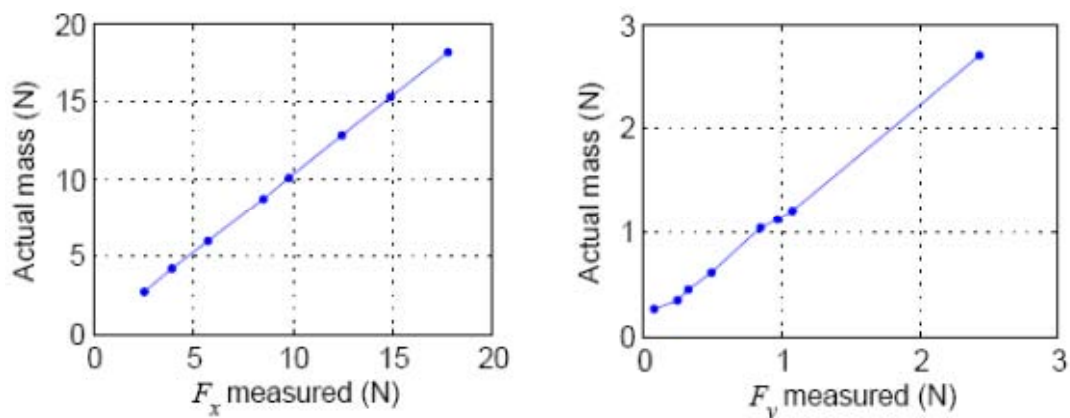


Figure A1 – Calibration plots for F_x and F_y

Appendix B – Efficiency Plots for Force Measurements

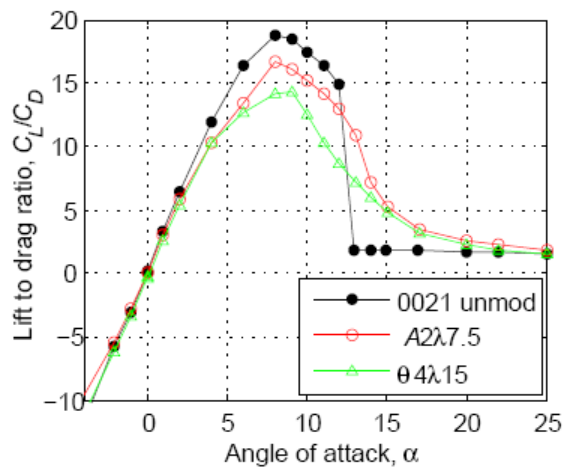


Figure B1 – Lift-to-drag ratio against angle of attack for full-span NACA 0021, $Re = 120,000$.

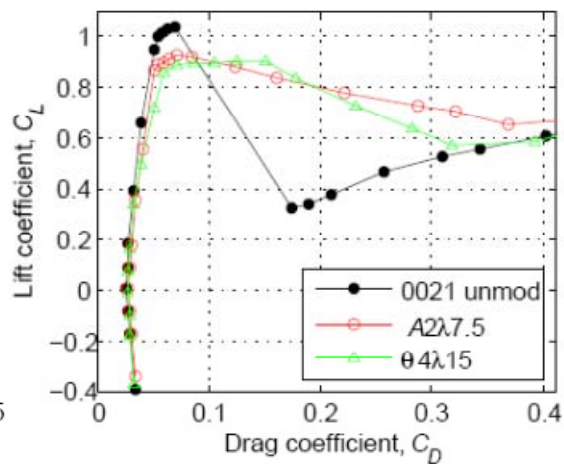


Figure B2 – Polar plot for full-span NACA 0021, $Re = 120,000$.

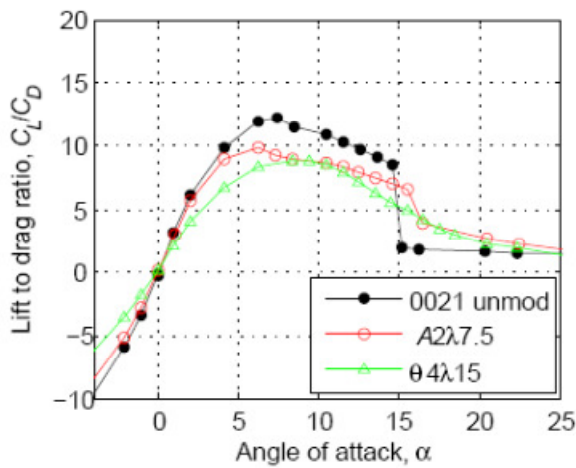


Figure B3 – Lift-to-drag ratio against angle of attack for half-span NACA 0021, $Re = 120,000$.

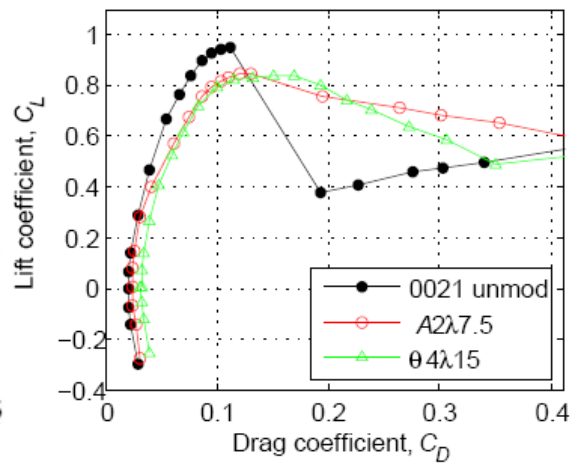


Figure B4 – Polar plot for half-span NACA 0021, $Re = 120,000$.

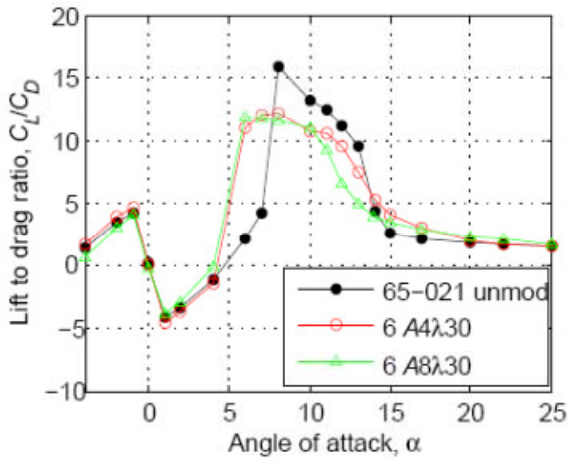


Figure B5 – Lift-to-drag ratio against angle of attack for full-span NACA 65-021, $Re = 120,000$.

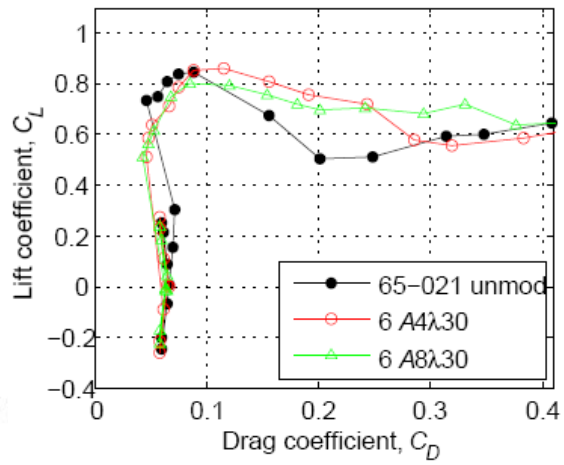


Figure B6 – Polar plot for full-span NACA 65-021, $Re = 120,000$.

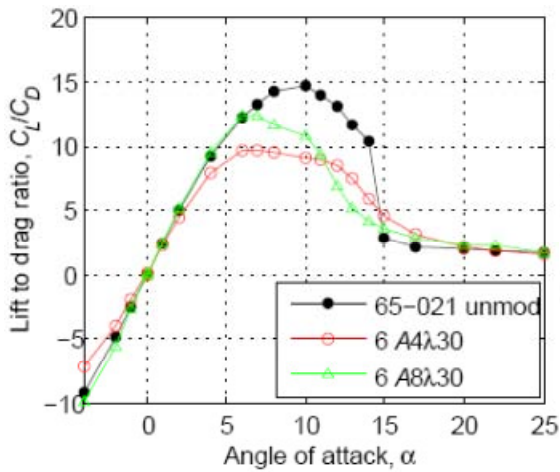


Figure B7 – Lift-to-drag ratio against angle of attack for tripped NACA 65-021, $Re = 120,000$.

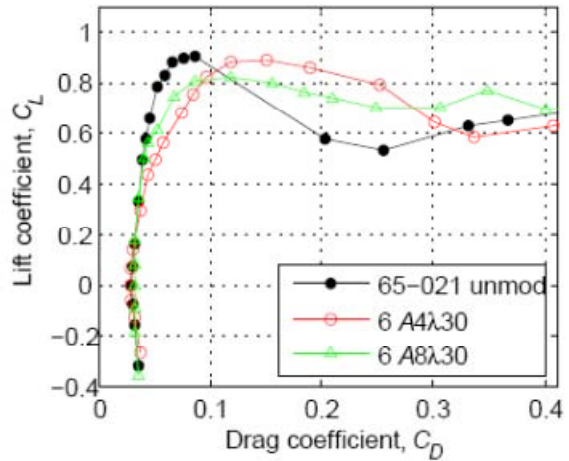


Figure B8 – Polar plot for full-span tripped NACA 65-021, $Re = 120,000$.

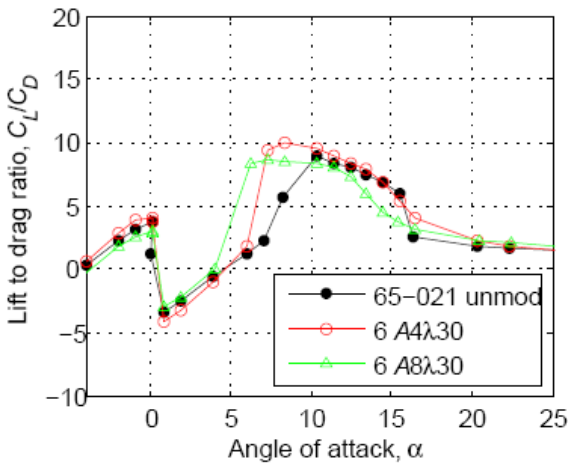


Figure B9 – Lift-to-drag ratio vs. angle of attack for half-span NACA 65-021, $Re = 120,000$.

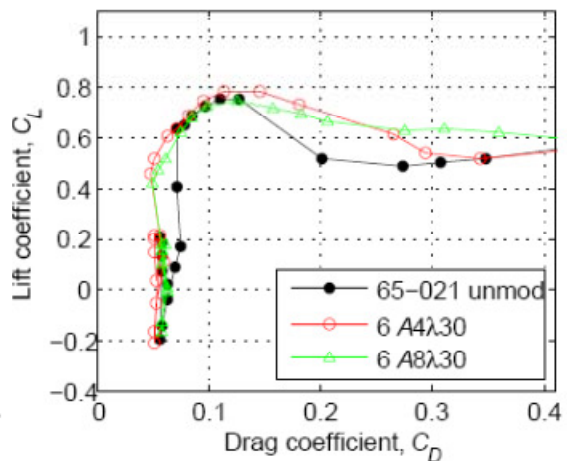


Figure B10 – Polar plot for half-span NACA 65-021, $Re = 120,000$.

Appendix C – Surface pressure measurement feasibility study

C1 Expected pressure forces

An estimate of the pressure forces was obtained for $U_\infty = 25\text{m/s}$ using XFOIL, which is a program capable of performing a viscous analysis of a given airfoil geometry. The expected pressures (kPa) are shown in Figure B1 for angles of attack, $\alpha = 0^\circ, 5^\circ, 10^\circ$ and 12° .

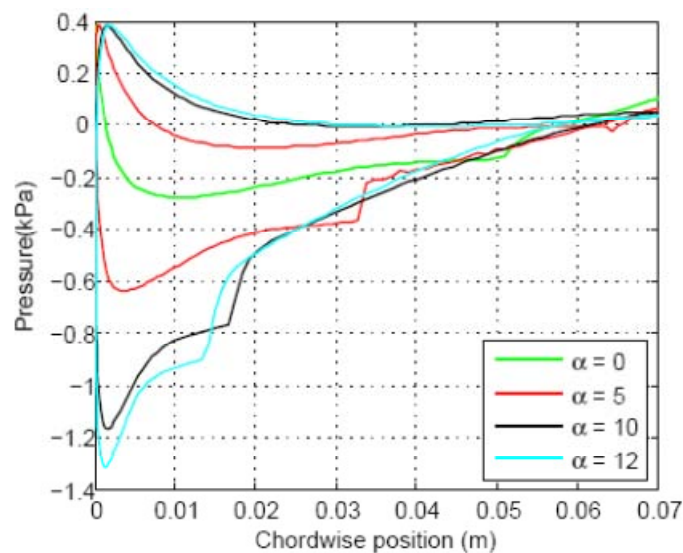


Figure C1 – Plot of expected pressure distribution obtained using XFOIL

Nakano Fujisawa, Oguma, Takagi & Lee (2006) found consistency between measurements taken with a pressure transducer and liquid crystal visualisation results of separation and reattachment points for pressures in the range of 0 - 0.9kPa, which is close to the expected pressures shown in Figure B1. The usable range for liquid crystals is quoted in terms of surface shear stress, τ , and lies in the range of $\tau = 5\text{-}50\text{Pa}$ (Reda & Wilder, n.d.). According to XFOIL calculations, the expected shear stress for the current experiments is in the range $\tau = 0\text{-}25\text{Pa}$. Pressure sensitive paint is capable of measuring

pressures in the range of 0 - 0.35kPa with a resolution of ~ 0.02 kPa (Bell, 2004). The upper limit for this technique is at least 170kPa (Morris Donovan, Kegelmann, Schwab, Levy & Crites, 1993). Pressure taps are a standard technique for measuring the pressure distribution around airfoils and have been used extensively by previous researchers. More specifically, the viability of this method has been demonstrated for similar flow conditions to the current study (Traub & Cooper, 2008). Thus, these three methods are capable of resolving the expected pressure forces.

C2 Complexity

The existing test rig which was bolted to the wind tunnel contraction is made of wood and has a single acrylic window. For the liquid crystal surface visualisation technique, it is necessary to utilise two cameras and a source of illumination as shown in Figure B2. This method would therefore require a custom built test section to be implemented.

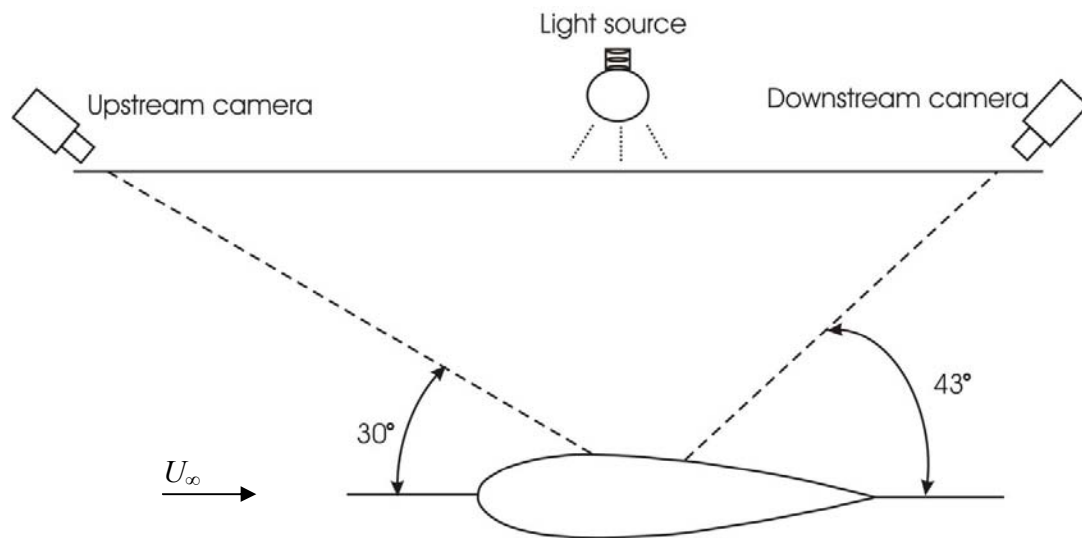


Figure C2 – Top view of set-up required for liquid crystal surface visualisation

The pressure sensitive paint technique is complicated for a number of reasons. These include: the tendency for the luminescent molecules in the paint to degrade with time of exposure to illumination, sensitivity to temperature and humidity, and requirements of uniform illumination and even distribution of paint over the object's surface (Torgerson, Liu & Sullivan, 1996). Overall, this technique requires a very careful setup, especially when the pressures involved are relatively low, as shown in Figure B1.

The simplest method of sensing steady or slowly-varying static pressure at a wall is through drilling small holes (taps) and connecting them via tubing to a pressure transducer (Tavoularis, 2005). However, the accuracy of this technique decreases with increasing hole diameter and there can be some difficulty in machining small holes that are clean and perpendicular to the surface.

C3 Difficulty in interpreting images

Implementation of the china clay technique with a mixture of toothpaste, cornflour and water was successfully carried out by Lee (2009). However, despite the fact that several different ratios of these constituents were mixed and applied to the airfoils in the current experiments, the resulting images lacked clarity and thus did not provide any conclusive information. Figure B3 shows the separation line of an airfoil at ($\alpha = 10^\circ$).



Figure C3 – Surface flow visualisation of mid-span using toothpaste ($\alpha = 10^\circ$, $U_\infty = 25\text{m/s}$)

Appendix D – Airfoil structural resonance frequency measurements

Figures D1 to D4 provide more details about the coherence and signal to noise ratio for the transfer functions presented in Section 3.8. The coherence is a measure of how well the impact hammer and accelerometer signals are correlated and should be close to 1 at the frequencies of interest. It can be seen that at the frequencies corresponding to the peaks in the transfer function, the coherence is high. The figures in the right-hand columns show that the measurements are well above the noise floor of the impact hammer and accelerometer.

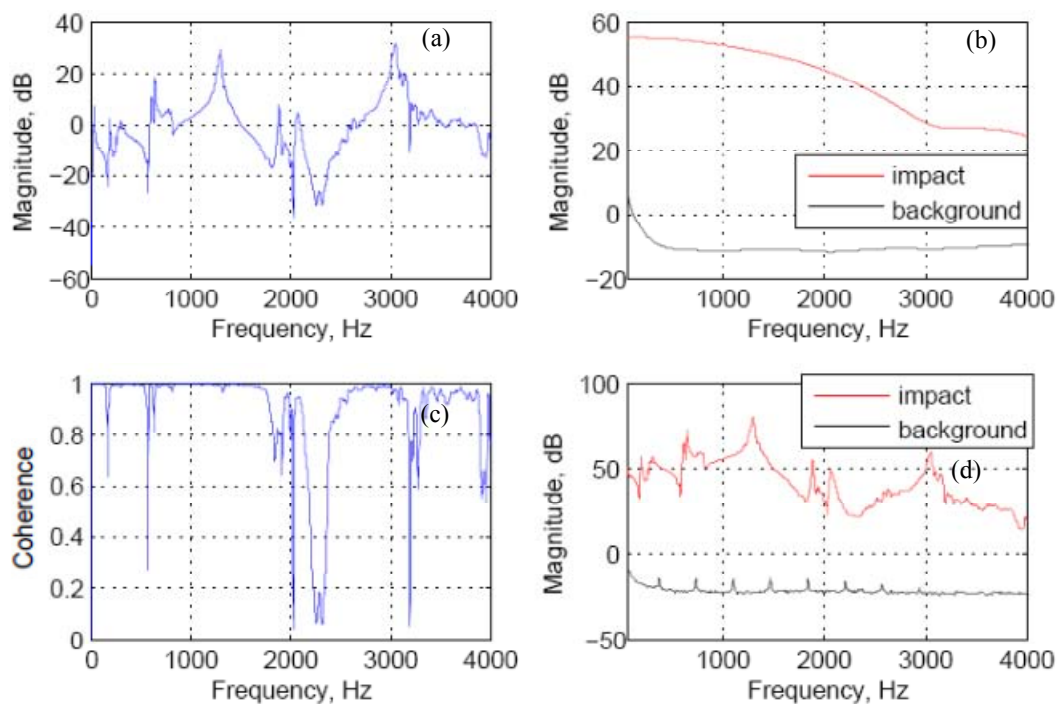


Figure D1 – Structural resonance frequencies for unmodified NACA 0021 airfoil in vertical mount.

(a) Transfer function (b) impact hammer magnitude (c) coherence (d) accelerometer magnitude

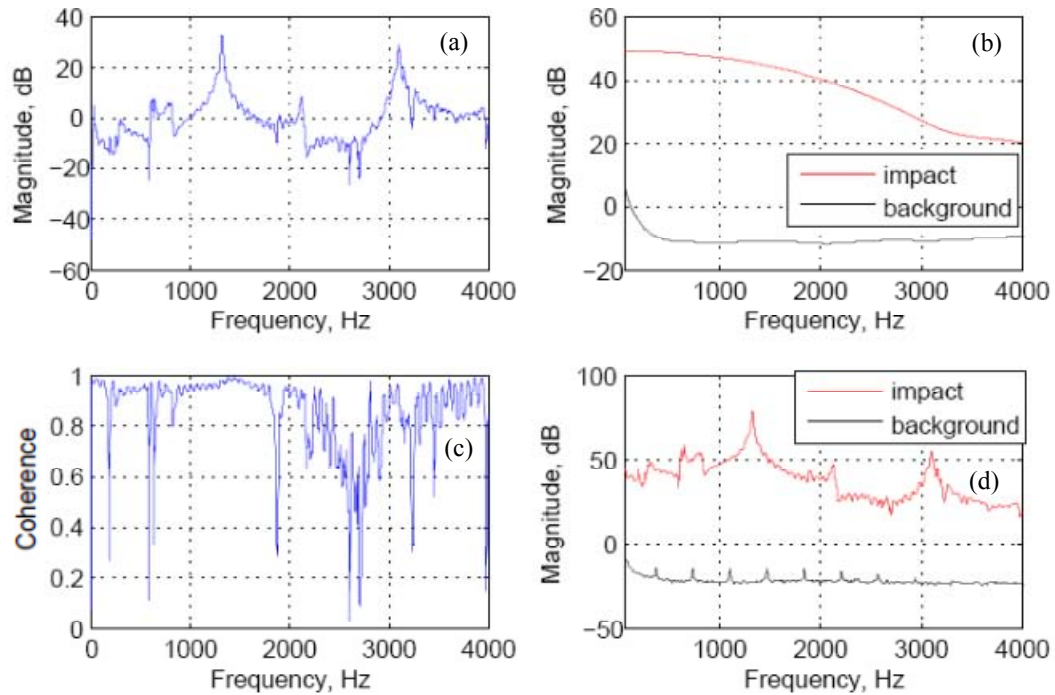


Figure D2 – Structural resonance frequencies for NACA 0021 airfoil in vertical mount with *A2A7.5* tubercle configuration. (a) Transfer function (b) impact hammer magnitude (c) coherence (d) accelerometer magnitude

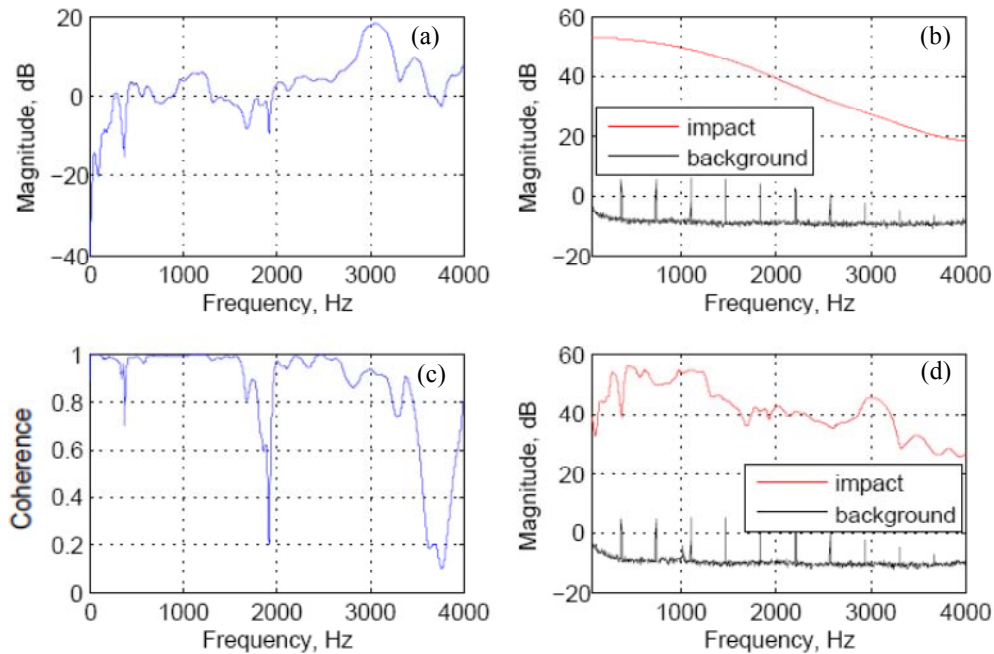


Figure D3 – Structural resonance frequencies for unmodified NACA 0021 airfoil in horizontal mount. (a) Transfer function (b) impact hammer magnitude (c) coherence (d) accelerometer magnitude

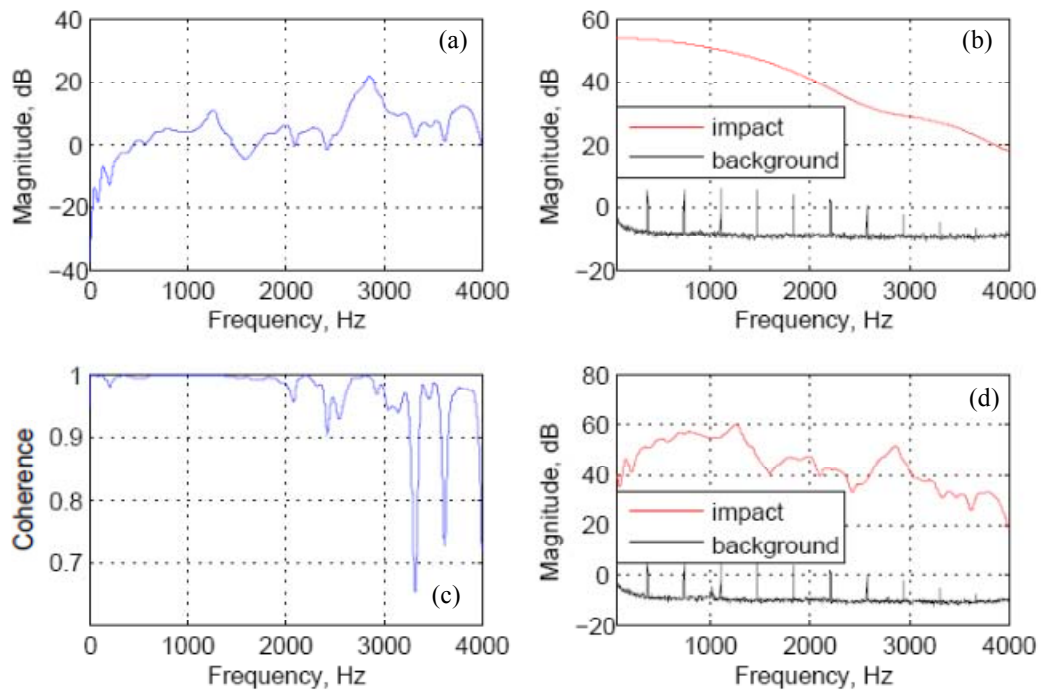


Figure D4 – Structural resonance frequencies for NACA 0021 airfoil in horizontal mount with $A2\lambda7.5$ tubercle configuration. (a) Transfer function (b) impact hammer magnitude (c) coherence (d) accelerometer magnitude

Appendix E – Proposed Flow Topology for a Tubercle

NOTE:

This figure/table/image has been removed to comply with copyright regulations. It is included in the print copy of the thesis held by the University of Adelaide Library.

Figure E1 – Sequence of possible skin-friction line patterns in the nose region of a slender configuration, which approximates the shape of a single tubercle (Tobak & Peake, 1979).

NOTE:

This figure/table/image has been removed to comply with copyright regulations. It is included in the print copy of the thesis held by the University of Adelaide Library.

Figure E2 – One possible vortex skeleton for an owl-face of the second kind, where the primary vortices are located below the secondary vortices. Image vortices under the horizontal surface are not shown (Perry & Chong, 1987).